LEABHARLANN CHOLÁISTE NA TRÍONÓIDE, BAILE ÁTHA CLIATH
Ollscoil Átha Cliath

TRINITY COLLEGE LIBRARY DUBLIN
The University of Dublin

Terms and Conditions of Use of Digitised Theses from Trinity College Library Dublin

Copyright statement

All material supplied by Trinity College Library is protected by copyright (under the Copyright and Related Rights Act, 2000 as amended) and other relevant Intellectual Property Rights. By accessing and using a Digitised Thesis from Trinity College Library you acknowledge that all Intellectual Property Rights in any Works supplied are the sole and exclusive property of the copyright and/or other IPR holder. Specific copyright holders may not be explicitly identified. Use of materials from other sources within a thesis should not be construed as a claim over them.

A non-exclusive, non-transferable licence is hereby granted to those using or reproducing, in whole or in part, the material for valid purposes, providing the copyright owners are acknowledged using the normal conventions. Where specific permission to use material is required, this is identified and such permission must be sought from the copyright holder or agency cited.

Liability statement

By using a Digitised Thesis, I accept that Trinity College Dublin bears no legal responsibility for the accuracy, legality or comprehensiveness of materials contained within the thesis, and that Trinity College Dublin accepts no liability for indirect, consequential, or incidental, damages or losses arising from use of the thesis for whatever reason. Information located in a thesis may be subject to specific use constraints, details of which may not be explicitly described. It is the responsibility of potential and actual users to be aware of such constraints and to abide by them. By making use of material from a digitised thesis, you accept these copyright and disclaimer provisions. Where it is brought to the attention of Trinity College Library that there may be a breach of copyright or other restraint, it is the policy to withdraw or take down access to a thesis while the issue is being resolved.

Access Agreement

By using a Digitised Thesis from Trinity College Library you are bound by the following Terms & Conditions. Please read them carefully.

I have read and I understand the following statement: All material supplied via a Digitised Thesis from Trinity College Library is protected by copyright and other intellectual property rights, and duplication or sale of all or part of any of a thesis is not permitted, except that material may be duplicated by you for your research use or for educational purposes in electronic or print form providing the copyright owners are acknowledged using the normal conventions. You must obtain permission for any other use. Electronic or print copies may not be offered, whether for sale or otherwise to anyone. This copy has been supplied on the understanding that it is copyright material and that no quotation from the thesis may be published without proper acknowledgement.

The Chemistry of the Uranyl Moiety

Aurora Walshe

Doctor of Philosophy

University of Dublin, Trinity College

Supervisor: Professor Robert Baker

Submitted to the University of Dublin, Trinity College

Declaration

I submit this work for the degree of PhD from Trinity College Dublin. I declare that this thesis has not been submitted as an exercise for a degree at this or any other university and it is a description of my own work. Due acknowledgement and references are given to the work of others where necessary.

I agree to deposit this thesis in the University's open access institutional repository or allow the library to do so on my behalf, subject to Irish Copyright Legislation and Trinity College Library conditions of use and acknowledgement.

Aurora Walshe B. Sc. (Hons.)

Summary

Uranium has had a "Jekyll and Hyde" reputation for many years, stemming from its ability to both create clean and cheap energy and from its ability to create powerful and dangerous weapons. This Thesis examines the chemistry of uranium(VI) in the form of uranyl, $[UO_2]^{2+}$. **Chapter 1** will introduce the chemistry of the *f* block, uranium, uranyl, the known activity of uranium in its +3 to +6 oxidation states and uranium in the nuclear industry. In nature uranium preferentially exists as uranyl and will most often form minerals that can affect the solubility and mobility of uranium in the environment. These minerals can also form as phase transitions on the surface of stored spent nuclear fuel (SNF) and in areas of high uranium concentration – whether naturally or from anthropogenic affects such as mining or nuclear weapons testing. This will also be discussed in **Chapter 1**.

One of these phase transitions is the formation of the uranyl peroxide mineral studtite, $[(UO_2)(\eta^2\text{-}O_2)(H_2O)_2]\cdot 2H_2O$. Studtite is not the only product, but it has been found to be the thermodynamically favoured product in deionised water over two years: uranyl oxyhydroxide minerals schoepite, $[(UO_2)_8O_2(OH)_{12}]\cdot 12H_2O$, and metaschoepite, $[(UO_2)_8(O)_2(OH)_{12}]\cdot 10H_2O$, and uranyl silicates such as soddyite, $[(UO_2)_2(SiO_4)]\cdot 2H_2O$, have all been found to evolve into studtite, indicating the long-term relevance of studtite to the stability of SNF. For this reason, studtite has become a focus of research in the last decade. **Chapter 2** will explore the structural and electronic differences between studtite and its dehydrated congener metastudtite, $[(UO_2)(\eta^2\text{-}O_2)(H_2O)_2]$. The effect of dehydration (i.e. removal of the two interstitial water molecules from the unit cell) upon the uranyl moiety and the bonding within the mineral will be investigated using XANES (X-ray Absorption Near-Edge Structure Spectroscopy) and the resulting structural changes explored with EXAFS (Extended X-ray Absorption Fine Structure). The solid-state electrochemistry of studtite has also been reported to understand and predict interactions with radionuclides in SNF and to elucidate the mechanism for the mobilisation or immobilisation of

radionuclides such as iodine and neptunium, i.e. whether these elements are sorbed on the surface or if they react *via* redox processes.

Chapter 3 shall explore the structural relationships of nine uranyl minerals: four uranyl oxyhydroxide minerals, two carbonate minerals and three natural samples of phosphate minerals were analysed using solid-state cyclic voltammetry. The reduction potentials and diffusion properties of the minerals were analysed and compared according to their chemistry (i.e. different interstitial cations and anionic ligands) and structure (i.e. layered sheets or framework) thus allowing the deduction of probable interactions with SNF.

In **Chapter 4** the non-aqueous chemistry of uranyl complexes will be explored. The ability of uranyl complexes to catalyse the formation of C–O bonds will be explored by the reaction of uranyl with oxygen containing monomers to undergo the ring-opening oligomerisation of epoxides and lactones. The mechanism of this reaction will be examined and explored in detail using spectroscopic and computational techniques.

Acknowledgements

So many people have helped me both inside and outside the lab, but here are some of the important ones:

I would like to thank my supervisor Dr Bob Baker for all of his support, assistance and limitless enthusiasm; the project students and interns for making working in the lab more fun, and my colleague and friend Emi Hashem for all of her help in the lab, for her sense of humour during coffee breaks, and for allowing me to live vicariously through her!

This work wouldn't have been possible without the wonderful technical staff at Trinity. I would like to thank Dr Manuel Reuther for his kindness, willingness to help, and encyclopaedic knowledge of almost every spectroscopic instrument known to man, and Dr John O'Brien for his eagerness and his incredible passion for extravagant NMR experiments, and for keeping me up to date on the Agilent drama; Dr Martin Feeney for all of his help with MS, GPC and MALDI-TOF and his willingness to accommodate my last minute demands; Dr Gary Hessman for helping me track down years-old data and for keeping me entertained during demonstrating in the Cocker Lab. To Patsy, Teresa, Tess, Helen, Jill, Noelle and Anna: thanks for helping with the little problems and preventing bigger ones!

I would like to thank Dr Carola Schulzke for donating her time and assistance with the electrochemical methods and for sharing her glassware and equipment and Dr Luis Léon-Vintró, UCD, for helping us with the studtite analysis, giving us access to his Υ-Spectrometer to monitor the ^{241}Am incorporation.

During my PhD I was very fortunate to be able to spend time working in other labs:

I would like to thank Dr Tonya Vitova for allowing me to travel to Karlsruhe Institute of Technology to use her allocated beamtime at the ANKA facility. Her support and patience both during my stay and since while helping me analyse my data has been invaluable. During my stay, Tim Prüßmann was fantastic. He taught me about the instruments and ran my samples and helped me understand each step of the process. He,

Jorg Röthe, Melissa Denecke and so many others at the INE made me feel so welcome; I thoroughly enjoyed my time there and count this as a life experience. I would like to acknowledge the EU COST Programme for funding my trip.

I would like to thank Dr Colm Mallon, DCU, for performing the electrochemical analysis of studtite. Professors Tia Keyes and Robert Forster were wonderful in their assistance – allowing use of their equipment and for helping to understand the wealth of data. Dr Elaine Spain needs special mention for training me on the equipment and keeping an eye on me for six weeks, and for running over 100 EDX samples!

I would also like to thank the Irish Research Council and Trinity College Dublin for funding for my four years. I would also like to thank the Young Chemists' Crossing Borders Exchange Programme for financial assistance to attend the ACS Fall Meeting in Indianapolis, September 2013. The Trinity Trust Travel Fund, the Institute of Chemistry of Ireland, the European Young Chemists' Network and the Royal Society of Chemistry also supported me to travel and present my work at conferences such as the EuCheMS Chemistry Congresses in 2010 and 2012 and to RSC Young Members Meetings; and special thanks go to the COST f Element Network for education and support and for the chance to meet so many like-minded researchers.

To the members of EYCN – Fred, Cris, Vivi, Santi, Luke, Colin, Jens and so many more – for giving me the opportunity to travel, to network, to write and to speak on behalf of young chemists in Brussels, Indianapolis, St. Petersburg and beyond. These experiences have helped me grow as a chemist and as a person and have given me a wonderful group of friends spread over 20 countries.

And last, but very definitely not least, I would like to thank my family and closest friends for keeping me sane and happy, even when nothing was working...

Mum, Dad, Paul, Kim, Fleur, Laila, Tim, Gary, Dave, Big Dave, Ryan, Ronan, Paul, Dee... You guys rock. To Fiona: I wish you could be here.

Abbreviations

α	alpha particle ($^{4}_{2}He^{2+}$)
β	beta particle (e^-)
γ	gamma particle

An	Actinoid
βBL	β-Butyrolactone
γBL	γ-Butyrolactone
εCL	ε-Caprolactone
CCI	Cation-cation Interaction
CHO	Cyclohexene Oxide
COT	Cyclooctatetraenyl, $[C_8H_8]^{2-}$
Cp	Cyclopentadienyl, $[C_5H_5]^-$
Cp*	Pentamethylcyclopentadienyl, $[C_5Me_5]^-$
dcm	Dichloromethane
DMBO	Dimethylbutene Oxide
DOSY	Diffusion Oriented NMR Spectroscopy
dipp	2,6-diisopropylphenyl $[2,6\text{-}i\text{Pr}_2C_6H_3]^-$
EDX	Energy Dispersive X-Ray Spectroscopy
Et	Ethyl, C_2H_5
Et_2O	Diethyl ether
EtOH	Ethanol
EXAFS	Extended X-Ray Absorption Fine Structure
EXSY	Exchange Spectroscopy
FDTO	Fluorine-Doped Tin Oxide
GPC	Gel permeation chromatography
*i*Pr	Isopropyl, $-CH(CH_3)_2$
L	Ligand

lac	*rac*-Lactide
Ln	Lanthanoid
M	Metal
MALDI-ToF	Matrix Assisted Laser Desorption Ionisation - Time of Flight
Me	Methyl, CH_3
MeCN	Acetonitrile
MS	Multiple Scattering
NA	Nucleophilic Attack
NMR	Nuclear magnetic resonance
^{1}H NMR	Proton NMR
^{13}C NMR	Proton decoupled carbon NMR
PFGSTE	Pulsed Field Gradient Stimulated Echo NMR Spectroscopy
PO	Propylene Oxide
PUREX	Plutonium and Uranium Reduction and Extraction
ROP	Ring-Opening Polymerisation
SEM	Scanning Electron Microscopy
SNF	Spent Nuclear Fuel
tacn	1,4,7-triazocyclononane
*t*Bu	Tertbutyl, $-C(CH_3)_3$
thf	Tetrahydrofuran
TM	Transition Metal
TS	Transition State
δVL	δ-Valerolactone
XANES	X-Ray Absorption Near-Edge Spectroscopy
XAS	X-Ray Absorption Spectroscopy

Uranyl Minerals

* = mineral analysed within this Thesis

Carbonate Minerals:

Agricolaite	$K_4[(UO_2)(CO_3)_3]$
Andersonite*	$Na_2Ca[UO_2(CO_3)_3]\cdot 6H_2O$
Calcite	$CaCO_3$
Grimselite*	$K_3Na[UO_2(CO_3)_3]\cdot H_2O$
Leibigite	$Ca_2[(UO_2)(CO_3)_3]\cdot 11H_2O$
Rutherfordine	$UO_2(CO_3)$
Voglite	$Ca_2Cu[(UO_2)(CO_3)_4]\cdot 6H_2O$
Zellerite	$Ca[(UO_2)(CO_3)_2]\cdot 5H_2O$

Oxyhydroxide Minerals:

Becquerelite*	$Ca[(UO_2)_6O_4(OH)_6]\cdot 8H_2O$
Compreignacite*	$K_2[(UO_2)_6O_4(OH)_6]\cdot 7H_2O$
Curite	$Pb_3[(UO_2)_8O_8(OH)_6\cdot 3H_2O$
Fourmarierite	$Pb[(UO_2)_4O_3(OH)_4]\cdot 4H_2O$
Schoepite*	$[(UO_2)_8O_2(OH)_{12}]\cdot 12H_2O$
Metaschoepite*	$[(UO_2)_8(O)_2(OH)_{12}]\cdot 10H_2O$ (or $UO_3\cdot 2H_2O$)
Studtite*	$[(UO_2)(\eta^2\text{-}O_2)(H_2O)_2]\cdot 2H_2O$ or $[(UO_2)(O_2)(H_2O)_2]\cdot 2H_2O$
Metastudtite*	$[(UO_2)(\eta^2\text{-}O_2)(H_2O)_2]$ or $[(UO_2)(O_2)(H_2O)_2]$
Uraninite	UO_2

Phosphate Minerals:

Autunite	$Ca[(UO_2)_2(PO_4)_2]\cdot 11H_2O$
Meta-autunite*	$Ca[(UO_2)_2(PO_4)_2]\cdot 6\text{-}8H_2O$

Lehnerite	$Mn[(UO_2)_2(PO_4)_2]\cdot 8H_2O$
Meta-ankoleite	$K_2[(UO_2)_2(PO_4)_2]\cdot 6H_2O$
Parsonsite	$Pb_2[(UO_2)_2(PO_4)_2]\cdot 2H_2O$
Phosphuranylite	$KCa(H_3O)[(UO_2)_7(PO_4)_4O_4]\cdot 8H_2O$
Torbernite	$Cu[(UO_2)_2(PO_4)_2]\cdot 12H_2O$
Meta-torbernite*	$Cu[(UO_2)_2(PO_4)_2]\cdot 8H_2O$
Uranocircite*	$Ba[(UO_2)_2(PO_4)_2]\cdot 10H_2O$
Metauranocircite	$Ba[(UO_2)_2(PO_4)_2]\cdot 6\text{-}8H_2O$

Silicate Minerals:

Boltwoodite	$Na,K[(UO_2)(HSiO_4)]\cdot 0.5H_2O$
Sklodowskite	$Mg[(UO_2)_2(HSiO_4)_2]\cdot 6H_2O$
Soddyite	$(UO_2)_2(SiO_4)\cdot 2H_2O$
Uranophane	$Ca[(UO_2)_2(HSiO_4)_2]\cdot 5H_2O$

Publications

An EXAFS and HR-XANES study of the uranyl peroxides $[UO_2(\eta^2\text{-}O_2)(H_2O)_2]\cdot nH_2O$ (n = 0, 2) and uranyl (oxy)hydroxide $[(UO_2)_4O(OH)_6]\cdot 6H_2O$

Aurora Walshe, Tim Prüßmann, Tonya Vitova, Robert J. Baker *Dalton Transactions* **2014**, *43*, 4400

A New Mechanism for the Ring-Opening Polymerization of Lactones: Uranyl Aryloxides Induce Intermolecular Catalysis

Aurora Walshe, Jian Fang, Laurent Maron, Robert J. Baker, *Inorganic Chemistry* **2013**, *52,* 9077

Ring-Opening Polymerization of Epoxides Catalyzed by Uranyl Complexes: An Experimental and Theoretical Study of the Reaction Mechanism

Jian Fang, Aurora Walshe, Laurent Maron, Robert J. Baker, *Inorganic Chemistry* **2012,** *51*, 9132

The Physical Characterization and Reactivity of the Uranyl Peroxide $[UO_2(\eta^2\text{-}O_2)(H_2O)_2].2H_2O$: Implications for Storage of Spent Nuclear Fuels

Colm Mallon, Aurora Walshe, Tia Keyes, Robert Forster, Robert J. Baker, *Inorganic Chemistry* **2012,** *51*, 8509

New Reactivity of the Uranyl Ion: Ring Opening Polymerization of Epoxides

Robert J. Baker, Aurora Walshe, *Chemical Communications* **2012,** *48*, 985

The Coupling of Pyridine and Dichloromethane Mediated by UO_2Cl_2

Robert J. Baker, Emtithal Hashem, Majid Motevalli, Helen V. Ogilvie, Aurora Walshe, *Zeitschrift für Anorganische und Allgemeine Chemie* **2010**, *636*, 443

Table of Contents

List of Figures

Chapter 3: Uranyl Minerals Relevant to the Long Term Storage of Spent Nuclear Fuel II: Uranyl Oxyhydroxides, Phosphates and Carbonates............ 103

Chapter 4: Uranyl Complexes as Catalysts for C-O Bond Formation 191

List of Schemes

Chapter 1: Introduction 1

Chapter 4: Uranyl Complexes as Catalysts for C-O Bond Formation............... 191

List of Tables

Chapter 1:

Introduction

1.1. Introduction

This Thesis will describe research into the chemistry of uranium in its +6 oxidation state in the form $[UO_2]^{2+}$, known as uranyl. Uranium is the heaviest naturally occurring element. It is the fourth element in the actinide group in the *f*-block. The *f*-block is the term for the two rows of elements at the bottom of the periodic table and is named in the same manner as the *s*-, *p*- and *d*-blocks.

This Introduction will depict the differences between the *d*- and *f*-block elements and the differences between the *4f* (lanthanide) and *5f* (actinide) elements, focussing on the known properties of uranium. The electronic structure of the uranyl moiety will be discussed, as will some samples of the variety of catalytic transformations possible with uranium. **Chapter 4** of this Thesis will discuss the hitherto unknown ability of uranyl compounds to act as ring-opening oligomerisation catalysts. These Lewis acidic, highly oxophilic species have been observed to ring-open oxygen containing monomers, cyclic epoxides[1] and lactones,[2] to yield oligomers with low polydispersities.

The nuclear fuel cycle, fuel reprocessing methods, and the effects of the local environment on the spent nuclear fuel – such as phase transitions and the formation of uranyl minerals – will be introduced. **Chapters 2** and **3** of this Thesis will describe the chemistry of uranyl in the environment in more detail, examine the electronic character of uranyl minerals and consider the possible impact of this on the long-term storage of nuclear fuel.

1.1.1. Lanthanides and Actinides

The first row of the *f*-block is the lanthanide series, (Ln). The lanthanide *4f* orbitals are shielded by the *5d* and *6s* orbitals and so are not part of the valence shell and can be considered "core-like" [**Figure 1.1 (top)**]. This gives the lanthanides interesting magnetic properties, as the orbital angular momentum is not quenched by crystal field splitting in a complex as it is in transition metals.[3] It also means that, without the orbital overlap, they form complexes mainly through electrostatic interactions.[4]

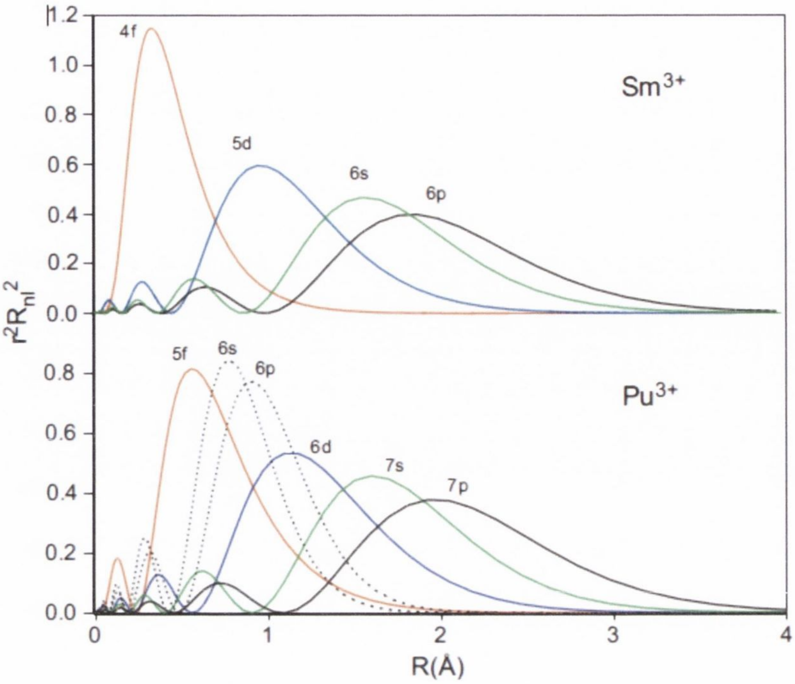

Figure 1.1: A representation of the radial probability factor for selected orbitals of the fifth lanthanide and actinide, respectively, showing the more diffuse actinide orbitals. Taken from reference 5.

The first example of covalency in organolanthanide complexes were the zero-valent bis(arene) sandwich complexes reported by Marks and Cloke.[6] Complexes of $M(TTB)_2$ (where M = Y, Gd, Dy–Er; TTB = η^6–1,3,5–tri*tert*butylbenzene) were found to have unprecedented thermal stability – sublimable at 100 °C – and were the first indication of strong metal→ligand back-bonding in the lanthanoids,[6b] although calculations on $Gd(C_6H_6)_2$ imply that this arises from the *5d* and not from the *4f* orbitals.[7] This work was expanded upon by Evans *et al.* by showing covalency in lanthanide(III) complexes: dysprosium(III) shows side-on binding and reduction of dinitrogen to $[N_2]^{2-}$ in $[(ArO)_2Dy(thf)]_2(\mu\text{–}\eta^2\text{:}\eta^2\text{–}N_2)$ **[Figure 1.2(a)]** and the unusual $[N_2]^{3-}$ ion observed in $[(ArO)_2Dy(thf)]_2(\mu\text{–}\eta^2\text{:}\eta^2\text{–}N_2)[K(thf)_6]$, **[Figure 1.2(b)]**, where Ar = 2,6–di*tert*butylphenyl.[8]

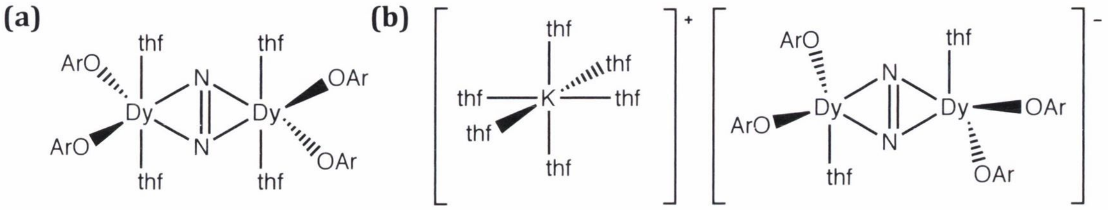

Figure 1.2: The first example of covalency in a lanthanide(III) complex, Ar = 2,6–di*tert*butylphenyl.[9]

These and the diamagnetic ^{15}N–yttrium(III) analogues were synthesised and the dinitrogen anions analysed using ^{15}N NMR, Electron Paramagnetic Resonance (EPR) and Raman spectroscopies to confirm the presence of the anionic dinitrogen species. However, subsequent analysis of the Kohn-Sham orbitals suggests that the *5d* orbitals are symmetry appropriate for the nodal structure of the N_2 π^* orbitals and therefore the covalent character of the complexes arises from *5d* interaction and not the *4f*, indicating that the core-like lanthanide *f* orbitals still do not participate in bonding.[9] Evans and co-workers have recently expanded Ln(II) chemistry across the lanthanide series by reducing the Ln(III) complex Cp'_3Ln, where Cp′ = $C_5H_4SiMe_3$, with KC_8 in the presence of the 2.2.2-cryptand to yield [K(2.2.2-cryptand)][Cp'_3Ln].[10] This work has shown that upon reduction to Ln(II) there is a preference for the $4f^n$ $5d^1$ electron configurations,[10a] as opposed to the $4f^{n+1}$ configurations of the traditional Eu^{2+}, Yb^{2+}, Sm^{2+}, Tm^{2+}, Dy^{2+}, and Nd^{2+} ions.[11] This configuration has been confirmed using EPR and UV/vis spectroscopy and X-ray crystallographic diffraction. Density Functional Theory (DFT) calculations indicate that the large extinction coefficients arise from the large degree of overlap between unoccupied metal *d* and ligand π^* orbitals. This would imply that the *5d* orbitals are lowered to the appropriate energy range for chemical interactions, while the *4f* orbitals remain core-like and do not interact strongly with the ligand field.

The second row of the *f*-block is the actinide series, (An). In general, early actinide chemistry differs substantially from that of the late actinides. In the early actinides the *5f* orbitals are not core-like and extend out, along with the *6d* and *7s* orbitals [**Figure 1.1(bottom)**]. These outer electrons can participate in bonding, potentially giving covalent character to the bonding in the early actinide complexes.[12] The transuranic elements, however, are shown to have properties similar to the lanthanides: relativistic effects cause the contraction of the *5f* orbitals across the actinides, lowering the energy of the *5f* electrons and mimicking the core-like lanthanide *4f* orbitals.[13]

This can be revealed upon closer examination of cyclopentadienyl (Cp) actinide complexes. The atomic ground state of the early actinide elements (Pa – Pu) can occupy both *5f* and *6d* orbitals (**Table 1.1**). In these elements the *5f* and *6d* orbitals are very close in energy and these elements can use either the *5f* or *6d* orbitals or both in bonding, allowing them to follow the *d*-block elements in their chemical behaviour.[14] A 1989 review of the available experimental and theoretical studies of Cp–actinide bonding arrived at the conclusion that the Cp–actinide interaction is more covalent than Cp-lanthanide interactions, but more ionic than Cp–transition metal bonding.[15]

Table 1.1: Ground state electronic configuration of actinides in the ground state.

Actinide	Electronic Configuration	Actinide	Electronic Configuration
Actinium (Ac)	$6d^1\ 7s^2$	Berkelium (Bk)	$5f^9\ 7s^2$
Thorium (Th)	$6d^2\ 7s^2$	Californium (Cf)	$5f^{10}\ 7s^2$
Protactinium (Pa)	$5f^2\ 6d^1\ 7s^2$	Einsteinium (Es)	$5f^{11}\ 7s^2$
Uranium (U)	$5f^3\ 6d^1\ 7s^2$	Fermium (Fm)	$5f^{12}\ 7s^2$
Neptunium (Np)	$5f^4\ 6d^1\ 7s^2$	Mendelevium (Md)	$5f^{13}\ 7s^2$
Plutonium (Pu)	$5f^6\ 7s^2$	Nobelium (No)	$5f^{14}\ 7s^2$
Americium (Am)	$5f^7\ 7s^2$	Lawrencium (Lr)	$5f^{14}\ 6d^1\ 7s^2$
Curium (Cm)	$5f^7\ 6d^1\ 7s^2$		

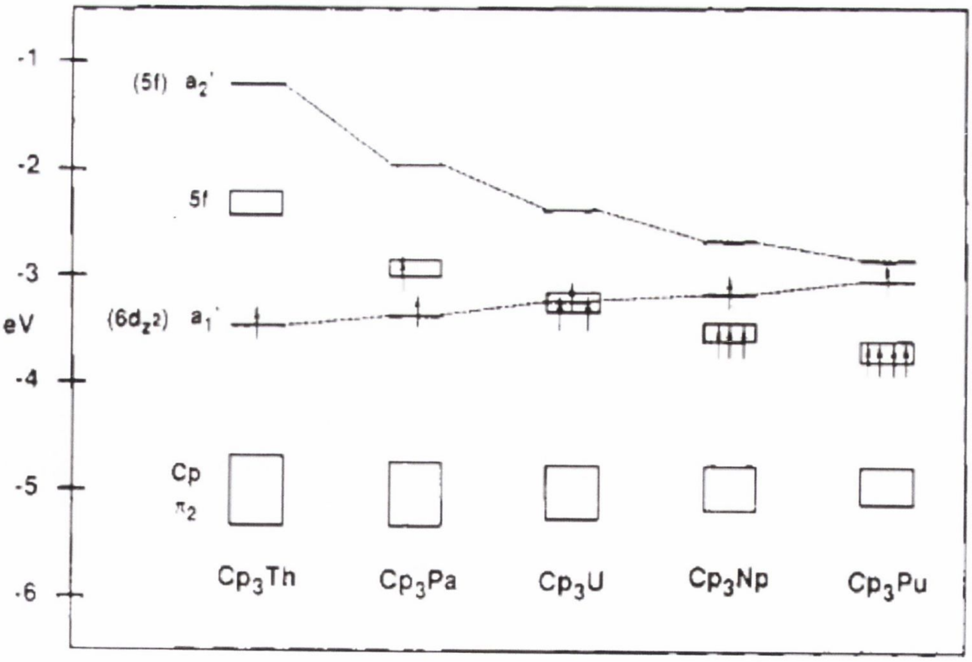

Figure 1.3: MOs spanning the a irreducible representation (in pseudo-D_{3h} symmetry) and the *5f* metal-based orbitals of planar Cp_3An (An = Th, Pa, U, Np, Pu) complexes. All orbital energies are for the $5f^{n-1}6d^1$ ground state electron configurations. Taken from reference 14.

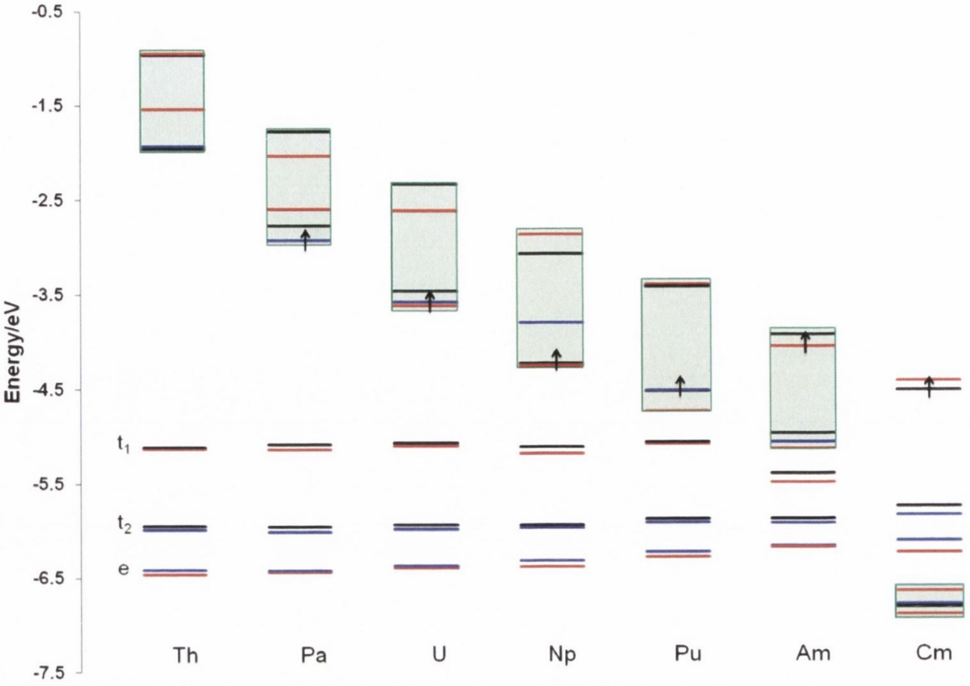

Figure 1.4: MO energy-level diagram from Kaltsoyannis *et al.* for AnCp$_4$ (An = Th – Cm) showing the Cp $\pi_{2,3}$-based levels of *e*, t_2, and t_1 symmetry and the metals' *5f*-based orbitals. MOs spanning the *a* irreducible representation (in the S$_4$ point group) are given in red, *b* in blue and *e* in black. Green boxes surround the *5f*-based orbitals. The HOMOs are indicated by an arrow (except for ThCp$_4$, where the t_1 Cp $\pi_{2,3}$-based combination is the HOMO). Taken from reference 16.

When investigating the series of Cp$_3$An (An = Th – Pu) more closely, the higher atomic number results in an increased effective nuclear charge across the series. This has been shown theoretically by Bursten *et al.* and is illustrated in **Figure 1.3** for the "base free" tris-cyclopentadienyl actinide complexes, Cp$_3$An.[14] The gap between the *5f* and *6d* orbitals begins to decrease in energy until the orbital energies invert: the *5f* orbitals become lower in energy than the *6d*, and as a consequence of the now localised *f*-orbital, only ionic bonding is observed.[14] This was contradicted somewhat by Prodan *et al.* in 2007, whereupon AnO$_2$ (An = Th – Es) was found to "borrow" oxygen spin density across the row. The mechanism for this process was determined to be the increasing degeneracy between the actinide *5f* orbitals and the oxygen *2p* levels across the series,[17] implying that covalency *increases* towards the centre of the actinide series. Kaltsoyannis *et al.* explored this hypothesis using Cp$_4$An (An = Th – Cm).[16] They found the highest occupied molecular orbitals (HOMOs) to be a combination of Cp $\pi_{2,3}$ and metal *d* and *f* orbitals of *e*, t_1 and t_2 symmetry. The conclusion was that with increasing atomic number the HOMOs were largely unaltered but the metal-based orbitals were significantly stabilised (**Figure 1.4**),[16,18] which is consistent with Bursten's findings.[14] It is interesting, however, to note that the significant increase in the metal *5f* contribution to the t_1 orbitals from thorium to americium would appear to support the conclusion of Prodan *et al.* as this contribution fell dramatically for curium (**Figure 1.4**). However Atoms-in-Molecules analysis (AIM) of the series indicated that the An-Cp bonding was very ionic, more so with increasing atomic number, i.e. there is not enhancement in covalent character across the series.[16]

Describing the covalency in *5f* metal complexes has been achieved experimentally using optical spectroscopy and measuring the thermodynamics of complexation; early separation studies all concluded that the degree of orbital overlap and covalency is highly dependent on the oxidation state and the nature of the ligand.[19] The analysis of the degree of covalency in transition metals can be determined using spectroscopic methods,[20] however, the actinide metals are more complicated and many experimental techniques are used, often in collaboration with computational studies, to provide an insight and an understanding of the role the *5f* and *6d* orbitals play in metal-ligand bonding.[5,19c,21] Experimental techniques used to determine covalency in a molecule include Electron Paramagnetic Resonance Spectroscopy (EPR),[22] Mössbauer Spectroscopy[23] and X-ray Absorption Spectroscopy (XAS).[24] In a paramagnetic system, EPR can use the coupling of the electron spin on the metal with the ligand nuclear spin to directly measure the delocalisation of the electron spin density in the ligand valence orbitals and quantify covalency.[3a] Mössbauer Spectroscopy uses the Mössbauer effect to measure small changes in nuclear transitions due to environmental variations and can provide information on the shielding of *s*-orbitals by valence electrons, thereby providing insight into the participation of ligand orbitals in bonding and metal–ligand covalency.[23b] A benefit of this technique is that it is a solid-state technique, arising from the Mössbauer effect being the recoil-free resonant absorption of gamma rays in solids. However, this technique is only applicable to certain Mössbauer-active nuclei, thus limiting its use in *f*-block research; most of the spectroscopy related to bonding and covalency in *f*-block elements has focused on the *5f* ^{237}Np or the *4f* ^{151}Eu.[23b] XAS is a technique that is element and orbital specific. By targeting the *1s* orbital (K-edge) on the ligand, the data provides a direct probe of the covalency of a metal–ligand bond by quantifying the amount of ligand *p* character in the primarily metal-based anti-bonding orbitals,[25] therefore identifying the valence and excited states of the metal[24,26] and ligand[25] separately. XAS is sufficiently versatile to unravel both electronic and structural information of solids, solutions or gases.[27] The theory behind XAS and its applicability to actinides - specifically uranium - will be discussed more completely in **Chapter 2**.

The reason for the desire to predict the covalent character of the actinides, particularly of the transuranic elements, becomes apparent when considering the chemical similarity between lanthanides and the transuranic actinides. This similarity was first observed experimentally by Seaborg while separating trivalent lanthanides from americium and curium in 1950[28] and identifying efficient methods of separation is now a key area of research in the nuclear power industry (**Section 1.2.2**).[29] Synthesising and analysing compounds such as $M[N(EP^iPr_2)_2]_3$, where M = La, Ce, U, Pu and E = S, Se, Te (**Scheme 1.1**),[30] allows a direct comparison of *4f* and *5f* complexes to determine covalency.

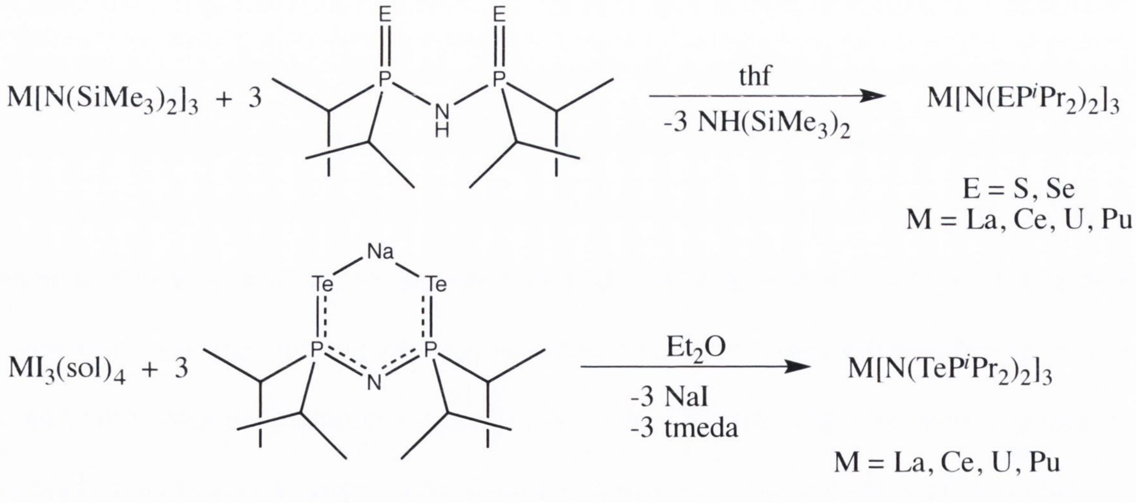

Scheme 1.1: Synthesis of actinide and lanthanide chalcogen complexes.[30]

Gaunt and co-workers found that comparing actinide and lanthanide metal ions of similar ionic radii showed the An–E bond lengths to be shorter than the Ln–E bond lengths, which was consistent with an increase in covalent interactions in the actinide bonding relative to the lanthanide bonding. DFT, Mulliken and MO analyses illustrated that an increase in *f*-orbital participation resulted in the magnitude of the differences in bonding, which was slightly greater with increasing softness of the chalcogen donor atom, i.e. S < Se < Te, and that although this was less significant for Pu–E than U–E, the enhanced covalency was postulated to be still evident for Am(III) and Cm(III).[30] This hard/ soft differentiation between lanthanides and actinides is the basis for *4f*/*5f* separation techniques.

1.1.2. Uranium and the Uranyl Moiety

Uranium can exist in +3 to +6 oxidation states, although recently Evans and co-workers synthesised the first uranium(II) molecular complex *via* reduction of UCp'_3 to yield [K(2.2.2-cryptand)][Cp'_3U], where Cp' = $C_5H_4SiMe_3$.[31] The most common oxidation states are +4 and +6. The hard, highly Lewis acidic +6 centre (U^{+6}: [Rn] $5f^0$ $6d^0$ $7s^0$) is most often found in the form of uranyl: $[O{=}U{=}O]^{2+}$ or $[UO_2]^{2+}$. The uranyl moiety is the central component of the chemistry discussed within this thesis.

Originally a useful synthetic tool because of its stability to moisture and oxygen, the uranyl moiety is also analytically useful due to the IR and Raman active asymmetric and symmetric stretches. The asymmetric, non-degenerate stretching frequency, ν_3, typically occurs in the range 910 to 980 cm^{-1} in the infra-red spectrum; the symmetric, non-degenerate stretching frequency, ν_1, is observed in the Raman spectrum as a strong band at 810–880 cm^{-1}.[32] This can be exploited when examining the effect of ligands on the metal centre: the frequency of the $U{=}O_{yl}$ stretch is inversely related to the donor strength of the equatorial ligands surrounding the uranyl moiety as the increased π donation competes with the U(*6d*) orbitals in the $U{=}O_{yl}$ π bond.[33] The uranyl cation has been studied extensively as the air- and moisture-stable form of uranium most common in aqueous solutions, and its associated importance in the chemistry of the nuclear fuel cycle and waste reprocessing,[34] but in recent years $[UO_2]^{2+}$ chemistry has seen a detour into non-aqueous chemistry which has resulted in an array of complexes hitherto inaccessible and has provided detailed electronic structure and bonding information not otherwise possible.[35] Furthermore, actinide-ligand complex formation in organic solvents is of direct importance to understanding and developing new biphasic aqueous organic actinide separation chemistry, which is a cornerstone of existing reprocessing schemes and proposed advanced nuclear fuel cycle technology.[35a,36] This research has also seen the expansion of the understanding of the activity of uranium(VI) as a catalyst for the conjugate addition of thiols to cyclic and acyclic enones.[37] The ring-opening oligomerisation of epoxides[1] and lactones[2] by a uranyl phenoxide complex will be described thoroughly in **Chapter 4**.

This linear moiety is almost unique to the actinides. In fact, several studies have focused on the role of semi-core *6p* involvement, and have shown that $5f_{z^3}$–$6p_z$ hybridisation forms an unusually strong metal–oxygen σ bond, and stabilises the linear geometry.[5,38] The first example of a linear dioxo cation outside the actinides was the osmyl cation, first reported as $K_2OsO_2Cl_4$ in 1934 by Hoard and Grenko,[39] the structure was refined by Kruse in 1961.[40] The osmyl cation lacks the stability of the uranyl moiety however, as it decomposes in neutral aqueous solutions to yield a black precipitate presumed to be osmic acid, H_2OsO_4.[41] There are further examples of trans dioxo cations in group 7 and 8: the Re(V) dioxo cation is a much more stable linear cation,[42] even being used for catalytic processes.[43]

Actinide ions have two valence orbitals available to form the σ and π bonds with oxygen in uranyl: *5f* and *6d*. Uranyl has been investigated thoroughly experimentally and computationally to understand the participation of the uranium *5f*, *6d* or indeed the oxygen *2p* orbitals in the bonds. **Figure 1.5** is a qualitative molecular orbital diagram of the free uranyl cation. The highest occupied molecular orbitals (HOMOs) are highlighted in the red box. These HOMOs are nominally centred on the oxygen atoms,[44] with predominant *2p* character (**Figure 1.6**),[5] and contain the 12 valence electrons for UO_2^{2+}. The ground electronic configuration of $\pi_g^4\pi_u^4\sigma_g^2\sigma_u^2$ gives rise to formal uranium-oxygen triple bonds comparable with CO.[5] The relative energies of these are hard to predict as the extent of *5f* or *6d* → *2p* overlap may or may not outweigh the energy difference of the atomic orbitals that form the new molecular orbital (MO),[5,21,38,44-45] however, it is important to mention the large separation between these and the σ_u HOMO, as this arises from a filled-filled interaction with the U(*6p*). This has been termed the "pushing from below" mechanism[12,46] as the repulsion from the electron density of the filled semi-core *6p* orbitals destabilises the σ_u orbital and keeps it at high energy. This gap has been verified experimentally by Denning *et al.* using XAS to examine the oxygen K_α edge of the oxygen atoms in $Cs_2UO_2Cl_4$.[21]

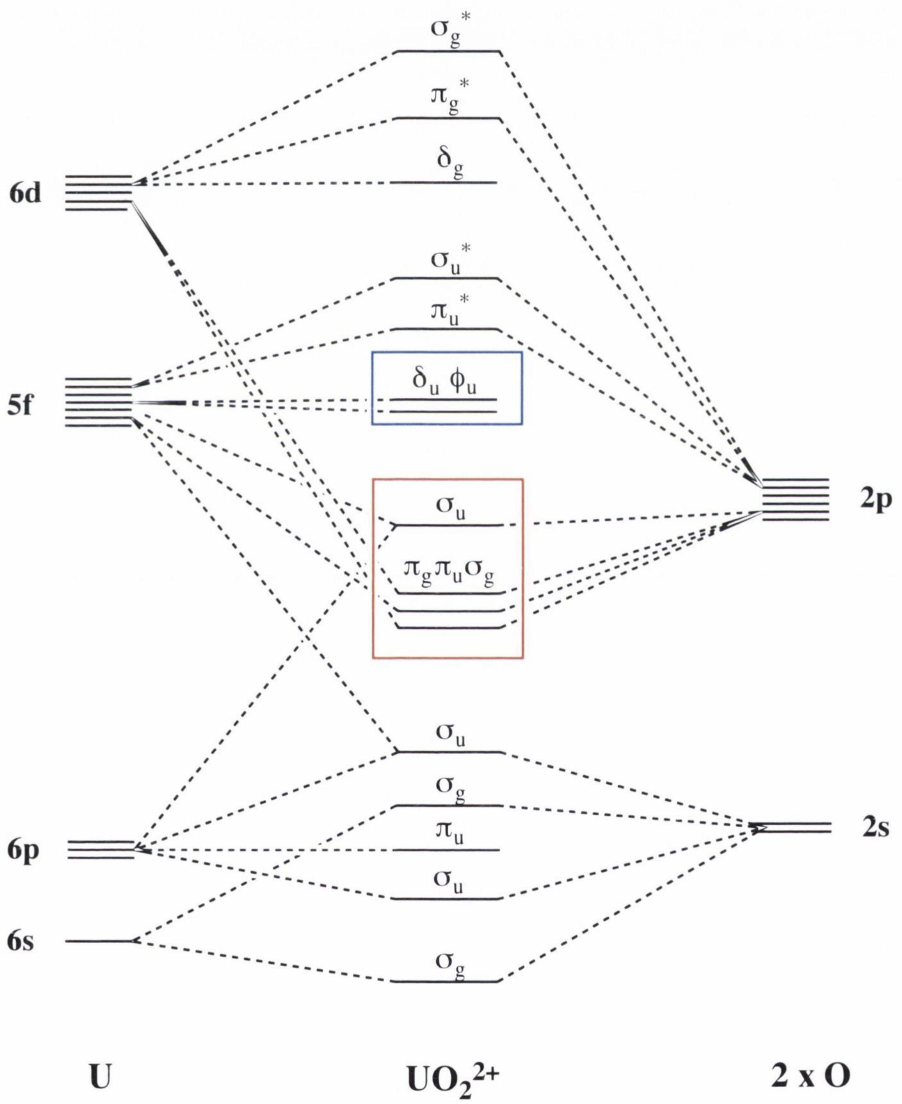

Figure 1.5: Qualitative molecular orbital diagram for the bonding in the free uranyl ion (in $D_{\infty h}$ symmetry). The highest occupied molecular orbitals (HOMOs) are within the red box and the lowest unoccupied molecular orbitals (LUMOs) are in the blue box.[44]

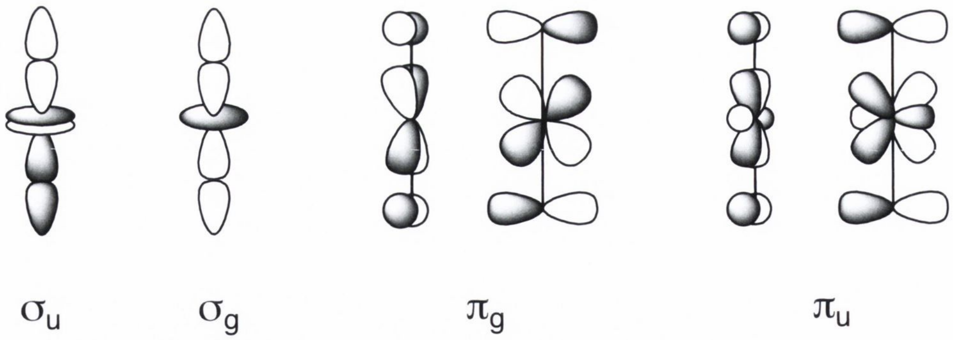

Figure 1.6: The uranyl metal-oxygen bonding orbitals.[5]

An interesting point is that the non-bonding LUMO (Lowest Unoccupied Molecular Orbital) is of predominantly *5f* character: the $5f_{\delta}$ and $5f_{\phi}$ orbitals are symmetry forbidden from overlapping with the oxygen atomic orbitals, and thus from participating in the $U{=}O_{yl}$ bond (**Figure 1.6**, blue box). This is the reason for the retention of linearity across the actinyls from uranyl, UO_2^{2+} (f^0), to americinyl, AmO_2^{2+} (f^3).

Optical spectroscopy (UV/vis absorption and emission spectroscopy) has given insight into these valence states and the allowed transitions within uranyl(VI): the absorption spectra show a maximum of 12 transitions (from the 12 bonding electrons) with the vibrationally resolved band at 420 nm that has been assigned to be a ligand to metal charge transfer (LMCT) transition from a bonding oxygen centred orbital (σ_u, σ_g, π_u or π_g) to a non-bonding uranium centred LUMO ($5f_{\delta}$ or $5f_{\phi}$). The emission spectra show up to six "hot bands" in both solution and solid state arising from deactivation of the excited triplet state and are centred at about 520 nm.[47] These techniques are often combined with computational calculations and have resulted in a clearer understanding of the electronic structure of the uranyl moiety.[48]

1.1.3. Uranium Mediated Activations and Transformations

As described previously, the *5f* orbitals of actinides can interact with the *2p* orbitals of ligands in organoactinide complexes. This ability to participate in bonding gives the early actinides a huge potential for catalysis – uranium has been known to activate small molecules for over a century and was the original catalyst chosen for the Haber-Bosch process in 1909.[49] For a long time the "Jekyll and Hyde" reputation of uranium hindered studies towards catalysis, but in recent years there has been a renewal of interest as attempts have been made to understand the variety of activations and transformations possible with uranium.[50] The chemistry of uranium changes with the oxidation state; it is suitable, therefore, to group research into the activity of uranium by oxidation state.

1.1.3.1. U(III)

Once facile synthetic routes to U(III) chemistry were available, the chemistry of this oxidation state was finally able to be explored.[51] U(III) has long since been useful as an analogue for the later transuranic elements formed during the nuclear power chain reaction[52] to examine the separation of trivalent actinides and lanthanides - essential research for the future of the nuclear industry.[53] Recent observations, however, such as the activation of dinitrogen and carbon monoxide,[54] have encouraged new research into the reactivity of U(III)[55] and its inherent single-molecule magnetic properties.[56]

U(III) has been identified as a powerful reducing agent,[13b,57] a fact visible in the reduction of dinitrogen[58] and nitric oxide, NO.[59] The first example of dinitrogen complexing with an actinide was Scott's triamidoamine uranium(III) complex: $\{U(NN'_3)\}_2[\mu\text{–}\eta^2\text{:}\eta^2\text{–}N_2]$, where $NN'_3 = N(CH_2CH_2NSi^tBuMe_2)_3$.[58a] This formally mixed valent U(III)–U(IV) complex increases the basicity of the bound dinitrogen, indicating $U \rightarrow N_2$ back-bonding.[58b] The more recent trisaryloxide complex $U(OAr)_3$, where Ar = 2,6–di*tert*butylphenyl, has been observed to bind dinitrogen in a η^2 side-on configuration to form a uranium(IV)–N_2^{2-} dimer,[58c] showing a greater Lewis acidity than the $U(NN'_3)$ complex. In the case of NO, reaction of $(C_5Me_4H)_3U$ with NO yielded $(C_5Me_4H)_3UNO$, the first *f* element nitrosyl compound reported.[59] The completely linear UNO bond angle is ordinarily indicative of a $M\text{–}(NO)^+$ unit, but structural and spectroscopic investigation found it to be a $U^{4+}/\ (NO)^{-1}$

complex with the UN bond having multiple bond character, inferring U(*5f*) and π^*_{NO} type orbital overlap.[60]

U(III) catalysis has also been reported, with the successful catalysis of Diels-Alder reactions by uranium triiodide, $UI_3(thf)_4$, where up to 100 % yield is observed in 5 min.[61] This electropositive activity has also been demonstrated in the activation of small molecules such as CO[62] and CO_2,[63] alkane C–H bonds,[64] and the ability to bind and partially reduce arenes to give a formal U(II) synthon.[65]

Lanthanide amidinate compounds show extremely high activity for the ring opening polymerisation (ROP) of ε-caprolactone (εCL),[66] and so, during a comparison of the structures of the analogous U(III) and Ln(III) amidinate compounds (Ln = La, Nd), the catalytic properties were also investigated.[67] ROP of εCL was found to go to completion in less than two minutes when reacted with 200 equivalents of the Nd amidinate complex, $Nd[MeC(NCy)_2]_3$, whereas for $U[MeC(NCy)_2]_3$ the reaction took five days. In this case, it appears that the covalent nature of uranium was a hindrance (the U-N distance was shorter than expected in an ionic model), or perhaps the reducing power of U(III) is the deciding factor: when the U(III) complex was reacted with 0.5 equivalents, a mixture of U(IV) derivatives formed, implying that the insertion of εCL into the U(IV)-O bond is more difficult than cleaving the Ln-N or Ln-O bonds.

1.1.3.2. U(IV)

U(IV) has been observed as a successful catalyst for many common chemical transformations[68] such as C-X bond formation (where X = O, N, S);[68d] hydroamination and hydrosilylation of terminal alkynes,[69] coupling of terminal alkynes with isonitriles,[70] and the polymerisation of α-olefins[68a,71] (**Scheme 1.2**). As a result, complexes featuring uranium have begun to find applications in chemical catalysis.[68c]

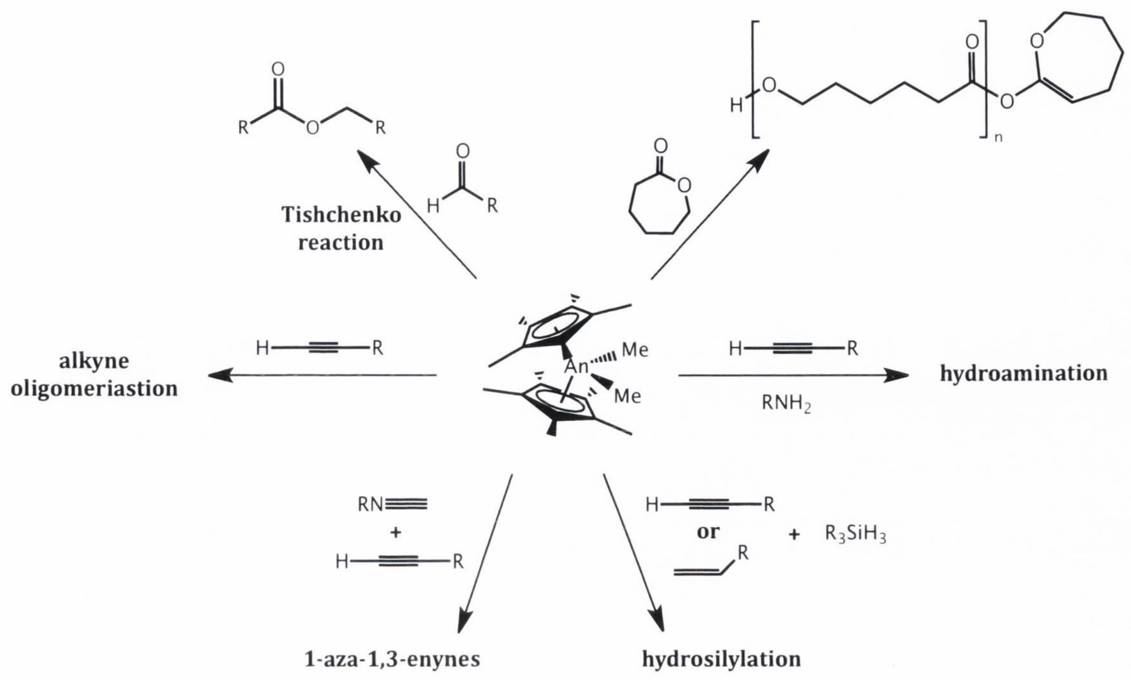

Scheme 1.2: A sample of transformations catalysed by $Cp^*_2AnMe_2$, where An = Th, U.

Despite this, it was a generally held view until quite recently that the highly oxophilic nature of the early actinides would result in reduced catalytic activity if oxygen-containing substrates were introduced.[68c] This affinity was shown experimentally in 1987: Lin and Marks' study into the hydrogenolysis of alkyls by organoactinides revealed that alkoxide substitution greatly depresses the rate of reaction; the rate falls by a factor of *circa* 4×10^3 M^{-1} s^{-1} when changing from $Cp^*_2ThMe_2$ to $Cp^*_2Th(Me)(OR)$.[72] That the rate was unaffected by the steric bulk of the alkoxide ligand (R = *t*Bu, CH(*t*Bu)$_2$) suggested that H_2 attack is sterically not very sensitive; instead the alkoxide effect is explicable in terms of decreased metal electrophilicity, arising from the demonstrated π-donor character of alkoxide ligands in d^0f^0 systems.[73]

Eisen and co-workers, however, showed the first example of organoactinides catalysing C-O bond formation, first with the ROP of lactones[74] and then by catalysing the coupling of aldehydes in the Tishchenko reaction.[75] U(IV) has been shown to have a very different affinity for εCL than U(III): $[U(NEt_2)_3][BPh_4]$ was observed to be an effective ROP catalyst that proceeded *via* a cationic mechanism with rates comparable to successful transition metal complexes.[74] $Cp^*_2AnMe_2$ was also examined (An = Th, U; **Scheme 1.2**) and while the thorium complex was comparable to $[U(NEt_2)_3][BPh_4]$, $Cp^*{}_2UMe_2$ required longer reaction times and produced lower weight polymers (61 % conversion after 24 h in toluene at 25 °C to yield polymers of $M_n = 5.8 \times 10^4$ instead of 100 % conversion after 90 min with $M_n = 3 \times 10^4$).[74]

This ability to react oxygen has been demonstrated in other ways: U(IV) has also been observed to perform Fischer-Tropsch like reactions with carbon monoxide. Cloke and co-workers used uranium(IV) COT^{tips2} (1,4-bistri*iso*propylsilyl-cycloocta-1,3,5,7-tetraene) complexes with the ability to activate CO and H_2 in toluene at low to ambient temperatures and pressures to yield the associated methoxide complex.[76]

1.1.3.3. *U(V)*

Uranium(V) imido complexes are typically formed by the addition of organic azides to uranium(III) complexes through N_2 extrusion, e.g. by treating $[(\eta^5\text{-}MeC_5H_4)_3U]$ with PhN_3 to produce the uranium(V) species $[(\eta5\text{-}MeC_5H_4)_3U(NPh)]$, with a formal U≡N triple bond;[77] or by use of the chelating triamidoamine ligand system, $[N_3N]$, to yield the uranium(V) trimethylsilylimido derivative, $[(N_3N)U(NSiMe_3)]$,[78] and a similar non-chelating analogous derivative, $[((Me_3Si)_2N)_3U(NSiMe_3)]$ with the very short $U\text{–}N_{imido}$ bond distance of 1.91 ± 0.02 Å, indicative of a formal triple bond.[79]

Uranium(V) imido complexes with $(RArO)_3$tacn ligands, where tacn = 1,4,7-triazacyclononane, have been shown to facilitate multiple bond metathesis chemistry with CO_2, forming the uranium(V) terminal oxo species *via* elimination of free isocyanate (**Scheme 1.3**).[80] Using these high-valent uranium precursors for the synthesis of terminal oxo-functionalities eliminates the decomposition and dimerisation reactions observed when the previously reported uranium(III) analogues were treated with CO_2 or traditional oxygen-atom transfer reagents.[54,62-63]

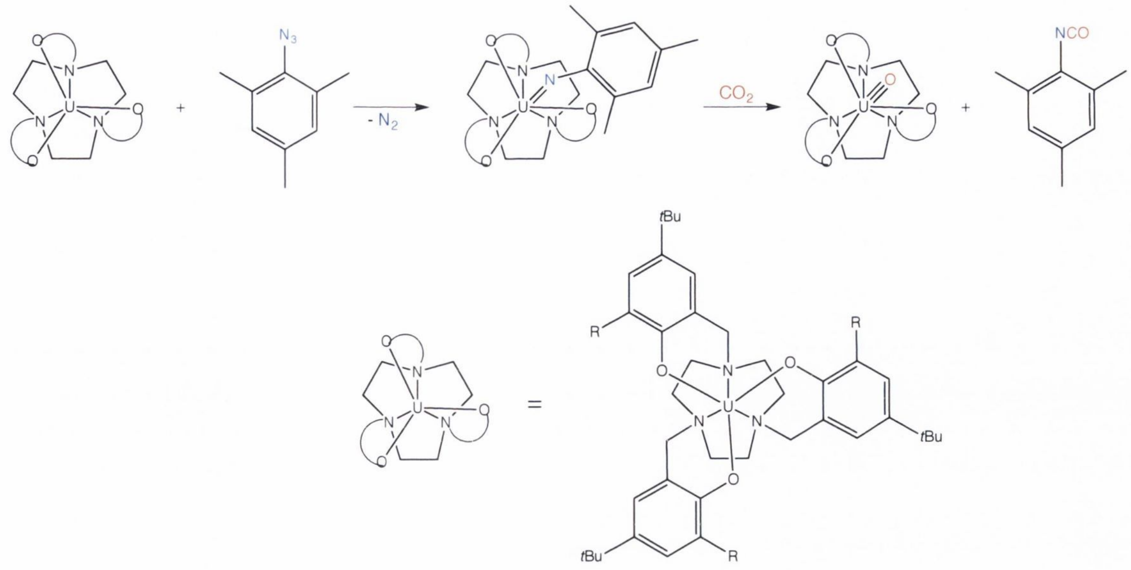

Scheme 1.3: The scheme for the reaction of uranium(V) imido complexes and CO_2, forming the uranium(V) terminal oxo species *via* elimination of the free isocyanate.[80]

1.1.3.4. U_3O_8

There have been many examples of uranium oxides (U_3O_8 is a mixture of U(V) and U(VI) centres) being used in conjunction with porous solids such as alumina or Zr_2O_3[81] for applications such as hydrogen production,[82] the Fischer-Tropsch process,[83] or the partial oxidation[84] or cracking[85] of hydrocarbons. The resistance of the U_3O_8 to common catalyst poisons such as sulfur, water and chlorine[86] makes it particularly advantageous for applications such as the purification of exhaust gases for environmental protection, for example, by oxidising waste HCl to Cl_2,[86] and provides a worthwhile use for depleted uranium derived from the nuclear industry.

1.1.3.5. U(VI)

Uranyl complexes have been observed to activate bonds in stoichiometric reactions. However, upon further study, catalytic conditions were realised by incorporating into the catalytic cycle a second metal to "disengage" the product from the uranium centre.[35g] Coordinating the uranyl moiety in a rigid and asymmetric coordination environment with coordinated potassium cations allows the reductive silylation of uranyl and enables the resultant highly oxidising pentavalent uranyl, $[\mathrm{O{=}U{\cdots}O}]^{+}$, to cleave the otherwise unreactive C–Si and N–Si bonds.

For the first example of uranyl catalysis, Mandolini and Reinhoudt showed a uranyl-salophen complex to be an efficient catalyst for the Michael-type addition of thiophenol to a cyclic α,β-unsaturated ketone.[37] The ketone coordinates to the Lewis acidic U(VI), thereby polarising the α,β-unsaturated system to allow for easier nucleophilic attack at the β carbon (**Figure 1.7**).

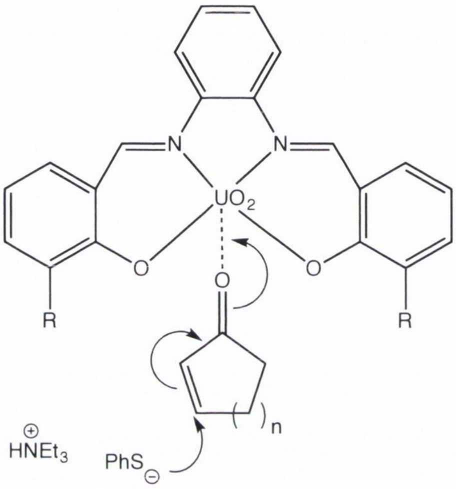

Figure 1.7: Schematic of the Michael-type addition observed with uranyl-salophen complexes, R = H, Ph; n = 1, 2.

Given the highly oxophilic and Lewis acidic nature of uranyl, the reversible binding of oxygen is unexpected and the ability to polarise the carbonyl and to allow for C–S bond formation notable. This work has been further developed by the recent discovery of a uranyl complex performing as a ring-opening polymerisation catalyst for epoxides[1] and lactones.[2] The coordination of the monomer to the uranyl centre polarises the C–O/ C=O bond, thus enabling the initiation step of the nucleophilic attack at the carbon. This will be examined and explored in detail in **Chapter 4.**

1.2. Uranium and the Nuclear Industry

Uranium is a naturally occurring radioactive element with no stable isotopes. The two primary isotopes are ^{238}U (approximately 99.28 % abundant) and ^{235}U (approximately 0.72 % in a natural sample). ^{238}U is an α-emitter with a half-life of 4.468 billion years.[87] It decays to ^{234}Th which in turn undergoes β-emission to yield ^{234}Pa and the ^{234}U.[88] As the half-lives of each species in the decay chain is known, the $^{238/234}$U ratio can be used for dating a uranium sample or for detecting environmental contamination – disequilibrium in the isotopic distributions can indicate uranium mobility in nature.[89]

$$^{238}_{92}\mathrm{U} \xrightarrow{-^{4}_{2}\alpha^{2+}} {}^{234}_{90}\mathrm{Th} \xrightarrow{-^{0}_{-1}\beta^{-}} {}^{234}_{91}\mathrm{Pa} \xrightarrow{-^{0}_{-1}\beta^{-}} {}^{234}_{92}\mathrm{U}$$

^{235}U is an α-emitter with a half-life of 703.7 million years.[87] ^{235}U is the only fissile isotope of uranium: most neutron absorptions will result in nuclear fission into products such as barium and krypton, but a small minority yield ^{236}U or elements with atomic numbers greater than 92 (e.g. ^{236}Np). This was first reported by Meitner and Frisch in 1939.[90]

$$^{235}_{92}\mathrm{U} + {}^{1}_{0}\mathrm{n} \longrightarrow {}^{141}_{56}\mathrm{Ba} + {}^{92}_{36}\mathrm{Kr} + 3\,{}^{1}_{0}\mathrm{n}$$

To be used in nuclear fuel, the uranium has to be "enriched", i.e. the amount of ^{235}U in the fuel has to be increased from 0.72 % to 2-5 % in order to sustain the fission chain reaction.[91] ^{235}U is the only fissile material found in nature and the nucleus can disintegrate after absorbing thermal or fast neutrons, leading to the existence of natural nuclear reactors in areas of natural uranium enrichment.[92] For example, 1.7 billion years ago the Oklo uranium ore contained approximately 3.1 % ^{235}U, allowing the uranium to achieve a critical mass and to undergo fission. Recent investigations into the geochemical and geological conditions of the uranium ores in Oklo[92a] and other natural sites such as the Alligator River Uranium Fields in the Northern Territory of Australia,[93] and the Ruprechtov site in the northwestern part of the Czech Republic[94] have provided information on a long-term scale, important for models used in repository performance assessment of the deep geological waste repositories for spent nuclear fuel.[95]

1.2.1. Nuclear Power

After the Fukushima Daiichi disaster in Japan in 2011 there was a drastic change in the public attitude to nuclear power. Since then Japan has reduced its electrical output from nuclear power from 29.2 % in 2010[96] to 2.1 % in 2012.[97] Across the world many countries – including Belgium, Germany and Italy – have decided to phase out and reduce the number of operational plants, partly as a consequence of lack of public support and – in some cases – public opposition. Countries such as China and India, however, are currently investing in new reactors and new reactor technologies to meet their ever-growing needs for clean energy.[97-98] Other countries are even accelerating their nuclear energy programmes: the Russian Federation seeks to double its nuclear energy output by 2020, with several reactors around the country currently under construction.[97]

The process begins with enriched uranium that is converted into reactor fuel, most often in the form of UO_2 pellets.[91,99] During this process, ^{235}U undergoes fission while U-238 quite often undergoes neutron capture to become ^{239}Pu. This is a fissile isotope and the contribution of ^{239}Pu to a light water reactor (one in which the coolant and moderator is H_2O) is almost 30 % of the total output.[91] Some of this plutonium is extracted from the spent fuel and recycled to make a blend of UO_2 and PuO_2 to form mixed-oxide fuel (MOX). This has the benefit of being compatible with low-enriched uranium.[91]

At the start of 2013, 273 out of 437 operating nuclear reactors were Pressurised Light-Water Cooled and Mediated Reactors (PWR), in which pressurised water is heated to power a steam turbine to generate electricity (**Figure 1.8**).[97] A Fast Breeder Reactor (FBR) is one in which ^{238}U is intentionally converted into ^{239}Pu to be used for nuclear fuel or nuclear weapons. According to the International Atomic Energy Agency, there were only two FBR reactors out of 437 operating reactors at the beginning of 2013 (**Figure 1.8**).[97] FBR reactors use kinetically fast neutrons rather than allowing a thermal chain reaction and create as much or more fuel than they use. The ability of the FBR to recycle isotopes that would otherwise be stored as waste (fertile nuclei such as ^{238}U or ^{232}Th) and convert them to fissile material (^{239}Pu or ^{233}U) has the potential to increase available nuclear fuel resources 50-fold.[91] In fact, thorium is three times as abundant as uranium in the earth's crust and the ability to use thorium-232 as nuclear fuel would allow countries such as India and Brazil to develop energy independence.[98b]

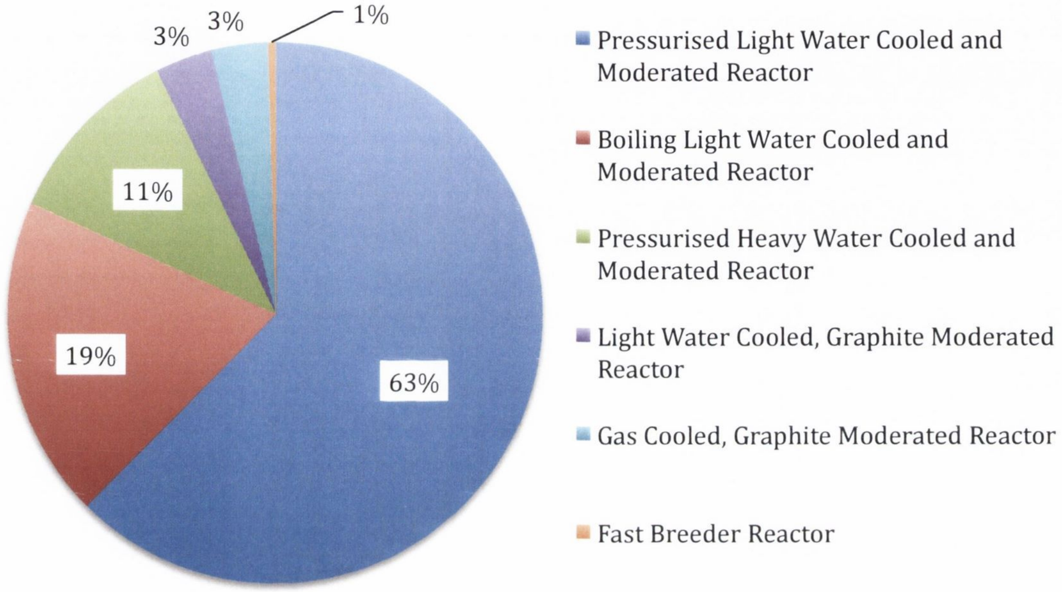

Figure 1.8: Worldwide operational nuclear reactors categorised by the coolant type, as of 1st Jan 2013.[97]

There was much research into creating a thorium light water reactor during the 1950s to mid 1970s and this interest has been renewed recently due to the intrinsic resistance of the thorium fuel cycle to proliferation, i.e. the inability to produce nuclear weapons from a thorium power plant.[98a] The improved stability of ThO_2 relative to UO_2 is also a factor, as UO_2 has shown to be amenable to oxidation and proven to corrode in storage pools and in repositories over long periods.[100] This susceptibility of UO_2 to corrosion and dissolution affects the mobility of the fission products,[101] something that will be described later in this chapter (**Section 1.2.3**) and explored in more detail in **Chapter 2** and **Chapter 3**.

1.2.2. Spent Nuclear Fuel and Waste Reprocessing

The activity of the fuel rods is measured in GigaWatt days per metric ton of fuel (GWd/t). New fuel rods have an activity of around 3 GWd/t; after three to four years this can increase to around 40 GWd/t due to the increased activity of the fission products in the used fuel.[100f,102] One year after removal from the reactor the dose rate at one metre from the fuel assembly is approximately 1,000,000 millisieverts per hour[103] (the annual dose in Ireland from natural sources is 0.395 mSv in a *year*[104]) more than enough to kill a person in less than a minute.[103]

Spent nuclear fuel (SNF) typically consists of a large amount of radioactive isotopes that can no longer be used in sustaining the nuclear reaction: ~95 % ^{238}U, ~1 % ^{235}U, 1-2 % Pu isotopes, 2-3 % radioactive fission products (such as cesium-137 and various isotopes of iodine) and less than 0.1 % of other transuranic elements.[100f,103] After removal from the reactor, SNF is typically stored in interim storage ponds for five to ten years to allow cooling and to reduce issues of radioactivity with the chemical processes involved during reprocessing and storage (e.g. ligand binding, extraction).[105] The waste can then be either stored or reprocessed. Currently, nuclear waste in the United States is stored in cooling pools and in dry storage casks at nuclear power plants. This waste remains a hazard for tens of thousands of years but commercial reprocessing and recycling of plutonium was suspended indefinitely after concerns of nuclear weapon proliferation.[106] Moreover, the pools are running out of space[107] and with the recent decision to drop the plan of burying the waste deep underground in the Yucca Mountain Nuclear Waste Repository, the U.S. is without a path that could eventually lead to a permanent place to store radioactive waste, although in recent months the debate was revisited after a U.S. Court of Appeals order to continue the review of the site.[108]

Reprocessing is the chosen route for reducing both the volume and the activity of high-level radioactive nuclear waste in Europe. One of the larger reprocessing plants is at Sellafield in the UK and waste generated from the reprocessing method is then vitrified and sealed in stainless steel containers for dry storage above the ground at the Sellafield site.[109] Reprocessing can potentially recover up to 95% of the fissile material in spent nuclear fuel.[105,110] There are many methods in operation around the world today.[29a,100f,111] The remaining fractions can be recycled as fuel sources (^{238}U, ^{235}U and the Pu isotopes can be recycled as MOX or as fuel for a FBR) or for industrial applications (e.g. ^{241}Am in smoke detectors) or vitrified and stored.[111c] The later actinides can also be replaced in a reactor to undergo further neutron bombardment and transmutation into less stable nuclei, thereby reducing the time required for storage of this high level waste.[112] This waste, in turn, can be further divided into the short-lived fission products and the long-lived actinides: after 300 years the bulk of the activity comes from the actinides and daughter products and these will remain dangerous for 100,000 years (**Figure 1.10**).[103] Separating the waste reduces the amount of waste that has to be stored on a geological time scale.[106,111c]

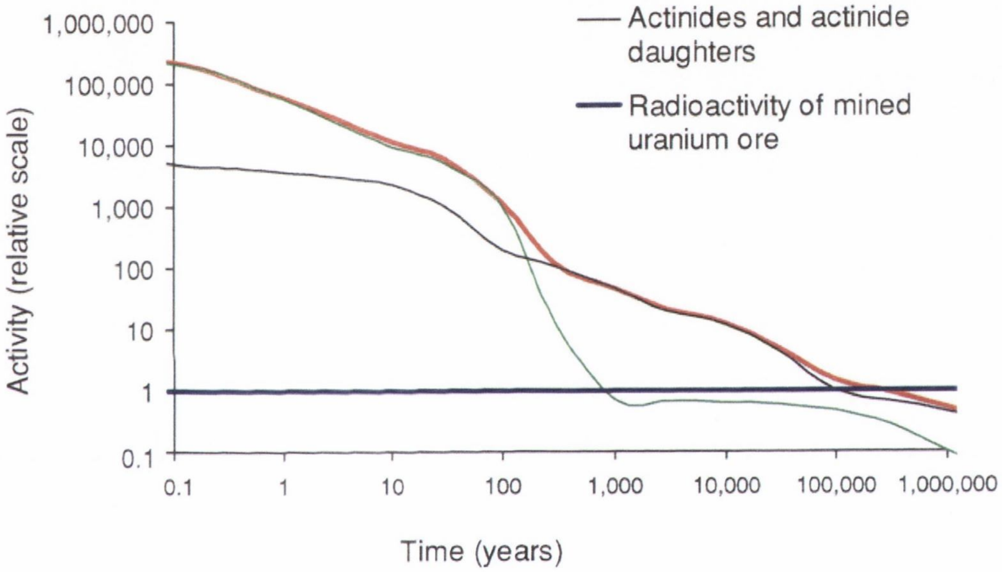

Figure 1.9: Predicted relative activity of SNF with a burnup activity of 38 GWd/ t. Taken from reference 103.

The difficulty in reprocessing is the chemical similarity between the transuranic elements and the lanthanides (**Section 1.1.1**); understanding the electronic structure of actinides is important to understand the separation of *4f* and *5f* elements. The high neutron absorption cross-section of some of the lanthanide ions present in SNF means the lanthanide ions effectively compete with UO_2 for neutrons during irradiation and poison the fuel.[113] Removing the lanthanide ions allows the fuel to be recycled more efficiently but is extremely difficult because of the chemical similarities between the trivalent lanthanides and the actinides.[13] Most current separation techniques focus on the preference for specific ligands to selectively bind an actinide and/ or lanthanide. This has often been done by trial and error, with a successful ligand being modified to be resistant to degradation by hydrolysis (from the concentrated acid) or radiolysis (from the intrinsic radiation of the raffinate).[111b,111e,114] All ligands and solvents must be recyclable for the process to be economical on an industrial scale. Recent investigations, however, into the theoretical examinations of the covalency of the actinides have attempted to understand and to predict the interactions with ligands and thus to design more efficient separation ligands.

In practice, extractants with "softer" donating atoms (e.g. S, N) allow better separation between lanthanides and actinides. Many pyridine[29d,29f,115] and pyrazolone[114b,116] containing ligands have been tested with the aim of the soft nitrogen aiding in selectivity. Some of the first successful separation ligands were the 2,6-bis(1,2,4-triazin-3-yl)pyridine ligand system [BTP, **Figure 1.10(left)**][115a] and the 6,6-bis-(5,5,8,8-tetramethyl-5,6,7,8-tetrahydro-1,2,4-benzotriazin-3-yl)-2,2-bipyridine ligands [CyMe$_4$BTBP, **Figure 1.10(right)**].[117]

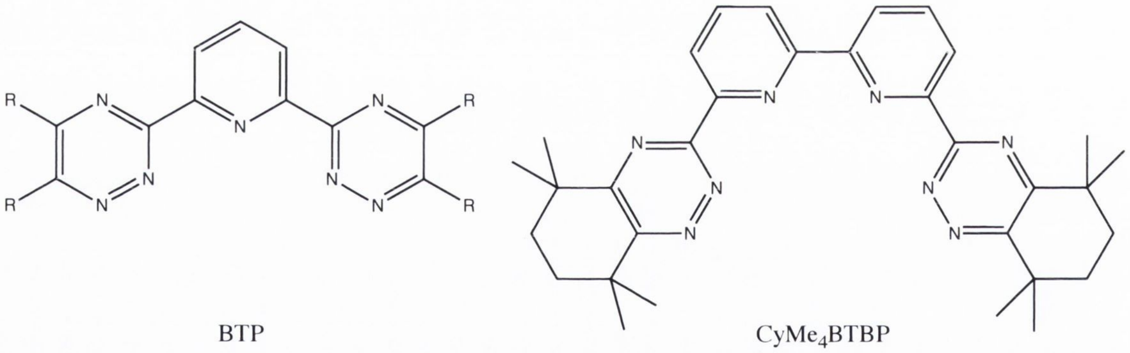

Figure 1.10: Ligands for trivalent actinide/ lanthanide separation: 2,6-bis(1,2,4-triazin-3-yl)pyridine ligand system (BTP)[115a] and the 6,6-bis-(5,5,8,8-tetramethyl-5,6,7,8-tetrahydro-1,2,4-benzotriazin-3-yl)-2,2-bipyridine ligands (CyMe$_4$BTBP).[117]

These ligands showed high selectivity for trivalent actinides over trivalent lanthanides with no alteration to lanthanide speciation but they demonstrated poor stability, slow extraction kinetics, and inefficient back-extraction due to high affinity for the actinides.[118] Modified forms of the BTP ligand – such as adding alkyl chains to increase stability – have demonstrated high potential for selective separation with separation factors of 100–200.[119] The highest separation factors, however, for trivalent lanthanides/actinides have been found with dialkyldithiophosphinic acids: Cyanex 301 (**Figure 1.11**) preferentially binds to An(III) by a factor of 2000-10000.[120] Cyanex 301 also seems to work synergistically with neutral extractants such as tribuylphosphate (TBP) and tri-n-octylphosphine oxide (TOPO).[121] The enhanced selectivity of ligands such as Cyanex 301 is thought to be due, in part, to a greater covalent character to the actinide-ligand bond[18] arising from orbital overlap of the sulfur ligands with the *5f* orbital of actinides.

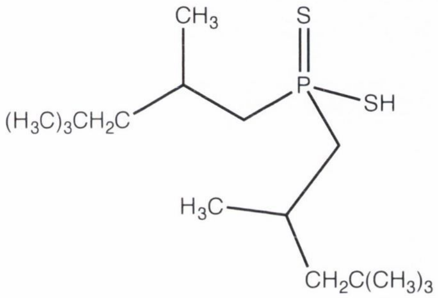

Cyanex 301

Figure 1.11: The commercial reagent Cyanex 301 shows remarkable separation of trivalent lanthanides and actinides.

However, there has been doubt regarding the origins of this perceived covalency: computational studies of electron density in molecules such as AnO_2,[17] Cp_4An[16] and Cp_3An[122] imply an ionic actinide-ligand bond, instead according the increased mixing of metal and ligand orbitals to the coincidental match of actinide *5f* orbitals and ligand orbitals, i.e. oxygen *2p* levels in AnO_2,[17] or with the π orbitals in Cp.[16,122] Orbital mixing arising from the near degeneracy of the orbitals rather than enhanced overlap of the *f*-orbitals has been termed "near-degeneracy driven covalency"[5] and is credited with the enhancements in separation factors (for Am(III)/Eu(III), for example) with soft donors.[18] Therefore the type of interaction between the *4f* and *5f* ions and the extractant ligands plays a key role in understanding the nature of metal-ligand bonding and *vice-versa*, allowing the design of ligands with greater efficiency and selectivity.

1.2.3. Uranyl Minerals: Phase Transitions on SNF

In places with high concentrations of uranium – whether naturally[94,123] or due to anthropogenic effects such as U mining[124] and processing;[125] nuclear weapons testing;[126] sites of nuclear accidents[127] or spent nuclear fuel (SNF) repositories[128] – there are complex interactions with the local soil and rocks that result in a variety of phase alterations.[129] There has been ample research into the geochemistry of uranium in areas of naturally high uranium concentration, for example, in the Alligator River Uranium Fields in the Northern Territory of Australia,[93] Oklo-Okelobondo in the République Gabonaise,[92a] and the Ruprechtov site in the Czech Republic.[94] These natural sites can be used as analogues for high-level radioactive waste disposal repositories in deep geological formations as these sites have geochemical and geological conditions which are similar to the overburden of host rocks for deep geological waste repositories.[95] In particular, sites with natural uranium enrichment such as the Oklo natural reactor have been studied to provide information on a long-term scale, important for models used in repository performance assessment.

The corrosion of UO_2 in a repository can be compared to the weathering of uraninite – the closest natural mineral analogue to SNF.[100b,130] In uraninite corrosion, the presence of uranium decay products has been shown to affect the speciation: both Fe and Mn oxides have been observed to adsorb U in Koongarra, Australia and are believed to affect the probability of uranyl silicate or uranyl phosphate formation and precipitation;[93,131] the presence of radiogenic Pb leads to formation of curite, $Pb_3[(UO_2)_8(O)_8(OH)_6]\cdot 3H_2O$, which in turn has been observed to encourage the formation of uranyl phosphate minerals (**Figure 1.12**).[130a] The presence of groundwater ions such as hydroxyls, silicates, carbonates and phosphates affect the formation of uranyl minerals; uranyl carbonate species, for example, will develop with < 1 mM *in situ* carbonate concentration.[132]

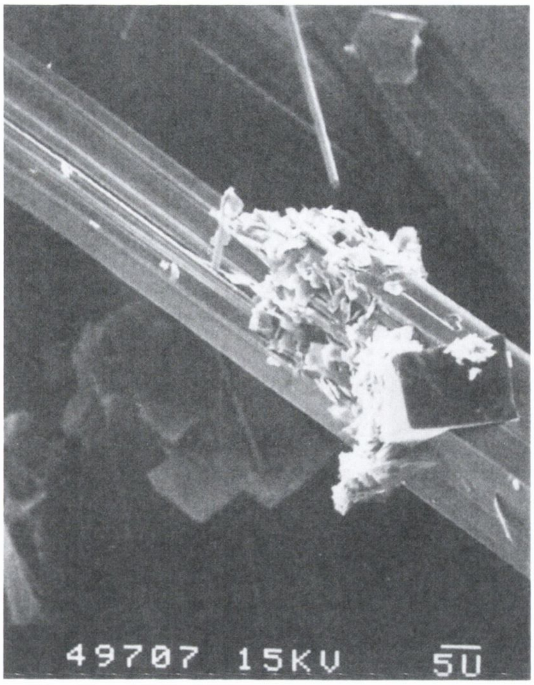

Figure 1.12: SEM micrograph of a curite crystal ($Pb_3[(UO_2)_8O_8(OH)_6]\cdot 3H_2O$) being replaced by a uranyl phosphate mineral. Taken from reference 133.

Studies on UO_2[134] and SNF[132,135] have revealed that chief among the surface phase transitions are the formation of minerals identified as the uranyl oxyhydroxide minerals schoepite, $[(UO_2)_8O_2(OH)_{12}]\cdot 12H_2O$, metaschoepite, $[(UO_2)_4O(OH)_6]\cdot 5H_2O$, becquerelite, $[Ca(UO_2)_6O_4(OH)_6]\cdot 8H_2O$, compreignacite $[K_2(UO_2)_6O_4(OH)_6]\cdot 7H_2O$, and a number of layered uranyl silicate or phosphate minerals formed by reaction of dissolved silicates and phosphates in groundwater. In areas where the local geology is primarily carbonate minerals (e.g. calcite, $CaCO_3$, or rosasite, $(Cu,Zn)_2(CO_3)(OH)_2$), uranyl carbonate minerals such as rutherfordine, $UO_2(CO_3)$, andersonite, $Na_2Ca[UO_2(CO_3)_3]\cdot 6H_2O$, and grimselite, $K_3Na[UO_2(CO_3)_3]\cdot H_2O$, can be found.[136] Wronkiewicz *et al.* performed extensive tests on UO_2 pellets and natural uraninite sources – the closest natural mineral analogue to SNF[100b,130] – in oxidising conditions for studies up to ten-year periods.[134b] They found a consistent trend in phase alterations from uraninite to uranyl oxyhydroxide minerals to uranyl silicate minerals – such as soddyite, $[(UO_2)(SiO_4)]\cdot 2H_2O$ – to uranyl alkaline silica hydrate minerals, such as boltwoodite, $Na,K[(UO_2)(HSiO_4)]\cdot 0.5H_2O$ (**Figure 1.13**). This is consistent with uraninite samples found in nature (**Figure 1.14**).

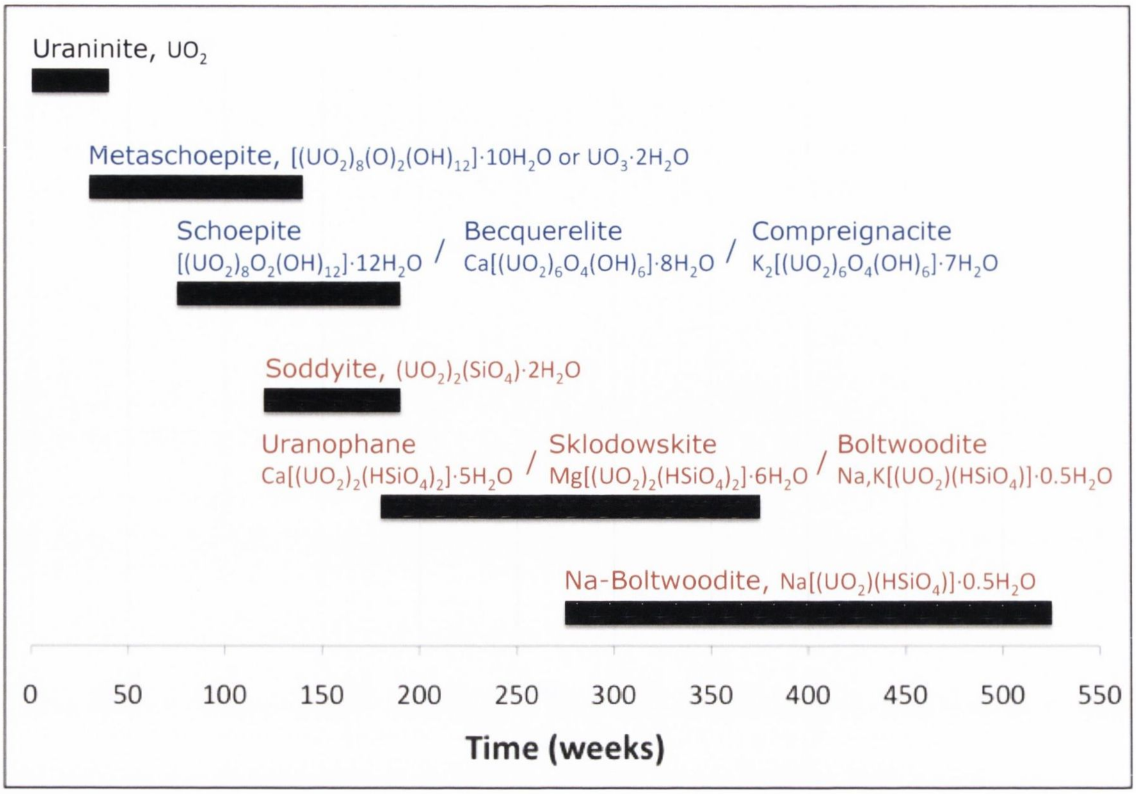

Figure 1.13: Uranium alteration phases found over a ten-year study. Blue minerals are uranyl oxyhydrates and uranyl silicates are in red. Adapted from reference 134b.

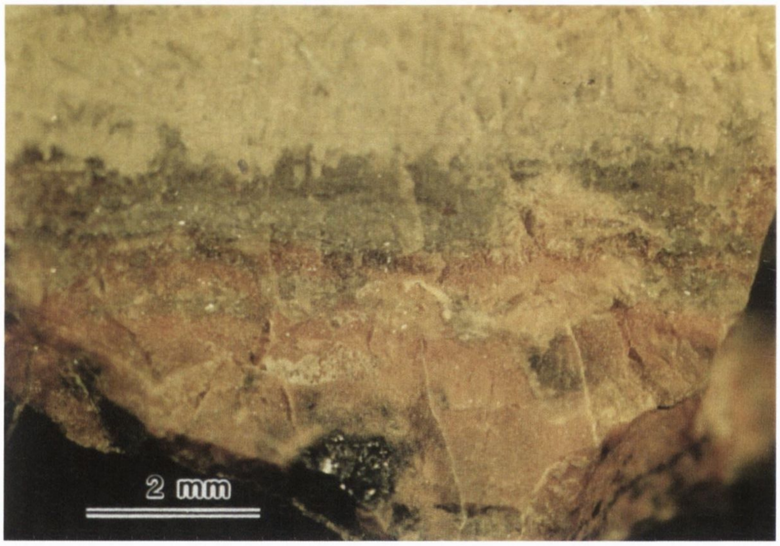

Figure 1.14: Photomicrograph of a corrosion rind on uraninite (black crystal in bottom centre). Yellow material (top) is a combination of schoepite and metaschoepite. Orange material is predominantly vandendriesscheite. Soddyite, kasolite and uranophane are also present and fill the veins. Taken from reference 133.

In a reducing or acidic environment, however, the uranium will remain as U(IV). There has been far less research into the effect of a reducing environment on spent nuclear fuel, as this is less common in nature, although there has been some study of the geochemistry of coffinite, $USiO_4.nH_2O$ ($0 < n < 2$).[137] The first synthesis of coffinite was recently reported;[138]

synthesis of coffinite study has proven difficult in the past as the formation of the pure silicate phase was hindered by dissolution and precipitation of side-products.[139]

In terms of SNF, phase alterations such as uranyl mineral formation on the surface have been shown to allow a mechanism for immobilising radionuclides such as ^{90}Sr and ^{137}Cs *via* incorporation into or sorption onto these minerals and thus inhibit leaching into the surrounding environment. However, redox mechanisms or ion-exchange pathways have the potential to allow migration of radionuclides (e.g. ^{237}Np) from the fuel. These migration mechanisms have become a key concern within the nuclear industry and in recent years there has been a significant increase in research aimed at understanding and predicting the speciation of the early actinides (and other radionuclides produced as a result of fission) that have the potential for a long-term impact on the environment.[29e,140] Neptunium incorporation has been particularly well studied.[141] Neptunium is most likely to exist in its +5 oxidation state as NpO_2^+ in oxic waters,[140e] Np(V) is water soluble and since ^{237}Np is potentially mobile with a long half-life (2.1×10^6 years) and a high specific activity of 26 MBq/ g, the leaching of neptunium is of significant environmental concern.[140g,141a,142] Np(V) and Np(VI) as $[NpO_2]^+$ and $[NpO_2]^{2+}$ have been observed replacing the uranyl moiety in uranyl minerals,[143] specific analysis of incorporation into uranyl phosphate minerals has revealed that it is most often Np(VI) incorporated, as Np(V) creates a charge imbalance that requires the further alterations to introduce counterions.[144] Ion-exchange pathways have also been examined – for example, Sr^{2+} exchanging for Ca^{2+} in becquerelite.[145] The uranyl oxyhydroxide phases, such as schoepite and becquerelite, also show incorporation of ^{237}Np as Np(IV),[143] and those phases with interlayer cations incorporated more ^{237}Np than those without.[141b,146]

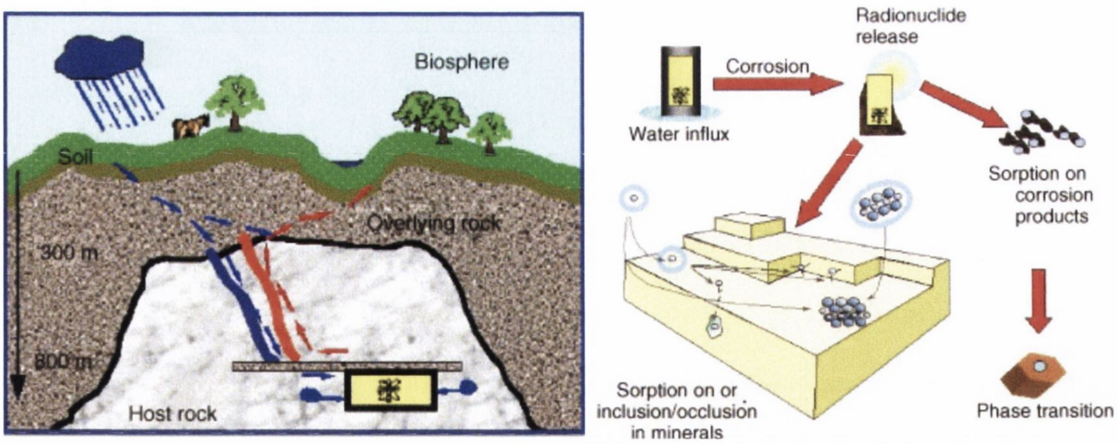

Figure 1.15: Schematic representation of the possible leaching or migration routes of radionuclides *via* sorption into or onto uranium minerals or corrosion products. Modified from reference 147.

The chemistry of the mineral affects the rate of mobilisation/ immobilisation of radionuclides: uranyl phosphates have been shown to immobilise uranium and hinder the migration of uranium into the surrounding environment,[148] something replicated in the laboratory and put into practice in spent fuel reprocessing.[149] Uranyl silicates, however, have been shown to increase the solubility of uranium and have been observed to cause contamination of surrounding soil and groundwater – for example at the Hanford reprocessing site in Washington.[125] Uranyl silicates have a layered structure and have been compared to clay minerals[150] as they display high surface areas, leading to radionuclide[151] and actinide sorption, typically as An(III).[143] This is consistent with the finding that in carbonate free waters, trivalent actinide hydroxyl species – particularly $Am(OH)^{2+}$ or $Am(OH)_2^+$ – adsorb onto colloids, sediments and humics.[140e]

1.2.3.1. Structural Motifs of Uranyl Minerals

There are several structural motifs common to uranyl mineral structures that arise from the arrangement of uranyl polyhedra: uranyl moieties with equatorial coordination numbers ranging from four to seven. These are polymerised in different ways (typically *via* edge or vertex sharing) to create individual topologies classed as isolated uranyl polyhedra, finite clusters, chains, sheets, and frameworks of polyhedra.[152]

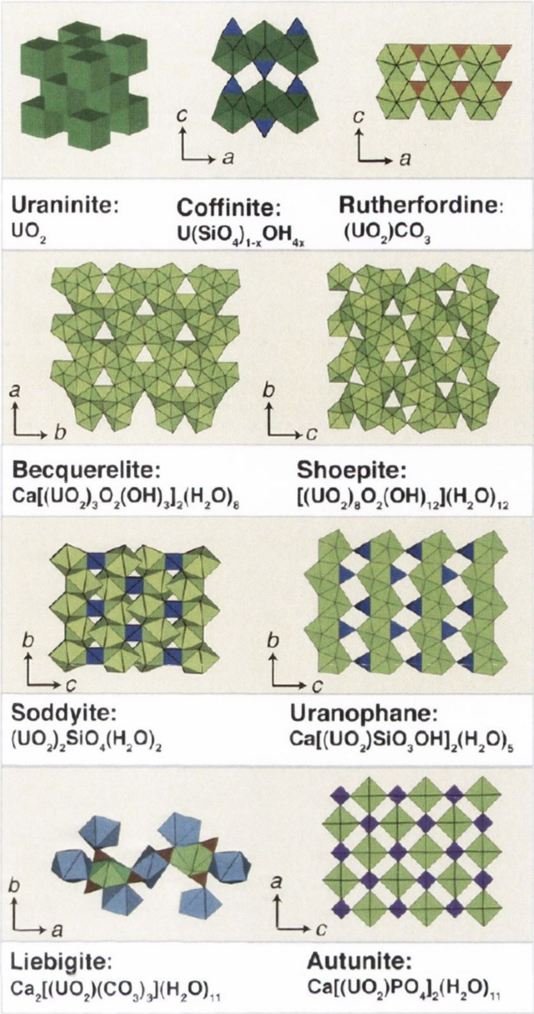

Figure 1.16: Scheme for the common shapes of uranyl polyhedra. polyhedra chain sheet framework clusters. Taken from reference 140g.

Isolated polyhedra are rare, typically amalgamating to form another topology. The polyhedra are not linked directly but rather *via* low-valent cations (for example Cs^+, Li^+ or $Ca^{2=}$) or anions (for example NO_3^- or PO_4^{3-}).[152] Finite clusters of uranyl polyhedra of sizes up to 120 units have been reported[153] connected *via* oxo, peroxo or hydroxo ligands,[154] although species with pyrophosphate or oxalate groups incorporated as bridges between uranyl polyhedra have also been reported.[155] The bonding in uranyl peroxide clusters has been well-studied,[127c] the enhanced covalent interactions between the uranium f_{xyz} orbital and the bridging peroxo π^* orbital that arise from the bent U-(O_2)-U dihedral angle has been described as the driving force for the formation of supramolecular clusters of uranyl peroxides.[156]

The chain structure is visible in studtite, $[(UO_2)(\eta^2\text{-}O_2)(H_2O)_2]\cdot 2H_2O$. The uranyl polyhedra are linked *via* edge sharing with the trans peroxo linkages creating the long 1D structure. There are many examples of layered minerals: schoepite, $[(UO_2)_8O_2(OH)_{12}]\cdot 12H_2O$, consists of layered networks of uranyl polyhedra bound *via* vertex sharing with η^2-oxo or edge sharing η^3-oxo and hydroxo ligands, with hydrogen-bound interstitial water molecules between the layers.

Minerals such as becquerelite or compreignacite have interstitial cations (Ca^{2+} and K^+, respectively) that create linkages between layers *via* hydrogen bonding or cation-cation interactions. For example: in the phosphate mineral autunite, $Ca[(UO_2)_2(PO_4)_2]\cdot 12H_2O$, the interstitial hydrated calcium cations are hydrogen bonded to the neighbouring layer.[157] The autunite sub-group is known for a characteristic repeating unit of uranyl square bipyramids and phosphate (or arsenate) tetrahedra connected by sharing vertices, linking each bipyramid to four tetrahedra, and each tetrahedron is in turn linked to four bipyramids.[152]

In a few structures, sheets of polyhedra are linked together by shared anions or through uranyl ions in interlayer positions, forming a framework. It is also possible that the anion will drive the formation of other structures: in dilute carbonate solutions in a high pH, uranyl tricarbonate clusters will crystallise. This tripodal building block allows for frameworks with zeolite-type structures; uranyl carbonate minerals such as andersonite, $Na_2Ca[(UO_2)(CO_3)_3]\cdot 6H_2O$,[158] and grimselite, $K_3Na[(UO_2)(CO_3)_3]\cdot H_2O$,[136d] are formed by these tripodal units binding with cations to form rigid 3D frameworks.

This Thesis will discuss the analysis of eleven uranyl minerals. **Chapter 2** will focus on the analysis of the 1D chain uranyl peroxide mineral studtite, $[(UO_2)(\eta^2\text{-}O_2)(H_2O)_2]\cdot 2H_2O$, and its dehydrated congener metastudtite, $[(UO_2)(\eta^2\text{-}O_2)(H_2O)_2]$, using solid-state electrochemistry and XAS. This will then be compared to a series of uranyl oxyhydroxide, phosphate and carbonate minerals in **Chapter 3**. The solid-state electrochemistry of these nine minerals will be described to find a structure-reactivity relationship between the minerals.

1.3. References

(1) (a) Baker, R. J.; Walshe, A. *Chem. Commun.* **2012**, *48*, 985(b) Fang, J.; Walshe, A.; Maron, L.; Baker, R. J. *Inorg. Chem.* **2012**, *51*, 9132.

(2) Walshe, A.; Fang, J.; Maron, L.; Baker, R. J. *Inorg. Chem.* **2013**, *52*, 9077.

(3) (a) McGarvey, B. R. In *Transition Metal Chemistry*; Carlin, R. L., Ed.; Marcel-Dekker: New York, 1967; Vol. 3(b) Crabtree, R. H. *The Organometallic Chemistry of the Transition Metals*, 2001.

(4) Slater, J. C. *Symmetry and Energy Bands in Crystals*; McGraw-Hill: New York, 1965.

(5) Neidig, M. L.; Clark, D. L.; Martin, R. L. *Coord. Chem. Rev.* **2013**, *257*, 394.

(6) (a) King, W. A.; Marks, T. J.; Anderson, D. M.; Duncalf, D. J.; Cloke, F. G. N. *J. Am. Chem. Soc.* **1992**, *114*, 9221(b) King, W. A.; Di Bella, S.; Lanza, G.; Khan, K.; Duncalf, D. J.; Cloke, F. G. N.; Fragala, I. L.; Marks, T. J. *J. Am. Chem. Soc.* **1996**, *118*, 627.

(7) Di Bella, S.; Lanza, G.; Fragal√†, I. L.; Marks, T. J. *Organomet.* **1996**, *15*, 3985.

(8) Evans, W. J.; Fang, M.; Zucchi, G.; Furche, F.; Ziller, J. W.; Hoekstra, R. M.; Zink, J. I. *J. Am. Chem. Soc.* **2009**, *131*, 11195.

(9) Fang, M.; Bates, J. E.; Lorenz, S. E.; Lee, D. S.; Rego, D. B.; Ziller, J. W.; Furche, F.; Evans, W. J. *Inorg. Chem.* **2011**, *50*, 1459.

(10) (a) MacDonald, M. R.; Bates, J. E.; Ziller, J. W.; Furche, F.; Evans, W. J. *J. Am. Chem. Soc.* **2013**, *135*, 9857(b) MacDonald, M. R.; Bates, J. E.; Fieser, M. E.; Ziller, J. W.; Furche, F.; Evans, W. J. *J. Am. Chem. Soc.* **2012**, *134*, 8420(c) MacDonald, M. R.; Ziller, J. W.; Evans, W. J. *J. Am. Chem. Soc.* **2011**, *133*, 15914.

(11) (a) Bochkarev, M. N. *Coord. Chem. Rev.* **2004**, *248*, 835(b) Nief, F. *Dalton Trans.* **2010**, *39*, 6589.

(12) Kaltsoyannis, N.; Hay, P. J.; Li, J.; Blaudeau, J. P.; Bursten, B. E. In *The Chemistry of the Actinide and Transactinide Elements*; Morss, L. R., Edelstein, N., Fuger, J., Eds.; Springer: Dordrecht, The Netherlands, 2006.

(13) (a) Kaltsoyannis, N.; Scott, P. *The f Elements*; Oxford University Press, 1999(b) Ephritikhine, M. *Dalton Trans.* **2006**, *21*, 2501.

(14) Bursten, B. E.; Rhodes, L. F.; Strittmatter, R. J. *J. Am. Chem. Soc.* **1989**, *111*, 2756.

(15) Burns, C. J.; Bursten, B. E. *Comm. Inorg. Chem.* **1989**, *2*, 61.

(16) Tassell, M. J.; Kaltsoyannis, N. *Dalton Trans.* **2010**, *39*, 6719.

(17) Prodan, I. D.; Scuseria, G. E.; Martin, R. L. *Phys. Rev. B* **2007**, *76*, 033101.

(18) Kaltsoyannis, N. *Inorg. Chem.* **2013**, *52*, 3407.

(19) (a) Thompson, S. G.; Harvey, B. G.; Choppin, G. R.; Seaborg, G. T. *J. Am. Chem. Soc.* **1954**, *76*, 6229(b) Diamond, R. M.; Street, K.; Seaborg, G. T. *J. Am. Chem. Soc.* **1954**, *76*, 1461(c) Choppin, G. R. *J. Alloy. Compd.* **2002**, *344*, 55.

(20) Balzani, V.; Scandola, F. In *Comprehensive Supramolecular Chemistry*; Reinhoudt, D. N., Ed.; Pergamon Press: Oxford, 1996; Vol. 10.

(21) Denning, R. G.; Green, J. C.; Hutchings, T. E.; Dallera, C.; Tagliaferri, A.; Giarda, K.; Brookes, N. B.; Braicovich, L. *J. Chem. Phys.* **2002**, *117*, 8008.

(22) McGarvey, B. R. *Can. J. Chem.* **1984**, *62*, 1349.

(23) (a) Kalvius, G. M. *Hyperfine Interact.* **1985**, *26*, 793(b) Kalvius, G. M. *J. Less Comm. Met.* **1986**, *121*, 353.

(24) Vitova, T.; Kvashnina, K. O.; Nocton, G.; Sukharina, G.; Denecke, M. A.; Butorin, S. M.; Mazzanti, M.; Caciuffo, R.; Soldatov, A.; Behrends, T.; Geckeis, H. *Phys. Rev. B* **2010**, *82*, 235118.

(25) Solomon, E. I.; Hedman, B.; Hodgson, K. O.; Dey, A.; Szilagyi, R. K. *Coord. Chem. Rev.* **2005**, *249*, 97.

(26) (a) Vitova, T.; Denecke, M. A.; Göttlicher, G.; Jorissen, K.; Kas, J. J.; Kvashnina, K.; Prüßmann, T.; Rehr, J. J.; Rothe, J. *J. Phys. Conf. Ser.* **2013**, *430*, 012117(b) Kosog, B.; La Pierre, H. S.; Denecke, M. A.; Heinemann, F. W.; Meyer, K. *Inorg. Chem.* **2012**, *51*, 7940.

(27) Koningsberger, D. C.; Prins, R. *Principles, Application, Techniques of EXAFS, SEXAFS and XANES*; John Wiley & Sons, 1987.

(28) Street, K.; Seaborg, G. T. *J. Am. Chem. Soc.* **1950**, *72*, 2790.

(29) (a) Zhu, Y. J.; Jiao, R. Z. *Nucl. Technol.* **1994**, *108*, 361(b) Wei, Y. Z.; Kumagai, M.; Takashima, Y.; Asou, M.; Namba, T.; Suzuki, K.; Maekawa, A.; Ohe, S. *J. Nucl. Sci. Technol.* **1998**, *35*, 357(c) Schmieder, H.; Galla, U. *J. Appl. Electrochem.* **2000**, *30*, 201(d) Suzuki, T.; Aida, M.; Ban, Y.; Fujii, Y.; Hara, M.; Mitsugashira, T. *J. Radioanal. Nucl. Chem.* **2003**, *255*, 581(e) Windt, L. d.; Schneider, H.; Ferry, C.; Catalette, H.; Lagneau, V.; Poinssot, C.; Poulesquen, A.; Jegou, C. *Radiochim. Acta* **2006**, *94*, 787(f) Suzuki, T.; Otake, K.; Sato, M.; Ikeda, A.; Aida, M.; Fujii, Y.; Hara, M.; Mitsugashira, T.; Ozawa, M. *J. Radioanal. Nucl. Chem.* **2007**, *272*, 257(g) Serrano-Purroy, D.; Clarens, F.; Glatz, J.-P.; Wegen, D.; Christiansen, B.; de Pablo, J.; Giménez, J.; Casas, I.; Martínez-Esparza, A. *Radiochim. Acta* **2009**, *97*, 491.

(30) Gaunt, A. J.; Reilly, S. D.; Enriquez, A. E.; Scott, B. L.; Ibers, J. A.; Sekar, P.; Ingram, K. I. M.; Kaltsoyannis, N.; Neu, M. P. *Inorg. Chem.* **2008**, *47*, 29.

(31) MacDonald, M. R.; Fieser, M. E.; Bates, J. E.; Ziller, J. W.; Furche, F.; Evans, W. J. *J. Am. Chem. Soc.* **2013**, *135*, 13310.

(32) (a) Bullock, J. I. *J. Chem. Soc. A* **1969**, *0*, 781(b) Bart, S. C.; Meyer, K. In *Organometallic and Coordination Chemistry of the Actinides*; Albrecht-Schmitt, T. E., Ed.; Springer-Verlag Berlin: Berlin, 2008.

(33) Zazhogin, A. A.; Lutz, H. D.; Komyak, A. I. *J. Mol. Struct.* **1999**, *482-483*, 189.

(34) (a) Latimer, W. M. *The Oxidation States of the Elements and Their Potentials in Aqueous Solutions*, 1952(b) Mohapatra, P. K.; Manchanda, V. K. *Talanta* **1998**, *47*, 1271(c) Morris, D. E. *Inorg. Chem.* **2002**, *41*, 3542(d) Altmaier, M.; Gaona, X.; Fanghanel, T. *Chem. Rev.* **2013**, *113*, 901.

(35) (a) Baker, R. J. *Chem. Eur. J.* **2012**, *18*, 16258(b) Tsushima, S. *Dalton Trans.* **2011**, *40*, 6732(c) Seaman, L. A.; Schnaars, D. D.; Wu, G.; Hayton, T. W. *Dalton Trans.* **2010**, *39*, 6635(d) Baker, Robert J.; Hashem, E.; Motevalli, M.; Ogilvie, Helen V.; Walshe, A. *Z. Anorg. Allg. Chem.* **2010**, *636*, 443(e) Fillaux, C.; Guillaumont, D.; Berthet, J.-C.; Copping, R.; Shuh, D. K.; Tyliszczak, T.; Auwer, C. D. *Phys. Chem. Chem. Phys.* **2010**, *12*, 14253(f) Hayton, T. W.; Wu, G. *Inorg. Chem.* **2009**, *48*, 3065(g)

Arnold, P. L.; Patel, D.; Wilson, C.; Love, J. B. *Nature* **2008**, *451*, 315(h) Berthet, J.-C.; Siffredi, G.; Thuerry, P.; Ephritikhine, M. *Chem. Commun.* **2006**, 3184(i) Coupez, B.; Wipff, G. *Inorg. Chem.* **2003**, *42*, 3693(j) Duval, P. B.; Burns, C. J.; Buschmann, W. E.; Clark, D. L.; Morris, D. E.; Scott, B. L. *Inorg. Chem.* **2001**, *40*, 5491(k) Barnhart, D. M.; Burns, C. J.; Sauer, N. N.; Watkin, J. G. *Inorg. Chem.* **1995**, *34*, 4079(l) Ryzhkov, M. V.; Gubanov, V. A. *J. Radioanal. Nucl. Chem.* **1990**, *143*, 85.

(36) Jones, M. B.; Gaunt, A. J. *Chem. Rev.* **2012**, *113*, 1137.

(37) (a) van Axel Castelli, V.; Cort, A. D.; Mandolini, L.; Reinhoudt, D. N. *J. Am. Chem. Soc.* **1998**, *120*, 12688(b) van Axel Castelli, V.; Dalla Cort, A.; Mandolini, L.; Reinhoudt, D. N.; Schiaffino, L. *Chem. Eur. J.* **2000**, *6*, 1193(c) van Axel Castelli, V.; Dalla Cort, A.; Mandolini, L.; Reinhoudt, David N.; Schiaffino, L. *Eur. J. Org. Chem.* **2003**, *2003*, 627.

(38) Kaltsoyannis, N. *Inorg. Chem.* **2000**, *39*, 6009.

(39) Hoard, J. L.; Grenko, J. D. *Z. Kristallogr.* **1934**, *87*, 100.

(40) Kruse, F. H. *Acta Crystallogr.* **1961**, *14*, 1035.

(41) Villars, P.; Cenzual, K.; Daams, J.; Gladyshevskii, R.; Shcherban, O.; Dubenskyy, V.; Kuprysyuk, V.; Savysyuk, I.; Zaremba, R. In *Structure Types. Part 10: Space Groups (140) I4/mcm - (136) P42/mnm*; Villars, P., Cenzual, K., Eds.; Springer Berlin Heidelberg, 2011; Vol. 43A10.

(42) Pipes, D. W.; Meyer, T. J. *Inorg. Chem.* **1986**, *25*, 3256.

(43) Reddy, K. R.; Domingos, Ç.; Paulo, A. n.; Santos, I. *Inorg. Chem.* **1999**, *38*, 4278.

(44) Denning, R. G. *J. Phys. Chem. A* **2007**, *111*, 4125.

(45) Denning, R. G. *Struct. Bonding (Berlin)* **1992**, *79*, 215.

(46) Jørgensen, C. K. *Chem. Phys. Lett.* **1982**, *89*, 455.

(47) (a) Sessler, J. L.; Melfi, P. J.; Pantos, G. D. *Coord. Chem. Rev.* **2006**, *250*, 816(b) Aquilante, F.; Malmqvist, P. A.; Pedersen, T. B.; Ghosh, A.; Roos, B. O. *J. Chem. Theory Comput.* **2008**, *4*, 694.

(48) (a) Redmond, M. P.; Cornet, S. M.; Woodall, S. D.; Whittaker, D.; Collison, D.; Helliwell, M.; Natrajan, L. S. *Dalton Trans.* **2011**, *40*, 3914(b) Natrajan, L. S. *Coord. Chem. Rev.* **2012**, *256*, 1583.

(49) (a) Haber, F. *Z. Elektrochem. Angew. Physik. Chem.* **1910**, *16*, 244(b) Haber, F.; DE 229126 ed.; DPMA, Ed. Deutschland, 1909.

(50) Fox, A. R.; Bart, S. C.; Meyer, K.; Cummins, C. C. *Nature* **2008**, *455*, 341.

(51) (a) Avens, L. R.; Bott, S. G.; Clark, D. L.; Sattelberger, A. P.; Watkin, J. G.; Zwick, B. D. *Inorg. Chem.* **1994**, *33*, 2248(b) Carmichael, C. D.; Jones, N. A.; Arnold, P. L. *Inorg. Chem.* **2008**, *47*, 8577(c) Baker, R. J. *Coord. Chem. Rev.* **2012**, *256*, 2843.

(52) Kaltsoyannis, N. *Inorg. Chem.* **2012**, *52*, 3407.

(53) (a) Kolarik, Z. *Chem. Rev.* **2008**, *108*, 4208(b) Jarvinen, G. D.; Barrans, R. E.; Schroeder, N. C.; Wade, K. L.; Jones, M. M.; Smith, B. F.; Mills, J. L.; Howard, G.; Freiser, H.; Muralidharan, S.; Nash, K. L.; Choppin, G. R. *Separation of f Elements*, 1995(c) Neidig, M. L.; Clark, D. L.; Martin, R. L. *Coord. Chem. Rev.* **2012**, *257*, 394.

(54) Summerscales, O. T.; Cloke, F. G. N. In *Organometallic and Coordination Chemistry of the Actinides*; Albrecht-Schmitt, T., Ed.; Springer Berlin: Heidelberg, 2008.

(55) (a) Arnold, P. L. *Chem. Commun.* **2011**, *47*, 9005(b) Gardner, B. M.; Liddle, S. T. *Eur. J. Inorg. Chem.* **2013**, *2013*, 3753.

(56) Moro, F.; Mills, D. P.; Liddle, S. T.; van Slageren, J. *Angew. Chem., Int. Ed.* **2013**, *52*, 3430.

(57) Evans, W. J.; Kozimor, S. A. *Coord. Chem. Rev.* **2006**, *250*, 911.

(58) (a) Roussel, P.; Scott, P. *J. Am. Chem. Soc.* **1998**, *120*, 1070(b) Roussel, P.; Tinker, N. D.; Scott, P. *J. Alloy. Compd.* **1998**, *271*, 150(c) Mansell, S. M.; Kaltsoyannis, N.; Arnold, P. L. *J. Am. Chem Soc.* **2011**, *133*, 9036.

(59) (a) Siladke, N. A.; Meihaus, K. R.; Ziller, J. W.; Fang, M.; Furche, F.; Long, J. R.; Evans, W. J. *J. Am. Chem. Soc.* **2011**, *134*, 1243(b) Rinehart, J. D.; Fang, M.; Evans, W. J.; Long, J. R. *Nat. Chem.* **2011**, *3*, 538.

(60) Hayton, T. W.; Legzdins, P.; Sharp, W. B. *Chemical Reviews* **2002**, *102*, 935.

(61) Collin, J.; Maria, L.; Santos, I. *J. Mol. Cat. A Chem.* **2000**, *160*, 263.

(62) Aitken, G.; Hazari, N.; Frey, A. S. P.; Cloke, F. G. N.; Summerscales, O.; Green, J. C. *Dalton Trans.* **2011**, *40*, 11080.

(63) (a) Summerscales, O. T.; Cloke, F. G. N.; Hitchcock, P. B.; Green, J. C.; Hazari, N. *Science* **2006**, *311*, 829(b) Castro-Rodriguez, I.; Nakai, H.; Zakharov, L. N.; Rheingold, A. L.; Meyer, K. *Science* **2004**, *305*, 1757.

(64) Castro-Rodriguez, I.; Olsen, K.; Gantzel, P.; Meyer, K. *J. Am. Chem. Soc.* **2003**, *125*, 4565.

(65) (a) Diaconescu, P. L.; Arnold, P. L.; Baker, T. A.; Mindiola, D. J.; Cummins, C. C. *J. Am. Chem. Soc.* **2000**, *122*, 6108(b) Diaconescu, P. L.; Cummins, C. C. *J. Am. Chem. Soc.* **2002**, *124*, 7660.

(66) Luo, Y.; Yao, Y.; Shen, Q.; Sun, J.; Weng, L. *J. Organomet. Chem.* **2002**, *662*, 144 –149.

(67) Villiers, C.; Thuery, P.; Ephritikhine, M. *Eur. J. Inorg. Chem.* **2004**, 4624.

(68) (a) Andrea, T. E., Moris S. *Chem. Soc. Rev.* **2008**, *37*, 550(b) Barnea, E.; Eisen, M. S. *Coord. Chem. Rev.* **2006**, *250*, 855(c) Burns, C. J.; Eisen, M. S. In *The Chemistry of the Actinide and Transactinide Elements*; Morss, L. R., Edelstein, N. M., Fuger, J., Eds.; Springer: Dordrecht, The Netherlands, 2006; Vol. 5(d) Eisen, M. S. In *C-X Bond Formation*; Vigalok, A., Ed.; Springer Berlin Heidelberg, 2010; Vol. 31.

(69) (a) Dash, A. K.; Gourevich, I.; Wang, J. Q.; Wang, J.; Kapon, M.; Eisen, M. S. *Organomet.* **2001**, *20*, 5084(b) Haskel, A.; Straub, T.; Eisen, M. S. *Organomet.* **1996**, *15*, 3773.

(70) Barnea, E.; Andrea, T.; Kapon, M.; Berthet, J.-C.; Ephritikhine, M.; Eisen, M. S. *J. Am. Chem. Soc.* **2004**, *126*, 10860.

(71) Yang, X.; Stern, C.; Marks, T. J. *Organomet.* **1991**, *10*, 840.

(72) Lin, Z.; Marks, T. J. *J. Am. Chem Soc.* **1987**, *109*, 7979.

(73) (a) Marks, T. J.; Bursten, B. E.; Casarin, M.; Ellis, D. E.; Fragala, I. *Inorg. Chem.* **1986**, *25*, 1257(b) Cotton, F. A.; Marler, D. O.; Schwotzer, W. *Inorg. Chim. Acta* **1984**, *95*, 207(c) Cotton, F. A.; Marler, D. O.; Schwotzer, W. *Inorg. Chim. Acta* **1984**, *85*, L31.

(74) Barnea, E.; Moradove, D.; Berthet, J.-C.; Ephritikhine, M.; Eisen, M. S. *Organomet.* **2006**, *25*, 320.

(75) Andrea, T.; Barnea, E.; Eisen, M. S. *J. Am. Chem. Soc.* **2008**, *130*, 2454.

(76) Frey, A. S. P.; Cloke, F. G. N.; Coles, M. P.; Maron, L.; Davin, T. *Angewandte Chemie International Edition* **2011**, *50*, 6881.

(77) Brennan, J. G.; Andersen, R. A. *J. Am. Chem. Soc.* **1985**, *107*, 514.

(78) Roussel, P.; Boaretto, R.; Kingsley, A. J.; Alcock, N. W.; Scott, P. *Dalton Trans.* **2002**, 1423.

(79) Zalkin, A.; Brennan, J. G.; Andersen, R. A. *Acta Crystallogr., Sect. C* **1988**, *44*, 1553.

(80) Bart, S. C.; Anthon, C.; Heinemann, F. W.; Bill, E.; Edelstein, N. M.; Meyer, K. *J. Am. Chem. Soc.* **2008**, *130*, 12536.

(81) Ismagilov, Z. R.; Lazareva, S. V.; Shikina, N. V.; Kuznetsov, V. V.; Kerzhentsev, M. A.; Ostrovsky, Y. V.; Rudina, N. A.; Rogov, V. A.; Ushakov, V. A. *Mendeleev Communications* **2011**, *21*, 209.

(82) Lei, Y.; Cant, N. W.; Trimm, D. L. *Catal Lett* **2005**, *103*, 133.

(83) Chang, C.-C. *Inorg. Chim. Acta* **1984**, *94*, 259.

(84) Ismagilov, Z. R.; Kuntsevich, S. V.; Shikina, N. V.; Kuznetsov, V. V.; Kerzhentsev, M. A.; Ushakov, V. A.; Rogov, V. A.; Boronin, A. I.; Zaikovsky, V. I. *Catalysis Today* **2010**, *157*, 217.

(85) Cottingham, P. L.; Barker, L. K. *Ind. Eng. Chem. Prod. Res. Dev.* **1973**, *12*, 41.

(86) Amrute, A. P.; Krumeich, F.; Mondelli, C.; Perez-Ramirez, J. *Chemical Science* **2013**, *4*, 2209.

(87) Cotton, S. *Lanthanides and actinides*; Macmillan Education: London, 1991.

(88) Sutton, G. A.; Napier, S. T.; John, M.; Taylor, A. *Science of The Total Environment* **1993**, *130-131*, 393.

(89) (a) Taylor, G. H. In *Studies in Environmental Science*; Trudinger, P. A., Swaine, D. J., Eds.; Elsevier, 1979; Vol. Volume 3(b) Aellen, T. C.; Umbricht, O.; Goerlich, W. *Science of The Total Environment* **1993**, *130-131*, 253(c) Kanai, Y.; Sakamaki, Y.

Appl. Geochem. **1994**, *9*, 547(d) Skwarzec, B.; Borylo, A.; Struminska, D. *Journal of Environmental Radioactivity* **2002**, *61*, 345(e) Pekala, M.; Kramers, J. D.; Waber, H. N. *Appl. Radiat. Isot.* **2010**, *68*, 984.

(90) Meitner, L.; Frisch, O. R. *Nature* **1939**, *143*, 239.

(91) "Nuclear Energy Today " OECD Nuclear Energy Agency, 2003.

(92) (a) Gauthier-Lafaye, F. *Compt. Rend. Phys.* **2002**, *3*, 839(b) Fayek, M.; Utsunomiya, S.; Ewing, R. C.; Riciputi, L. R.; Jensen, K. A. *Am. Miner.* **2003**, *88*, 1583(c) Utsunomiya, S.; Ewing, R. C. *Radiochim. Acta* **2006**, *94*, 749.

(93) Horie, K.; Hidaka, H. *Radiochim. Acta* **2004**, *92*, 805.

(94) Noseck, U.; Brasser, T.; Rajlich, P.; Laciok, A.; Hercik, M. *Radiochim. Acta* **2004**, *92*, 797.

(95) Bruno, J.; Duro, L.; Grivé, M. *Chem. Geol.* **2002**, *190*, 371.

(96) "Nuclear Power Reactors in the World," International Atomic Energy Agency, 2011.

(97) "Nuclear Power Reactors in the World," International Atomic Energy Agency, 2013.

(98) (a) "Thorium Fuel Cycle – Potential Benefits and Challenges," International Atomic Energy Agency, 2005(b) Kazimi, M.; Moniz, E. J.; Forsberg, C. W.; Ansolabehere, S.; Deutch, J. M.; Driscoll, M. J.; Golay, M. W.; Kadak, A. C.; Parsons, J. E.; Regalbuto, M.; Apostolakis, G.; Hejzlar, P.; Shwageraus, E. "The Future of the Nuclear Fuel Cycle," Massachusetts Institute of Technlogy, 2011.

(99) Wilson, P. D. *The Nuclear Fuel Cycle: From Ore to Waste*; Oxford University Press: Oxford, 1996.

(100) (a) Wronkiewicz, D. J.; Bates, J. K.; Gerding, T. J.; Veleckis, E.; Tani, B. S. *J. Nucl. Mat.* **1992**, *190*, 107(b) Janeczek, J.; Ewing, R. C.; Oversby, V. M.; Werme, L. O. *J. Nucl. Mater.* **1996**, *238*, 121(c) Sunder, S.; Shoesmith, D. W.; Miller, N. H. *J. Nucl. Mat.* **1997**, *244*, 66(d) Senanayake, S. D.; Rousseau, R.; Colegrave, D.; Idriss, H. *J. Nucl. Mat.* **2005**, *342*, 179(e) Clarens, F.; Giménez, J.; Pablo, J. d.; Casas, I.; Rovira, M.;

Dies, J.; Quiñones, J.; Martínez-Esparza, A. *Radiochim. Acta* **2005**, *93*, 533(f) Bruno, J. E., Rodney C. *Elements* **2006**, *2*, 343(g) Amme, M.; Svedkauskaite, J.; Bors, W.; Murray, M.; Merino, J. *Radiochim. Acta* **2007**, *95*, 683(h) Jegou, C.; Muzeau, B.; Broudic, V.; Roudil, D.; Deschanels, X. *Radiochim. Acta* **2007**, *95*, 513(i) Meca, S.; Marti, V.; de Pablo, J.; Giménez, J.; Casas, I. *Radiochim. Acta* **2008**, *96*, 535(j) Forbes, T. Z.; Horan, P.; Devine, T.; McInnis, D.; Burns, P. C. *Am. Mineral.* **2011**, *96*, 202(k) van Veelen, A.; Copping, R.; Law, G. T. W.; Smith, A. J.; Bargar, J. R.; Rogers, J.; Shuh, D. K.; Wogelius, R. A. *Mineral. Mag.* **2012**, *76*, 3095.

(101) (a) Olsson, M.; Glanneskog, H.; Jakobsson, A. M.; Nilsson, H.; Albinsson, Y. *Radiochim. Acta* **2005**, *93*, 341(b) Shuller, L. C.; Ewing, R. C.; Becker, U. *Am. Mineral.* **2010**, *95*, 1151(c) Giménez, J.; Martínez-Lladó, X.; Rovira, M.; de Pablo, J.; Casas, I.; Sureda, R.; Martinez-Esparza, A. *Radiochim. Acta* **2010**, *98*, 479.

(102) Grambow, B.; Poinssot, C. *Elements* **2012**, *8*, 213.

(103) Hedin, A. "Spent nuclear fuel - how dangerous is it?," Svensk Kärnbränslehantering AB, 1997.

(104) McGinnity, P.; Currivan, L.; Dowdall, A.; Hanley, O.; Kelleher, K.; McKittrick, L.; Colmáin, M. O.; Pollard, D.; Somerville, S.; Wong, J.; McMahon, C. "Radioactivity Monitoring of the Irish Environment 2010–2011," Radiological Protection Institute of Ireland, 2012.

(105) Denniss, I. S.; Jeapes, A. P. In *The Nuclear Fuel Cycle: From Ore to Waste*; Wilson, P. D., Ed.; Oxford University Press: Oxford, 1996.

(106) Efremenkov, V. M. "The IAEA activities and programs on technologies and methodologies for processing of old legacy radioactive waste," International Atomic Energy Agency, 2004.

(107) "Status of Used Nuclear Fuel Storage at U.S. Commercial Nuclear Plants," Nuclear Energy Institute, 2011.

(108) Wald, M. L. In *New York Times* New York, 2013.

(109) Deissmann, G.; Neumeier, S.; Modolo, G.; Bosbach, D. *Mineral. Mag.* **2012**, *76*, 2911.

(110) McFarlane, H. F. In *Encyclopedia of Energy*; Cutler, J. C., Ed.; Elsevier: New York, 2004.

(111) (a) Mathur, J. N.; Murali, M. S.; Nash, K. L. *Solv. Extr. Ion Exch.* **2001**, *19*, 357(b) Paiva, A. P.; Malik, P. *J. Radioanal. Nucl. Chem.* **2004**, *261*, 485(c) Neerdael, B.; Nachmilner, L. "Disposal Approaches for Long Lived Low and Intermediate Level Radioactive Waste," International Atomic Energy Agency, 2009(d) Burr, J. G. *Radiation Research* **1958**, *8*, 214(e) Mincher, B.; Modolo, G.; Mezyk, S. *Solv. Extr. Ion Exch.* **2009**, *27*, 1(f) Kumar, S.; Kamachi Mudali, U.; Natarajan, R. *J. Radioanal. Nucl. Chem.* **2011**, *289*, 587(g) Poineau, F.; Mazaubrun, J. D.; Ford, D.; Fortner, J.; Kropf, J.; Silva, G. W. C.; Smith, N.; Long, K.; Jarvinen, G.; Czerwinski, K. *Radiochim. Acta* **2008**, *96*, 527(h) Pereira, C.; Vandegrift, G. F.; Regalbuto, M. C.; Aase, S. B.; Bakel, A. J.; Bowers, D.; Byrnes, J. P.; Clark, M. A.; Emery, J. W.; Falkenberg, J. R.; Gelis, A. V.; Hafenrichter, L.; Leonard, R.; Quigley, K. J.; Tsai, Y.; Vander Pol, M. H.; Laidler, J. J. 2005 Waste Management Symposium Proceedings, Tucson, AZ, 2005(i) Romanovskiy, V. N.; Smirnov, I. V.; Babain, V. A.; Todd, T. A.; Herbst, R. S.; Law, J. D.; Brewer, K. N. *Solv. Extr. Ion Exch.* **2001**, *19*, 1(j) Law, J. D.; Herbst, R. S.; Todd, T. A.; Romanovskiy, V. N.; Babain, V. A.; Esimantovskiy, V. M.; Smirnov, I. V.; Zaitsev, B. N. *Solv. Extr. Ion Exch.* **2001**, *19*, 23(k) Schulz, W. W.; Horwitz, E. P. *Sep. Sci. Technol.* **1988**, *23*, 1191.

(112) (a) Baudin, G.; Lefevre, J.; Pruner, C.; Salvatores, M. "Proc. Technical Committee on Safety and Environmental Aspects of Partitioning and Transmutation of Actinides and Fission Products," 1995(b) Beauvy, M.; Duverneix, T.; Berlanga, C.; Mazoyer, R.; Duriez, C. *J. Alloy. Compd.* **1998**, *271*, 557(c) Madic, C. *Actinide and Fission Product Partitioning and Transmutation*, 2000(d) Nitsche, H. *Chem. Rev.* **2013**, *113*, 855.

(113) (a) Nilsson, M.; Nash, K. L. *Solv. Extr. Ion Exch.* **2007**, *25*, 665(b) Jensen, M. P.; Bond, A. H. *J. Am. Chem. Soc.* **2002**, *124*, 9870(c) Choppin, G. R.; Jensen, M. P.; Katz, J. J. In *The Chemistry of the Actinide and Transactinide Elements*; Morss, L. R., Edelstein, N.

M., Fuger, J., Eds.; Springer: Dordrecht, The Netherlands, 2006(d) Mehdoui, T.; Berthet, J. C.; Thuery, P.; Ephritikhine, M. *Dalton Trans.* **2004**, 579(e) Mazzanti, M.; Wietzke, R. L.; Pecaut, J.; Latour, J. M.; Maldivi, P.; Remy, M. *Inorg. Chem.* **2002**, *41*, 2389(f) Gaunt, A. J.; Scott, B. L.; Neu, M. P. *Angew. Chem.* **2006**, *118*, 1668.

(114) (a) Bullock, J. I.; King, M. E. *Inorg. & Nucl. Chem. Lett.* **1975**, *11*, 605(b) Pai, S. A.; Lohithakshan, K. V.; Mithapara, P. D.; Aggarwal, S. K. *J. Radioanal. Nucl. Chem.* **2000**, *245*, 623(c) Takeishi, H.; Kitatsuji, Y.; Kimura, T.; Meguro, Y.; Yoshida, Z.; Kihara, S. *Anal. Chim. Acta* **2001**, *431*, 69(d) Pavithran, R.; Reddy, M. L. P. *Radiochim. Acta* **2003**, *91*, 163(e) Dhami, P. S.; Dudwadkar, N. L.; Achuthan, P. V.; Jambunathan, U.; Dey, P. K. *Sep. Sci. Technol.* **2004**, *39*, 3143(f) Mincher, B. J.; Modolo, G.; Mezyk, S. P. *Solv. Extr. Ion Exch.* **2009**, *27*, 579(g) Mincher, B. J.; Modolo, G.; Mezyk, S. P. *Solv. Extr. Ion Exch.* **2009**, *27*, 331(h) Atanassova, M.; Dukov, I. *J. Solut. Chem.* **2009**, *38*, 289.

(115) (a) Berthet, J. C.; Miquel, Y.; Iveson, P. B.; Nierlich, M.; Thuery, P.; Madic, C.; Ephritikhine, M. *J. Chem. Soc., Dalton Trans.* **2002**, 3265(b) Mehdoui, T.; Berthet, J. C.; Thuery, P.; Salmon, L.; Rivière, E.; Ephritikhine, M. *Chem. Eur. J.* **2005**, *11*, 6994(c) Denecke, M. A.; Rossberg, A.; Panak, P. J.; Weigl, M.; Schimmelpfennig, B.; Geist, A. *Inorg. Chem.* **2005**, *44*, 8418(d) Berthet, J. C.; Thuery, P.; Foreman, M. R. S.; Ephritikhine, M. *Radiochim. Acta* **2008**, *96*, 189(e) Panak, P. J.; Geist, A. *Chem. Rev.* **2013**, *113*, 1199.

(116) (a) Reddy, M. L. P.; Sahu, S. K.; Chakravortty, V. *Solv. Extr. Ion Exch.* **2000**, *18*, 1135(b) Meera, R.; Varma, R. L.; Reddy, M. L. P. *Solvent Extr. Res. Dev.-Jpn.* **2003**, *10*, 13.

(117) Drew, M. G. B.; Foreman, M. R. S. J.; Hill, C.; Hudson, M. J.; Madic, C. *Inorg. Chem. Commun.* **2005**, *8*, 239.

(118) (a) Magnusson, D.; Christiansen, B.; Foreman, M. R. S.; Geist, A.; Glatz, J. P.; Malmbeck, R.; Modolo, G.; Serrano-Purroy, D.; Sorel, C. *Solv. Extr. Ion Exch.* **2009**,

27, 97(b) Magnusson, D.; Christiansen, B.; Malmbeck, R.; Glatz, J. P. *Radiochim. Acta* **2009**, *97*, 497.

(119) Lewis, F. W.; Harwood, L. M.; Hudson, M. J.; Drew, M. G. B.; Desreux, J. F.; Vidick, G.; Bouslimani, N.; Modolo, G.; Wilden, A.; Sypula, M.; Vu, T. H.; Simonin, J. P. *J. Am. Chem. Soc.* **2011**, *133*, 13093.

(120) (a) Zhu, Y. J.; Chen, J.; Jiao, R. Z. *Solv. Extr. Ion Exch.* **1996**, *14*, 61(b) Modolo, G.; Odoj, R. *J. Radioanal. Nucl. Chem.* **1998**, *228*, 83(c) Peterman Dean, R.; Law Jack, D.; Todd Terry, A.; Tillotson Richard, D. In *Separations for the Nuclear Fuel Cycle in the 21st Century*; American Chemical Society, 2006; Vol. 933.

(121) (a) Ionova, G.; Ionov, S.; Rabbe, C.; Hill, C.; Madic, C.; Guillaumont, R.; Krupa, J. C. *Solv. Extr. Ion Exch.* **2001**, *19*, 391(b) Wang, X.; Zhu, Y.; Jiao, R. *Solv. Extr. Ion Exch.* **2001**, *19*, 1007.

(122) Kirker, I.; Kaltsoyannis, N. *Dalton Trans.* **2011**, *40*, 124.

(123) (a) Walenta, K. *Am. Mineral.* **1974**, *59*, 166(b) Smellie, J. *Radwaste Mag.* **1995**, *2*, 18(c) Gauthier-Lafaye, F.; Holliger, P.; Blanc, P. L. *Geochim. Cosmochim. Acta* **1996**, *60*, 4831.

(124) Naftz, D. L.; Fuller, C. C.; Davis, J. A.; Morrison, S. J.; Feltcorn, E. M.; Freethey, G. W.; Rowland, R. C.; Wilkowske, C.; Piana, M. J. In *Handbook of Groundwater Remediation Using Permeable Reactive Barriers. Application to Radionuclides, Trace Metals, and Nutrients*; Naftz, D. L., Morrison, S. J., Davis, J. A., Fuller, C. C., Eds.; Academic Press: San Diego, 2002.

(125) Wang, Z.; Zachara, J. M.; Gassman, P. L.; Liu, C.; Qafoku, O.; Yantasee, W.; Catalano, J. G. *Geochim. Cosmochim. Acta* **2005**, *69*, 1391.

(126) (a) LoPresti, V.; Conradson, S. D.; Clark, D. L. *J. Alloys Compd.* **2007**, *444*, 540(b) Neu, M. P.; Runde, W. H.; Clark, D. L.; Conradson, S. D.; Efurd, D. W.; Janecky, D. R.; Kaszuba, J. P.; Tait, C. D.; Haire, R. G. *Abstr. Pap. Am. Chem. Soc.* **1999**, *218*, U1084.

(127) (a) Burakov, B. E.; Strykanova, E. E.; Anderson, E. B. *Mater. Res. Soc. Symp. Proc.* **1997**, *465*, 1309(b) McKinley, J. P.; Zachara, J. M.; Wan, J.; McCready, D. E.; Heald, S.

M. *Vadose Zone J.* **2007**, *6*, 1004(c) Armstrong, C. R.; Nyman, M.; Shvareva, T.; Sigmon, G. E.; Burns, P. C.; Navrotsky, A. *Proceedings of the National Academy of Sciences* **2012**, *109*, 1874.

(128) (a) Johnson, L. H.; Shoesmith, D. W.; Lutze, W.; Ewing, R. C. *Radioactive Waste Forms for the Future*, 1988(b) Abrefah, J.; Marschmann, S.; Jenson, E. D. *PNNL-11806*, 1998.

(129) Burns, P. C.; Finch, R. J. *Uranium: Mineralogy, Geochemistry and the Environment*, 1999.

(130) (a) Finch, R. J.; Ewing, R. C. *J. Nucl. Mater.* **1992**, *190*, 133(b) Zhao, D.; Ewing, R. C. *Radiochim. Acta* **2000**, *88*, 739.

(131) Murakami, T.; Isobe, H.; Nagano, T.; Nakashima, S. *Mater. Res. Sot. Symp. Proc.* **1992**, *257*, 473.

(132) Shoesmith, D. W. *J. Nucl. Mat.* **2000**, *282*, 1.

(133) Finch, R. J.; Ewing, R. C. *J. Nucl. Mat.* **1992**, *190*, 133.

(134) (a) Wronkiewicz, D. J.; Bates, J. K.; Gerding, T. J.; Veleckis, E.; Tani, B. S. *J. Nucl. Mater.* **1992**, *190*, 107(b) Wronkiewicz, D. J.; Bates, J. K.; Wolf, S. F.; Buck, E. C. *J. Nucl. Mat.* **1996**, *238*, 78.

(135) (a) Finn, P. A.; Hoh, J. C.; Wolf, S. F.; Slater, S. A.; Bates, J. K. *Radiochim. Acta* **1996**, *74*, 65(b) Finch, R. J.; Buck, E. C.; Finn, P. A.; Bates, J. K. *Mater. Res. Soc. Symp. Proc.* **1999**, *556*, 431.

(136) (a) Clark, D. L.; Hobart, D. E.; Neu, M. P. *Chemical Reviews* **1995**, *95*, 25(b) Frost, R. L.; Čejka, J. *J. Raman Spectrosc.* **2009**, *40*, 1096(c) Frost, R. L.; Čejka, J.; Ayoko, G. A.; Dickfos, M. J. *J. Raman Spectrosc.* **2008**, *39*, 374(d) Li, Y.; Burns, P. C. *Can. Mineral.* **2001**, *39*, 1147.

(137) Deditius, A. P.; Utsunomiya, S.; Ewing, R. C. *Chem. Geol.* **2008**, *251*, 33.

(138) Labs, S.; Hennig, C.; Weiss, S.; Curtius, H.; Z√§nker, H.; Bosbach, D. *Env. Sci. Technol.* **2013**, *48*, 854.

(139) (a) Costin, D. T.; Mesbah, A.; Clavier, N.; Dacheux, N.; Poinssot, C.; Szenknect, S.; Ravaux, J. *Inorg. Chem.* **2011**, *50*, 11117(b) Szenknect, S.; Costin, D. T.; Clavier, N.; Mesbah, A.; Poinssot, C.; Vitorge, P.; Dacheux, N. *Inorg. Chem.* **2013**, *52*, 6957.

(140) (a) Choppin, G. R. *Eur. J. Solid State Inorg. Chem.* **1991**, *28*, 319(b) Kim, J. I.; Zeh, P.; Delakowitz, B. *Radiochim. Acta* **1992**, *58-9*, 147(c) Dozol, M.; Hagemann, R. *Pure Appl. Chem.* **1993**, *65*, 1081(d) Jedináková-Krizová, V. *J. Radioanal. Nucl. Chem.* **1998**, *229*, 13(e) Choppin, G. R. *J. Radioanal. Nucl. Chem.* **2007**, *273*, 695(f) Havlovu, V.; Ve$f$çernik, P.; Najser, J.; Sosna, K.; Breiter, K. *Mineral. Mag.* **2012**, *76*, 3191(g) Maher, K.; Bargar, J. R.; Brown, G. E. *Inorg. Chem.* **2012**, *52*, 3510.

(141) (a) Kaszuba, J. P.; Runde, W. H. *Env. Sci. Technol.* **1999**, *33*, 4427(b) Burns, P. C.; Deely, K. M.; Skanthakumar, S. *Radiochim. Acta* **2004**, *92*, 151(c) Douglas, M.; Clark, S. B.; Friese, J. I.; Arey, B. W.; Buck, E. C.; Hanson, B. D.; Utsunomiya, S.; Ewing, R. C. *Radiochim. Acta* **2005**, *93*, 265(d) Burns, P. C.; Klingensmith, A. L. *Elements* **2006**, *2*, 351(e) Klingensmith, A. L.; Burns, P. C. *Am. Mineral.* **2007**, *92*, 1946.

(142) (a) Ikeda-Ohno, A.; Hennig, C.; Rossberg, A.; Funke, H.; Scheinost, A. C.; Bernhard, G.; Yaita, T. *Inorg. Chem.* **2008**, *47*, 8294(b) Rao, L.; Tian, G.; Xia, Y.; Friese, J.; Zanonato, P.; Di Bernardo, P.; Wai, C. M.; Mincher, B. J. *Nuclear Energy and the Environment*, 2010(c) Sundararajan, M.; Assary, R. S.; Hillier, I. H.; Vaughan, D. J. *Dalton Trans.* **2011**, *40*, 11156(d) Walther, C.; Denecke, M. A. *Chem. Rev.* **2013**, *113*, 995.

(143) Burns, P. C.; Ewing, R. C.; Miller, M. L. *J. Nucl. Mat.* **1997**, *245*, 1.

(144) Meredith, N. A.; Polinski, M. J.; Cross, J. N.; Villa, E. M.; Simonetti, A.; Albrecht-Schmitt, T. E. *Cryst. Growth Des.* **2012**, *13*, 386.

(145) Burns, P. C.; Li, Y. *Am. Mineral.* **2002**, *87*, 550.

(146) (a) Fortner, J. A.; Finch, R. J.; Kropf, A. J.; Cunnane, J. C. *Nucl. Technol.* **2004**, *148*, 174(b) Klingensmith, A. L.; Deely, K. M.; Kinman, W. S.; Kelly, V.; Burns, P. C. *Am. Mineral.* **2007**, *92*, 662.

(147) Denecke, M. A. *Coord. Chem. Rev.* **2006**, *205*, 730.

(148) (a) Jerden Jr, J. L.; Sinha, A. K.; Zelazny, L. *Chem. Geol.* **2003**, *199*, 129(b) Murakami, T.; Ohnuki, T.; Isobe, H.; Sato, T. *Am. Mineral.* **1997**, *82*, 888(c) Jensen, M. P.; Nash, K. L.; Morss, L. R.; Appelman, E. H.; Schmidt, M. A. In *Humic and Fulvic Acids - Isolation, Structure, and Environmental Role*; Gaffney, J. S., Marley, N. A., Clark, S. B., Eds.; Amer Chemical Soc: Washington, 1996; Vol. 651(d) Gauglitz, R.; Holterdorf, M.; Franke, W.; Marx, G. *MRS Online Proc. Lib.* **1991**, *257*, 331.

(149) (a) Dacheux, N.; Clavier, N.; Robisson, A. C.; Terra, O.; Audubert, F.; Lartigue, J. E.; Guy, C. *C. R. Chim.* **2004**, *7*, 1141(b) Terra, O.; Dacheux, N.; Audubert, F.; Podor, R. *J. Nucl. Mat.* **2006**, *352*, 224.

(150) Wall, N. A.; Clark, S. B.; McHale, J. L. *Chem. Geol.* **2010**, *274*, 149.

(151) Parker, A.; Rae, J. E. *Environmental Interactions of Clays: Clays and the Environment*, 2010.

(152) Burns, P. C. *Can. Mineral.* **2005**, *43*, 1839.

(153) (a) Ling, J.; Qiu, J.; Burns, P. C. *Inorg. Chem.* **2012**, *51*, 2403(b) Qiu, J.; Nguyen, K.; Jouffret, L.; Szymanowski, J. E. S.; Burns, P. C. *Inorg. Chem.* **2012**, *52*, 337(c) Sigmon, G. E.; Burns, P. C. *J. Am. Chem. Soc.* **2011**, *133*, 9137(d) Sigmon, G. E.; Ling, J.; Unruh, D. K.; Moore-Shay, L.; Ward, M.; Weaver, B.; Burns, P. C. *J. Am. Chem. Soc.* **2009**, *131*, 16648.

(154) Qiu, J.; Burns, P. C. *Chem. Rev.* **2012**, *113*, 1097.

(155) (a) Burns, P. C. *Mineral. Mag.* **2011**, *75*, 1(b) Unruh, D. K.; Ling, J.; Qiu, J.; Pressprich, L.; Baranay, M.; Ward, M.; Burns, P. C. *Inorg. Chem.* **2011**, *50*, 5509.

(156) (a) Kubatko, K.-A. H.; Helean, K. B.; Navrotsky, A.; Burns, P. C. *Science* **2003**, *302*, 1191(b) Vlaisavljevich, B.; Gagliardi, L.; Burns, P. C. *J. Am. Chem. Soc.* **2010**, *132*, 14503.

(157) Locock, A. J.; Burns, P. C. *Am. Mineral.* **2003**, *88*, 240.

(158) Coda, A.; Della Giusta, A.; Tazzoli, V. *Acta Crystallogr., B* **1981**, *B37*, 1496.

Aims of the Project

This Thesis aims to:

- Synthesise studtite, the uranyl peroxide phase alteration found on SNF and in nature, and its dehydrated congener metastudtite (**Chapter 2**).
- Investigate the structural and electronic effects of dehydration on the studtite uranyl centre using XAS (**Chapter 2**).
- Synthesise a diverse range of uranyl minerals that exist as common phase transitions in nature (**Chapter 3**).
- Investigate the stability of these phase transitions with respect to possible redox reactions (**Chapters 2 and 3**).
- Compare the relative stability of uranyl minerals according to structural motifs, anion type and cation–cation interactions (**Chapter 3**).
- Synthesise a uranyl phenoxide complex and investigate its activity towards the ring-opening polymerisation of oxygen containing monomers (**Chapter 4**).
- Use a combination of spectroscopic and theoretical techniques to understand the mechanism of catalysis and the role of uranyl (**Chapter 4**).

Chapter 2:

Uranyl Minerals Relevant to the Long Term Storage of Spent Nuclear Fuel: Investigating the Chemistry of Studtite

2.1. Introduction

As described in **Section 1.2.3.**, phase transitions from U(IV) in UO_2[1] and SNF[2] to uranyl(VI) are likely in oxidising environments, resulting in many uranyl minerals being formed. Interactions with humics in soil or groundwater ions such as hydroxyls, silicates, carbonates and phosphates affect the speciation of uranium[3] and so will result in a variety of transformations and phase alterations.[4] This chapter describes the investigation of one of these phase transitions: the uranyl peroxide mineral studtite, $[(UO_2)(\eta^2\text{-}O_2)(H_2O)_2]\cdot 2H_2O$, and its dehydrated congener metastudtite, $[(UO_2)(\eta^2\text{-}O_2)(H_2O)_2]$.

In tests, studtite has been found to be the thermodynamically favoured product of various uranyl minerals:[5] uranyl oxyhydroxide minerals schoepite, $[(UO_2)_8(O)_2(OH)_{12}]\cdot 12H_2O$, and metaschoepite, $[(UO_2)_8(O)_2(OH)_{12}]\cdot 10H_2O$, and uranyl silicates such as soddyite, $[(UO_2)_2(SiO_4)]\cdot 2H_2O$, have all been found to evolve into studtite in deionised water over two years.[6] It appears that the radiolysis of water creates an oxidising environment that triggers the formation of the uranyl peroxide.[7] This indicates the importance of studtite as a long-term product of the dissolution of UO_2 in a repository and, as such, has made studtite a focus for research in the last decade.[5-8]

The work described within this chapter will detail the use of solid-state electrochemistry to explain potentially viable redox interactions with radionuclides in SNF and the use of X-ray absorption spectroscopy (XAS) to explain the unexpectedly large shift in the optical absorption spectra caused by the removal of the interstitial water molecules in studtite to form metastudtite.[9] The use of XAS gives structural information as well as electronic information (see **Section 2.1.2.3.**) and this is the first reported example of an experimental elucidation of the structure of metastudtite.

2.1.1. The Effects of Studtite Formation on SNF

The formation of studtite has been ascribed to the reaction of SNF and H_2O_2 (formed by the α-radiolysis of water).[5] This mechanism has been observed to be retarded by the presence of Fe(II) ions as decomposition of H_2O_2 appears to be faster than precipitation of studtite.[10] Fe(II) concentration appears to have a significant effect on the long-term stability of the nuclear mass – at the natural reactors in Gabon, for example, while U(VI) is predominant in the aqueous phase, the uraninite (the natural form of pitchblende or UO_2) reactors were preserved for two billion years due to the presence of Fe(II) minerals (chlorite, pyrite, siderite, etc.) and organic matter that maintained the reduced potential around the reactor.[11] Without the inhibitive effects of Fe(II), however, studtite will form. Studtite has been found on the surface of SNF,[12] 'lava' from the Chernobyl Nuclear Plant accident,[13] and in naturally occurring uranium ores.[14] Uranyl peroxides have also been observed in the presence of carbonate[15] and hydroxide[16] ions, indicating that a partial pressure of carbon dioxide or a high pH will not hinder the peroxide phase transition, although a high pH has been observed to yield nanoclusters of uranyl peroxide building blocks.[17] These nanoclusters are predicted to form in the cooling tanks of the Fukushima-Daiichi nuclear reactor in Japan[18] from the interaction with the "corium" (the lava like material resulting from the melted fuel, steel and concrete from the reactor) and seawater.

The first mention of a uranium peroxide was by Fairley in 1877,[19] who described the structure as containing a double peroxide. The solid state structure was determined experimentally in 2003 to be an infinite linear chain bridged by peroxides [**Figure 2.1(a)**].[7b] In 1961, Sato found that two crystalline forms of uranium peroxide hydrate exist and that the product is temperature dependent: synthetic studtite precipitates below 50 °C following addition of H_2O_2 to an aqueous solution containing uranyl ions, whereas synthetic metastudtite, the dihydrate $[(UO_2)(\eta^2\text{-}O_2)(H_2O)_2]$, precipitates above 70 °C [**Figure 2.1(b)**]. At 60 °C, a mixture of the two solid phases will precipitate out.[20] Sato also demonstrated that studtite is converted to metastudtite by drying in air at 100 °C or in vacuum for 24 hours at room temperature. The thermal decomposition of both $[(UO_2)(\eta^2\text{-}O_2)(H_2O)_2]\cdot 2H_2O$ and $[(UO_2)(\eta^2\text{-}O_2)(H_2O)_2]$ was also studied by Cordfunke *et al.* in 1963.[21] Further analysis of the thermal decomposition of studtite by Rey *et al.* revealed that heating metastudtite to 230°C will yield metaschoepite, $[(UO_2)_8O_2(OH)_{12}]\cdot 10H_2O$, or simply $UO_3\cdot 2H_2O$, confirmed by Powder X-ray Diffraction (PXRD).[22]

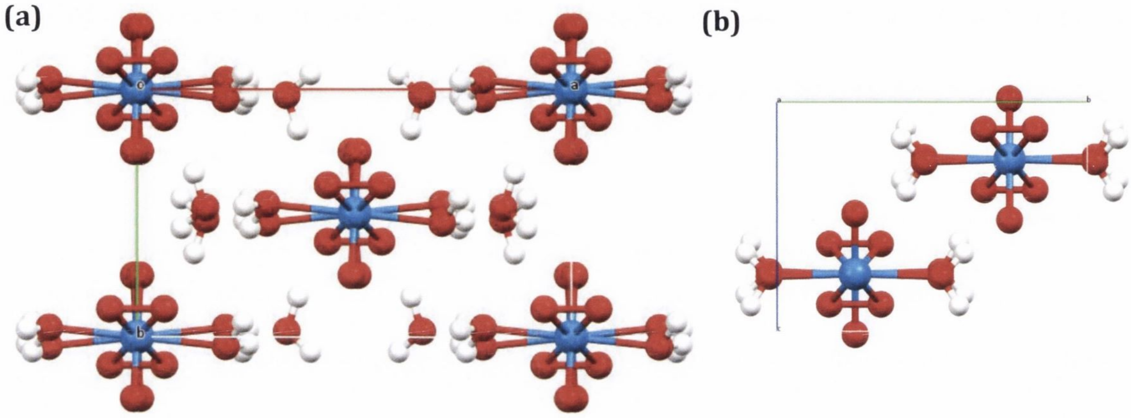

Figure 2.1: Crystal structure of studtite[7b] as viewed along the infinite 1D chain that lies along the c axis (left) and the calculated structure of metastudtite,[8c] wherein the 1D chain lies along the a axis (right). The interstitial water molecules in studtite are removed upon heating at 100°C for one hour to yield metastudtite (Key: blue = uranium; red = oxygen; white = hydrogen).

Although studtite is the thermodynamically favourable product of uranyl minerals in deionised water,[6a,23] studtite and metastudtite are the only known stable peroxo-containing minerals in nature. The *trans* arrangement of the peroxo ligands is typically not observed in transition metal peroxides; for group VI transition metals (chromium, molybdenum and tungsten) in the +6 oxidation state the *cis* arrangement is the favourable stereochemistry of the complexes so that the $\eta^2\text{-}O_2^{2-}$ π-donor will interact with different metal (t_{2g} in O_h) orbitals.[24] The bonding in studtite is therefore a point of interest: a computational examination of supramolecular uranyl peroxide clusters[18] characterised the bonding in these uranyl peroxide nanomaterials as an overlap of U(*6p*) orbitals with the peroxo π* bond.[17] The *6p* orbitals are normally considered core-like but as the *6d* and *5f* orbitals are involved in bonding to the axial uranyl oxygens, these are the next energetically accessible orbitals of the correct symmetry.[25] There has been contradictory work from Schreckenbach, however, that indicates that it is in fact the U(*6d*) orbitals, instead of the *6p*, which are involved in this covalent interaction, allowing greater overlap of the peroxo π bond.[26] This is something that is observed in the molecular $[UO_2(O_2)_2]^{2-}$ compounds, where there is evidence for increased mixing between the uranium *d* and peroxo π orbitals.[26] The bent U–(O_2)–U dihedral angle allows enhanced covalent interactions between the uranium f_{xyz} orbital, and the bridging peroxo π* orbital[17,27] as the constructive overlap of orbital lobes above and below the bond is encouraged. This has been described as the driving force for the formation of supramolecular clusters of up to 120 uranyl moieties.[5,28] Further evidence for the covalent interaction comes from the synthesis and concurrent quantum chemical analysis of the analogous hydroxy complexes, i.e. U–$(OH)_2$–U instead of U–O_2–U. These complexes yield a linear 180° U–O–U angle as without the analogous π bond there is no available molecular orbital of the correct symmetry for interaction with the U orbitals.[17]

Given that studtite is the thermodynamically favourable product, studying the incorporation of radionuclides into or onto studtite has become an important issue. There are three possible mechanisms for the incorporation of radionuclides into or onto studtite and metastudtite: (a) substitution of an isostructural UO_2^{2+} fragment; (b) sorption on the surface; or (c) outer-sphere redox processes.

Caesium[8a] and strontium[29] have both been shown to be sorbed onto studtite; ^{90}Sr, ^{137}Cs, ^{99}Tc, ^{237}Np and ^{239}Pu have been observed to concentrate in metastudtite on the basis of a two-year immersion study of SNF.[30] Interestingly, ^{241}Am and ^{244}Cm do not concentrate to such a degree. Metastudtite was shown to incorporate 6500 ppm ^{237}Np,[31] although the oxidation state of the neptunium in this species is uncertain. $[NpO_2]^+$ is water soluble and the incorporation and subsequent leaching through dissolution of the surfaces can have serious environmental ramifications.[31-32] There are conflicting mechanisms in the literature, postulating both the oxidation[31] and reduction[6c] of $[NpO_2]^+$ by hydrogen peroxide. The oxidation of the initial $[NpO_2]^+$ to $[NpO_2]^{2+}$ by hydrogen peroxide would enable the $[NpO_2]^{2+}$ – which is isostructural with uranyl – to replace UO_2^{2+}.[31] This is corroborated by DFT calculations.[8b] The proposed reduction pathway entails the reduction of $[NpO_2]^+$ to insoluble Np^{4+} by the addition of H_2O_2 during the formation of studtite.[6c] This Np(IV) subsequently precipitates out as a discrete phase, followed by gradual oxidation and release into solution as Np(V) (or $[NpO_2]^+$).[6c] More research is clearly needed to elucidate the mechanism in order to take measures to prevent the potential negative environmental effects.

2.1.2. X-ray Absorption Spectroscopy (XAS) of Uranyl Compounds

As discussed in **Chapter 1**, the uranyl moiety, $[O{=}U{=}O]^{2+}$, is the most prevalent form of uranium(VI). Actinide ions have two valence shells available to form σ and π bonds with oxygen: *5f* and *6d*. Uranyl has been investigated thoroughly experimentally and computationally to understand the participation of the uranium *5f*, *6d* and the oxygen *2p* orbitals in the bonds.[33] X-ray absorption spectroscopy (XAS) is an element specific technique – allowing independent analysis of the ligand[34] and metal[35] transitions – and is capable of unravelling both electronic and structural information of solids, solutions or gases.[36]

As in other forms of spectroscopy (infrared, UV, etc.), in XAS a photon of a specific energy is absorbed and the effects are measured. For XAS the photon is an X-ray and the effect is the excitation or emission of a core electron. As the electron is emitted, it is scattered by the neighbouring atoms. This series of interference patterns can be resolved into a spectrum showing the distances between atoms in the coordination sphere of the element being examined. This extended spectrum is the Extended X-ray Absorption Fine Structure (EXAFS) spectrum (**Figure 2.2**) and is element and isotope specific as the scattering of an electron is related to the atomic number and the mass number of any atom it interacts with.[36]

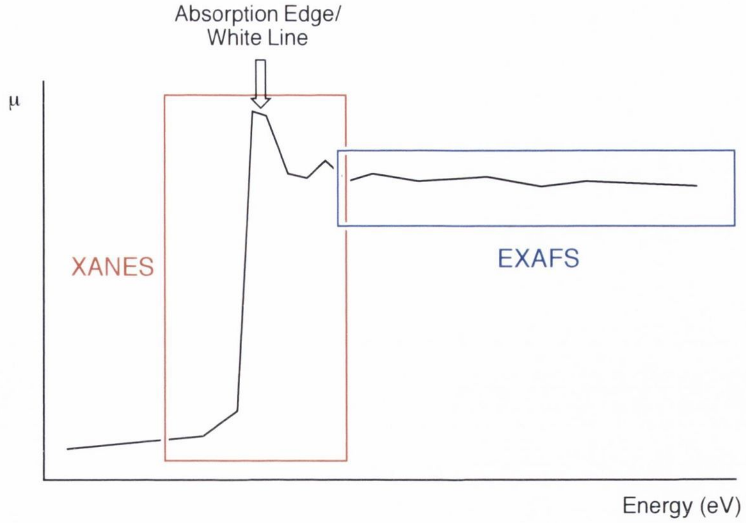

Figure 2.2: A sample XAS spectrum showing the XANES and EXAFS regions relative to the Absorption edge, E_o.

The maximum absorption, μ, is called the absorption edge or the white line, WL, and is the energy for removing an electron from the orbital in question completely from the atom. It is typically defined as E_0. The 50 eV before E_0 to ~100 eV after is referred to as the XANES (X-ray Absorption Near-Edge Structure) region; pre- and post-edge features can be indicative of electron population in the valence shell and of hybridisation around the atom in question (**Figure 2.2**).

The use of XAS for actinide systems is a recent development, for three reasons: (i) the need for high-energy beams (as a result of the high atomic number of the actinides); (ii) the lack of reliable model compounds and (iii) the safety concerns associated with the high specific activity of these samples mean limited access to suitable facilities.[37] In fact, in 2006 there were only seven institutes in five countries worldwide with synchrotron facilities aimed at the analysis of the actinides.[38] However, with increased availability of synchrotron facilities, improved computational techniques and better experimental equipment, XAS has come to be a common tool in the analysis of the structural and electronic properties of actinide materials.[35c,38-39]

XAS is element and orbital specific. The energy of the excitation X-ray can be tuned to the binding energy of the core orbitals; the absorption edge energies of the early actinides are shown in **Table 2.1**. The K, L and M edges are named for the principal quantum number of the electron being excited and indicate the shell from which the electron is emitted. A common emission edge for uranium experiments is the *L₃* edge – the emitted electrons are from the $2p_{3/2}$ orbital (**Figure 2.3**).

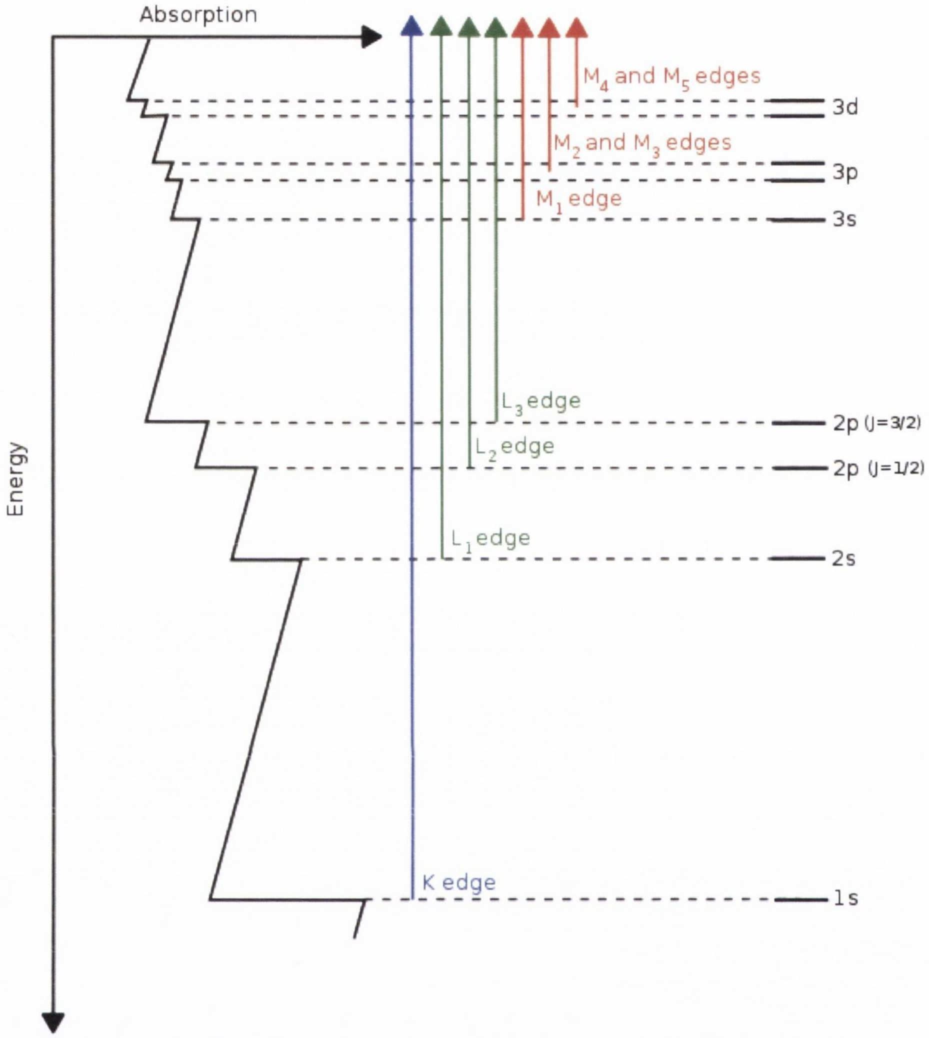

Figure 2.3: A schematic of the common emission edges in XAS.

Table 2.1: Absorption edge energies (E_0) for the early actinide elements in eV.[40]

Element	E (K)	E (L_1)	E (L_2)	E (L_3)
Th	109648	20470	19691	16300
Pa	112598	21100	20314	16733
U	115596	21756	20946	17165
Np	118689	22438	21615	17608
Pu	121790	23112	22270	18060
Am	124986	23808	22952	18056

2.1.2.1. *X-ray Absorbed Near-Edge Structure: XANES*

The XANES region encompasses the energies immediately below and above the maximum absorption, E_0 (also known as the White Line, WL). At energies slightly above E_0 the emitted photoelectron is scattered in all directions – the f(k) function for photoelectrons with low kinetic energy, E_{kin}, has significant values at all angles, and not only at 0°.[38] This, combined with the longer wavelength, $\lambda(k)$, at these same energies, leads to multiple scattering (MS) of the photoelectron. If the photoelectron has sufficient E_{kin} to escape the potential of the absorbing atom it is scattered on neighbouring atoms until it is eventually reabsorbed by the atom in question. These scattering processes give rise to the fine structures in the XANES spectra that contain information about the coordination geometry of the absorbing atom.[36] In fact, as well as the coordination geometry and interatomic distances within the coordination sphere, XANES features and their intensity and energy position are observed to be dependent on a number of factors including the oxidation state of the absorbing atom, orbital occupancy, and electronegativity of coordinating atoms. This combination of factors renders interpretation of XANES spectra difficult. Spectra can be "fingerprinted" by comparison with observed features of known compounds or predicted using theoretical XANES calculations under variation of specified parameters such as atomic cluster size to explain observed trends in experimental data.

When analysing a spectrum of the uranyl moiety, the WL absorbance corresponds to transitions to the partially filled *6d* orbitals.[39a] Because the XANES region involves transitions about E_0, the valence state of the absorbing atom can also be determined from XANES data. **Figure 2.4** shows that the edge shifts towards higher energies in the order UO_2, U_3O_8, UO_3 due to reduced shielding of the core electrons (i.e., the energy required to emit a core electron is increased) associated with the shift from U(IV) to U(VI) across the series.[38]

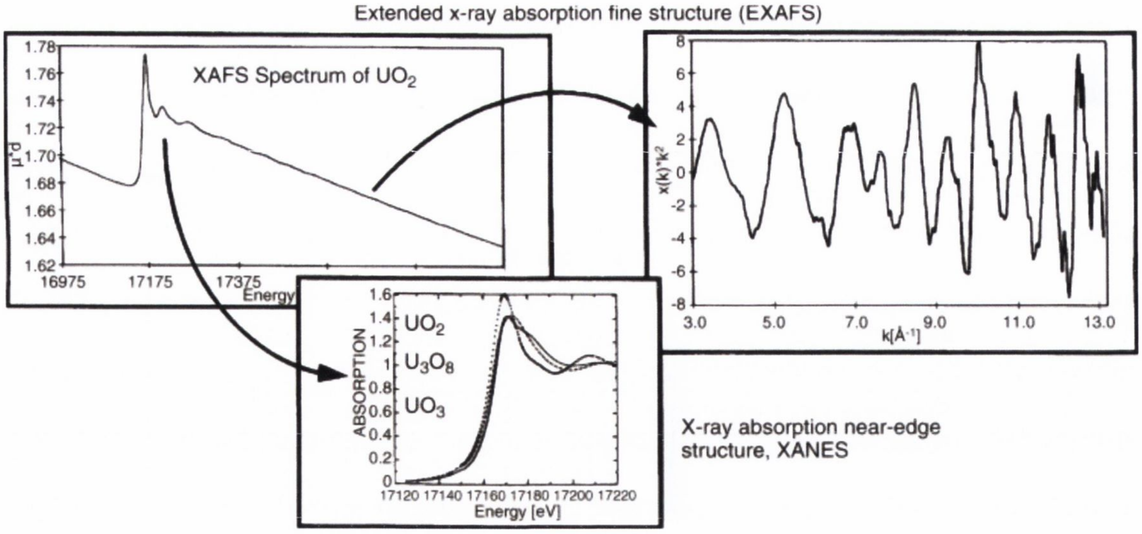

Figure 2.4: Raw data U *L₃* edge XAFS spectrum of solid UO_2 (left). This is normalised to unity, background subtracted and separated into XANES (bottom) and EXAFS data which is converted from eV into wavenumbers (k) and k^3-weighted (right). The XANES data of U(IV) in UO_2 is compared to that for the mostly U(V) population in U_3O_8 and for U(VI) in UO_3, with an observable shift in E_0 to increasing energies. Taken from reference 38.

By comparing XANES edge energies of samples with known oxidation states with that of an unknown, the oxidation state of the unknown can be identified.[35b] There is also a post-edge feature in the uranyl spectrum that is observed at approximately 15 eV above the WL. This MS XANES feature is characteristic for L_3 or L_2 edge XANES of all actinyl cations, not just uranyl,[39a] resulting from scattering along the axial oxygen bonds (An=O_{yl}) of the linear actinyl moiety.[41] The energy position of this MS feature depends greatly on the actual An=O_{yl} bond distance. The area of these peaks measures the oscillatory strength for a transition and is directly related to mixing coefficients of metal with ligand valence orbitals.[42]

2.1.2.2. *High-Resolution XANES*

The general set up of the XAS spectrometer is similar to most optical spectrometers except that it is possible to collect data in both transmission and fluorescence modes. Typically the fluorescence detector is situated at a right angle to the sample, on the horizontal plane to minimise scattered photons, but in recent years a more sensitive set-up involving analyser crystals that focus emitted photons onto a detector has been used.[43] These crystals increase the sensitivity and resolution of the experiment and drastically reduce collecting times. The arrangement of the components of the spectrometer is very particular: the crystals diffract the incoming photons according to Bragg's law and the scattered photons are aimed towards a detector sitting on the Rowland circle with a radius equal to the bending radius of the crystal (**Figure 2.5**). In this way any and all photons that hit the crystal will be focused onto the detector. With more crystals - crystals with equal bending radii - it is possible to greatly improve the resolution of the spectrometer as they can all focus on the same detector.

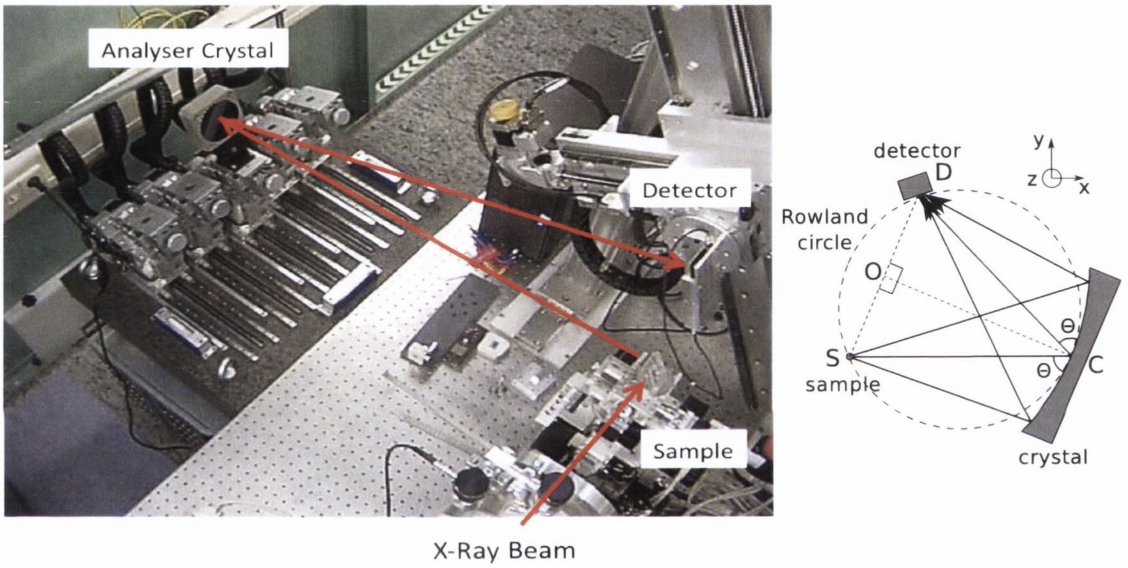

Figure 2.5: The Johann type spectrometer set-up at the Institute for Nuclear Waste Disposal (INE) Beamline at the ANKA Synchrotron facility at the Karlsruhe Institute of Technology (KIT) (left), courtesy of Dr Tonya Vitova from the INE. The Johann Spectrometer works upon the principle of the Rowland circle (right). The Rowland circle is in a plane perpendicular to the incident x-ray; the detector lies above the sample.[43]

Density of states (DOS) calculations imply that the maximum absorption edge (WL) corresponds with transitions to the partially filled *6d* orbitals. When modelling the *5f* DOS there was an indication that these lie slightly lower in energy than the *6d* electrons.[39a] The development of the Johann type spectrometer (**Figure 2.5**) has brought about the development of High-Resolution XANES experiments and has allowed the discernment of a pre-edge feature within the L_3 or L_2 HR-XANES spectrum.[35a,35c,43]

Electronic transitions obey the spin selection rules of ΔS ± 1, i.e. an electron from a *p* orbital can transition into an *s* or a *d* orbital, but a *p*→*f* transition is spin forbidden. The weak pre-edge feature describes mainly the forbidden transitions of $2p_{5/2}$ electrons to the unoccupied U *5f* valence states,[39a] thus giving greater insight into the population of the valence states of the absorbing atom and the concomitant participation of the *5f* orbitals in the U=O_{yl} bond.[35c] This pre-edge feature gives a greater ability to accurately determine oxidation state of the sample – the position of the WL is also affected by coordination geometry and the hybridisation around the uranium, so direct comparison and differentiation of U(IV) and U(VI) spectra is only possible if the two complexes are of similar geometry.

2.1.2.3. Extended X-Ray Absorption Fine Structure: EXAFS

When an electron is emitted from the atom it is scattered off the neighbouring atoms. EXAFS is a technique that uses the interference patterns of scattered electrons to produce a spectrum with peaks at discrete distances, corresponding to the bond lengths around the target atom. Raw EXAFS data is recorded as absorption as a function of energy, $\mu(E)$, as visible in **Figure 2.4(left)**. This is extracted according to **Equation 2.1**:

$$\chi(E) = \frac{\mu(E) - \mu_0(E)}{\Delta\mu_0(E)} \qquad \textbf{2.1}$$

where $\mu(E)$ is the measured absorption coefficient, $\mu_0(E)$ is a smooth background function representing the absorption of an isolated atom, and $\Delta\mu_0(E)$ is the measured jump in the absorption $\mu(E)$ at the threshold energy E_0. As the wave-behaviour of the photoelectron is important in the data analysis, the data is converted to wavenumbers, Å^{-1}, known as "k-space" according to **Equation 2.2**:

$$k = \sqrt{\frac{2m(E - E_0)}{\hbar^2}} \qquad \textbf{2.2}$$

where E_0 is the absorption edge energy and *m* is the mass of the emitted electron. This representation of EXAFS data as $\chi(k)$, the oscillations as a function of photo-electron wave number, is seen in **Figure 2.4**. A Fourier transform of $\chi(k)$ will yield the data as a function of distance (Å). This data is fitted using a model (a solved crystal structure or computed theoretical structure, for example). The FEFF code, named after the *f(k)* function itself (FEFF = $f_{eff}(k)$, the notation for effective curved-wave scattering amplitude) is the code for calculating the scattering pathways of emitted photoelectrons.[44] This is to provide theoretical values for the experimental variables for fitting to the EXAFS equation, **Equation 2.3**:[36]

$$\chi(k) = \sum_j \frac{N_j e^{-2k^2\sigma_j^2} e^{-2R_j/\lambda(k)} f_j(k)}{kR_j^2} \sin\left[2kR_j + \delta_j(k)\right] \qquad \textbf{2.3}$$

where N_j is the number of atoms, k is Boltzmann's constant, σ_j^2 is the mean square displacement of the path length, R_j is the experimental path length (the calculations, in fact, find the path length deviation: ΔR, i.e. $R_j - R_0$, where the model path length is R_0), $\lambda(k)$ is the mean free path length of the photoelectron, $f(k)$ is the scattering amplitude and $\delta_j(k)$ the total phase shift of the photoelectron. E_0 is also taken as an experimental variable to counteract potential errors in identifying the local maximum - these errors would affect calculated bond lengths.[38]

EXAFS data is often reported in "k space" or "q space". Where k space is Fourier transformed to reveal the data in Å, in "R space", this can in turn be reverse Fourier transformed to yield q space data. This is a measure of the efficacy of the fitted data as, ideally, k and q space results should be almost identical. Data is often k^2 or k^3 weighted, i.e. the k space data will be squared or cubed to amplify changes in intensity over smaller wavenumbers. This allows for a better comparison between experimental and fitted data and an easier determination of the goodness of the fit.

2.2. Studtite and Metastudtite

2.2.1. Physical Comparison

2.2.1.1. Structural Comparison – Theoretical

As mentioned in **Section 2.1.1.**, it was almost 130 years from the first reported synthesis of a uranyl peroxide[19] to the full determination of the structure of studtite by Burns and Hughes in 2003.[7b] The powder X-ray diffraction (PXRD) pattern of synthetic studtite, $[(UO_2)(\eta^2\text{–}O_2)(H_2O)_2]\cdot 2H_2O$, was published by Ukazi in 1959[45] and expanded upon by Debets in 1963, who proposed a hydrated uranyl bis-peroxide structure;[46] this was confirmed by Burns in 2003.[7b]

Studtite consists of infinite 1D chains with uranyl units linked by trans peroxo (O_2^{2-}) ligands in a repeating pattern [**Figure 2.6 (left)**] with interstitial water molecules that form hydrogen bonds with the axial oxygens of the uranyls and the equatorial peroxo oxygens [**Figure 2.6 (right)**]. Due to the covalent interaction of the U(*6p*) – or U(*6d*) - orbitals with the peroxy π bond the dihedral angle is 126.60° which yields a "zig-zag" structure in which the uranyl moieties are not parallel.[8c] The chains are relatively spread out, with a O_{H2O}–O_{H2O} distance of 7.05 Å.

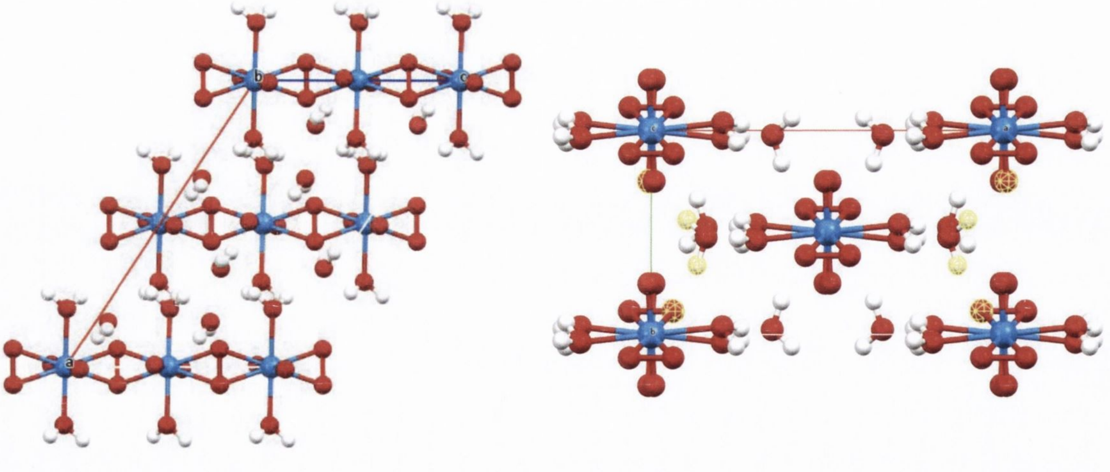

Figure 2.6: The packing structure of studtite along the b axis (left) and c axis (right).[7b] The interstitial water molecules lie between the infinite 1D chains, acting as hydrogen bond acceptors from the bound water molecules and H-bond donors to the neighbouring uranyl and peroxo oxygen atoms (yellow highlighted atoms, right). (Blue = U; red = O; white = H).

As described by Sato, the interstitial water molecules are removed upon heating for one hour at 100°C to yield metastudtite, the dehydrated congener of studtite.[20,47] The single crystal x-ray structure of metastudtite has not been solved, but it has been calculated by DFT[8c] and *ab initio*[48] methods. This predicted structure shows an asymmetric uranyl moiety, most likely affected by hydrogen bonding within the structure [**Figure 2.7 (right)**], with predicted bond lengths of 1.80 and 1.85 Å (**Table 2.2**). The structure has much closer packing than that of studtite – the O_{H2O}–O_{H2O} distance is 3.94 Å rather than 7.05 Å.

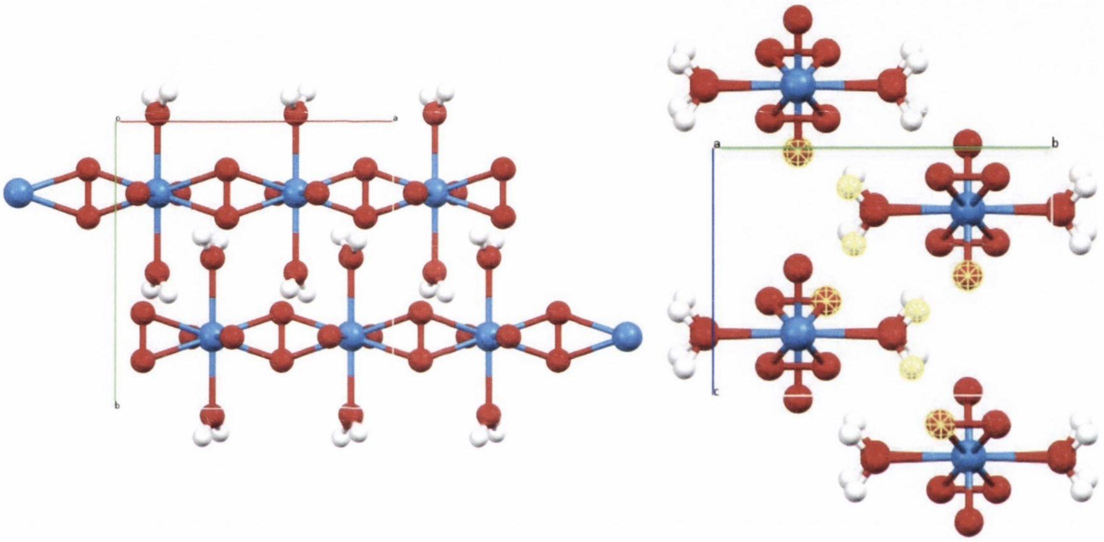

Figure 2.7: The packing structure of metastudtite as viewed along the c axis (left) and a axis (right).[8c] The 1D chains are substantially closer together. The bound water molecules act as H-bond donors to the uranyl and peroxo oxygen atoms (yellow highlighted atoms, right). (Blue = U; red = O; white = H).

A key point to note is that the calculated bond lengths for studtite are longer than the XRD values (**Table 2.2**). This will become important when analysing the experimental data for metastudtite, **Section 2.2.1.2.**

Table 2.2: Calculated and experimental bond lengths (Å) for studtite and metastudtite.

	Studtite		Metastudtite
Bond	**X-Ray[7b]**	**DFT[8c]**	**DFT[8c]**
U=O_{yl}	1.769	1.83	1.85
			1.80
U–O_{peroxo}	2.365	2.38	2.39
U–O_{water}	2.395	2.41	2.42

2.2.1.2. *Structural Comparison – Experimental*

To analyse the similarities and differences between studtite and metastudtite, a combination of PXRD; Raman spectroscopy and IR spectroscopy was used. In addition, uranium *L_3* edge EXAFS spectroscopy was used to obtain structural information from around the uranium centre in both minerals and to investigate the effect of removing the interstitial water molecules (**Figure 2.8**).

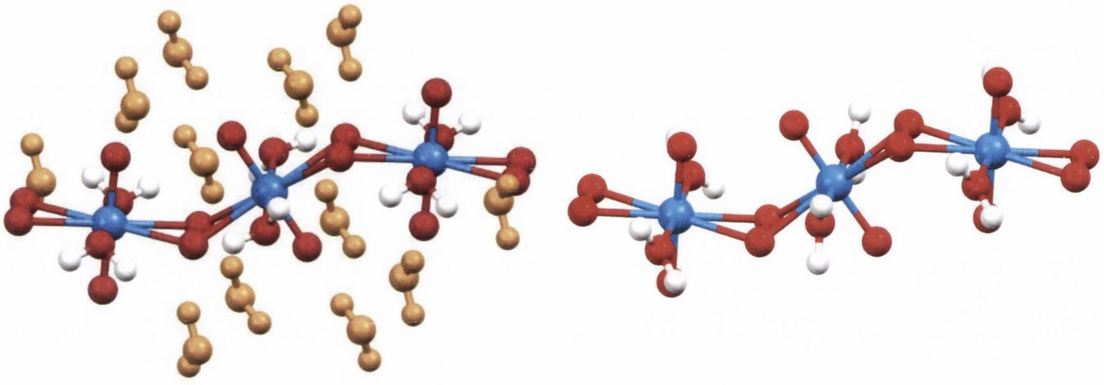

Figure 2.8: Removal of the interstitial water molecules from studtite[7b] (left) theoretically yields the metastudtite structure calculated by Weck *et al.*[8c] (right). Both minerals have similar 1D chain structures but there are subtle differences in bond lengths (Table 2). (Blue = U; red = O; white = H; yellow = interstitial water).

The EXAFS data was originally analysed with respect to the known and calculated structures of studtite[7b] and metastudtite,[8c] respectively, but the fit for the metastudtite data was very poor. Instead, the studtite structure was used as the model for both sets of results. This was decided for two reasons: given the sensitivity of the data, only one uranyl path was to be included for the fit for metastudtite; the structure for metastudtite predicted by Weck *et al.* had an asymmetric uranyl with two $U{=}O_{yl}$ paths.[8c] Secondly, the interstitial water molecules were not taken into account in the studtite fit – the scattering pathway from these was expected to have low enough intensity for them to not impact the overall fit greatly. It was also decided that as the minerals were to be compared directly then using a single model would give a better baseline. From this, three paths – $U{=}O_{yl}$, $U{-}O_{peroxo}$, and $U{-}O_{water}$ – were included in each fit and the differences from the data to the model yielded the results for each mineral. Using the studtite structure, the r factor of the metastudtite fit was reduced to 0.02 (i.e. the fit was within 2 % of the experimental data).

The studtite and metastudtite spectra and the best fits are shown in **Figure 2.9** and **2.10**, respectively, and the structural information is compared with previous data in **Table 2.3**.

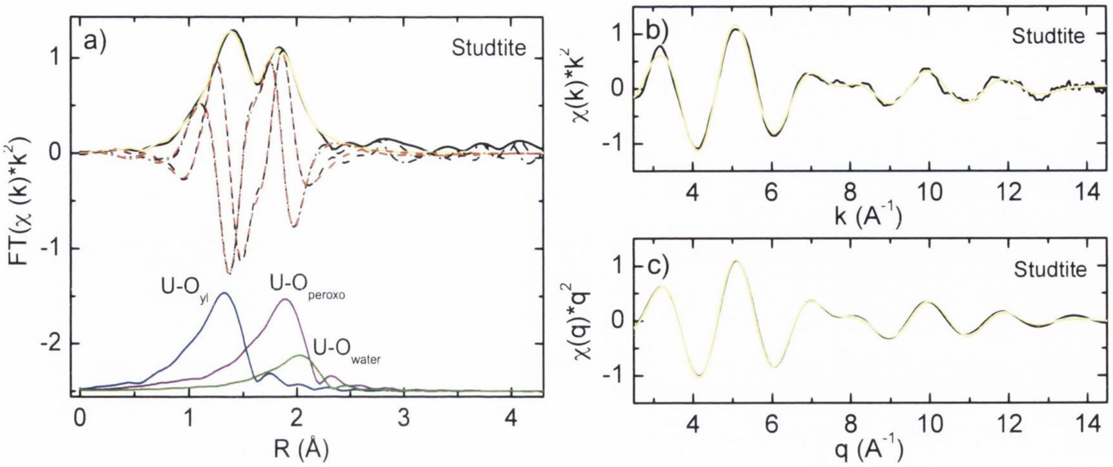

Figure 2.9: a) U-L_3 edge Fourier transformed EXAFS and vertically shifted used single scattering paths, b) k^2 weighted and c) q^2 weighted EXAFS spectra (black) and best fits (yellow) for studtite.

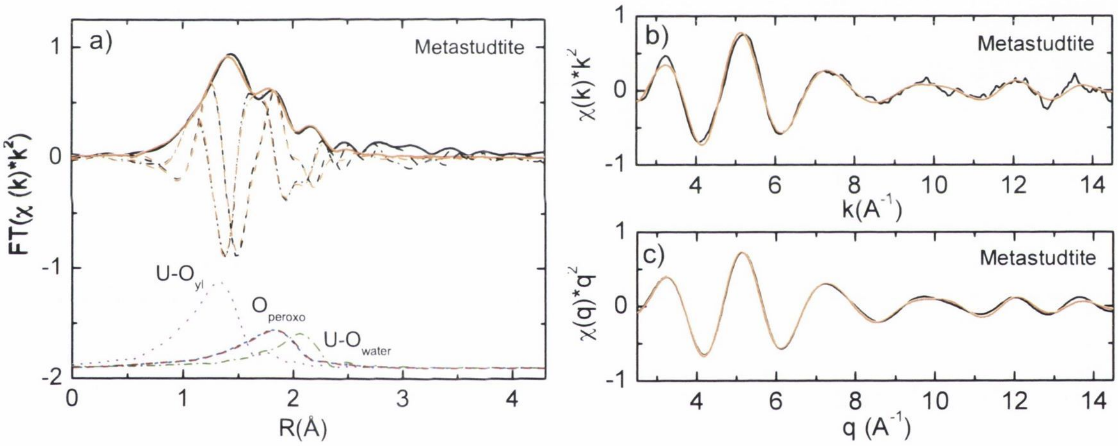

Figure 2.10: a) U-L_3 edge Fourier transformed EXAFS and vertically shifted used single scattering paths, b) k^2 weighted and c) q^2 weighted EXAFS spectra (black) and best fits (orange) for metastudtite.

Table 2.3: Experimental, calculated and found bond lengths (Å) for studtite and metastudtite.

	Studtite			Metastudtite	
Bond	**EXAFS**	**X-Ray**[7b]	**DFT**[8c]	**EXAFS**	**DFT**[8c]
U=O_{yl}	1.78	1.769	1.83	1.79	1.85 1.80
U-O_{peroxo}	2.36	2.365	2.38	2.32	2.39
U-O_{water}	2.50	2.395	2.41	2.52	2.42

There is good agreement between the XRD and EXAFS results for studtite, although the U–O$_{water}$ bond is about 0.1 Å longer than the calculated/ measured bond length. This difference is possibly due to the short-range atomic order sensitivity of the EXAFS spectrum (from local deviations from the average structure) and is observed in the metastudtite results also (2.52 Å instead of the expected 2.42 Å). For U=O$_{yl}$ and U–O$_{peroxo}$, however, DFT reports longer distances than those obtained from XRD and EXAFS. When examining the change upon dehydration, the EXAFS results indicate a slight lengthening of the uranyl bond and a significant shortening of the U–O$_{peroxo}$ bond (0.04 Å). The apparent lack of asymmetry in the uranyl is consistent with IR and Raman spectra (**Figures 2.11–13**) as there is no observable difference in either the O–H or U=O$_{yl}$ stretching or bending modes. Whilst the O–O bond length cannot be obtained from the U-L_3 edge EXAFS data, the IR and Raman spectra show slight variation in the O–O stretching modes, implying that this distance does change (**Figure 2.12**).

It should be noted that while it was suitable to set the coordination number to four for the studtite U–O$_{peroxo}$ paths, creating four equal U–O$_{peroxo}$ bonds of 2.36 Å, the fit for metastudtite was better when using two separate uranium-peroxo paths, finding two U–O$_{peroxo}$ bonds each of 2.32 and 2.33 Å.

Table 2.4: Summary of EXAFS results for studtite and metastudtite. From left to right: the name of the mineral (Mineral), scattering path (Path), coordination number (N), bond length (R) energy shift of the ionization potential (ΔE), mean squared atomic displacement/ Debye-Waller factor (σ²), goodness of fit (r factor).

Mineral	Path	N	R (Å)	ΔE (eV)	σ^2 (Å^2)	r factor
Studtite	U=O$_{yl}$	2.0 ± 0.2	1.78 ± 0.01	-0.6 ± 0.6	0.003 ± 0.0005	0.01
	U–O$_{peroxo}$	4.0 ± 0.5	2.36 ± 0.01	-0.6 ± 0.6	0.004 ± 0.002	0.01
	U–O$_{water}$	2	2.5 ± 0.01	-0.6 ± 0.6	0.004 ± 0.002	0.01
Metastudtite	U=O$_{yl}$	1.7 ± 0.3	1.79 ± 0.01	-1.0 ± 0.9	0.004 ± 0.0007	0.02
	U–O$_{peroxo}$	2.0 ± 1.3	2.32 ± 0.01	-1.0 ± 0.9	0.007 ± 0.002	0.02
	U–O$_{peroxo}$	2	2.33 ± 0.01	-1.0 ± 0.9	0.007 ± 0.002	0.02
	U–O$_{water}$	1.4 ± 0.3	2.52 ± 0.01	-1.0 ± 0.9	0.002 ± 0.0018	0.02

Therefore upon dehydration of studtite to metastudtite the structural data suggests that the coordinated water molecules are slightly further away from the uranium centre, but the uranium peroxide bonds become shorter by 0.03 Å. This is observable in the slight shift and decrease in the metastudtite O–O stretch in the Raman (**Figure 2.12**).

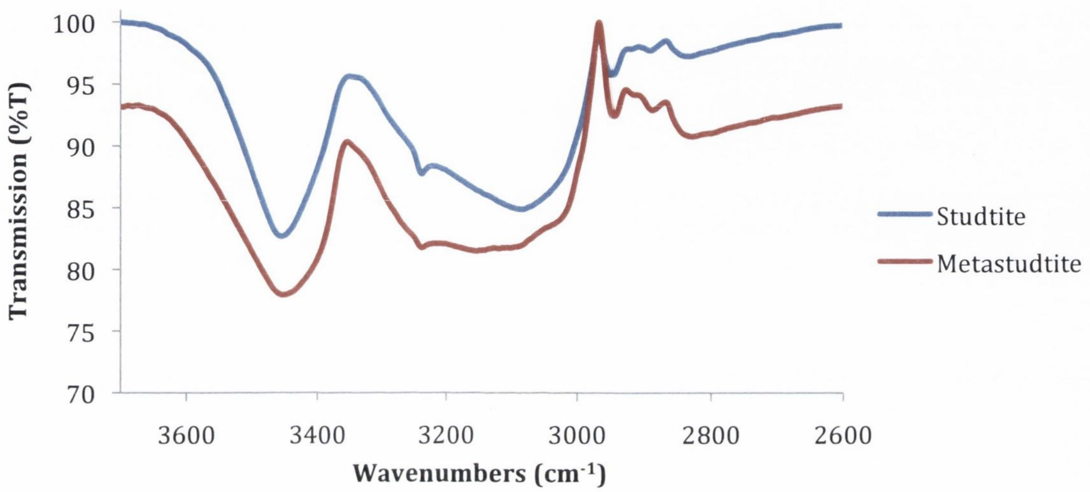

Figure 2.11: The water OH regions in the infrared spectra of studtite and metastudtite.

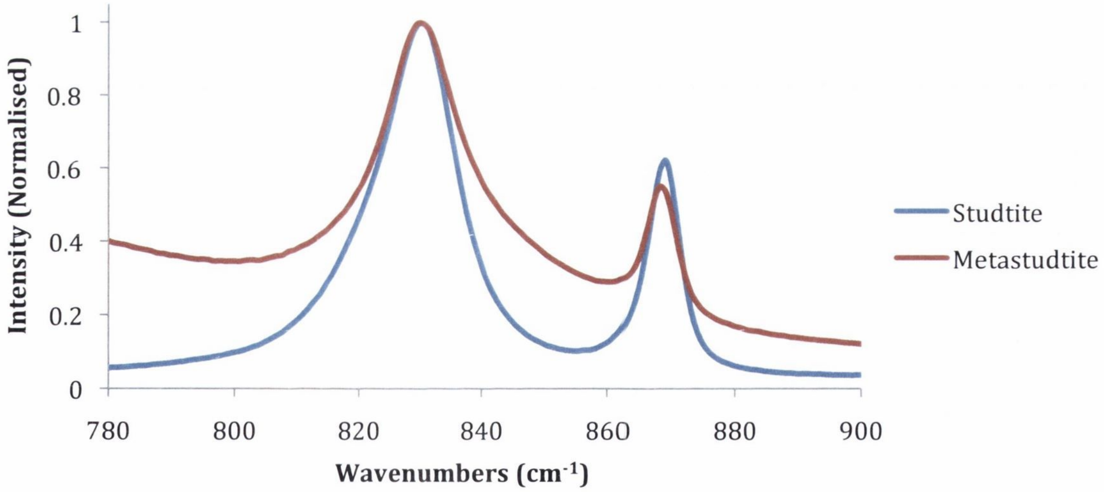

Figure 2.12: The uranyl stretching region and the O–O stretch (870 cm^{-1}) in the Raman spectra of studtite and metastudtite.

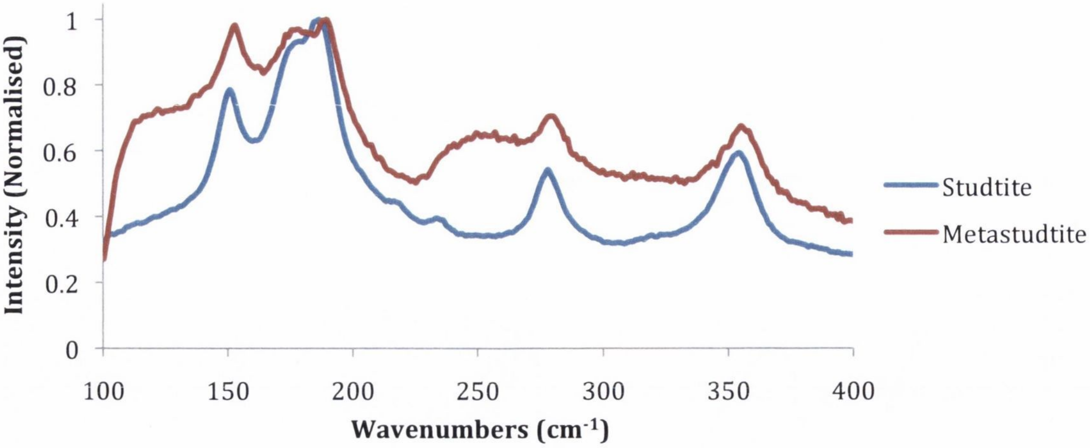

Figure 2.13: The uranyl bending region in the Raman spectra of studtite and metastudtite.

2.2.2. Electronic Structure

While there may not be a drastic change in the structure upon dehydration, there is a startling change in colour from yellow to orange. Typically, colour is determined by the electronic arrangement around the metal, i.e. by the possible electronic transitions from one orbital to another, but as only the interstitial water molecules were affected, a more in-depth analysis of the effect of dehydration upon the electronic environment around the uranium was undertaken using optical and HR-XANES spectroscopy.

2.2.2.1. Optical Properties

Given that the synthetic minerals were amorphous powders (**Figure 2.14**), diffuse reflectance UV-Vis spectroscopy was used to analyse the absorption of the solids (**Figure 2.15**).

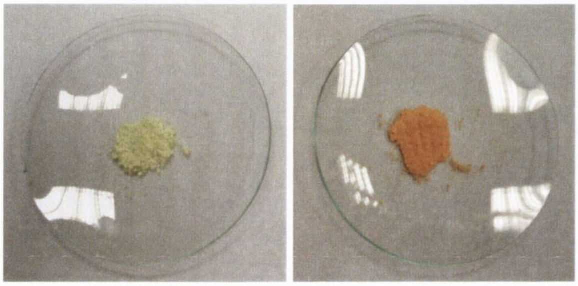

Figure 2.14: Synthetic studtite (left) and metastudtite (right).

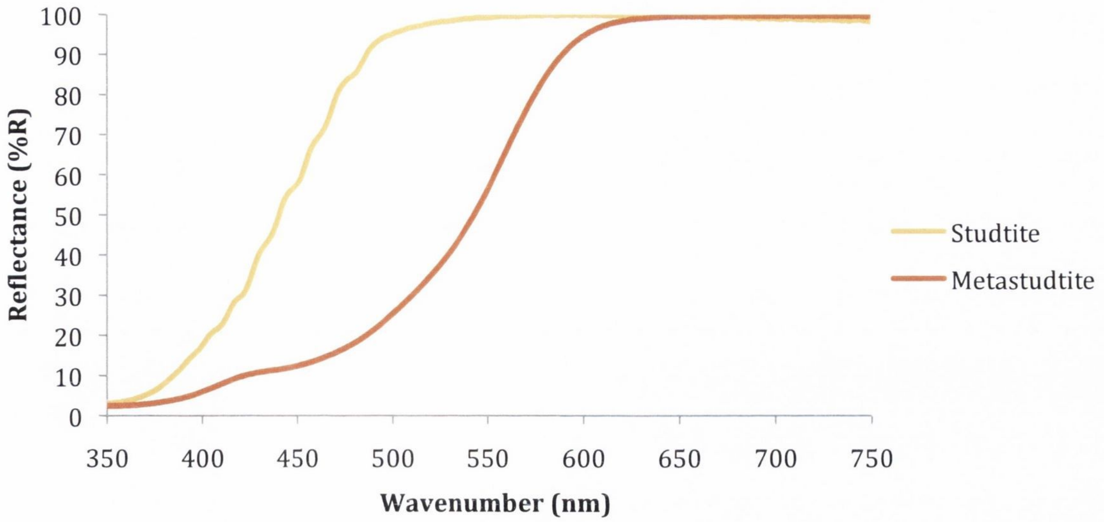

Figure 2.15: The diffuse reflectance UV-Vis spectra of studtite and metastudtite.

As reflectance is related to absorption *via* an inverse relationship, minimum reflectance corresponds to maximum absorption. This allows the measurement of a bandgap at the absorption edge of 3.45 eV and 2.71 eV for studtite and metastudtite respectively.[9] This indicates a significant alteration in the uranium electronic environment, not consistent with the simple removal of interstitial water molecules. The Weck DFT structure[8c] implied an asymmetry in the uranyl arising from H-bonding in the crystal structure. This could account for the 100 nm shift in the absorption edge (359 to 457 nm) but is inconsistent with the structural data – there was no indication of asymmetry in the $U{=}O_{yl}$ bonds of metastudtite.

Attempts were made to measure the emission spectra of studtite and metastudtite, however the characteristic uranyl emission typically observed around 510 nm was not observed. This is of note as the uranyl moiety is normally a strong emitter,[49] although carbonate ligands[50] and coordinated water[51] can quench the emission. Given the calculations on the electronic structure, it is likely that quenching occurs *via* fast energy transfer to the peroxy group or, more likely, vibrational quenching *via* the coordinated water molecules. Given the relationship between reflectance and absorption, it is also worth mentioning that the uranyl ligand-to-metal charge transfer (LMCT) is not visible in the diffuse reflectance spectrum.

2.2.2.2. HR-XANES study of Studtite and Metastudtite

HR-XANES spectroscopy was used to analyse the minerals and to identify a change in the valence shell corresponding to the removal of the interstitial water molecules. As discussed in **Section 2.1.3.1.**, HR-XANES data can reveal information about the oxidation state, electronic structure and hybridisation of the orbitals at the atom in question. In uranyl peroxides, the HOMO is thought to comprise of the uranium *6d* orbitals overlapping with the peroxo π orbitals; this has been calculated for both studtite and metastudtite,[8c] and for mononuclear uranyl peroxides with H_2O, F^-, OH^-, CO_3^{2-} and NO_3^- in the coordination sphere.[26]

Schoepite, $[(UO_2)_8O_2(OH)_{12}]\cdot12H_2O$, was also analysed as a comparison material. Schoepite and metaschoepite are often used as standards for U(VI) HR-XANES measurements, but in this case the predominantly ionic uranyl-hydroxo interactions in schoepite[48,52] will be compared to the covalent uranyl-peroxo interactions. This will test the ability of the HR-XANES technique to differentiate between small amounts of covalency in these systems; covalency in An-L interactions is of significant interest as it is postulated to be a reason for enhanced An/ Ln separations in nuclear waste treatment (**Section 1.2.2.**).[53]

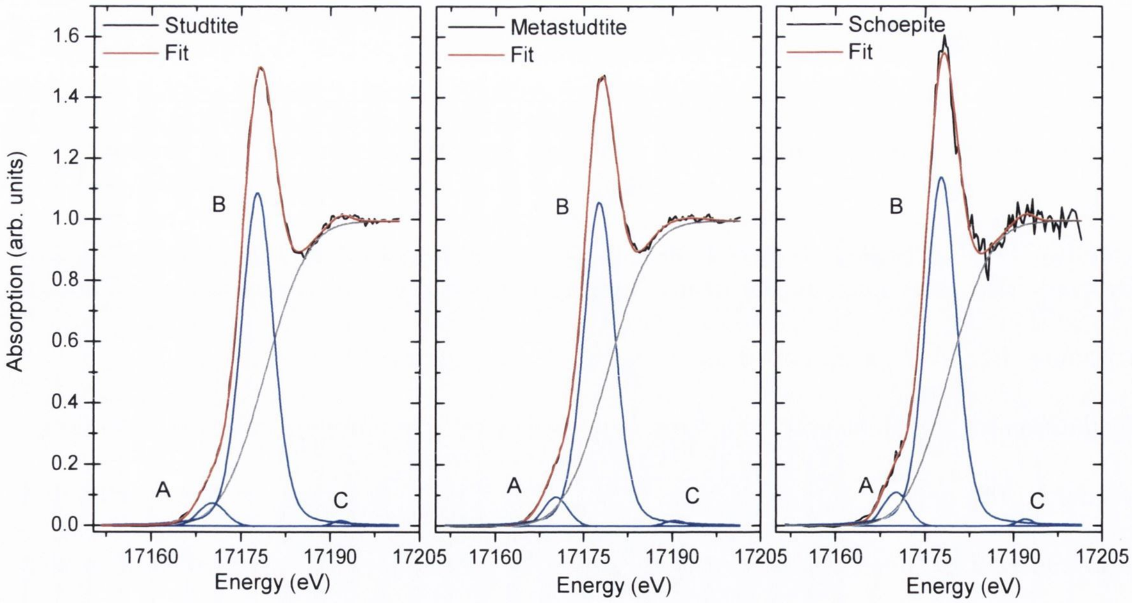

Figure 2.16: The normalised U L_3 edge HR-XANES spectra of studtite and metastudtite. The pseudo-Voigt (P.V.) functions describe the pre-edge (A), white line (B) and post-edge (C) features. The P.V. parameters are described in Table 2.5.

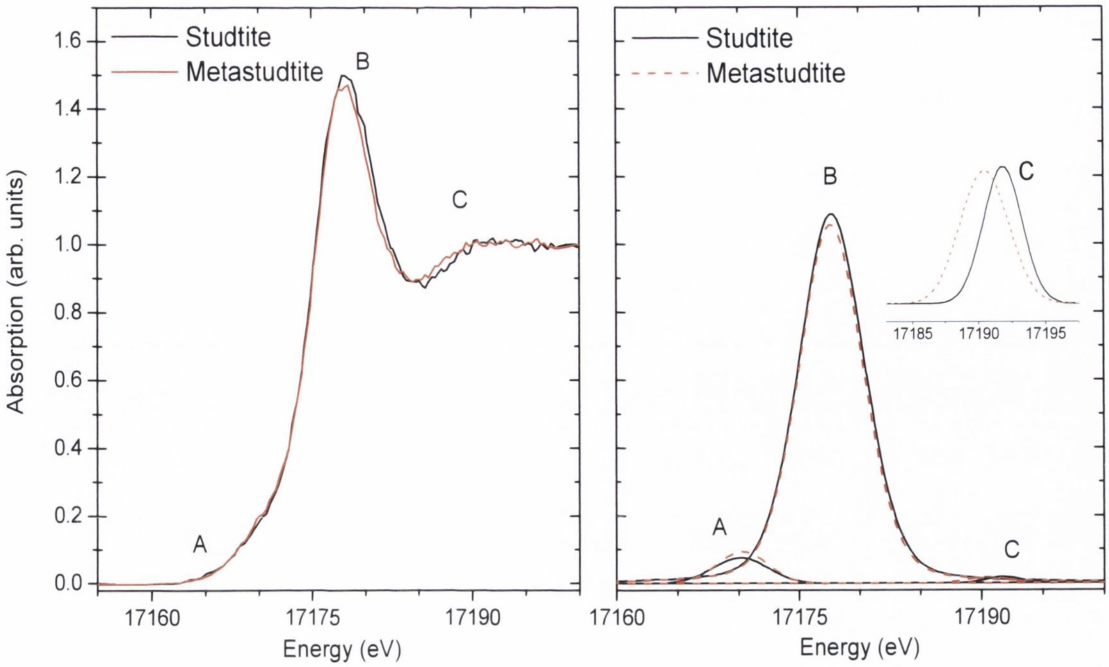

Figure 2.17: The U L_3 edge HR-XANES spectra of studtite and metastudtite (left) and the overlapped P.V. functions (right).

To compare the data more accurately, the background arctangent function (step) and α (the Lorentzian component of the pseudo-Voigt function) parameters were kept constant between the three samples (**Figure 2.16**, **Table 2.5**). Energy positions and intensities of the three main features – the pre-edge (A), the white line (WL, B) and post-edge (C) – for studtite and metastudtite are superimposed in **Figure 2.17**.

The larger pre-edge area of the metastudtite spectrum implies less mixing of U(*5f*) with O(*2p*) states in metastudtite compared to studtite – there is a higher number of transitions to vacant U(*5f*) states in metastudtite. In contrast to this, the larger area of the WL in the studtite spectrum suggests more vacancies in the U(*6d*) in studtite relative to metastudtite, i.e. there is less hybridisation of U(*6d*) states with O(*2p*) states for studtite compared to metastudtite.

It is known that for all actinides with –yl type of bonding, the energy distance (ΔE) between features B and C (B–C) decreases upon elongation of the U(V/VI)=O_{yl} bond (R), according to the relationship: $\Delta E \cdot R^2 = cst.$[39a,41,54] The metastudtite post-edge peak appears at a B-C distance 1.3 ± 0.1 eV lower than that of studtite, implying that the metastudtite uranyl bond is longer.[39a] This is in agreement with the observed EXAFS data: the metastudtite U=O_{yl} bond was found to be 0.01 Å longer (1.79 Å as opposed to 1.78 Å for studtite). The EXAFS data showed the metastudtite U–O_{peroxo} bond to be 0.04 Å shorter compared to studtite, but this is unlikely to greatly influence the B–C distance.

Table 2.5: Height, position, and FWHM parameters of the pseudo-Voigt functions used to model the HR-XANES resonance features A, B and C for studtite, metastudtite and schoepite and the arctangent (step) function to model the edge jump (Figure 2.16). The Lorentzian part of the P.V. function (α) and the area of the P.V. peaks are also given.

Sample	Feature	Height ±0.001	Position ±0.1	FWHM ±0.3	α ±0.01	Area ±0.06
Studtite	A	0.076	17170.2	2.7	0	0.43
Metastudtite	A	0.112	17170.3	2.5	0	0.50
Schoepite	A	0.111	17170.1	2.5	0	0.58
Studtite	B	1.090	17177.7	3.2	0.3	8.18
Metastudtite	B	1.050	17177.7	3.1	0.3	7.80
Schoepite	B	1.141	17177.7	3.1	0.3	8.33
Studtite	C	0.019	17191.8	1.7	0	0.07
Metastudtite	C	0.021	17190.5	2.1	0	0.08
Schoepite	C	0.023	17192.0	1.7	0	0.08
Studtite	step	0.497	17179.0	8.0	-	-
Metastudtite	step	0.497	17179.0	8.0	-	-
Schoepite	step	0.497	17179.0	8.0	-	-

The HR-XANES spectrum of schoepite exhibits slightly higher B intensity compared to the B features of studtite and metastudtite (**Figure 2.16**) indicating less mixing of metal and ligand atomic orbitals, i.e. the bonds within schoepite are more ionic. A similar effect is observed in the U L_3-edge XANES of $RbUO_2(NO_3)_3$[33] and $Cs_2UO_2Cl_4$[55] single crystals. It is also worth noting that structural[56] and *ab initio* calculations[48] on schoepite and metaschoepite show difference in hydrogen bonding upon dehydration but there is no major alteration in the Raman spectrum of metastudtite from studtite.

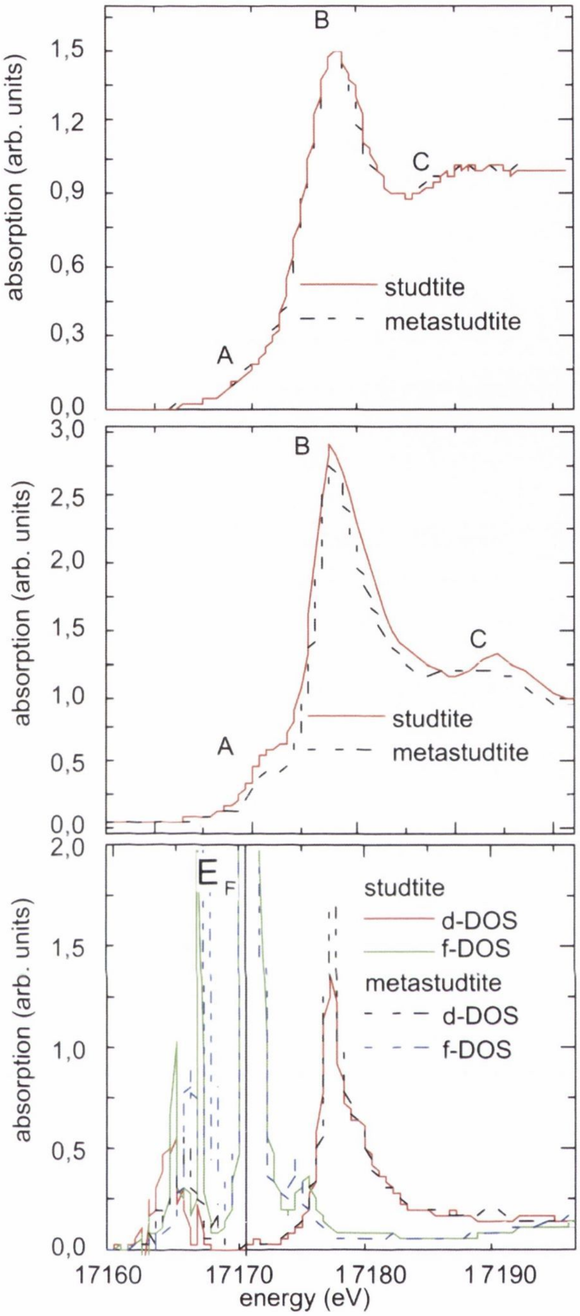

Figure 2.18: Experimental (top) and calculated (middle) U L_3-Edge HR-XANES spectra and calculated U d- and f-DOS (bottom) of studtite and metastudtite. The E_F line separates the occupied from the unoccupied DOS.

The calculated U-L_3 edge HR-XANES spectra of studtite and metastudtite were generated by Dr Tonya Vitova of the INE in the Karlsruhe Institute of Technology and the results are shown in **Figure 2.18(middle)**. Energy positions and intensities of the A, B and C features agree reasonably well between experiment and calculation. The pre-edge describes transitions of uranium $2p_{5/2}$ electrons to electronic states with dominating *f* character. The *f*-DOS intensity dominates at this energy position, whereas no unoccupied *d*-DOS contribution is visible [**Figure 2.18 (bottom)**].

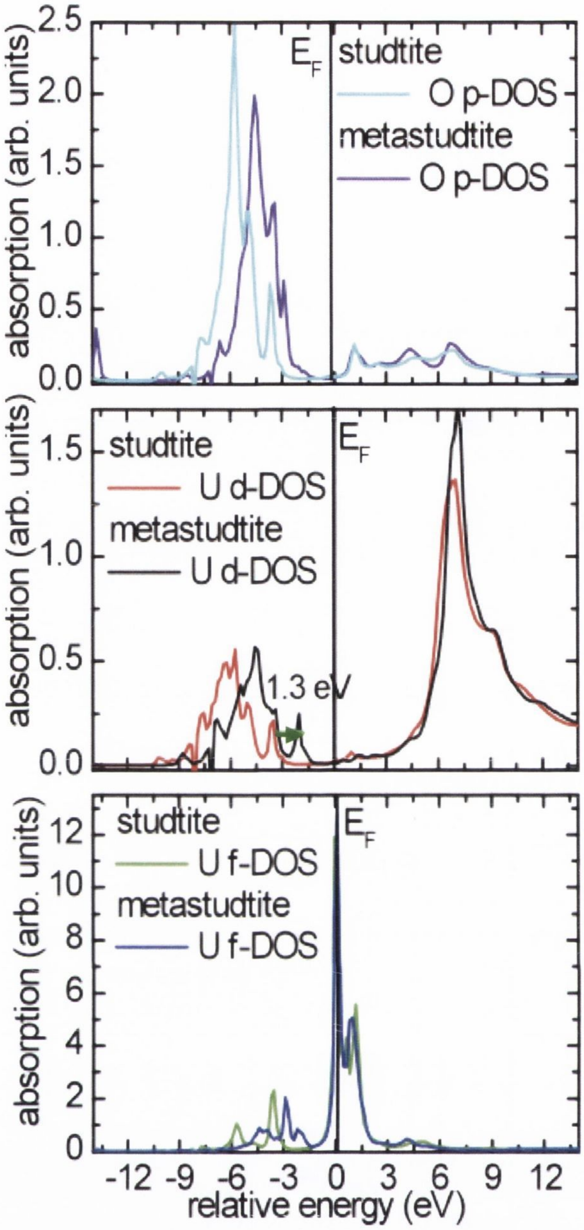

Figure 2.19: The O p-DOS (top), U d-DOS (middle) and f-DOS (bottom) of metastudtite. The E_F line separates the occupied from the unoccupied DOS.

The occupied O *p*-DOS and U *d*- and *f*-DOS of metastudtite (calculated for 225 atoms), plotted in **Figure 2.19**, are shifted to higher energies, decreasing the band gap of metastudtite by about 1.3 eV compared to studtite [see arrow in **Figure 2.19 (middle)**]. By repeating the calculations for small clusters of nine atoms and varying $U=O_{yl}$, O_{peroxo} and O_{water} distances, it was found that the change in the $U=O_{yl}$ bond had the greatest effect on the reduction of the size of the bandgap. Using the structural results from the EXAFS analyses, the metastudtite bandgap is reduced by about 1.3 eV compared to studtite. This electronic structural change explains the difference in the band gaps (0.74 eV) determined by diffuse reflectance UV-Vis spectroscopy.

Therefore, on the basis of the EXAFS and HR-XANES spectra, it is likely that upon dehydration of studtite the $U–O_{peroxo}$ bond lengths slightly decrease by 0.03 Å, whilst the $U=O_{yl}$ bond lengths slightly increase by 0.01 Å, which might decrease the energy gap between the peroxo π type orbitals of the HOMO and the *5f* non-bonding orbitals of the LUMO.

2.2.3. Reactivity Studies of Studtite

The reactivity of studtite towards possible radionuclides was investigated to observe possible sorption or incorporation. Investigations with studtite and Cs^{+}[8a] and Sr^{2+}[29] and many radionuclides (including the transuranic ^{237}Np, ^{239}Pu, ^{241}Am and ^{244}Cm) with metastudtite[30] have already been reported; however, this body of work will focus on investigating the interactions of metals in their +3 oxidation state - layered minerals have been posulated to incorporate An(III) (An = Am, Cm) into the sheets[57] - and to examine the interaction of ^{241}Am with studtite.

The possibility of a redox mechanism will also be investigated by examining the electrochemical properties of studtite, thus inferring a possible mechanism for Np interaction. This hypothesis will be tested by reaction with iodine and iodide.

2.2.3.1. Sorption/ Incorporation studies

A series of metal ions relevant to the nuclear fuel cycle were examined for sorption onto or incorporation into studtite. Early and late lanthanides Nd and Ho as well as Am(III) analogue Eu(III)[58] and Pu(IV) analogue Fe(III)[59] were chosen. Studtite was suspended in solutions of $NdCl_3$, $HoCl_3$, $EuCl_3$ and $FeCl_3$ but IR and emission spectroscopy showed that these were not sorbed to the surface after one week.

Incorporation into the studtite matrix was attempted by setting up solutions of uranyl nitrate, hydrogen peroxide and the desired metal salt and examining the resulting precipitate. Again, IR and emission spectroscopy showed negative results although the precipitation was slower than in previous syntheses and the yield of studtite was lower.

It is likely that the metal ions chosen are incompatible with the insertion mechanism, whether due to size or electronic nature. A large ion will be slow to permeate the studtite network and it is likely that incorporation into the structure would necessitate an isoelectronic or isostructural relationship to uranyl .

2.2.3.2. Sorption/ Incorporation studies: Americium

Approximately 1 % of the SNF from a reactor will be plutonium.[60] This will, over time, decay to americium, meaning that americium-241 and americium-243 will accumulate and is, therefore, an isotope worthy of investigation. As ^{243}Am is a highly toxic γ-emitter, the isotope ^{241}Am was used. ^{241}Am is primarily a β-emitter but also emits low energy γ-rays at 59 and 125 keV. Am(III) was used as the americinyl cation was unlikely to form under experimental conditions.[61]

Incorporation into the studtite matrix was attempted by reacting a solution of uranyl nitrate, hydrogen peroxide and 1 kBq of $AmCl_3$ and examining the resulting precipitate. The precipitate was characterised using γ-spectroscopy: monitoring the characteristic emission lines at 59 and 125 keV [**Figure 2.20 (right)**], the majority of peaks in the spectrum are from uranium and its daughter products. Less than 1 % of the Am(III) was revealed to have been incorporated (0.749 Bq out of 1 kBq).

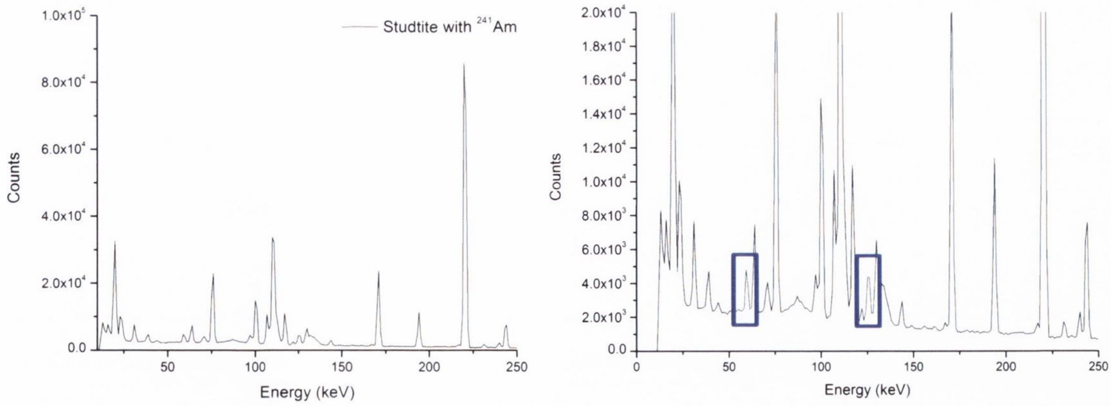

Figure 2.20: The γ spectrum of the ^{241}Am-studtite sample (left). The expanded view (right) with the characteristic peaks highlighted in blue shows 0.749 Bq of americium is incorporated into the sample. These measurements were performed by Dr Luis Léon-Vintro in University College Dublin.

2.2.3.3. Electrochemical Properties of Studtite

Previous investigations show that there is interaction between studtite and Np, although the oxidation state of the Np species is unknown.[30] The redox behaviour of neptunium in acidic[62] and basic[63] media has been well investigated to understand the environmental speciation[64] of neptunium. An important point in understanding redox chemistry is the difficulty in determining the formal potential for the redox couple between $[NpO_2]^+$ and Np^{4+} conventional voltammetry or polarography: the electrode reaction between $[NpO_2]^+$ and Np^{4+} is slow or irreversible because Np–O bonds must be made or broken. The formal potential (relative to the Ag/AgCl electrode) in basic media[62] can be summarised thus:

$$NpO_5^{3-} \xrightarrow{+0.78} NpO_2(OH)_2 \xrightarrow{+0.8} NpO_2OH \xrightarrow{+0.5} NpO_2 \xrightarrow{-1.9} Np(OH)_3 \xrightarrow{-2.0} Np$$

The formal potential in acidic media[62,65] can be summarised also:

$$NpO_2^{2+} \xrightarrow{+1.356} NpO_2^{+} \xrightarrow{+0.801} Np^{4+} \xrightarrow{+0.416} Np^{3+} \xrightarrow{-1.575} Np$$

This data also states that in acidic solutions the formal redox potential of the Np^{6+}/ Np^{4+} couple is +1.079 V and the Np^{4+}/ Np^0 couple is -1.077 V. The E^0 for $[NpO_2]^+$/ Np^{4+} couple (0.801 V) was evaluated from data of Gibbs energy of formation.[66]

While the redox chemistry of neptunium has been studied comprehensively, there has been no such undertaking with a uranyl mineral – these minerals are not soluble and as such most of the characterisation to date has been *via* spectroscopic means (EXAFS, IR, etc.) or powder X-Ray diffraction. Given the relevance of studtite as a possible phase transition on SNF, investigating the redox chemistry of studtite seemed a logical course of action to explore the possibility of a UO_2^{2+} to UO_2^{+} or U(IV) reduction facilitating the oxidation of Np^{4+} to $[NpO_2]^{+}$.

During a collaboration with Professors Tia Keyes and Robert Forster at Dublin City University, the electrochemical investigation of studtite was performed by Dr Colm Mallon. Solid state electrochemistry is a straightforward and versatile method established by Bond and co-workers for studying redox active solid materials via their mechanical attachment to an electrode surface such as fluorine doped tin oxide, or FDTO.[67] The main stipulation is that the solid and its redox partners are not soluble in the contacting solution/ electrolyte. In this case the studtite was suspended in acetone and drop cast onto the conductive side of an FDTO electrode before analysis in an aqueous electrolyte.

Given the potential importance of solid-state redox reactions in transuranic minerals and in spent nuclear fuels,[60,68] solid-state electrochemistry is an attractive means of considering these processes but one that has been poorly utilised: there has been only one report on the solid-state electrochemistry of uranium prior to the results discussed herein, an analysis of the insertion species of uranium oxides to determine the mechanism of insertion of cations into UO_3.[69]

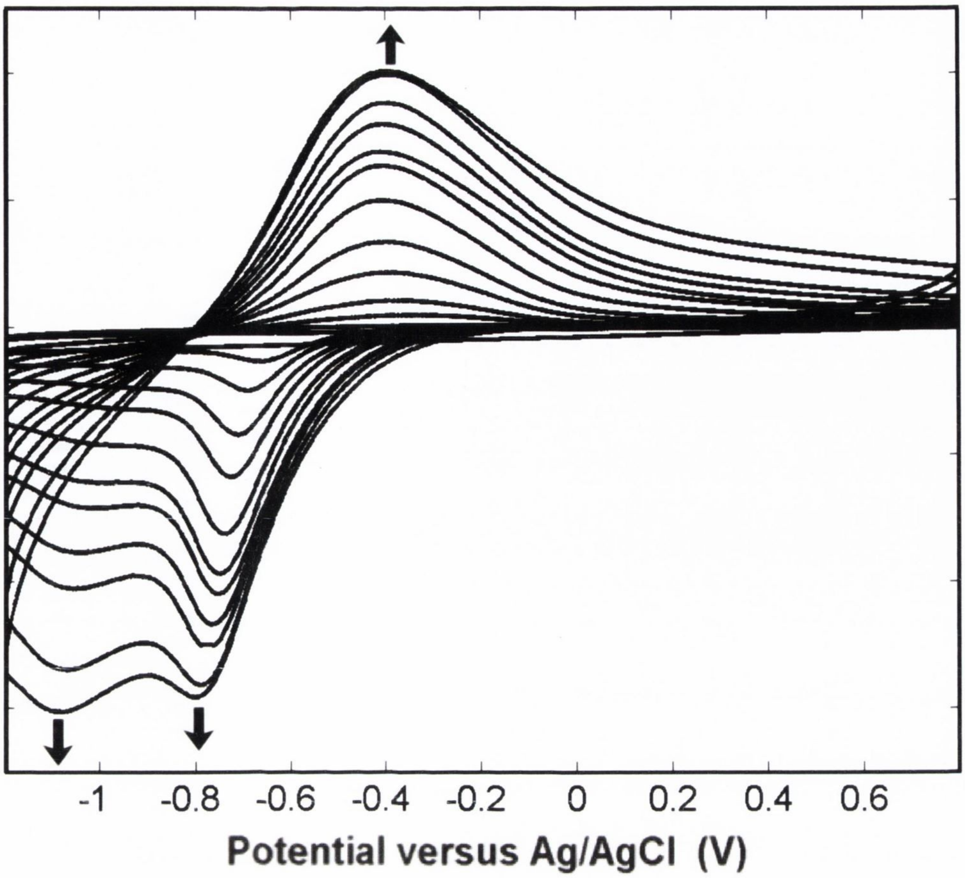

Figure 2.21: Cyclic voltammograms of studtite on FDTO in water with 0.2 M $LiClO_4$ as the supporting electrolyte (scan rate = 0.1 V s^{-1}).

During the initial potential cycles, little faradaic current is observed but a reduction peak grows in at approximately -0.73 V, linked to the oxidative process at -0.35 V. The intensity of the voltammetric waves increases with increasing number of scans, over a period of several hours. A second reduction peak becomes evident at -1.10 V with a coupled oxidation process that overlaps with the previous oxidative process to give a broad peak centred at -0.4 V. The second reduction process shows a slower current increase compared to the reduction at -0.73 V, but both peaks stabilise at similar current values (**Figure 2.21**). As the film is reduced, it is expected to incorporate electrolyte ions to maintain charge stability. The gradual increase of the intensity of the peaks in the CV is attributable to improved penetration of ions through the film, as the morphology of the film is changed with time to a black solid. Interestingly, this appears to be driven solely by the electrochemical process, as contact with 0.2 M $LiClO_4$ electrolyte over 24 hours without applying potential did not decrease the rate of growth of the major reduction peak. The studtite and the black electrolysis product [**Figure 2.22 (top)**] were analysed with SEM [**Figure 2.22 (bottom)**], showing that the linear chains of studtite were destroyed to leave an amorphous powder.

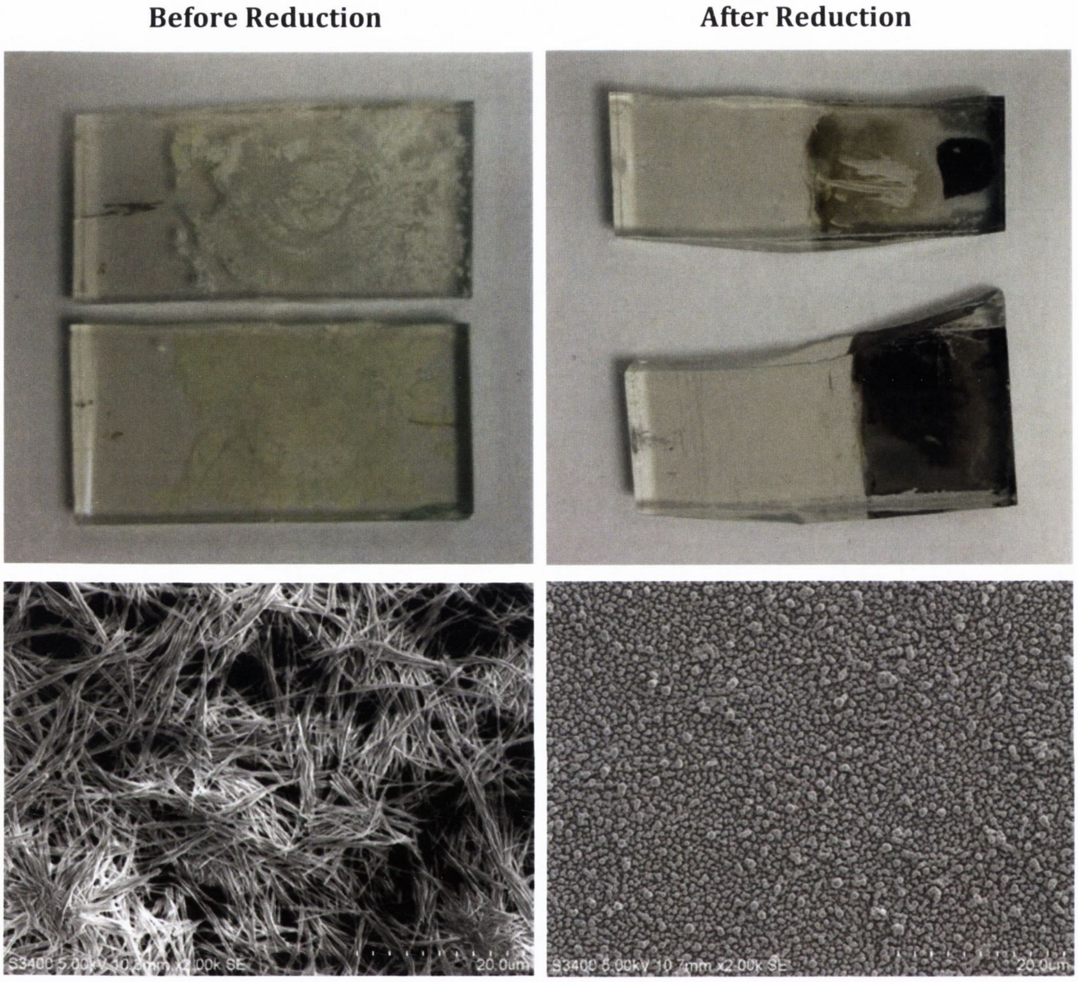
Before Reduction

After Reduction

Figure 2.22: Photo (top) and SEM images (bottom) of studtite on an FDTO electrode before (left) and after (right) electrolysis at -1.2 V.

Raman spectroscopy showed the destruction of the uranyl and both peroxo stretches (at 831 and 870 and 360 cm^{-1}, respectively) over time (**Figure 2.23**). The product is almost black in colour, which will affect its ability to scatter 633 nm excitation. This is consistent with a report on Raman spectra of UO_2, which found this material to be a very poor Raman scatterer under red irradiation.[70] With this data, in conjunction with the results of Energy Dispersive X-Ray (EDX) analysis (**Table 2.6**) showing that the compound only contained uranium and oxygen, the reduced product was assigned to be UO_2. Unfortunately there was insufficient sample for powder diffraction to confirm this hypothesis. It is interesting, however, that upon exposure to air the black compound slowly changed to a yellow colour, indicating a possible re-oxidation to U(VI).

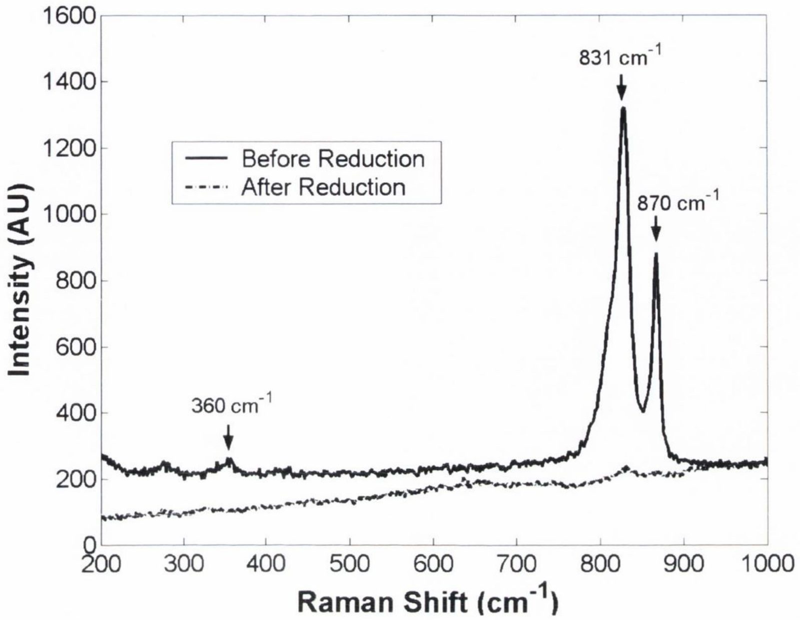

Figure 2.23: The Raman spectra of studtite before and after electrolysis at -1.2 V for 12 h.

Table 2.6: EDX data showing the elemental composition of the sample. Sn is from the surface of the electrode. Daughter products arise from the decay of uranium.

Element	% Wt.	Atomic %
U	55.43	9.98
O	32.11	81.77
Sn	9.39	3.39
Daughter Products (Po, etc.)	3.07	4.86
Total	100.00	100.00

To examine the effect of cation and anion on the studtite redox potential, $LiClO_4$, $NaClO_4$, $KClO_4$ and Na_2SO_4 were used as electrolytes. In 0.2 M $LiClO_4$ the first reduction occurs at a potential of -0.73 V, while in 0.2 M $NaClO_4$ this value shifts to -0.76 V and in 0.2 M $KClO_4$ it occurs at -0.79 V. In contrast, the first reduction occurred at a potential of -0.76 V in 0.2 M Na_2SO_4, indicating that the anion has little influence on the sample's electrochemical properties. The increasingly cathodic reduction potentials observed with increasing cation size suggest that cation diffusion is a limiting factor, a feature observed before by Bond *et al.* when examining the U(VI)/U(V) electron transfer in uranium oxides attached to graphite electrodes.[69] Therefore, $LiClO_4$ was used as the electrolyte for further investigations.

Table 2.7: U(VI)/U(V) redox couples for selected uranyl compounds (*vs.* Ag/AgCl).

Compound	Solvent[a]	E_{red} (V)	Reference
$[(UO_2)(\eta^2\text{-}O_2)(H_2O)_2]\cdot 2H_2O$	Solid-state	-0.76	This Work
$[UO_2(H_2O)_5]^{2+}$	H_2O	-0.68	71
$[UO_2(dmso)_5]^{2+}$	DMSO	-1.71	72
$[UO_2(acac)_2(DMSO)]$	DMSO	-2.19	73
$[UO_2Cl_4]^{2-}$	H_2O	-0.065	74
$[UO_2Cl_4]^{2-}$	$EMI^+BF_4^-/Cl^-$	-1.72	75
$[U(CO_3)_5]^{6-}$	H_2O	-1.20	76
$[UO_2(CO_3)_3]^{4-}$	H_2O	-0.86	77

[a] EMI = 1-ethyl-3-methylimidazolium

There is a wide range of redox potentials observed for the U^{6+}/U^{5+} couple (**Table 2.7**). Recently there has been a growing body of evidence that suggests the redox couple is mainly dependent on the π-donation of the ligand as this can mix with U(*6d*) orbitals, thus stabilising higher oxidation states, whilst ligand denticity and solvation effects play a more subtle role.[78] There has been similar discussion on the effect of the π-donation of the ligand and the correlation between the symmetric uranyl Raman stretching frequency and the U(VI)/(V) reduction potential,[79] with Clark and co-workers postulating that a strong π-donor will compete for the *6d* orbitals in the uranyl π-bond and "activate" the U=O bond.[76b] As a consequence, the more π-donating the ligand, the more negative the $U^{VI/V}$ redox couple, and the lower the symmetric uranyl Raman stretching frequency.

The U(VI)/U(V) couple is considered to be quasi-reversible, however U(V) will disproportionate into U(VI) and U(IV) over time. Therefore the reduction peak at -0.76 V with its corresponding oxidation peak at -0.35 V is assigned to the U(VI)/U(V) couple. The second reduction peak (-1.10 V) that is seen to grow in slowly and then to reach a similar level to the peak at -0.76 V is assigned as the U(V)/U(IV) redox potential. This is reinforced by the electrolysis of studtite at -0.9 V and -1.2 V yielding a brown-black product with identical characteristics to the product of the cycling experiments described above. This is consistent with the hypothesis that the first reduction involves reduction to U^{V} that would then spontaneously disproportionate to U^{IV} and U^{VI}, while the second reduction involves the reduction of U^{V} to U^{IV} electrochemically. Therefore, the final product is likely to contain U^{IV} and no peroxide linkers, which is confirmed by Raman spectroscopy.

Varying the scan rate of the electrochemical experiment can provide valuable information on the movement of charge within the sample. Under semi-infinite diffusion conditions, the Randles-Sevcik equation (**Equation 2.4**) can be applied to determine the diffusion of charge transport, D_{CT}, within the film:

$$i_p = 0.4463\, n\, F\, A\, C \left(\frac{n\, F\, v\, D_{CT}}{RT} \right)^{\frac{1}{2}} \qquad \textbf{2.4}$$

$$= 2.69 \times 10^5 . n^{\frac{3}{2}} A\, C\, v^{\frac{1}{2}}\, D_{CT}^{\frac{1}{2}} \text{ when T = 273 K}$$

where i_p is the peak current, n is the number of electrons transferred, A is the area of the electrode, C is the concentration of redox centres on the surface and ν is the scan rate. **Figure 2.24** shows a plot of the peak current for the first reduction wave versus the square root of the scan rate and a linear trend is clearly observed. The concentration of redox centres (i.e. uranium atoms) in the film can be calculated from the crystallographic parameters[7b] as 19.5 M. Assuming the first reduction is the U(VI)/U(V) couple (i.e. n = 1), a D_{CT} of $4.8 \pm 0.4 \times 10^{-11}$ cm^2s^{-1} can be calculated. This value is the limiting charge transfer step, typically due to the movement of either electrons or ions through the film. Ion diffusion coefficients for other minerals are typically lower than the value reported here,[80] perhaps suggesting that the D_{CT} is dominated by ion movement.

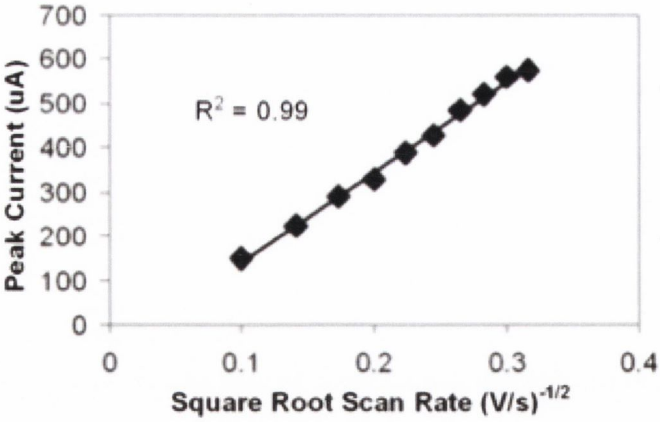

Figure 2.24: The relationship between the peak current and the scan rate at scan rates of 0.01, 0.02, 0.04, 0.06, 0.08, 0.1 V s^{-1} with 0.2 M $LiClO_4$ as the supporting electrolyte for the first reduction.

2.2.3.4. *Confirmation of the Redox Mechanism: Studtite and Iodine*

Iodine is a fission product that is highly environmentally and biologically relevant; ^{129}I contamination at the Savannah River[81] and Hanford[82] sites in the US has become a serious environmental concern. Iodine has 37 isotopes with half-lives from less than seven hours (^{135}I) to 15.7 million years (^{129}I), most of the isotopes of iodine, however, have half-lives between eight and sixty days meaning that many of these fission products have biological activity and are of toxicological concern. Iodine, with known reduced (I^-, I_3^-) and oxidised (IO_3^-) species, was therefore considered worthy of investigation as a test of the redox activity of studtite.

In the terrestrial environment, iodine can be found as iodine, iodide and iodate as well as organic iodine. Iodine, I_2, was examined for possible redox interactions with studtite, but over two weeks there was no change in the concentration or the development of new peaks in the UV spectrum. Potassium iodide, however, was observed to react slowly. The colour change indicated the development of another species in solution (**Figure 2.25**); monitoring by UV-Vis spectroscopy showed two new peaks growing at 288 and 350 nm, indicating the production of I_3^- ($\lambda_{max}(I^-)$ = 193 and 226 nm; $\lambda_{max}(I_3^-)$ = 288 and 350 nm). The formation was faster in studtite, most likely due to the fact that metastudtite has to rehydrate to studtite before any reaction will occur.

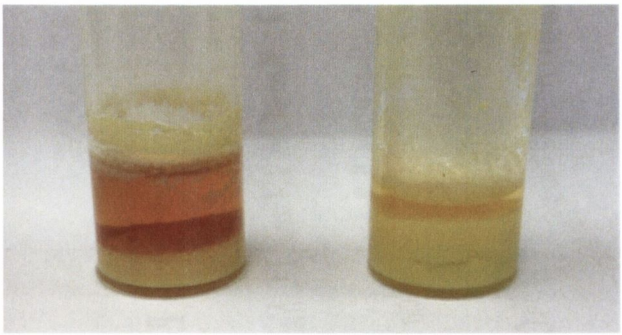

Figure 2.25: Studtite (left) and Metastudtite (right) in 5 mL 0.02 M KI after two weeks.

The redox potential of I_2 oxidation to IO_3^- is reported to be +1.19 V, while the redox potentials of the I^-/I_3^- redox couple is 0.746 V (*vs.* Ag/AgCl).[83] The successful oxidation of I^- was indicative of a potential redox mechanism.

2.3. Conclusions

Upon dehydration of studtite, a colour change from yellow to orange, and subsequent reduction in the bandgap by 0.74 eV, occurs. This shift could result from the structural and electronic changes that occur at the uranium centre. These changes were investigated using X-ray Absorption Spectroscopy techniques EXAFS and HR-XANES, resulting in the first experimental elucidation of the structure of metastudtite.

The EXAFS data shows that the major structural change upon dehydration is the shortening of the $U–O_{peroxo}$ bond length. There is a concomitant change in the HR-XANES data with a shortening of the B–C distance in the metastudtite spectrum by 3.4 eV. The local electronic environment of metastudtite differs with less mixing of U(*5f*) with O(*2p*) states in metastudtite compared to studtite and less hybridisation of U(*6d*) states with O(*2p*) states for studtite compared to metastudtite. This is in agreement with density of states calculations showing a shift in the occupied O *p*-DOS and U *d*- and *f*-DOS of metastudtite to higher energies, thus decreasing the band gap of metastudtite by about 1.3 eV compared to studtite, which is in rough agreement with that of the experimental value of 0.74 eV. This equates to a decrease in the energy gap between the highest occupied peroxo π orbitals and the *5f* non-bonding orbitals of the LUMO.

Given the relevance that studtite has as a possible phase transition on SNF, experiments for sorption and incorporation were undertaken. The results showed that the reduction potential of studtite determines the viability of the interaction in the short term (previous sorption studies have examined studtite over a two year period,[8a] the results within this Thesis are based on one- to two-week testing times). The fact that $LiClO_4$ was the best electrolyte for the electrochemical tests also explains the negative result for the metal incorporation tests. The small $Li^=$ cation was slow to permeate the studtite and the addition of a "break-in" time did not affect the results. It is likely therefore that the cations in question (Fe, Nd, Ho and Eu) were too large to incorporate.

The solid state electrochemistry yielded a U(VI)/U(V) reduction couple of -0.73 V. This result was consistent with the ability of studtite to oxidise I^- to I_3^- ($E_{I-/I3-}$ = +0.733 V) and yet the failure to oxidise I_2 to IO_3^- ($E_{I2/IO3-}$ = +1.19 V). When examining this result in terms of the interaction of neptunium, the formal redox potential of the Np^{5+}/ Np^{4+} couple in acidic media is +0.801 V with respect to the Ag/AgCl reference electrode.[65] This implies that the Np^{5+}/Np^{4+} couple is within range of the studtite U^{6+}/ U^{5+} couple at -0.73 V, meaning that the oxidation of Np(IV) to Np(V) and concomitant reduction of the studtite uranyl to UO_2^+ would be favourable. Therefore during previous batch dissolution studies which have shown the decrease in neptunium concentration in solution,[30] it appears that the mechanism hypothesised by Forbes *et al.* is correct:[6f] NpO_2^+ is reduced by H_2O_2 in solution to a discrete insoluble Np(IV) phase, which is then slowly reoxidised to Np(V) by studtite.

This work shows that studtite is, therefore, electrochemically non-innocent, something that should be borne in mind in the modelling of actinide ion migrations from SNF repositories. One interesting fact is that the electrochemical properties appear to be cation (rather than anion) dependent, resulting in the choice of $LiClO_4$ as the electrolyte for the system.

The slow oxidation of the black amorphous reduced compound in air gave rise to a potential redox mechanism (**Figure 2.26**) that has serious ramifications for the long-term stability and storage of SNF.

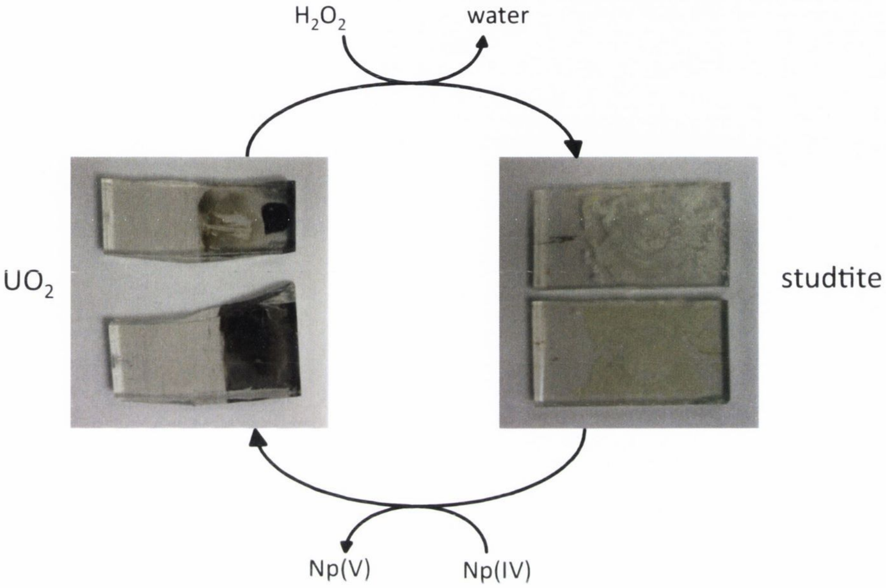

Figure 2.26: The potential redox cycle of studtite in a repository.

2.4. Experimental

2.4.1. General

$[UO_2(NO_3)_2].6H_2O$, studtite,[47] metastudtite[47] and schoepite[84] were prepared as described in the literature and analysed for purity by Raman spectroscopy and powder X-ray diffraction. $^{241}Am^{3+}$ was obtained from Amersham.

Powder diffraction was performed on a Siemens D500 diffractometer using a Bragg-Brentano geometry with step size of 0.02° at 16 s each for metastudtite and schoepite and 0.05° at 2.8 s each for studtite to prevent dehydration to metastudtite (see **Figure 2.27**). Infrared spectra were recorded on a Perkin Elmer Spectrum 100 FTIR Spectrometer with ATR attachment. Raman spectra were recorded on a Renishaw 1000 spectrometer with a 785 nm excitation. Diffuse Reflectance spectra were recorded on a Perkin Elmer Lambda 900 UV/VIS spectrometer with an integrating sphere attachment. Solid-state emission spectra were recorded using a sample holder with a quartz cover plate at angles between 0° and 90° on a Horiba-Jobin-Yvon Fluorolog-3 spectrometer.

Cyclic voltammetry was performed in Dublin City University on a CH Instruments Model 600 electrochemical workstation. Solid state electrochemistry was performed in a standard three electrode configuration using a platinum mesh as a counter electrode and a Ag/AgCl (sat. KCl) reference electrode. Fluorine doped tin oxide (FDTO) coated glass was employed as the working electrode. Studtite was suspended in acetone and the slurry mixture was dropped onto the FDTO electrode. The insolubility of studtite in aqueous solutions ensures no dissolution occurs. Although some material detaches from the electrode over the course of the measurements, this does not affect the results.

Mineral Powder Patterns:

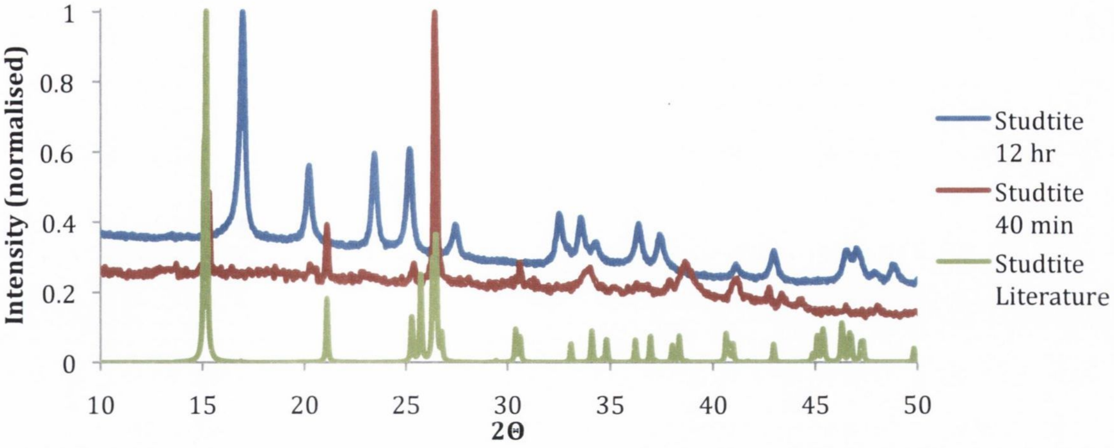

Figure 2.27: Literature[46] and product powder diffraction pattern of studtite. A longer exposure time resulted in dehydration and conversion to metastudtite (blue).

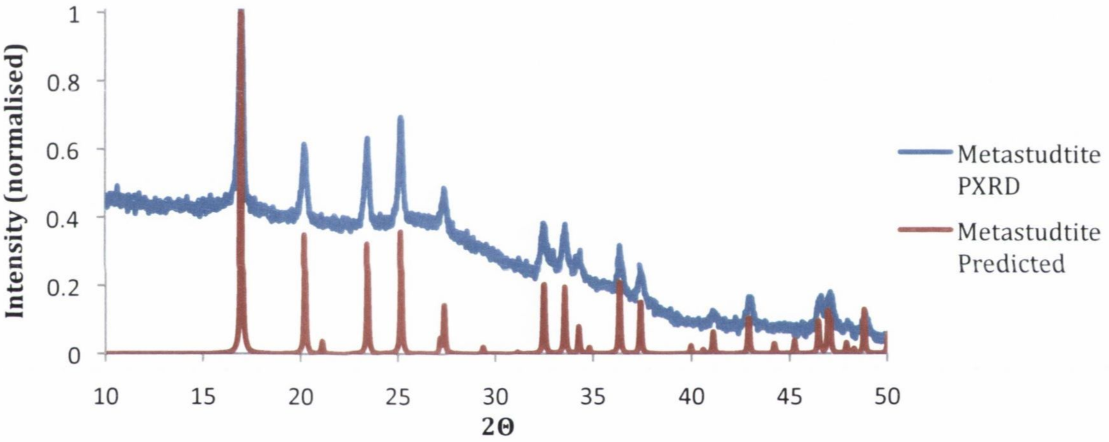

Figure 2.28: Predicted[8c] and found powder patterns of metastudtite.

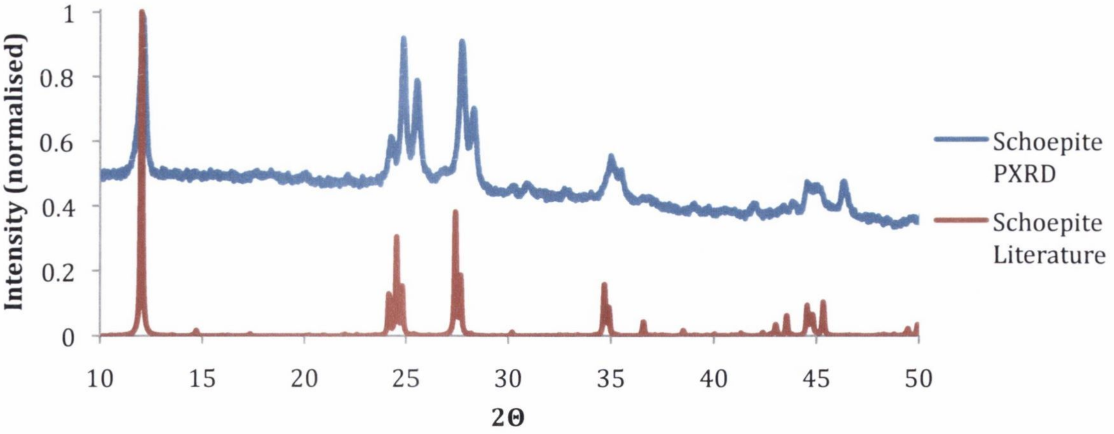

Figure 2.29: Literature[56] and found powder patterns of schoepite.

Sorption experiments: Studtite (100 mg) was suspended in water (100 mL). MCl_3 (50 mg, M = Fe, Nd, Eu, Ho) was added and the mixture was stirred for 7 days. The precipitate was isolated by filtration, washed with water (2 x 20 cm^3) and dried. The sample was analysed using IR, UV/ vis and fluorescence spectroscopy.

Incorporation experiments: $[UO_2(NO_3)_2].6H_2O$ (0.25 g, 0.49 mmol) was dissolved in H_2O (43 cm^3) and concentrated HNO_3 (2 cm^3) and MCl_3 (50 mg, M = Fe, Nd, Eu, Ho) was added. H_2O_2 (50 cm^3 of a 5% solution in water) was added drop wise and the mixture was left to stand for 3 days. The yellow precipitate was isolated by filtration, washed with water (2 x 20 cm^3) and dried. The sample was analysed using IR, UV/vis and fluorescence spectroscopy.

^{241}Am Radiotracer experiment: $[UO_2(NO_3)_2].6H_2O$ (0.25 g, 0.49 mmol) was dissolved in H_2O (43 cm^3) and concentrated HNO_3 (2 cm^3) and $^{241}Am^{3+}$ (5 cm^3 of a 200 kBq solution in water) was added. H_2O_2 (50 cm^3 of a 5 % solution in water) was added drop wise and the mixture was stirred for 3 days. The yellow precipitate was isolated by filtration, washed with water (2 x 20 cm^3) and dried.

The sample was placed inside a calibrated Marinelli beaker and a γ-spectrum obtained. The number of counts from the desired energies (59 keV and 125 keV) was divided by the total number of counts and the mass of the sample (152 mg) to give the amount of ^{241}Am in the sample.

Iodine experiment: Studtite (20 mg) was suspended in dichloromethane (10 mL). I_2 (5 mg) was added and the mixture was left to stand for 14 days. The supernatant solution was analysed using UV-Vis spectroscopy, $\lambda_{max}(I_2)$ = 203 nm.

Iodide experiment: Studtite (20 mg) was suspended in a solution of KI (5 mL, 0.02 M) for 14 days. The supernatant solution was analysed using UV-Vis spectroscopy, $\lambda_{max}(I^-)$ = 193 and 226 nm; $\lambda_{max}(I_3^-)$ = 288 and 350 nm.

2.4.2. XAS Experimental

2.4.2.1. Sample Preparation and Measurements

20 mg of each uranyl compound was ground with cellulose powder (100 mg) and pressed into 1 cm diameter pellets of homogeneous depth and concentration. The EXAFS and HR-XANES measurements were performed at the INE-Beamline, ANKA synchrotron radiation facility, Karlsuhe, Germany. The primary X-ray beam was vertically collimated by a cylindrically bent Rh coated mirror, monochromatised by a Ge(422) double crystal monochromator and focused by a toroidal double-focusing Rh-coated mirror to 500 x 500 μm^2 onto the sample. For detailed description of the INE-Beamline see ref [85].

The initial alignment of the multi-analyzer crystals spectrometer (MAC-spectrometer) was performed by using the elastically scattered from a Teflon sample incident X-rays with energy of 9570.4 eV diffracted by five Ge(555) analyser crystals (Saint-Gobain Crystals, France) set at 82.55° Bragg angle. The experimental energy resolution was estimated by measuring the full-width at half maximum of the elastically scattered peak. The obtained value was 0.1 eV larger than the calculated value 1.9 eV and implied minor deviations of the positions of the sample, crystal and/ or detector from the ideal Rowland circle geometry and/ or source size effects.

The emitted fluorescence from the uranium minerals was diffracted by five Ge(777) analyzer crystals and focused on a SDD VORTEX. The sample, crystals and detector were positioned on a Rowland circle in the vertical plane with diameter of 1 m equal to the bending radius of the spherically bent analyser crystals. The MAC-Spectrometer was set at the maximum of the U $L_{\alpha 1}$ emission line (77.39° Bragg angle), whereas the primary energy was scanned to obtain U L_3 edge (17166 eV) HR-XANES spectra. It was not possible to measure the experimental energy resolution at this photon energy due to the low elastic scattering cross section.

2.4.2.2. Data Manipulation

The oscillating $\chi(k)$ part of the EXAFS spectrum was extracted, Fourier transformed (FT) and modelled by using the ATHENA and ARTEMIS programs, respectively, parts of the IFFEFIT program package.[86] The single scattering paths were generated with the FEFF8.2 code[87] by using the structural models reported in References [47] and [84]. The $\chi(k)$ spectra within 2.5 – 14.5 Å^{-1} range were weighted by k = 1, 2 or 3. Hanning windows with sills equal to 2 (dk = 2) were used. The fit was performed in R space for 1.07 – 2.38 Å range. The obtained goodness of fit (r factor) reports 1 % (r = 0.01, studtite, schoepite) or 2 % (r = 0.02, metastudtite) difference between data and model.

The background subtraction and normalisation of the XANES part of the experimental spectra was performed with ATHENA. The HR-XANES and angular momentum projected density of states (DOS) were calculated by the FEFF9.2 *ab-initio* quantum chemical theoretical code based on the multiple scattering theory.[44] The scattering potentials were calculated on a cluster of 225 atoms by including the U *f* states in the self-consistent loop (FMS, SCF and UNFREEZEF cards).[35a] Final state rule approximation was used to account for core-hole effects (default). The core-hole lifetime broadening was reduced by 2.8 eV and the Fermi energy was shifted by 1 eV to lower energies. Electronic transitions to *5f* states were allowed (MULTIPOLE card). Hedin-Lundqvist exchange correlation potential was used.

The line shape analysis of the HR-XANES data was performed using the open source curve-fitting software Fityk (version 0.9.8)[88] using a Levenberg-Marquardt algorithm to show the pre- and post-edge features with the step function defined as the error function f(x) = step*(erf((x-centre)/width) + 1). The step function and α parameter were varied for metastudtite and then fixed for the remaining samples during the fit. The α parameter indicates the Lorentzian component of the pseudo-Voigt (P.V.) function; the Gaussian component of the P.V. function is defined as 1-α.

2.5. References

(1) (a) Wronkiewicz, D. J.; Bates, J. K.; Gerding, T. J.; Veleckis, E.; Tani, B. S. *J. Nucl. Mater.* **1992**, *190*, 107(b) Wronkiewicz, D. J.; Bates, J. K.; Wolf, S. F.; Buck, E. C. *J. Nucl. Mater.* **1996**, *238*, 78.

(2) (a) Finn, P. A.; Hoh, J. C.; Wolf, S. F.; Slater, S. A.; Bates, J. K. *Radiochim. Acta* **1996**, *74*, 65(b) Finch, R. J.; Buck, E. C.; Finn, P. A.; Bates, J. K. *Mater. Res. Soc. Symp. Proc.* **1999**, *556*, 431(c) Shoesmith, D. W. *J. Nucl. Mater.* **2000**, *282*, 1.

(3) Choppin, G. R. *J. Radioanal. Nucl. Chem.* **2007**, *273*, 695.

(4) Burns, P. C.; Finch, R. J. *Uranium: Mineralogy, Geochemistry and the Environment*, 1999.

(5) Kubatko, K.-A. H.; Helean, K. B.; Navrotsky, A.; Burns, P. C. *Science* **2003**, *302*, 1191.

(6) (a) McNamara, B.; Buck, E.; Hanson, B. *Mater. Res. Soc. Symp. Proc.* **2002**, *757*, 401(b) Hanson, B. D.; McNamara, B.; Buck, E. C.; Friese, J. I.; Jenson, E.; Krupka, K.; Arey, B. W. *Radiochim. Acta* **2005**, *93*, 159(c) Forbes, T. Z.; Horan, P.; Devine, T.; McInnis, D.; Burns, P. C. *Am. Mineral.* **2011**, *96*, 202.

(7) (a) Clarens, F.; de Pablo, J.; Díez-Pérez, I.; Casas, I.; Giménez, J.; Rovira, M. *Environ. Sci. Technol.* **2004**, *38*, 6656(b) Burns, P. C.; Hughes, K.-A. *Am. Mineral.* **2003**, *88*, 1165.

(8) (a) Giménez, J.; Martínez-Lladó, X.; Rovira, M.; de Pablo, J.; Casas, I.; Sureda, R.; Martinez-Esparza, A. *Radiochim. Acta* **2010**, *98*, 479(b) Shuller, L. C.; Ewing, R. C.; Becker, U. *Am. Mineral.* **2010**, *95*, 1151(c) Weck, P. F.; Kim, E.; Jove-Colon, C. F.; Sassani, D. C. *Dalton Trans.* **2012**, *41*, 9748.

(9) Mallon, C.; Walshe, A.; Forster, R. J.; Keyes, T. E.; Baker, R. J. *Inorg. Chem.* **2012**, *51*, 8509.

(10) Amme, M.; Bors, W.; Michel, C.; Stettmaier, K.; Rasmussen, G.; Betti, M. *Environ. Sci. Technol.* **2005**, *39*, 221.

(11) Gauthier-Lafaye, F. *C. R. Phys.* **2002**, *3*, 839.

(12) Abrefah, J.; Marschmann, S.; Jenson, E. D. *PNNL-11806*, 1998.

(13) Burakov, B. E.; Strykanova, E. E.; Anderson, E. B. *Mater. Res. Soc. Symp. Proc.* **1997**, *465*, 1309.

(14) (a) Walenta, K. *Am. Mineral.* **1974**, *59*, 166(b) Deliens, M.; Piret, P. *Am. Mineral.* **1983**, *68*, 456.

(15) (a) Kim, K. W.; Kim, Y. H.; Lee, S. Y.; Lee, J. W.; Joe, K. S.; Lee, E. H.; Kim, J. S.; Song, K.; Song, K. C. *Environ. Sci. Technol.* **2009**, *43*, 2355(b) Goff, G. S.; Brodnax, L. F.; Cisneros, M. R.; Peper, S. M.; Field, S. E.; Scott, B. L.; Runde, W. H. *Inorg. Chem.* **2008**, *47*, 1984.

(16) Meca, S.; Martinez-Torrents, A.; Marti, V.; Giménez, J.; Casas, I.; de Pablo, J. *Dalton Trans.* **2011**, *40*, 7976.

(17) Vlaisavljevich, B.; Gagliardi, L.; Burns, P. C. *J. Am. Chem. Soc.* **2010**, *132*, 14503.

(18) Armstrong, C. R.; Nyman, M.; Shvareva, T.; Sigmon, G. E.; Burns, P. C.; Navrotsky, A. *Proc. Natl. Acad. Sci.* **2012**, *109*, 1874.

(19) Fairley, T. *J. Chem. Soc.* **1877**, *31*, 125.

(20) Sato, T. *Naturwissenschaften* **1961**, *48*, 668.

(21) (a) Cordfunke, E. H. P.; Van Der Giessen, A. A. *J. Inorg. Nucl. Chem.* **1963**, *25*, 553(b) Cordfunke, E. H. P.; Aling, P. *Rec. Trav. Chim. Pays-Bas* **1963**, *82*, 257.

(22) Rey, A.; Utsunomiya, S.; Giménez, J.; Casas, I.; de Pablo, J.; Ewing, R. C. *Am. Mineral.* **2009**, *94*, 229.

(23) Hanson, B.; McNamara, B.; Buck, E.; Friese, J.; Jenson, E.; Krupka, K. *Radiochim. Acta* **2005**, *93*, 159.

(24) Dickman, M. H.; Pope, M. T. *Chem. Rev.* **1994**, *94*, 569.

(25) Vlaisavljevich, B.; Gagliardi, L.; Burns, P. C. *J. Am. Chem. Soc.* **2010**, *132*, 14503.

(26) Odoh, S. O.; Schreckenbach, G. *Inorg. Chem.* **2013**, *52*, 5590.

(27) Miro, P.; Pierrefixe, S.; Gicquel, M.; Gil, A.; Bo, C. *J. Am. Chem. Soc.* **2010**, *132*, 17787.

(28) (a) Burns, P. C. *Mineral. Mag.* **2011**, *75*, 1(b) Qiu, J.; Burns, P. C. *Chem. Rev.* **2012**, *113*, 1097(c) Ling, J.; Qiu, J.; Burns, P. C. *Inorg. Chem.* **2012**, *51*, 2403.

(29) Sureda, R.; Martínez-Lladó, X.; Rovira, M.; de Pablo, J.; Casasa, I.; Giménez, J. *J. Hazard. Mater.* **2010**, *181*, 881.

(30) McNamara, B.; Hanson, B. D.; Buck, E. C.; Soderquist, C. *Radiochim. Acta* **2005**, *93*, 169.

(31) Douglas, M.; Clark, S. B.; Friese, J. I.; Arey, B. W.; Buck, E. C.; Hanson, B. D. *Environ. Sci. Technol.* **2005**, *39*, 4117.

(32) Burns, P. C.; Deely, K. M.; Skanthakumar, S. *Radiochim. Acta* **2004**, *92*, 151.

(33) Denning, R. G. *J. Phys. Chem. A* **2007**, *111*, 4125.

(34) Solomon, E. I.; Hedman, B.; Hodgson, K. O.; Dey, A.; Szilagyi, R. K. *Coord. Chem. Rev.* **2005**, *249*, 97.

(35) (a) Vitova, T.; Denecke, M. A.; Göttlicher, G.; Jorissen, K.; Kas, J. J.; Kvashnina, K.; Prüßmann, T.; Rehr, J. J.; Rothe, J. *J. Phys. Conf. Ser.* **2013**, *430*, 012117(b) Kosog, B.; La Pierre, H. S.; Denecke, M. A.; Heinemann, F. W.; Meyer, K. *Inorg. Chem.* **2012**, *51*, 7940(c) Vitova, T.; Kvashnina, K. O.; Nocton, G.; Sukharina, G.; Denecke, M. A.; Butorin, S. M.; Mazzanti, M.; Caciuffo, R.; Soldatov, A.; Behrends, T.; Geckeis, H. *Phys. Rev. B* **2010**, *82*, 235118.

(36) Koningsberger, D. C.; Prins, R. *Principles, Application, Techniques of EXAFS, SEXAFS and XANES*; John Wiley & Sons, 1987.

(37) Karim, D. P.; Georgopoulos, P. *Nucl. Tech.* **1980**, *51*, 162.

(38) Denecke, M. A. *Coord. Chem. Rev.* **2006**, *205*, 730.

(39) (a) Den Auwer, C.; Simoni, E.; Conradson, S. D.; Madic, C. *Eur. J. Inorg. Chem.* **2003**, *2003*, 3843(b) Antonio, M. R.; Staub, U.; Xue, J. S.; Soderholm, L. *Chem. Mat.* **1996**, *8*, 2673(c) Sukharina, G. B.; Soldatov, A. V.; Batuk, O. N.; Denecke, M. A. *Nucl. Instrum. Methods Phys. Res., Sect. A* **2009**, *603*, 125(d) Rothe, J.; Walther, C.; Brendebach, B.; Buchner, S.; Fuss, M.; Denecke, M. A.; Geckeis, H. *14th International Conference on X-Ray Absorption Fine Structure (Xafs14), Proceedings*, 2009(e) Brendebach, B.; Banik, N. L.; Marquardt, C. M.; Rothe, J.; Denecke, M. A.; Geckeis, H. *Radiochim. Acta*

2009, *97*, 701(f) Schmeide, K.; Reich, T.; Sachs, S.; Bernhard, G. *Inorg. Chim. Acta* **2006**, *359*, 237.

(40) Deslattes, R. D.; Indelicato Jr, E. G. K. P.; Billy, L. D.; Lindroth, E.; Anton, J. *Rev. Mod. Phys.* **2003**, *75*, 35.

(41) Hudson, E. A.; Allen, P. G.; Terminello, L. J.; Denecke, M. A.; Reich, T. *Phys. Rev. B* **1996**, *54*, 156.

(42) Denning, R. G.; Green, J. C.; Hutchings, T. E.; Dallera, C.; Tagliaferri, A.; Giarda, K.; Brookes, N. B.; Braicovich, L. *J. Chem. Phys.* **2002**, *117*, 8008.

(43) Kleymenov, E.; Bokhoven, J. A. v.; David, C.; Glatzel, P.; Janousch, M.; Alonso-Mori, R.; Studer, M.; Willimann, M.; Bergamaschi, A.; Henrich, B.; Nachtegaal, M. *Rev. Sci. Instrum.* **2011**, *82*, 065107.

(44) Rehr, J. J.; Kas, J. J.; Vila, F. D.; Prange, M. P.; Jorissen, K.; 9.5.1 ed.; Phys. Chem. Chem. Phys., 12, 5503-5513, 2010.

(45) Ukazi, R. *J. Atom. Energ. Soc. Jpn* **1959**, *1*, 405.

(46) Debets, P. C. *J. Inorg. Nucl. Chem.* **1963**, *25*, 727.

(47) Bastians, S.; Crump, G.; Griffith, W. P.; Withnall, R. *J. Raman Spectrosc.* **2004**, *35*, 726.

(48) Ostanin, S.; Zeller, P. *Phys. Rev. B: Condens. Matter* **2007**, *75*, 073101.

(49) (a) Denning, R. G. *Struct. Bonding (Berlin)* **1992**, *79*, 215(b) Geipel, G. *Coord. Chem. Rev.* **2006**, *250*, 844.

(50) Balzani, V.; Bolleta, F.; Gandolfi, M. T.; Maestri, M. *Top. Curr. Chem.* **1978**, *75*, 1.

(51) Kimura, T.; Nagaishi, R.; Kato, Y.; Yoshida, Z. *Radiochim. Acta* **2001**, *89*, 125.

(52) Gaunt, A. J.; Reilly, S. D.; Enriquez, A. E.; Scott, B. L.; Ibers, J. A.; Sekar, P.; Ingram, K. I. M.; Kaltsoyannis, N.; Neu, M. P. *Inorg. Chem.* **2008**, *47*, 29.

(53) (a) Jarvinen, G. D.; Barrans, R. E.; Schroeder, N. C.; Wade, K. L.; Jones, M. M.; Smith, B. F.; Mills, J. L.; Howard, G.; Freiser, H.; Muralidharan, S.; Nash, K. L.; Choppin, G. R. *Separation of f Elements*, 1995(b) Petit, L.; Borel, A.; Daul, C.; Maldivi, P.; Adamo, C. *Inorg. Chem.* **2006**, *45*, 7382(c) Maldivi, P.; Petit, L.; Adamo, C.; Vetere, V. *C. R. Chim.*

2007, *10*, 888(d) Girnt, D.; Roesky, P. W.; Geist, A.; Ruff, C. M.; Panak, P. J.; Denecke, M. A. *Inorg. Chem.* **2010**, *49*, 9627(e) Neidig, M. L.; Clark, D. L.; Martin, R. L. *Coord. Chem. Rev.* **2012**, *257*, 394(f) Kaltsoyannis, N. *Inorg. Chem.* **2012**, *52*, 3407.

(54) (a) Williams, C. W.; Blaudeau, J. P.; Sullivan, J. C.; Antonio, M. R.; Bursten, B.; Soderholm, L. *J. Am. Chem. Soc.* **2001**, *123*, 4346(b) Ankudinov, A. L.; Conradson, S. D.; de Leon, J. M.; Rehr, J. J. *Phys. Rev. B* **1998**, *57*, 7518.

(55) Denecke, M. A.; Borchert, M.; Denning, R. G.; de Nolf, W.; Falkenberg, G.; Hönig, S.; Klinkenberg, M.; Kvashnina, K.; Neumeier, S.; Patommel, J.; Petersmann, T.; Pruessmann, T.; Ritter, S.; Schroer, C. G.; Stephan, S.; Villanova, J.; Vitova, T.; Wellenreuther, G. *MRS Online Proc. Lib.* **2012**, *1444*.

(56) Weller, M. T.; Light, M. E.; Gelbrich, T. *Acta Crystallogr., B* **2000**, *56*, 577.

(57) Burns, P. C.; Ewing, R. C.; Miller, M. L. *J. Nucl. Mater.* **1997**, *245*, 1.

(58) Kasha, M.; Seaborg, G. T.; Katz, J. J.; Manning, W. M. *The Transuranium Elements*, 1949.

(59) Duffield, J. R.; Taylor, D. M. *Inorg. Chim. Acta* **1987**, *140*, 365.

(60) Bruno, J. E., Rodney C. *Elements* **2006**, *2*, 343.

(61) Runde, W. H.; Mincher, B. J. *Chem. Rev.* **2011**, *111*, 5723.

(62) Yoshida, Z.; Johnson, S. G.; Kimura, T.; Krsul, J. R. In *The Chemistry of the Actinide and Transactinide Elements*; 3rd ed.; Morss, L. R., Fuger, J., Edelstein, N. M., Eds.; Springer: Dordrecht, The Netherlands, 2006.

(63) Zielen, A. J.; Cohen, D. *J. Phys. Chem.* **1970**, *74*, 394.

(64) (a) Kaszuba, J. P.; Runde, W. H. *Environ. Sci. Technol.* **1999**, *33*, 4427(b) Antonio, R.; Soderholm, L.; Williams, C. W.; Blaudeau, J. P.; Bursten, B. E. *Radiochim. Acta* **2001**, *89*, 17(c) Ikeda-Ohno, A.; Hennig, C.; Rossberg, A.; Funke, H.; Scheinost, A. C.; Bernhard, G.; Yaita, T. *Inorg. Chem.* **2008**, *47*, 8294(d) Runde, W.; Neu, M. P. In *The Chemistry of the Actinide and Transactinide Elements*; Morss, L. R., Edelstein, N. M., Fuger, J., Eds.; Springer: Dordrecht, The Netherlands, 2010.

(65) Runde, W. H.; Schulz, W. W. In *The Chemistry of the Actinide and Transactinide Elements*; 4th ed.; Morss, L. R., Edelstein, N. M., Fuger, J., Eds.; Springer: Dordrecht, The Netherlands, 2010.

(66) Martinot, L.; Fuger, J. *Standard Potentials in Aqueous Solutions*; Marcel Dekker: New York., 1985.

(67) (a) Nafadya, A.; Bond, A. M.; Bilyk, A.; Harris, A. R.; Bhatt, A. I.; O'Mullane, A. P.; De Marco, R. *J. Am. Chem. Soc.* **2007**, *129*, 2369(b) Bond, A. M.; Colton, R.; Daniels, F.; Fernando, D. R.; Marken, F.; Nagaosa, Y.; Van Steveninck, R. F. M.; Walter, J. N. *J. Am. Chem. Soc.* **1993**, *115*, 9556.

(68) Grambow, B. *J. Contam. Hydrol.* **2008**, *102*, 180.

(69) Dueber, R. E.; Fleetwood, J. M.; Dickens, P. G. *Solid State Ionics* **1992**, *50*, 329.

(70) Senanayake, S. D.; Rousseau, R.; Colegrave, D.; Idriss, H. *J. Nucl. Mater.* **2005**, *342*, 179.

(71) Austin, J. P.; Sundararajan, M.; Vincent, M. A.; Hillier, I. H. *Dalton Trans.* **2009**, 5902.

(72) Kim, S. Y.; Tomiyasu, H.; Ikeda, Y. *J. Nucl. Sci. Technol.* **2002**, *39*, 160.

(73) Lee, S. H.; Mizuguchi, K.; Tomiyasu, H.; Ikeda, Y. *J. Nucl. Sci. Technol.* **1996**, *33*, 190.

(74) Morris, D. E. *Inorg. Chem.* **2002**, *41*, 3542.

(75) Ogura, T.; Takao, K.; Sasaki, K.; Arai, T.; Ikeda, Y. *Inorg. Chem.* **2011**, *50*, 10525.

(76) Hennig, C.; Ikeda-Ohno, A.; Emmerling, F.; Kraus, W.; Bernhard, G. *Dalton Trans.* **2010**, *39*, 3744.

(77) Mizuguchi, K.; Park, Y. Y.; Tomiyasu, H.; Ikeda, Y. *J. Nucl. Sci. Technol.* **1993**, *30*, 542.

(78) Hardwick, H. C.; Royal, D. S.; Helliwell, M.; Pope, S. J. A.; Ashton, L.; Goodacre, R.; Sharrad, C. A. *Dalton Trans.* **2011**, *40*, 5939.

(79) (a) Fortier, S.; Hayton, T. W. *Coord. Chem. Rev.* **2010**, *254*, 197(b) Clark, D. L.; Conradson, S. D.; Donohoe, R. J.; Keogh, D. W.; Morris, D. E.; Palmer, P. D.; Rogers, R. D.; Tait, C. D. *Inorg. Chem.* **1999**, *38*, 1456.

(80) Brady, J. B.; Cherniak, D. J. *Rev. Mineral. Geochem.* **2010**, *72*, 899.

(81) Denham, M. E. *Potential in-situ remediation of 129I and 99Tc in groundwater associated with the F-area seepage basins (U)*, 2002.

(82) Riley, R. G.; Zachara, J. M. *Nature of Chemical Contaminants on DOE Lands and Identification of Representative Contaminant Mixtures for Basic Subsurface Science Research*, 1992.

(83) (a) Popov, A. I.; Geske, D. H. *J. Am. Chem. Soc.* **1958**, *80*, 1340(b) Boschloo, G.; Gibson, E. A.; Hagfeldt, A. *J. Phys. Chem. Lett.* **2011**, *2*, 3016.

(84) Nipruk, O.; Knyazev, A.; Chernorukov, G.; Pykhova, Y. *Radiochemistry* **2011**, *53*, 146.

(85) Rothe, J.; Butorin, S.; Dardenne, K.; Denecke, M. A.; Kienzler, B.; Loble, M.; Metz, V.; Seibert, A.; Steppert, M.; Vitova, T.; Walther, C.; Geckeis, H. *Rev. Sci. Instrum.* **2012**, *83*, 043105.

(86) Ravel, B.; Newville, M. *Phys. Scr.* **2005**, *T115*, 1007.

(87) Rehr, J. J.; Albers, R. C. *Rev. Mod. Phys.* **2000**, *72*, 621.

(88) Wojdyr, M. *J. Appl. Crystallogr.* **2010**, *43*, 1126.

Chapter 3:

Uranyl Minerals Relevant to the Long Term Storage of Spent Nuclear Fuel II: Uranyl Oxyhydroxides, Phosphates and Carbonates

3.1. Introduction

There are over 200 known uranyl minerals,[1] although less than half of these have been structurally characterised. Each of these minerals has chemical and structural properties that have the potential to affect the solubility and mobility of uranium in nature. Uranyl phases can precipitate or dissolve in aqueous environments at different pH and ion concentrations; these phases can incorporate radionuclides into their structure or adsorb these contaminants onto their surface through a redox or ion-exchange pathway. In this way uranyl minerals can hinder or enhance the leaching of radionuclides into the surrounding environment. It is possible that if these minerals form on the surface of spent nuclear fuel (SNF) then these effects on the mobility of uranium and other radionuclides will have long-term implications for the stability of SNF.

This Chapter will detail the examination of a selection of natural phosphate minerals as well as synthetic oxyhydroxide and carbonate minerals using solid-state electrochemistry to determine their redox activity and to predict the potential effects of the evolution of these minerals on the stability of SNF. Structure–reactivity relationships will be investigated using diffusion charge transport experiments.

3.1.1. UO_2 Oxidation and Uranyl Speciation

Uranium(IV) is not stable in oxidising environments and will, over time, oxidise to the +6 oxidation state. This is particularly relevant given that spent nuclear fuel (SNF) is stored as UO_2. Studies on SNF[2] and uraninite[3] (the natural mineral form of UO_2) have shown that U(IV) will oxidise and react with alkali or alkaline earth cations and hydroxide, carbonate, phosphate or silicate anions to form uranyl mineral phases. The primary phases formed are uranyl oxyhydroxide or uranyl silicate minerals (**Figure 3.1**). In deionised water uranyl oxyhydroxide and uranyl silicate minerals have been shown to evolve into studtite, $[(UO_2)(\eta^2\text{–}O_2)(H_2O)_2]\cdot 2H_2O$, over two years.[4] This indicates the importance of studtite as a long-term product of the dissolution of UO_2, as discussed in **Chapter 2**. Four uranyl oxyhydroxide minerals, schoepite $[(UO_2)_8O_2(OH)_{12}]\cdot12H_2O$, Na-metaschoepite, $Na[(UO_2)_4O_2(OH)_5]\cdot5H_2O$, compreignacite $K_2[(UO_2)_6O_4(OH)_6]\cdot7H_2O$, and becquerelite, $Ca[(UO_2)_6O_4(OH)_6]\cdot8H_2O$, were chosen to be analysed as part of the series of minerals examined in this chapter. These four uranyl oxyhydroxide phases are all found as early alteration phases of uraninite[3a-c] and SNF[2] (**Figure 3.1**) and were therefore considered worthy of investigation to predict any potential redox-active migration pathways on the surface of SNF.

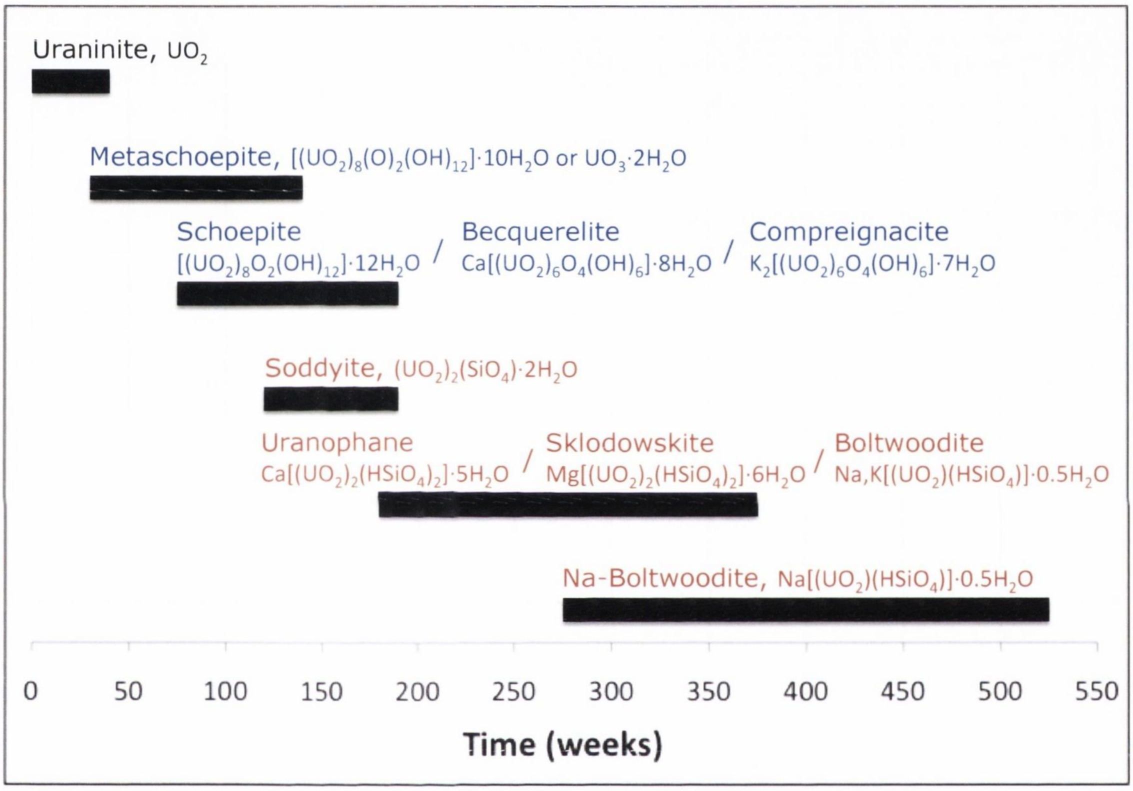

Figure 3.1: Uranium alteration phases found over a ten-year study. Blue minerals are uranyl oxyhydroxides and uranyl silicates are in red. Adapted from reference 2a.

Examining the energetics of interactions of UO_3 with acidic oxides (H_2O, SiO_2, CO_2 and P_2O_5) and calculating the energies of formation of uranyl phases gives key insight into the probable products of oxidation of UO_2 or UO_3 and their relative stability: uranyl phosphates would be the most stable minerals, followed by carbonates, silicates, and then oxides (or oxyhydroxides).[5] The high stability of uranyl phosphates is consistent with evidence of uranium immobilisation in uranyl phosphate minerals.[6] In the Coles Hill uranium deposit, Virginia, low uranium concentrations in the groundwater (<14 μg L^{-1}, less than half the EPA maximum contaminant level) were attributed to the formation of uranium(VI) phosphates in the bedrock.[7] This ability to immobilise uranium and hinder the migration of uranium into the surrounding environment has been replicated in the laboratory and put into practice in spent fuel storage.[8] Natural samples of three uranyl phosphate minerals, meta-autunite, $Ca[(UO_2)_2(PO_4)_2]\cdot6–8H_2O$, metatorbernite, $Cu[(UO_2)_2(PO_4)_2]\cdot8H_2O$, and meta-uranocircite, $Ba[(UO_2)_2(PO_4)_2]\cdot6–8H_2O$, were acquired to determine the stability of these minerals to redox processes.

Uranyl carbonate minerals are the next most thermodynamically stable uranyl minerals[5a] and are extremely common modifications of uranyl.[9] Carbonate is an important complexing ligand and carbonate–bicarbonate equilibria play a role in the pH of natural water systems. Natural carbonate minerals can incorporate U(IV) and U(VI) into their structure, thereby forming solid solutions. A number of EXAFS studies of the structures wherein uranium has been incorporated into carbonate minerals have been reported to gain a comprehensive view of the potential of carbonate minerals for sequestering uranium.[10] Calcite, ($CaCO_3$), is by far the most abundant carbonate mineral and comprises about 4 wt. % of the Earth's crust.[10] Single calcite crystals formed from solutions of uranyl coprecipitated with calcite have been investigated and have shown that uranyl incorporation starts with the adsorption of uranyl tricarbonate species, $[UO_2(CO_3)_3]^{-4}$.[11] The uranyl species were found to have different equatorial environments, and increased the local disorder of the calcite, implying that the uranyl incorporation decreases the stability of the calcite.[12] In dilute solutions, the formation of uranyl tricarbonate units can act as a driving force for self-assembly of uranyl carbonate minerals.[13] The two most energetically favourable uranyl carbonate phases are grimselite $K_3Na[UO_2(CO_3)_3]\cdot H_2O$ and andersonite $Na_2Ca[UO_2(CO_3)_3]\cdot5H_2O$.[14] For grimselite, the strong interaction between four basic sodium and potassium cations with a relatively strong Lewis acid, CO_3^{2-}, leads to a strongly negative enthalpy of formation, -989.3 ± 14.0 kJ mol^{-1}, from oxides. The less basic calcium cation in andersonite leads to a more positive enthalpy of formation: -710.4 ± 9.1 kJ mol^{-1}.[14] Grimselite and andersonite were chosen as the two uranyl carbonate minerals to be investigated during this study. The 3D framework that arises from the uranyl tricarbonate unit creates pores of different sizes. The resulting change in permeability will be investigated *via* electrochemical analysis with different electrolyte cations. It will also be possible to determine the effect of cation–cation interactions on the redox chemistry of uranyl, as grimselite and andersonite both contain uranyl cation–cation interactions; these are symmetrical in the case of grimselite and asymmetrical in andersonite.

Uranyl silicates have been found to be medium to long-term phase alterations on SNF[2] (**Figure 3.1**) and have been found to be environmentally relevant – they have been shown to increase the solubility of uranium and have been observed to cause contamination of surrounding soil and groundwater,[15] and have been found to immobilise radionuclides such as Cs-137 and Sr-90 by sorption into the layered network.[16] They have, however, been found to be preferentially replaced by uranyl phosphates in nature[6a,7] or, in the case of the Hanford Site Tank Leachants, by schoepite and uranyl carbonates such as andersonite.[17] Therefore, no uranyl silicates were synthesised for inclusion in this study.

3.1.2. Solid State Electrochemistry

Electrochemical analysis of solids is a recent development. The late development of solid-state electrochemistry was due to the lack of practical apparatus; it is only since the 1980s that techniques (such as manufacturing a conductive compound into an electrode, or binding a solid to an electrode via an organic binder or a polymer) have been developed to allow the measurement of the electrochemical properties of solids.[18] The main stipulation is that the solid and its redox partners are not soluble in the contacting solution/ electrolyte. In 1982, Roullier and Laviron explored the electrochemical properties of organic solids by depositing a "thick layer" on electrodes by evaporation of a solution of the compound in a volatile solvent.[19] This allowed the analysis of the compound without the mechanical or chemical alterations necessary for earlier techniques.[18] This method has been elaborated by Bond and co-workers for studying solid materials by depositing a slurry of the analyte in a volatile solvent on an electrode surface such as fluorine doped tin oxide (FDTO).[20] This allows electrochemical aspects to be studied in a similar fashion to the traditional solution redox systems and at fast scan rates,[21] however, the clarity of the voltammograms is dependant on the amount and the distribution of the analyte on the surface, which also affects the reproducibility of the data – unlike solution phase electrochemistry, stirring the solution had little effect on the resolution of the peaks. This has led to the conclusion that the surface area of the analyte plays a role in insertion processes of electrolyte ions into the analyte.[22]

The first example of solid-state electroanalysis of uranium samples was performed by Bond and co-workers to study the mechanism of formation of sodium, lithium and magnesium insertion compounds of uranium oxides by voltammetric reduction using Na^+, Li^+ and Mg^{2+} electrolytes.[22] This was the only such example of solid-state electroanalysis of a uranium species until the results of the investigations into the redox nature of studtite discussed in **Chapter 2** were published.[23] Bond pressed a graphite rod into finely ground uranium oxides for analysis in sodium, lithium and magnesium electrolytes to investigate the mechanism of insertion of the cation into the oxide. Previous analysis of the formation of insertion compounds revealed that the divalent Mg^{2+} diffused 10^3 to 10^4 times more slowly than the monovalent Li^+ and Na^+.[24] The reduction potential of the oxides was found to be unaffected by the anion (Cl^- or ClO_4^-) which was supported by the electroanalysis of studtite (SO_4^{2-} or ClO_4^-, **Chapter 2**).[23] The ability of Bond *et al.* to use electroanalytical methods to directly examine the diffusion of cations into the analyte demonstrated an unprecedented precision in the *in situ* examination of the permeation and migration of a cation into a solid. Given the potential importance of solid-state redox reactions in transuranic minerals and in spent nuclear fuels,[2c,25] solid-state electrochemistry is an attractive means of considering these processes and investigating the viability of redox processes at the surface.

The set-up in the experiments detailed within this chapter is shown in **Figure 3.2**. The analyte was suspended in acetone and drop cast onto the conductive side of fluorine-doped tin oxide (FDTO) to act as the working electrode in the system. All of the experiments were undertaken in degassed aqueous solutions of the desired electrolyte.

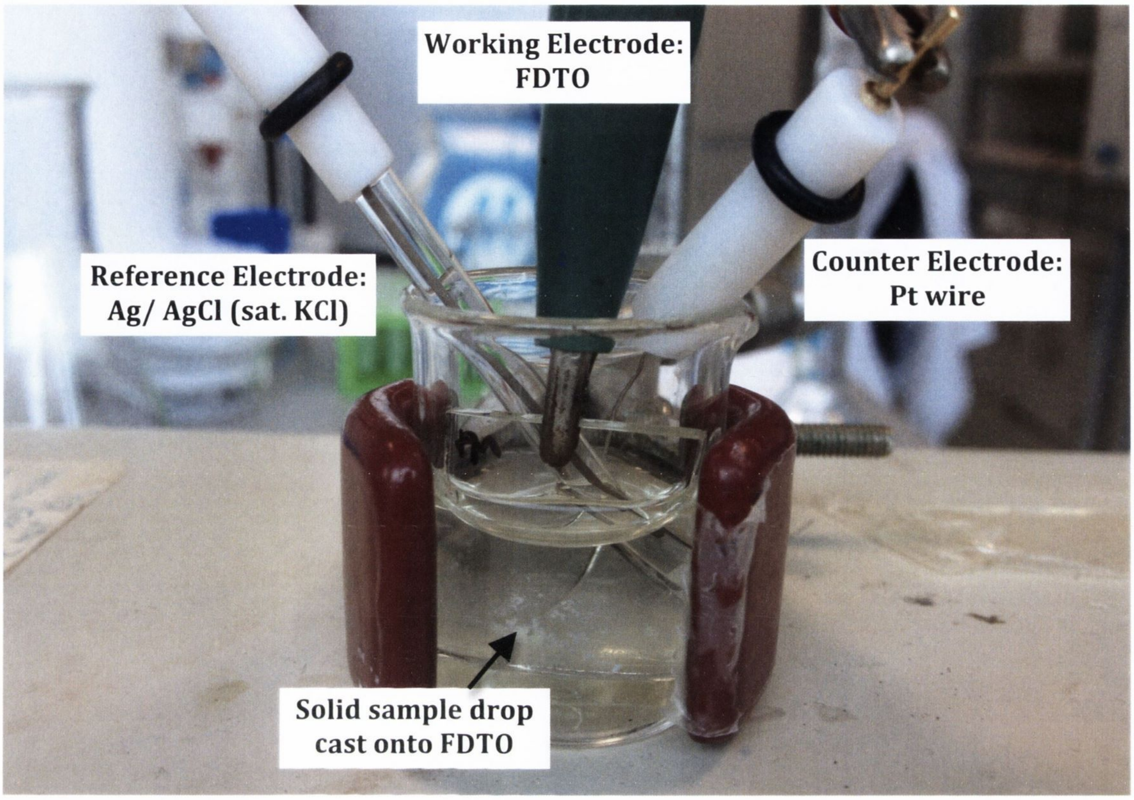

Figure 3.2: The experimental set-up for the electrochemical experiments. The sample is drop cast onto FDTO (Fluorine-Doped Tin Oxide) to act as the working electrode.

Following on from the analysis of studtite, the nine minerals were examined using solid-state cyclic voltammetry in 0.2 M $LiClO_4$ between +1 and -1.5 V for one and 12 hours without a break-in time. A break-in time would serve to stimulate or increase the break-in phenomenon, i.e. the rate of growth of the peak as electrolyte ions permeate – or "break into" – the sample, but in this case leaving the studtite electrode in the electrolyte solution for time periods ranging from one hour to overnight did not seem to affect the rate of growth of peaks during electrochemical experiments. Chronoamperometric methods were used to fully reduce the compound by holding the material at a potential of -1.2 V for one or 12-hour periods. The resulting products were analysed with Scanning Electron Microscopy (SEM), Raman spectroscopy and Energy Dispersive X-Ray spectroscopy (EDX) at multiple points on the surface to establish the differences (if any) between the reduced compounds and the products of the cyclic voltammetry.

For the two carbonate minerals in the survey, five electrolytes were used: Li_2CO_3, K_2CO_3, and $CaCO_3$, $LiClO_4$ and $KClO_4$. Andersonite contains sodium and calcium within its unit cell, grimselite contains potassium and sodium; electrolytes with different cations (Li^+, K^+, Ca^{2+}) were used to ascertain the possibility of size and charge dependence on the permeability of cations. Previous analysis of the solid state electrochemistry of uranium revealed that the divalent Mg^{2+} diffused 10^3 to 10^4 times more slowly than the monovalent Li^+ and Na^+.[24] Carbonate electrolytes were also used to determine the effect, if any, of the perchlorate anion on the CO_3^{2-} ligands.

3.2. Uranyl Oxyhydroxide Minerals

3.2.1. Structural Comparison

During this work, four synthetic oxyhydroxide minerals were synthesised and compared. As mentioned previously, the oxyhydroxide minerals commonly adopt a structure of 2D networks in layers. Schoepite, $[(UO_2)_8O_2(OH)_{12}]\cdot 12H_2O$, and metaschoepite, $[(UO_2)_8O_2(OH)_{12}]\cdot 10H_2O$ (often simplified to $UO_3\cdot 2H_2O$), are examples of uranyl oxyhydroxide minerals without bridging cations; the structures consist of layers of edge-sharing UO_7 pentagonal bipyramids, interspersed with hydrogen-bonded water molecules [**Figure 3.3(left)**]. The main effect of dehydration from schoepite to metaschoepite is the contraction along the a axis (perpendicular to the plane of the uranyl layer) by 2.8% in the metaschoepite unit cell.[26] This has been accredited to improved connectivity of the water molecules between the sheets, and the bridging by the dual acceptor nature of the two interstitial water molecules.

Synthetic schoepite was prepared *via* a reaction of dehydrated UO_3 and steam and the product verified using powder X-ray Diffraction (PXRD). For practical reasons, Na-metaschoepite, $Na[(UO_2)_4O_2(OH)_5]\cdot 5H_2O$, was synthesised instead of metaschoepite using NaOH as the source of hydroxyl ions, thereby introducing sodium cations into the structure [**Figure 3.3(right)**].[27] This was verified using PXRD. In nature, this sodium-substituted structure is common[28] given the prevalence of sodium cations in many soil and water environments, and so this compound was accepted as an alternative.

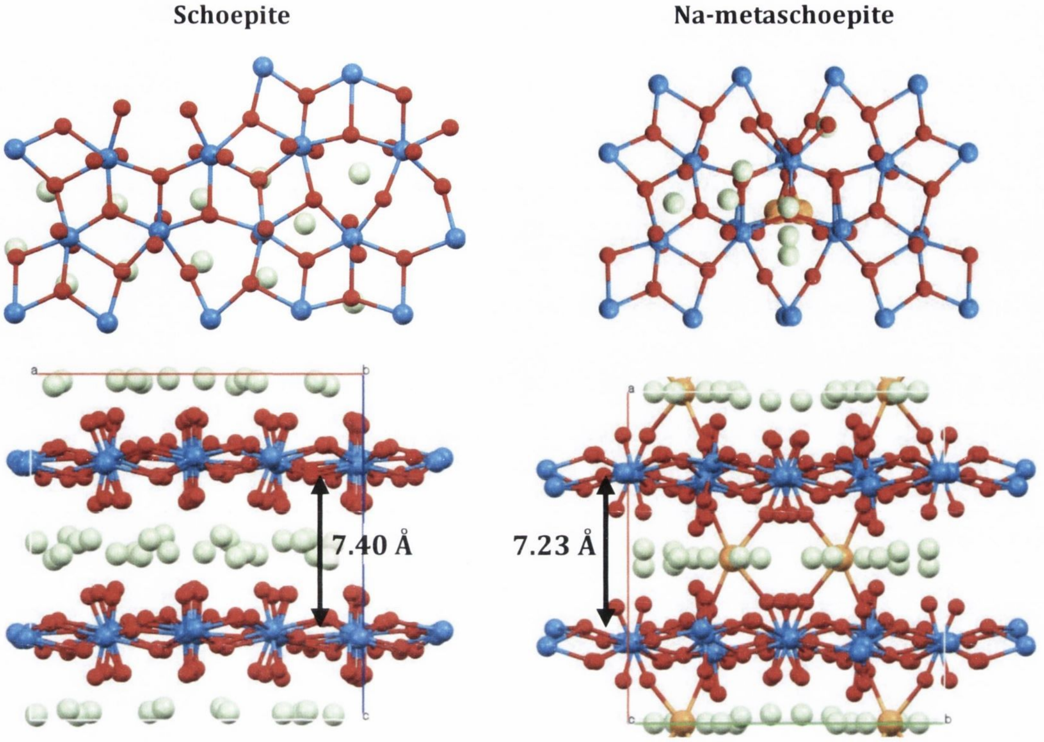

Figure 3.3: The view along the c axis (top) and a axis (bottom) of the unit cell of schoepite, $[(UO_2)_8O_2(OH)_{12}]\cdot 12H_2O$ (left),[29] and the view along the a axis (top) and c axis (bottom) of the unit cell of synthetic Na-metaschoepite, $Na[(UO_2)_4O_2(OH)_5]\cdot 5H_2O$.[27] (Key: Blue = U; Red = O; Orange = Na; Beige = Water)

Comparing vibrational spectra of schoepite and Na-metaschoepite shows that the uranyl region in the Raman is similar with schoepite showing three uranyl stretches at 828, 844 and 867 cm^{-1} and Na-metaschoepite showing three similar stretches at 824, 845 and 862 cm^{-1} (**Figure 3.4**). There is also similarity in the infrared uranyl stretch, observed at 838 cm^{-1} for schoepite and 834 cm^{-1} for Na-metaschoepite (**Figure 3.4**). There is a substantial difference in the hydrogen-bonding network within the Na-metaschoepite structure relative to the schoepite network, however, and this is visible in the IR spectrum as a broad peak around 930 cm^{-1}. This is mainly due to the extra OH^- in the network at O(11) giving the sheet an overall charge of -1, thus balancing the charge of the sodium and increasing hydrogen bonding between the UO network and the interlayer water molecules. This can be seen in the shorter distance between the layers (7.23 Å relative to schoepite at 7.40 Å) although the average uranyl bond length is almost identical: 1.776(8) Å compared to 1.779(6) Å in schoepite.

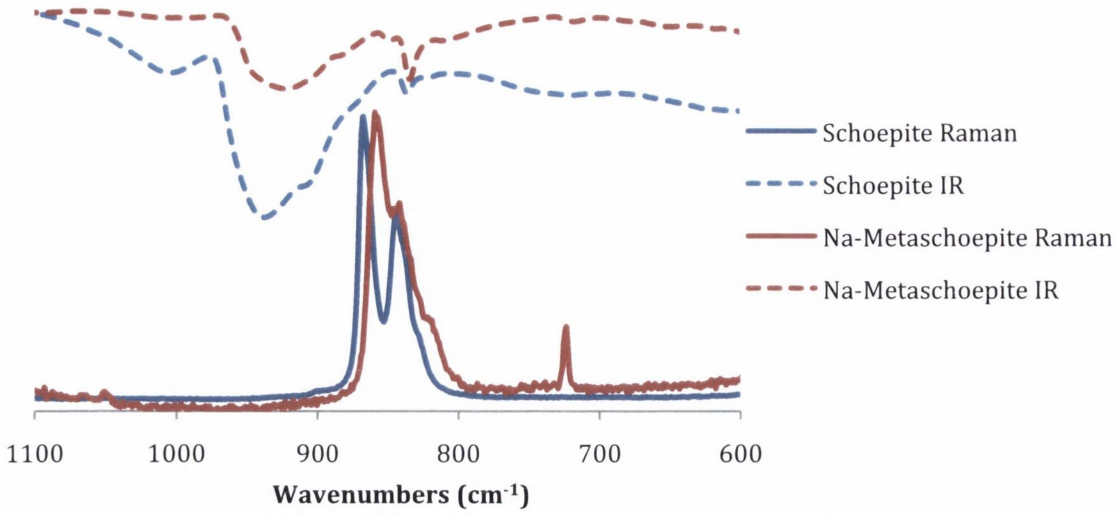

Figure 3.4: Infrared and Raman spectrum of uranyl region for schoepite and Na-metaschoepite.

The two other samples in the series were compreignacite, $K_2[(UO_2)_6O_4(OH)_6]\cdot 7H_2O$ (**Figure 3.5**), and becquerelite, $Ca[(UO_2)_6O_4(OH)_6]\cdot 8H_2O$ (**Figure 3.6**). These also contain the pentagonal bipyramids observed in the schoepite structure, connected *via* η^3-oxo ligands. These layers are again connected with hydrogen-bonded water molecules as well as cation–cation interactions with interstitial potassium and calcium ions, respectively.

For becquerelite, the bridging calcium cations provide a higher degree of connectivity between the layers than for schoepite, with the hydrated calcium ions connecting with four uranyl oxygens giving Ca–O distances of 2.444(8), 2.448(8) and 3.000(9) Å to uranyl oxygens from one sheet and a distance of 2.368(7) Å to the fourth uranyl oxygen, sitting in the opposite layer, and an interlayer distance that varies between 6.34 and 8.69 Å [**Figure 3.6(right)**]. This connectivity is observed to a greater degree in the case of compreignacite, [**Figure 3.5(right)**], where the cation–cation interactions between uranyl and the potassium ions yield rigid layers that approach a 3D framework with square "pores" among the interstitial hydrated potassium ions and a shorter interlayer distance (between 6.12 and 8.14 Å, compared to between 6.34 and 8.69 Å).

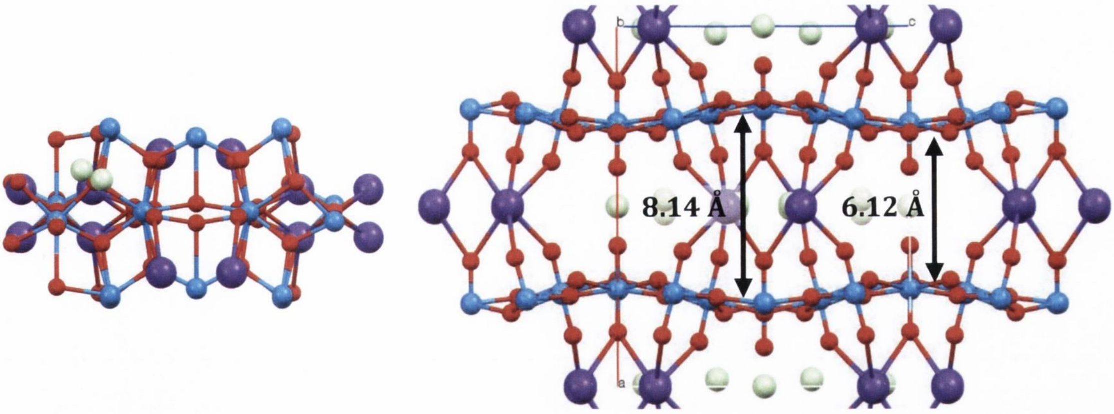

Figure 3.5: View along a axis (left) of the unit cell of compreignacite, $K_2[(UO_2)_6O_4(OH)_6]\cdot 7H_2O$,[28] showing the pentagonal bipyramids connected *via* η^3-oxo ligands and the view along the b axis (right) of the packing structure showing the framework arising from the cation-cation interactions between uranyl and the potassium ions. (Key: Blue = U; Red = O; Violet = K; Beige = Water)

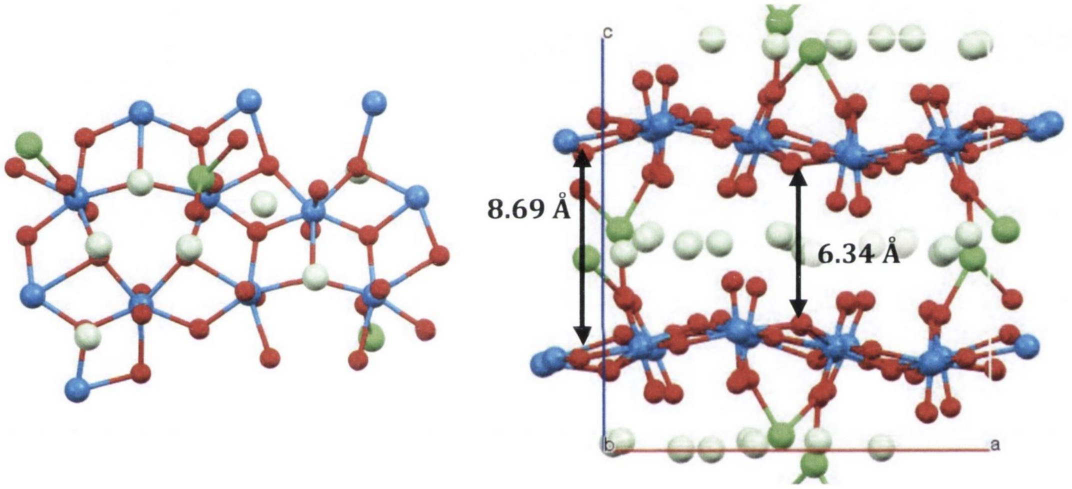

Figure 3.6: View along c axis (left) of the unit cell of becquerelite, $Ca[(UO_2)_6O_4(OH)_6]\cdot 8H_2O$,[30] showing the pentagonal bipyramids connected *via* η^3-oxo ligands and the view along the b axis of the packing structure showing the sheets connected *via* hydrated calcium cations. (Key: Blue = U; Red = O; Green = Ca; Beige = Water)

Comparing vibrational spectra of compreignacite and becquerelite (**Figure 3.7**) shows two distinct uranyl Raman stretches for compreignacite at 842 and 818 cm^{-1} and one broad stretch for becquerelite at 827 cm^{-1}. This is consistent with literature values of natural samples (848 and 824 cm^{-1} for compreignacite[31] and 838 cm^{-1} for becquerelite[32]), and also with the crystal structures: there are four different uranyl bonds in the compreignacite structure and 12 in becquerelite, leading to a broader, less defined peak.

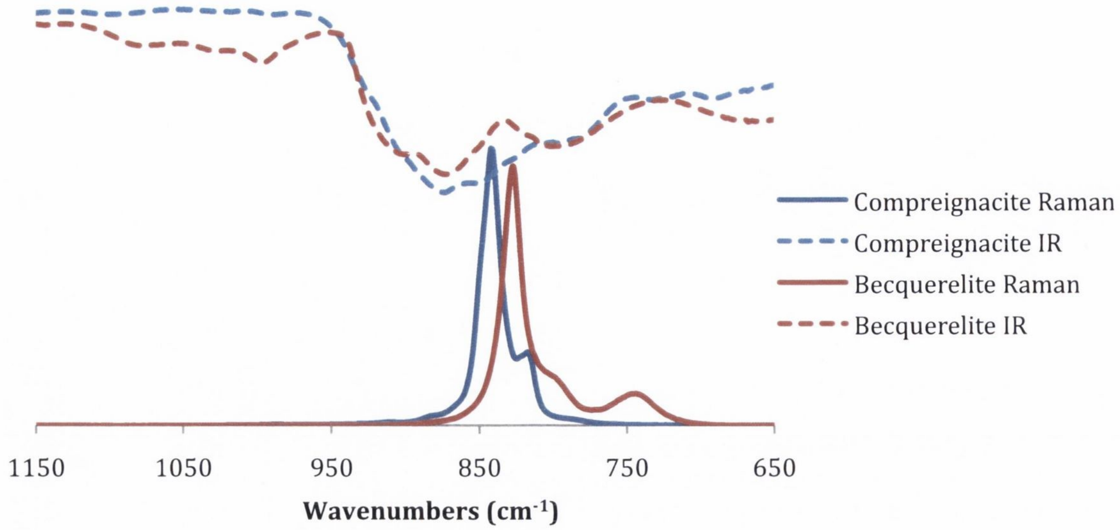

Figure 3.7: Infrared and Raman spectra of compreignacite and becquerelite.

Using Bartlett and Cooney's formula for calculating $d_{U=O}$ from the infrared spectrum (**Equation 3.1**),[33] the average predicted bond lengths are very close to the average $U{=}O_{yl}$ bond length from diffraction data (IR stretches at 880 and 857 cm^{-1} yield an average bond length of 1.808 *vs.* 1.806 Å for compreignacite and 905 and 877 cm^{-1} yield 1.791 *vs.* 1.794 Å for becquerelite).

$$d_{U=O} = 9141(\nu_3)^{-2/3} + 80.4 \tag{3.1}$$

A similar relationship exists for Raman data, (**Equation 3.2**).[33] Using this equation, it was found that the average predicted bond lengths differ slightly from the average $U{=}O_{yl}$ bond length from diffraction data (Raman stretches yield an average bond length of 1.781 *vs.* 1.806 Å for compreignacite and 1.799 *vs.* 1.794 Å for becquerelite).

$$d_{U=O} = 10650(\nu_1)^{-2/3} + 57.5 \tag{3.2}$$

3.2.2. Optical Properties

There have been increasing numbers of photochemical investigations into uranyl minerals in recent years, with the aim of finding a technique capable of *in situ* identification of minerals.[16] There are many minerals, however, that are non-emissive, e.g. studtite. This was attributed to vibrational quenching *via* the coordinated water molecules. In cases where the mineral is non-emissive, diffuse reflectance can be a viable alternative to analyse optical or electronic properties of the solid.

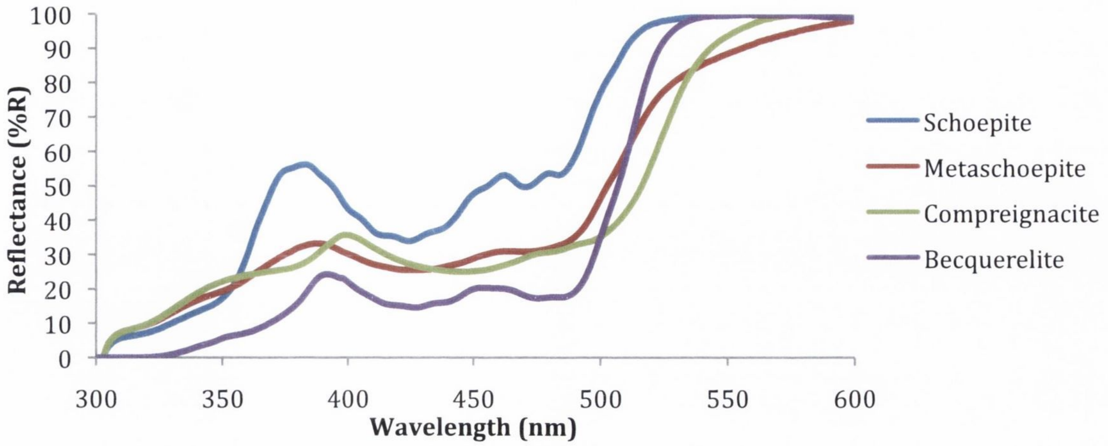

Figure 3.8: The diffuse reflectance spectra of the four uranyl oxyhydroxide minerals in the study in comparison to studtite.

Comparing the diffuse reflectance spectra of these compounds (**Figure 3.8**) shows the uranyl Ligand to Metal Charge Transfer (LMCT) with vibronic coupling between 450 and 500 nm and the LMCT bands from the equatorial oxygen atoms observed in each spectrum between 400 and 450 nm.

A property that can be estimated from the diffuse reflectance spectra, however, is the band-gap of the mineral. It is this calculation that stimulated the investigation into the electronic properties of studtite and metastudtite (**Chapter 2**) and the band-gaps of the oxyhydroxide minerals are listed in **Table 3.1**. This shows a distinct similarity between schoepite and Na-metaschoepite (despite the presence of the sodium cation) when compared to studtite and metastudtite. The energy of the band-gap is also related to the HOMO/LUMO gap in a solid; therefore, the electrochemical investigations of these minerals would be a valid method of verifying the relative band-gap energies of these minerals.

Table 3.1: The calculated band-gap values of the uranyl oxyhydroxide minerals.

Mineral	Band-Gap (eV)	Reported Band-Gap (eV)	Ref
Studtite	3.45	2.29	34
Schoepite	2.68	2.3	35
Na-metaschoepite	2.66	2.3[a]	35
Becquerelite	2.56	2.39[b]	36
Compreignacite	2.53	2.33[b]	37

[a] Calculated value for metaschoepite, $[(UO_2)_8O_2(OH)_{12}]\cdot10H_2O$, rather than Na-metaschoepite.

[b] The only reported calculated band-gap for these minerals are for the Np-incorporated compounds,[38] these values are derived from emission data.

In **Chapter 2**, it was found that changing the $U{=}O_{yl}$ distance had the greatest effect on the calculated band-gap, and that the difference in the band-gap between studtite and metastudtite was due to the longer uranyl bond in metastudtite. This will be investigated further in this chapter.

3.2.3. Electrochemical Activity

3.2.3.1. Schoepite, $[(UO_2)_8O_2(OH)_{12}]\cdot12H_2O$

In the initial scans of schoepite, there is a redox couple that decreases rapidly and disappears by Scan 30 (the reduction peak is observed at -0.343 V with a linked oxidation peak at 0.141 V, highlighted by the grey arrow in **Figure 3.9**). This process is a result of a delay in the equilibration of the FDTO electrode and the resulting overpotential on the surface.[20] This was observed in early scans of some samples and was removed from the spectra for clarity.

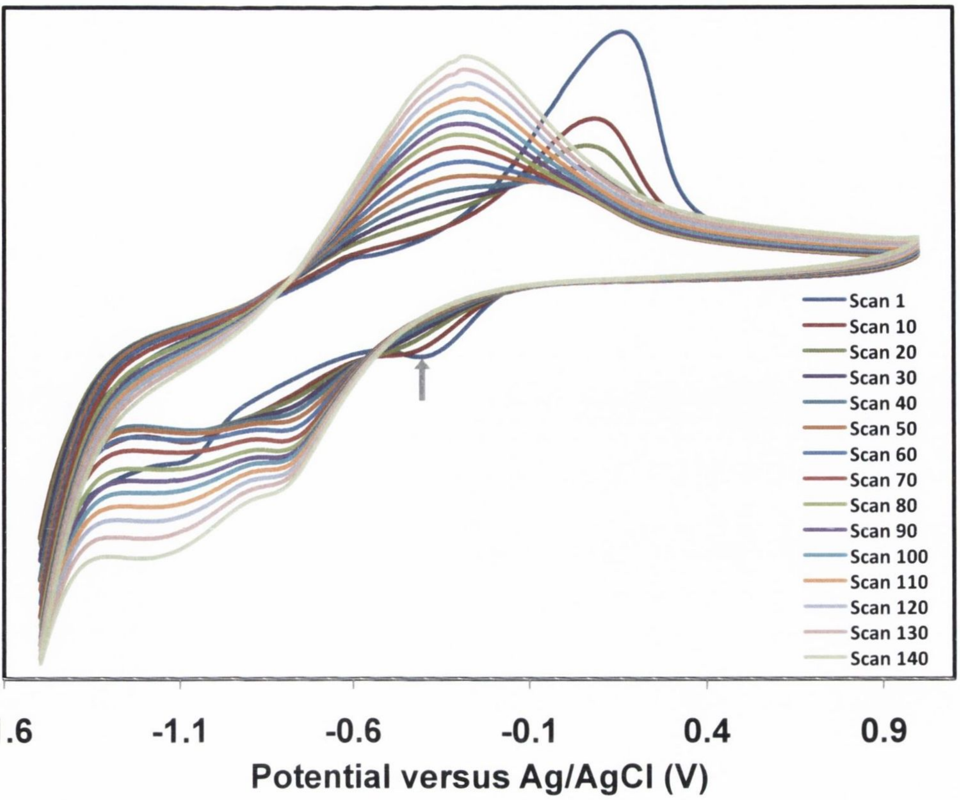

Figure 3.9: One hour cyclic voltammogram of schoepite, 0.2 M $LiClO_4$ as the electrolyte.

A second reduction peak becomes evident at -0.788 V with a coupled oxidative process at -0.335 V (**Figure 3.9**). A further reduction peak becomes evident at -1.148 V with a coupled oxidation process that overlaps with the previous oxidative process to give a broad peak centred at -0.276 V. As in the case of studtite, the primary reduction peak (at -0.788 V) is assigned to the U(VI)/(V) reduction couple, and the secondary peak that occurs at -1.148 V is assigned to the U(V)/(IV) couple. The intensity of the voltammetric waves increases with increasing number of scans over a period of several hours. As the film is reduced, it is expected to incorporate electrolyte ions to maintain charge stability. The gradual increase of the peaks in the CV is attributable to improved penetration of ions through the film – this is an example of the break-in phenomenon, associated with the growth of peaks over time as electrolyte ions permeate the sample.

It is interesting to note that – contrary to studtite – the morphology of the film is not changed with time: there does not appear to be an obvious alteration to the physical structure of schoepite when examined using SEM at multiple points on the surface (**Figure 3.10**). The Raman spectrum, however, shows a change in the molecular structure as the uranyl stretches at 845 and 867 cm^{-1} appear to move towards lower wavenumbers (845 to 833 to 814 cm^{-1}), implying the formation of a U(V) species (**Figure 3.11**).[39] Using **Equation 3.2**,[33] 814 cm^{-1} can be equated to a $d_{U=O}$ of 1.797 Å. This is longer than the average schoepite $d_{U=O}$ of 1.779(2) Å but shorter than reported experimental[40] and theoretical[39,41] values for $[UO_2]^+$ complexes, typically between 1.810 and 1.934 Å.

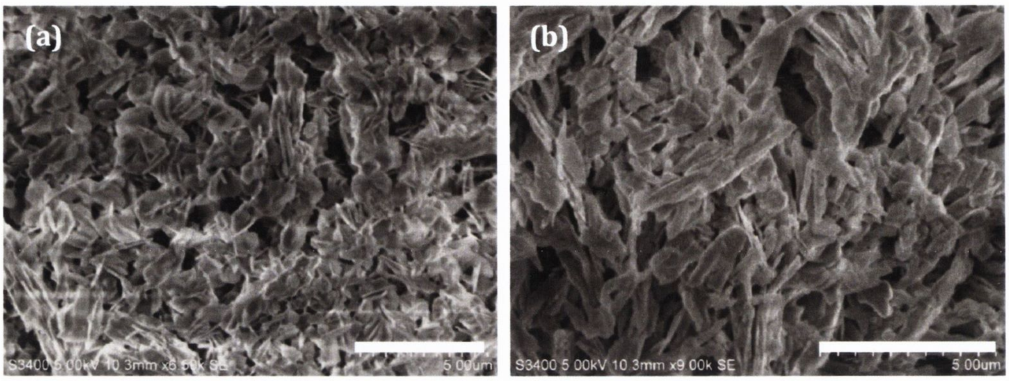

Figure 3.10: SEM micrographs of schoepite before (a) and after (b) cycling in 0.2 M $LiClO_4$. Scale bar is 5µm.

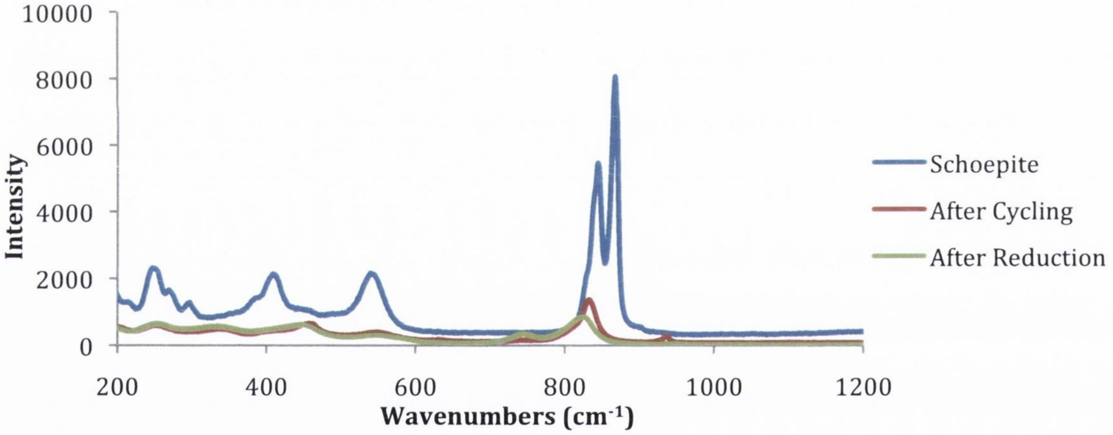

Figure 3.11: Raman spectra of schoepite before and after electrochemical treatment.

This $[UO_2]^+$ species is likely to disproportionate to U(IV) and U(VI), which in the case of the chronoamperometric treatment of schoepite at -1.2 V for one hour would provide further U(VI) to be reduced and to yield over time a U(IV) product. From Raman spectroscopy, the cycling product appears to be similar to the reduced compound formed by the chronoamperometric treatment. EDX spectroscopy was used to find the elemental composition of the reduced compounds and found that they were composed of only uranium and oxygen. The oxygen content was found to be too high for UO_2 (11.85% O), or even U_3O_8 (15.20% O) or UO_3 (16.78% O), but given that the recorded oxygen composition was higher than that of unreacted schoepite, this can most likely be attributed to oxygen from water or from the FDTO electrode. With this in mind it is likely that the reduced products are a combination of U(IV) in the form of UO_2 – a very poor Raman scatterer[23] – and a small amount of uranyl(VI) and uranyl(V) oxyhydroxides, thereby providing a low intensity $[UO_2]^{2+}/[UO_2]^{+}$ stretch in the Raman.

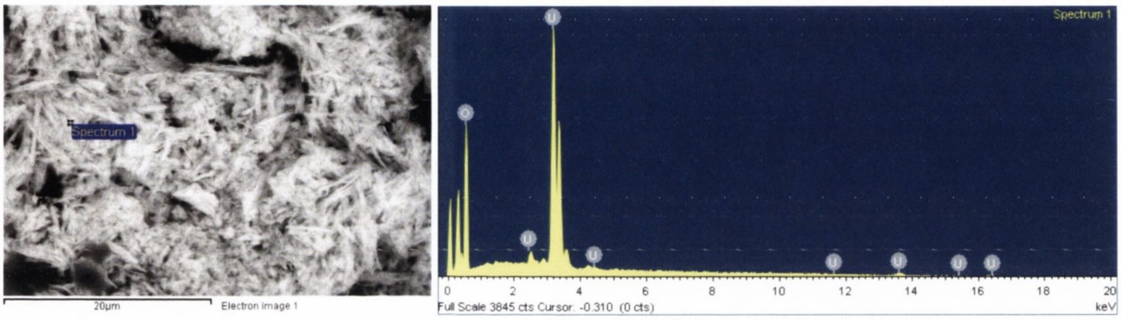

Figure 3.12: SEM micrograph and EDX spectrum of sample of schoepite after one-hour cycle in 0.2 M $LiClO_4$. Three spectra were taken at different points on the surface. For schoepite, only uranium and oxygen were detected.

A small ClO_4^- stretch (933 cm^{-1}) is visible in the Raman (**Figure 3.11**), indicative of the presence of perchlorate anions in the bulk of the sample. Chlorine was not detected by EDX analysis (**Figure 3.12**), implying that the perchlorate is not surface bound. Lithium was not detected on the surface, however, given that lithium is too light a nucleus to be detected by EDX,[42] this does not deny the possibility of cation transport. In order to determine the mode of ion transport in the film, diffusion experiments were undertaken. The diffusion coefficient, D_{CT}, was calculated using the Randles-Sevcik equation (**Equation 3.3**):

$$I_P = (2.69 \times 10^{-5}) \cdot n^{3/2} \cdot A \cdot D_{CT}^{1/2} \cdot C \cdot v^{1/2}$$

$$\Rightarrow D_{CT} = \left[\frac{1}{2.69 \times 10^{-5} \cdot n^{3/2} \cdot A \cdot C \cdot v^{1/2}} \right]^2 I_P \tag{3.3}$$

where I_P is the current of the peak, n is the number of electrons transferred, A is the area of the electrode (in cm^2), C is the concentration of the analyte at the surface (in mol cm^{-3}) and v is the scan rate (V s^{-1}). The sample was examined at scan rates between 10 and 500 mV s^{-1} and a plot of I_P *vs.* $v^{1/2}$ was generated to yield D_{CT} (**Figure 3.13**). The graph does not go through the origin but this is to be expected as the intercept is a correction factor for background current.[22]

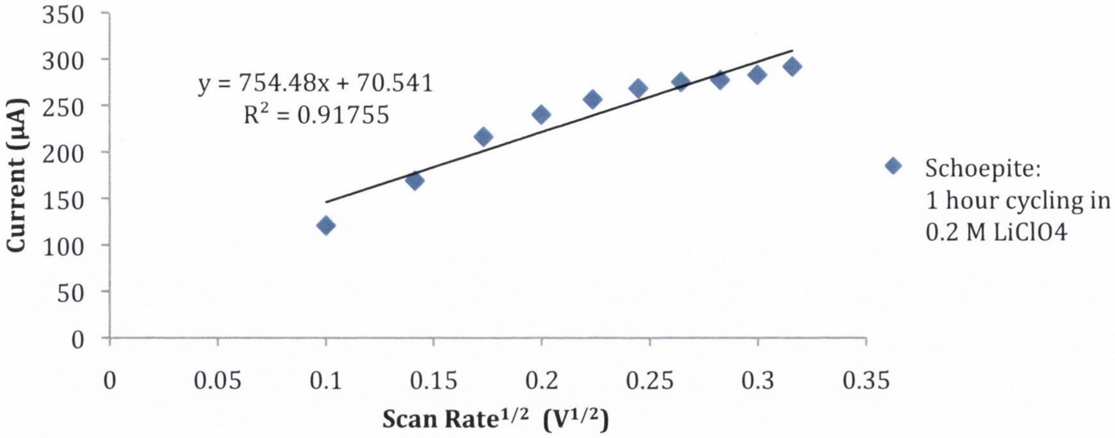

Figure 3.13: The graph from which the diffusion constant, D_{CT}, of schoepite can be calculated.

The D_{ct} of the reduction peak was found to be 3.842×10^{-15} cm^2 s^{-1} and the oxidation peak to be 8.852×10^{-14} cm^2 s^{-1}, implying that it is the oxidation step that is the rate-determining step. This is consistent with anion transport, which would be required for charge balance during a slower oxidative process, and explains the presence of perchlorate ions in the sample.

3.2.3.2. Oxyhydroxide minerals: Na-Metaschoepite, Compreignacite and Becquerelite

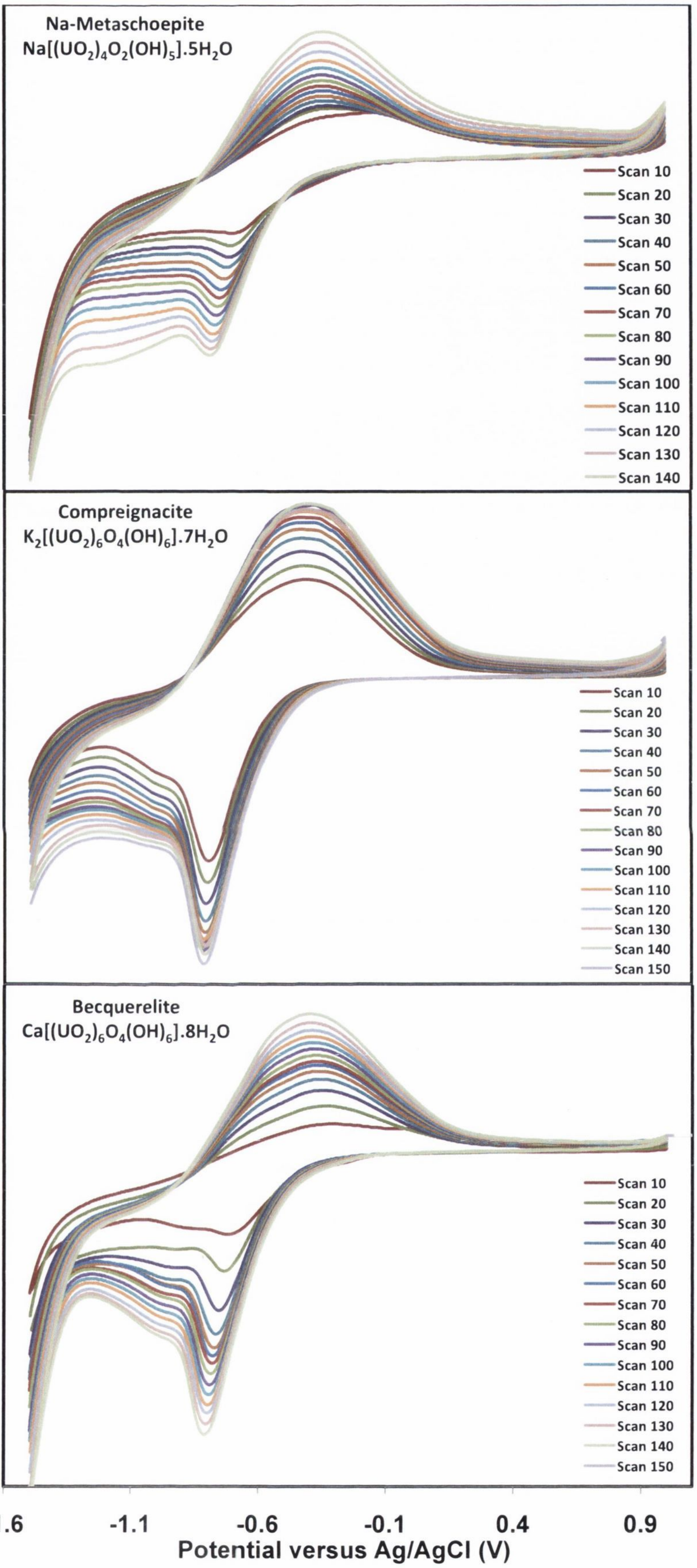

Figure 3.14: One hour cyclic voltammograms of Na-Metaschoepite, Compreignacite and Becquerelite in 0.2 M $LiClO_4$.

For Na-metaschoepite [**Figure 3.14(top)**] the primary reduction peak is observed at -0.755 V with a linked oxidation peak at -0.392 V and is assigned to the U(VI)/(V) couple. A second reduction peak at -1.145 V becomes evident over time with a coupled oxidation process that overlaps with the previous oxidative process. This is assigned to the U(V)/(IV) reduction couple. As in the case of schoepite (and studtite), the intensity of the voltammetric waves increases with increasing number of scans over a period of several hours with improved penetration of ions through the film.

In the early scans of compreignacite [**Figure 3.14(middle)**] there are two visible reduction processes with one broad oxidation peak at -0.416 V. The two reduction processes grow at different rates: after one hour, the primary reduction process peak is found to be a sharp peak at -0.814 V while the secondary reduction peak grows more slowly to become a diffuse peak centred at -0.997 V. The major reduction peak is assigned to the U(VI)/U(V) couple, and the minor diffuse peak is assigned to the U(V)/U(IV) couple. The weak U(V)/(IV) peak implies a lower concentration of U(V) species, perhaps from the dissociation of the U(V) species to U(IV) and U(VI).

It is a similar story in the voltammogram for becquerelite: the major and minor couples grow at different rates to yield a sharp and a diffuse peak [**Figure 3.14(bottom)**]. The major redox couple grows to yield a reduction potential of -0.785 V and an oxidation potential of -0.413 V after one hour. This couple has been assigned to the U(VI)/U(V) couple. The minor reduction peak grows more slowly to yield a diffuse peak centred at -0.983 V, which has been assigned to the U(V)/U(IV) couple.

Table 3.2: Summary of the electrochemical features of the uranyl oxyhydroxide minerals (Figure 3.14).

Mineral	Primary Reduction Peak (V)	Assignment	Secondary Reduction Peak (V)	Assignment
Na-metaschoepite	-0.755	U(VI)/ (V)	-1.145	U(V)/ (IV)
Compreignacite	-0.814	U(VI)/ (V)	-0.997	U(V)/ (IV)
Becquerelite	-0.785	U(VI)/ (V)	-0.983	U(V)/ (IV)

As with schoepite, there is no morphological alteration visible by SEM in Na-metaschoepite or compreignacite after cycling between +1 and -1.5 V for one hour [**Figure 3.15(a–d)**].

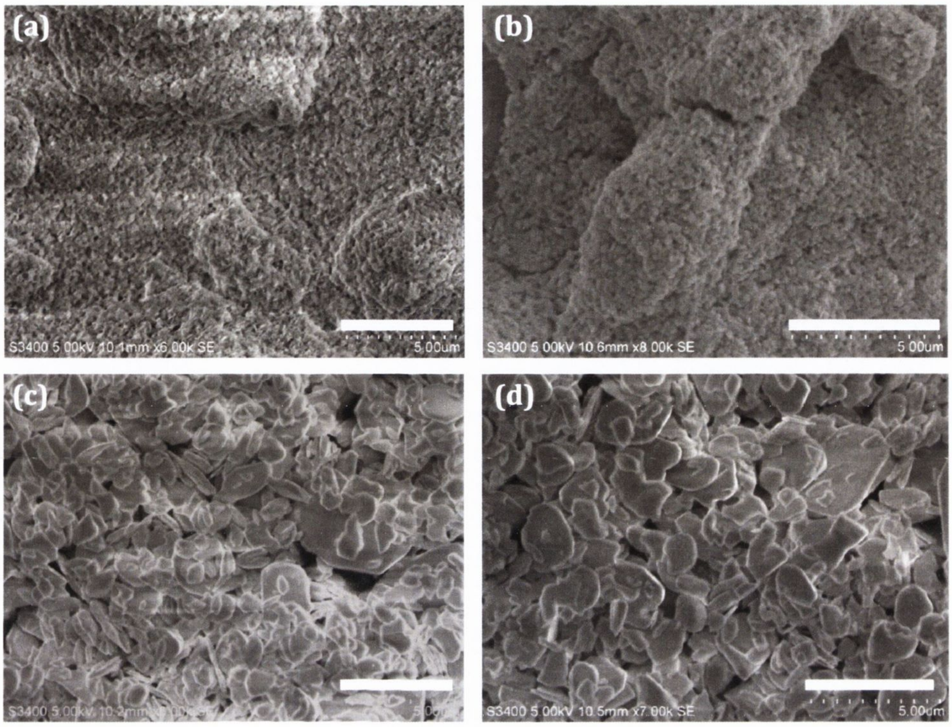

Figure 3.15: SEM micrographs of Na-metaschoepite before (a) and after (b) and compreignacite before (c) and after (d) one hour cycling (scale bar is 5 μm).

Raman spectroscopy shows that Na-metaschoepite appears to have decayed in a manner similar to schoepite: the uranyl stretch shifts from 840 to 833 to 824 cm^{-1} for Na-metaschoepite (**Figure 3.16**) and 845 to 833 to 814 cm^{-1} for schoepite (**Figure 3.11**). However, the compreignacite Raman features are retained after cycling and electrolysis at -1.2 V for one-hour periods (**Figure 3.17**) indicating that the compreignacite structure is partially retained – the reduced intensity is consistent with a reduced concentration on the surface, implying that the majority of the solid on the surface is not the U(VI) species but rather the fully reduced U(IV); U(IV) in the form of UO_2 is a poor Raman scatterer and will not be visible in the electrolysed Raman spectra. In the case of both Na-metaschoepite and compreignacite there is evidence of a perchlorate stretch observed in the Raman. A stretch at 930 cm^{-1} is visible in Na-Metaschoepite after electrochemical treatment and in the electrolysis product of compreignacite [**Figure 3.17(inset)**].

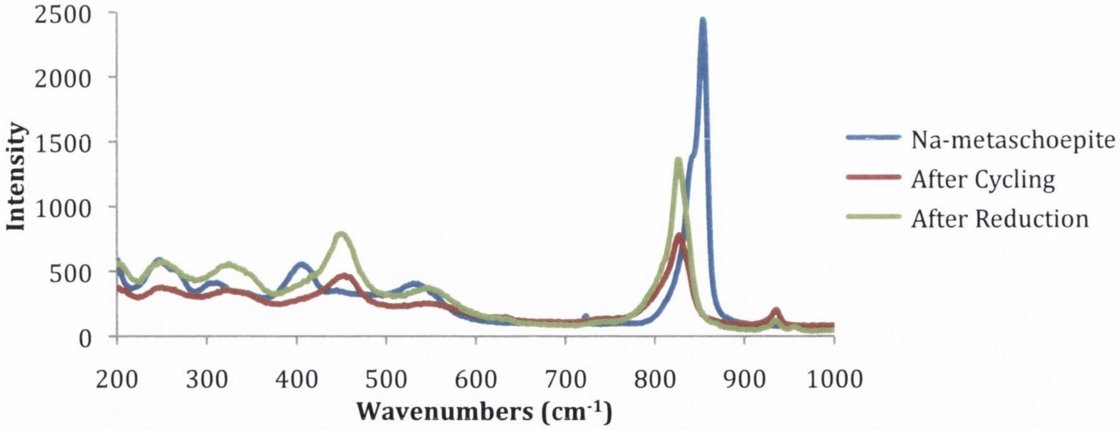

Figure 3.16: Raman of Na-metaschoepite before and after electrochemical analysis.

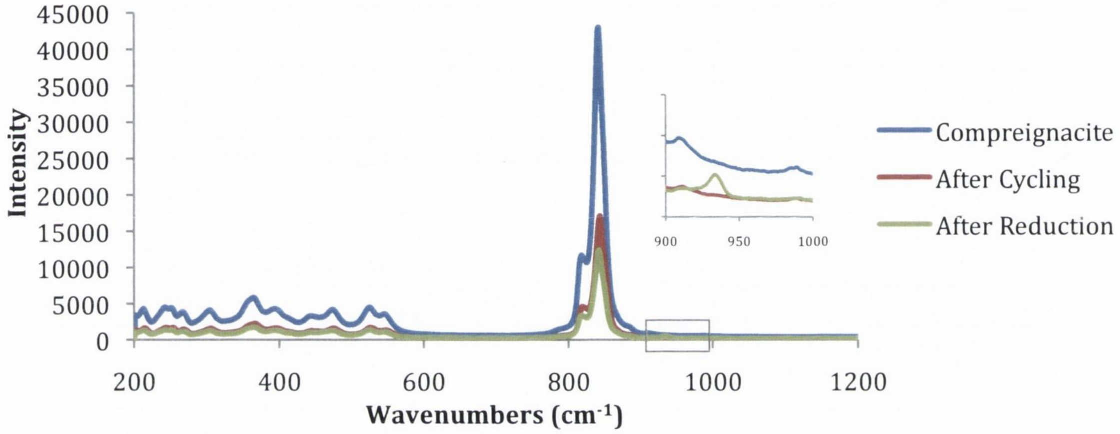

Figure 3.17: Raman spectra of compreignacite before and after electrochemical treatment. Inset shows region of spectrum characteristic of fundamental frequencies of the perchlorate anion.

EDX analysis was performed to confirm the presence of perchlorate within the reduced minerals and, in each case, chlorine is visible in some of the EDX analyses of points on the surface after cycling for one hour (**Figures 3.18** and **3.19**). The combination of chlorine in the EDX and perchlorate stretches in the Raman (930 cm^{-1}) implies permeation of the perchlorate anion into the interlayer gaps. Interestingly, there is a lack of potassium in the EDX results for compreignacite. This is a surface technique that was repeated at multiple points on the surface to get a better statistical representation of the solid, so it is possible that the reduced product is composed of uranium and oxygen (most likely UO_2) but there are points of compreignacite on the solid that did not decompose (implying reversible redox processes) and were picked up by Raman spectroscopy, a more diffuse surface technique. Once again, as lithium cannot be detected by EDX,[42] it is not possible to say if Li^+

ions are present on the reduced sample to balance the charge, although it is likely given the lack of K^+. The retention of sodium in the Na-metaschoepite sample is consistent with a mixture of uranyl(VI) and uranyl(V) oxides and the retention of Na^+ cations for charge balance. These $[UO_2]^+$ species would account for the broad Raman stretch at 814 cm^{-1}, although again this is too high a frequency for a fully U(V) species and is most likely a mix of U(V) and U(VI) products.

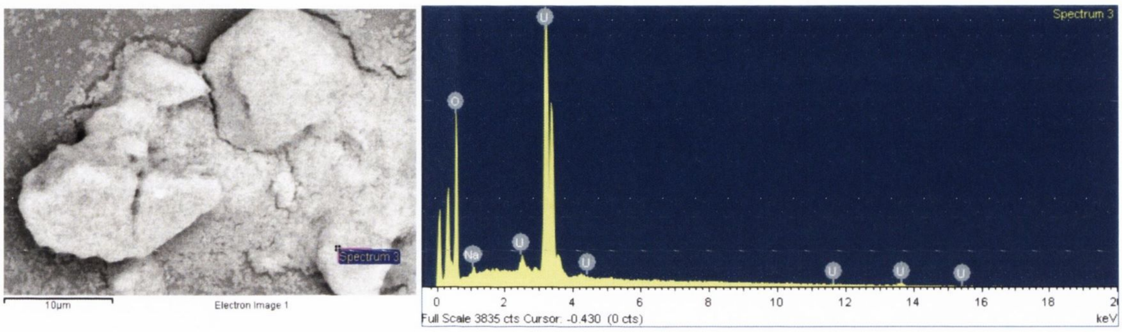

Figure 3.18: SEM micrograph and EDX spectrum of sample of Na-Metaschoepite after one hour CV in 0.2 M $LiClO_4$. Three spectra were taken at different points on the surface. For Na-metaschoepite, U, O, Na and traces of Cl were detected.

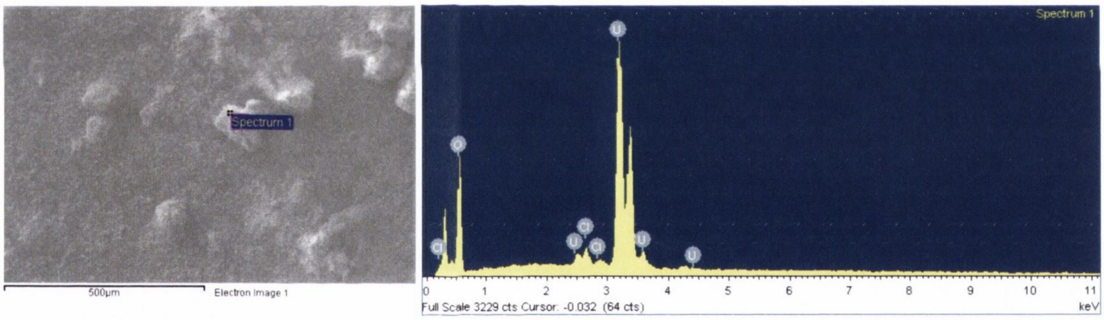

Figure 3.19: SEM micrograph and EDX spectrum of sample of compreignacite one hour CV in 0.2 M $LiClO_4$. Three spectra were taken at different points on the sample. For compreignacite, U, O and Cl were detected.

Inspection of becquerelite also shows no change in morphology after one hour [**Figure 3.20(a–b)**], but after twelve hours cycling there is a visible alteration of the sample from 2D flakes to pit-like structures on the surface [**Figure 3.20(c)**]. There are two possible reasons for these pits: the first is that the morphological change in the becquerelite sample is due to hydrogen bubbles forming at the FDTO surface. A recent study of the electrodeposition of uranyl hydroxide nanowires in aqueous solutions demonstrated that under high current density the electrolysis of water created hydrogen bubbles that acted as dynamic templates for nanotube formation.[43] The second hypothesis is etch pit formation within becquerelite.[44] Burns *et al.* found that etch pit formation in becquerelite is pH dependent,[44] and that the formation of etch pits encourages dissolution *via* a stepwave dissolution mechanism. The stepwave dissolution model was described by Lasaga and Luttge as being similar to a rock thrown into a still pond.[45] The etch pit acts as a nucleation site that becomes a constant source of stepwaves, meaning that the overall dissolution stems outwards from the etch pit in waves – much like those from a location where a rock has hit the water surface. It is possible that the morphological change in becquerelite is in fact a combination of these: the electrolysis of water at the FDTO surface raises the pH at the electrode *via* the formation of hydroxyl ions (**Equation 3.4**) and thus encourages the formation of etch pits on the surface.

$$2H_2O + 2e^- \longrightarrow 2OH^- + H_2\uparrow \qquad \textbf{3.4}$$

This mechanism would account for the morphology of the sample that was electrolysed at -1.2 V for 12 hours [**Figure 3.20(d)**]. The dissolution of becquerelite leaves only the reduced product: a black insoluble U(IV) solid, most likely UO_2, on the surface aligned along the electrode – this is a compound which does not scatter under Raman light (**Figure 3.21**). The Raman features of becquerelite are retained after one and 12 hours cycling, suggestive of a quasi-reversible redox process, but are of lower intensity, implying that the intermediate U(V) species must disproportionate to leave U(IV) or U(VI) deposits on the surface – as implied by the voltammogram and as in the case of compreignacite.

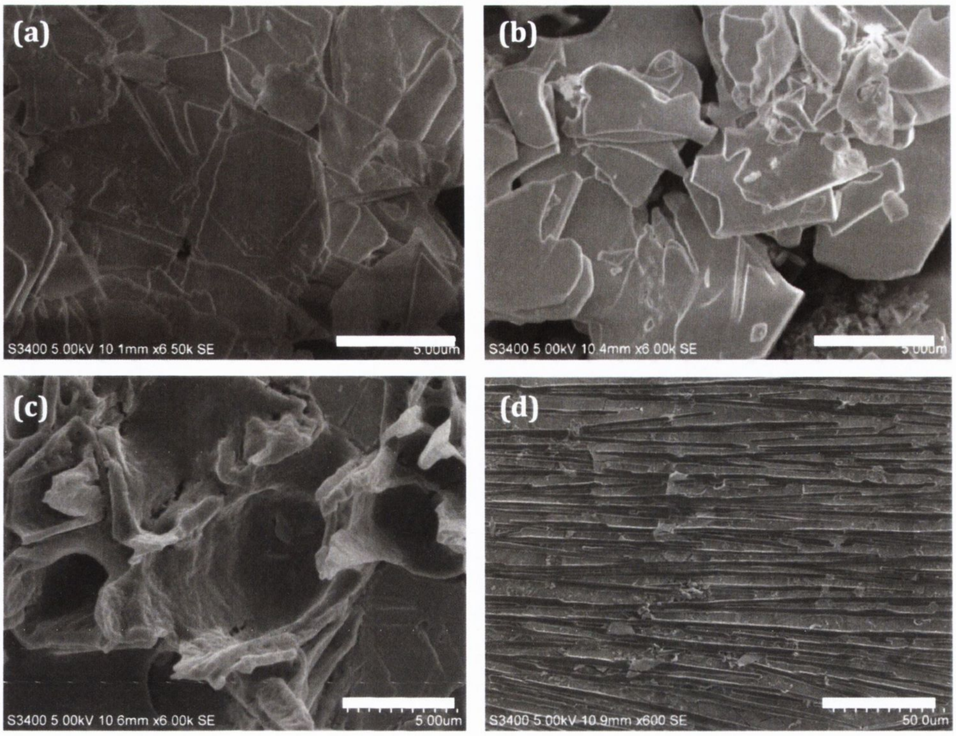

Figure 3.20: SEM image of becquerelite on FDTO (a) and after cycling for (b) one hour and (c) 12 hours (Scale bar is 5 μm). A wide view micrograph of the 12 hour electrolysis sample (d) shows elongation and rearrangement along the surface of electrode (Scale bar is 50 μm).

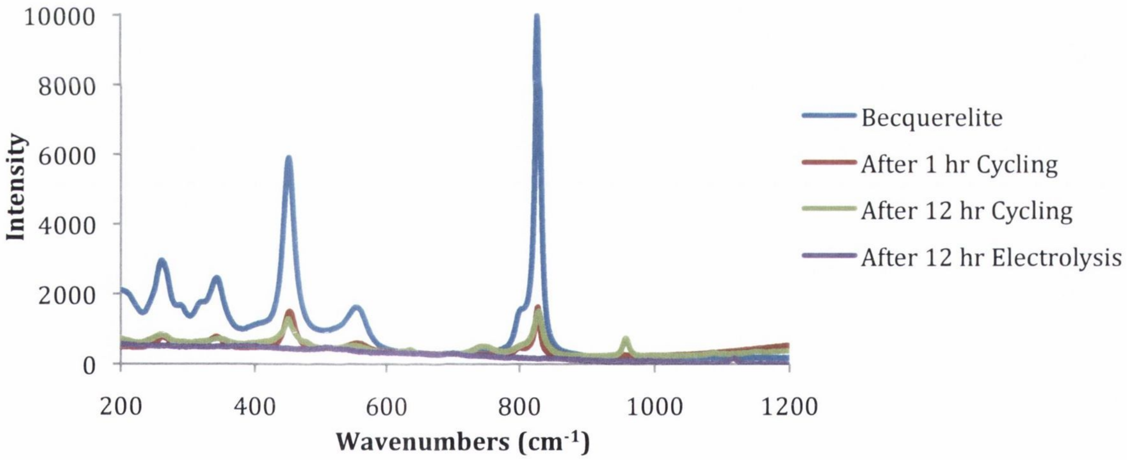

Figure 3.21: Raman spectra of becquerelite before and after electrochemical treatment.

The Raman spectra of electroanalysed becquerelite samples show the growth of a peak at 948 cm^{-1} with longer time intervals, consistent with the incorporation of perchlorate anions into the structure (**Figure 3.21**). Chlorine was found in the EDX spectra after one hour cycling (**Figure 3.22**). This corresponds to the penetration of electrolyte anions into the sample, responsible for the increased current in the voltammogram [**Figure 3.14(bottom)**]. For measuring EDX, the sample is placed on a carbon stub, which could account for the presence of carbon in occasional spectra.

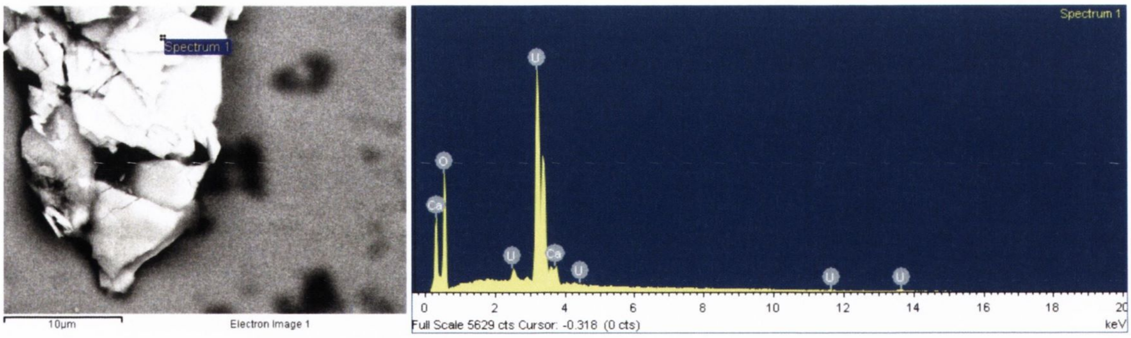

Figure 3.22: SEM micrograph and EDX spectrum of sample of becquerelite after one hour CV in 0.2 M $LiClO_4$. Three spectra were taken at different points on the sample. For becquerelite, U, O, Ca, and traces of Cl and C were detected.

In all four uranyl oxyhydroxide minerals there was indication from Raman and EDX spectroscopy of perchlorate incorporation into the mineral networks. Without evidence for lithium on the samples, diffusion studies were undertaken to determine the rate determining step, i.e. the oxidation or the reduction step, to confirm if it is anion transport and not cation transport that occurs. The diffusion coefficient, D_{CT}, was calculated using the Randles-Sevcik equation (**Equation 3.3**) by examining the sample at scan rates between 10 and 500 mV s^{-1} and plotting the results to generate D_{CT} (**Table 3.3**).

Table 3.3: Reductive and oxidative diffusion coefficients for the oxyhydroxide minerals.

Mineral	**Reductive Diffusion Coefficient ($cm^2\ s^{-1}$)**	**Oxidative Diffusion Coefficient ($cm^2\ s^{-1}$)**
	U(VI)/(V) in 0.2 M $LiClO_4$	**U(VI)/(V) in 0.2 M $LiClO_4$**
Schoepite $[(UO_2)_8O_2(OH)_{12}]\cdot 12H_2O$	3.842×10^{-15}	8.852×10^{-14}
Na-metaschoepite $Na[(UO_2)_4O_2(OH)_5]\cdot 5(H_2O)$	3.070×10^{-14}	8.872×10^{-14}
Compreignacite $K_2[(UO_2)_6O_4(OH)_6]\cdot 7H_2O$	2.096×10^{-14}	6.419×10^{-14}
Becquerelite $Ca[(UO_2)_6O_4(OH)_6]\cdot 8H_2O$	3.573×10^{-15}	3.573×10^{-15}
Becquerelite After 12 hours cycling	6.917×10^{-14}	3.293×10^{-13}

In each case the oxidative D_{CT} was larger than the D_{CT} for the reductive step, meaning that the oxidation process is the rate-determining step. In the case of becquerelite this was not readily apparent until examination of the 12-hour CV sample, where the reductive D_{CT} was found to be 6.917 x 10^{-14} cm^2 s^{-1} and the oxidation peak to be 3.293 x 10^{-13} cm^2 s^{-1}. The oxidation process being the rate-determining step is consistent with anion transport, which would be required for charge balance during a slower oxidative process.

Table 3.4: Reduction potentials of studtite and the oxyhydroxide minerals.

Mineral	Distance between layers (Å)	Average U=O_{yl} Bond Length (Å)	U(VI)/ (V) Potential (V)	U(V)/ (IV) Potential (V)
Studtite $[(UO_2)(O_2)(H_2O)_2]\cdot 2H_2O$	6.72	1.769	-0.73	-1.10
Schoepite $[(UO_2)_8O_2(OH)_{12}]\cdot 12H_2O$	7.40	1.779	-0.788	-1.148
Na-Metaschoepite $Na[(UO_2)_4O_2(OH)_5]\cdot 5(H_2O)$	7.23	1.771	-0.755	-1.145
Compreignacite $K_2(UO_2)_6O_4(OH)_6\cdot 7H_2O$	7.44	1.806	-0.814	-0.997
Becquerelite $Ca[(UO_2)_6O_4(OH)_6]\cdot 8H_2O$	7.46	1.794	-0.785	-0.983

When examining the electrochemical and physical data (**Table 3.4**), it was found that there was a correlation between the uranyl bond length and the U(VI) reduction potential (**Figure 3.23**).

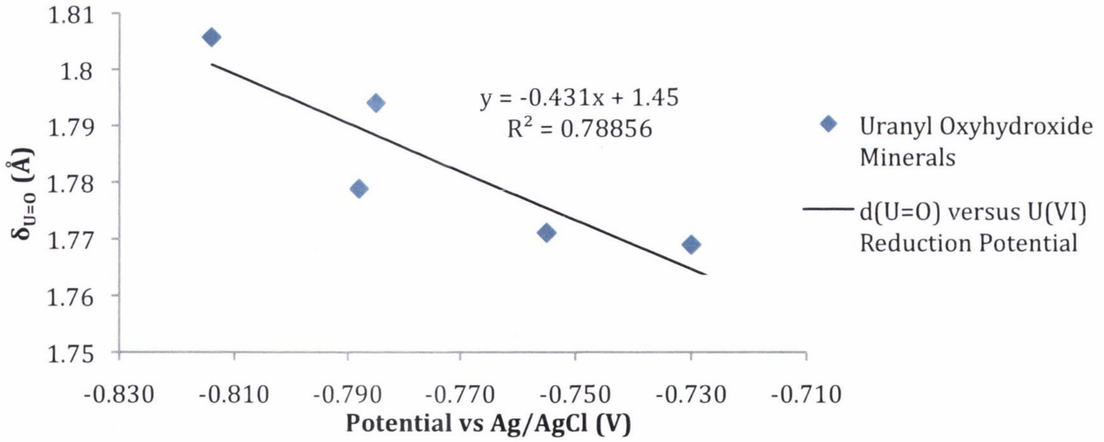

Figure 3.23: Graph of the average uranyl bond length in the uranyl oxyhydroxide minerals (including studtite) and the respective U(VI)/(V) reduction potential.

Although it is counter-intuitive for the longer bond length to be harder to reduce (one would assume that a longer bond is a weaker bond), it is logical to assume a similar situation to the effect of π donating ligands on the U=O_{yl} Raman stretching frequency:

when increased π donation competes with the U(*6d*) orbitals in the U=O_{yl} π bond, the U=O_{yl} bond is weakened and the frequency of the symmetric Raman stretch lowered.[46] In this way, it is likely that increased electron density at the metal has the combined effect of lengthening the U=O_{yl} bond and making the metal more difficult to reduce.

The relationship between bond length and reduction potential is not surprising as there is a relationship between bond length and the HOMO/LUMO gap, and the size of the HOMO/LUMO gap is a factor in the reduction potential of a compound. More trends will be investigated further in this chapter.

3.3. Uranyl Phosphate Minerals

Three natural uranyl phosphate minerals were obtained for analysis and comparison. Using a combination of PXRD and spectroscopic techniques they were identified as: meta-autunite, $Ca[(UO_2)_2(PO_4)_2]\cdot6\text{-}8H_2O$, metatorbernite, $Cu[(UO_2)_2(PO_4)_2]\cdot8H_2O$ and meta-uranocircite, $Ba[(UO_2)_2(PO_4)_2]\cdot6\text{-}8H_2O$.

3.3.1. Structural Comparison

The three uranyl phosphate minerals in the series were each members of the autunite group. The autunite group is known for a characteristic repeating unit of uranyl square bipyramids and phosphate (or arsenate) tetrahedra connected by shared vertices, linking each bipyramid to four tetrahedra, and each tetrahedron is in turn linked to four bipyramids.[1,47]

The first uranyl phosphate mineral acquired was sold as autunite (**Figure 3.24**). In the phosphate mineral autunite, $Ca[(UO_2)_2(PO_4)_2]\cdot11H_2O$, the interstitial calcium cations are bound to seven water molecules and occupying interstitial spaces with little connection to the uranyl phosphate network hydrogen-bonded to the neighbouring layer (**Figure 3.25**).[47a]

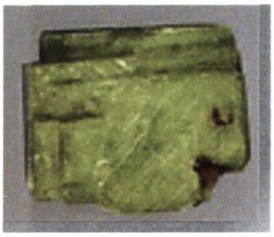

Figure 3.24: Photograph of natural meta-autunite sample.

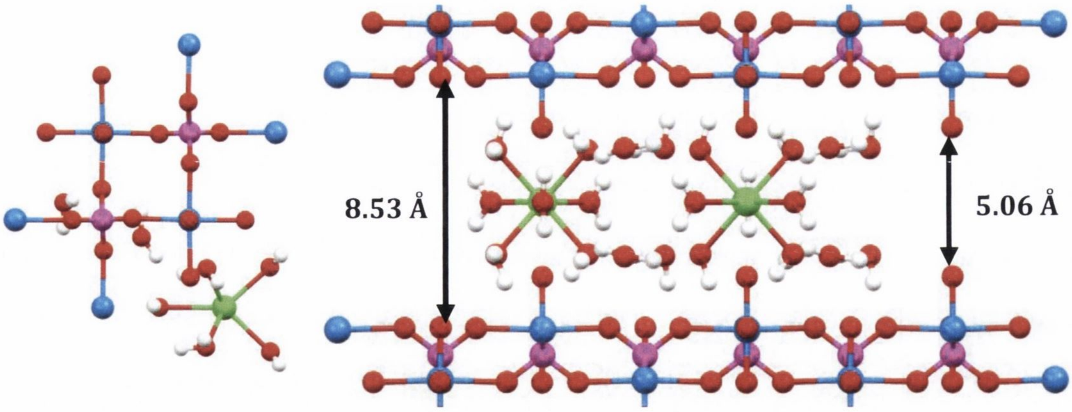

Figure 3.25: View along b axis (left) of the unit cell of autunite, $Ca[(UO_2)_2(PO_4)_2]\cdot 11H_2O$,[47a] and view along c axis (right), showing the packing structure connected *via* hydrated calcium cations. (Key: Blue = U; Red = O; Pink = P; Green = Ca; Beige = Water)

Using a combination of Raman spectroscopy and Powder X-Ray Diffraction (PXRD), the natural sample of autunite was determined to be a mixture of dehydrated forms of the mineral, and thus was assigned as meta-autunite, $Ca[(UO_2)_2(PO_4)_2]\cdot 6\text{-}8H_2O$.[47c,48] Most uranyl minerals are hydrated and as such both water and hydroxyls play a significant role in the structures. It is common for water to play a major role in the degree of polymerisation: water may bond to the interstitial cation or may be held in the structure through hydrogen bonding.[1] In this respect, meta-autunite is quite different from autunite.[48] The only reported structure for meta-autunite was from Makarov in 1960,[47c] but unfortunately this structure shows a high degree of disorder and $P(H_2O)_4$ instead of phosphate, PO_4^{3-}, anions. The Makarov structure shows a similar contraction upon dehydration to meta-autunite, showing an inter-layer distance of 6.61 instead of 8.53 Å, as seen upon the alteration from schoepite to metaschoepite,[26] however it is perhaps more accurate to take distances from the autunite structure. The structure of autunite has an average uranyl bond length of 1.789 Å.[47a] There is reported EXAFS data on meta-autunite that gives an average $d_{U=O}$ of 1.774(6) Å[49] which is consistent with the contraction upon dehydration noted previously.[26]

The second uranyl phosphate mineral analysed was a natural sample of torbernite (**Figure 3.26**). It was found to be a mixture of four allotropes of metatorbernite, $Cu[(UO_2)_2(PO_4)_2]\cdot 8H_2O$, using PXRD.[50]

Figure 3.26: Photograph of metatorbernite crystals growing on granite. Metatorbernite has the formula $Cu[(UO_2)_2(PO_4)_2]\cdot 8H_2O$, as defined by Locock *et al.*[50]

In the mineral metatorbernite the interstitial copper cations are in a Jahn-Teller distorted octahedral arrangement with four equatorial water molecules and connecting to two uranyl moieties with axial Cu–O distances of 2.685(8) and 2.391(7) Å. This yields to $U{=}O_{yl}$ distances of 1.781(3) and 1.758(4) Å. Apart from the bridging copper cation, the uranyl phosphate network is again connected *via* hydrogen-bonded water molecules to the neighbouring layer (**Figure 3.27**).[47a]

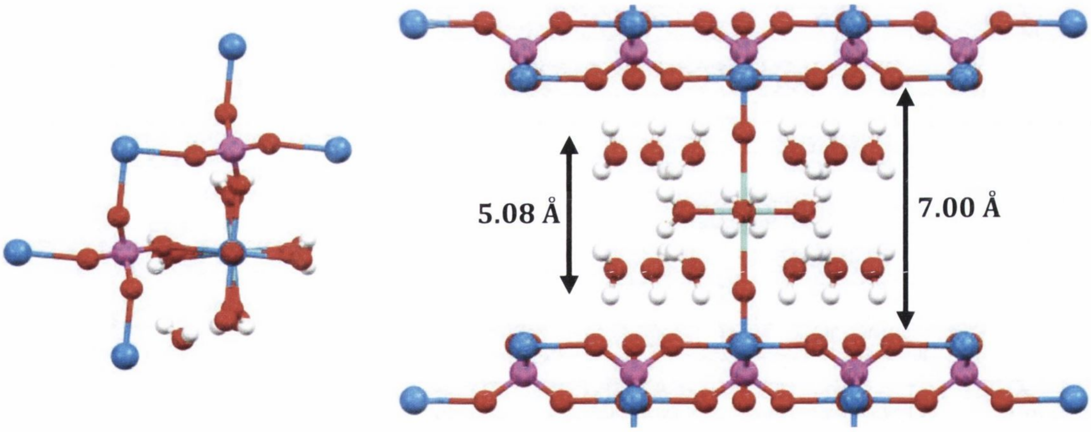

Figure 3.27: View along c axis (left) of the unit cell of metatorbernite, $Cu[(UO_2)_2(PO_4)_2]\cdot 8H_2O$, and the view along the a axis, showing the packing structure connected *via* hydrated copper(II) cations. (Key: Blue = U; Red = O; White = H; Pink = P; Turquoise = Cu)

The third uranyl phosphate mineral was identified to be meta-uranocircite, $Ba[(UO_2)_2(PO_4)_2]\cdot 6\text{-}8H_2O$, *via* PXRD, Raman and EDX spectroscopies (**Figure 3.28**). This was purchased as a sample of a natural uranyl carbonate mineral, urancalcarite, $Ca[(UO_2)_3(CO_3)(OH)_6]\cdot 3H_2O$, however Raman spectroscopy indicated that it was, in fact, a uranyl phosphate mineral. A combination of EDX spectroscopy and PXRD allowed elucidation of the mineral identity.

Figure 3.28: Photograph of meta-uranocircite, $Ba[(UO_2)_2(PO_4)_2]\cdot 6\text{-}8H_2O$.

In the phosphate mineral meta-uranocircite, $Ba[(UO_2)_2(PO_4)_2]\cdot 7H_2O$, the interstitial barium cations are bound to three oxygen atoms (two uranyl oxygens with Ba–O_{yl} distances of 2.934(14) and 2.952(15) Å and an oxygen from a bridging phosphate) and surrounded by six water molecules (**Figure 3.29**).[50]

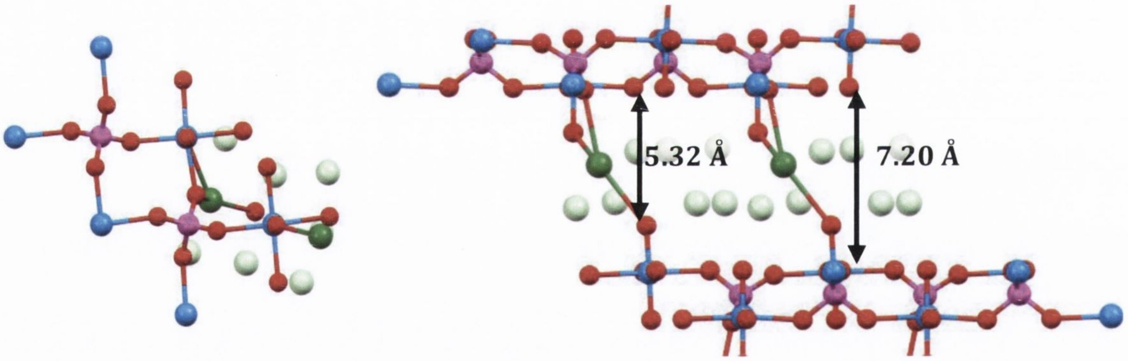

Figure 3.29: View along b axis (left) of the unit cell of meta-uranocircite, $Ba[(UO_2)_2(PO_4)_2]\cdot 7H_2O$,[50] and view of the c axis, showing layers connected *via* bridging hydrated barium cations. (Key: Blue = U; Red = O; Pink = P; Green = Ba; Beige = Water)

In each of the phosphate minerals there is an asymmetry at the uranyl arising from a cation–cation interaction at one end of the uranyl moiety. This can be observed in the Raman spectra (**Figure 3.30**) as asymmetric Raman peaks *ca.* 820 cm^{-1} and is common to minerals in the autunite structural sub-group as seen in **Table 3.5**. Taking the uranyl stretches from the IR and using Bartlett and Cooney's formula for finding the uranyl bond length (**Equation 3.1**),[33] the average predicted bond lengths are very close to the average $U{=}O_{yl}$ bond length from diffraction data (IR stretches at 878 and 911 cm^{-1} yield an average bond length of 1.789 *versus* 1.785 Å for metatorbernite; 887 and 908 cm^{-1} yield an average bond length of 1.787 *vs.* 1.784 Å for meta-uranocircite). For meta-autunite the IR stretches at 898 and 920 cm^{-1} yield a bond length of 1.778 Å *vs.* the autunite uranyl bond length of 1.789 Å.[50] Using **Equation 3.2** to find $d_{U=O}$ from the uranyl Raman stretch gives 1.777 Å for meta-autunite. These values (1.778 and 1.777 Å) are in good agreement with the predicted $U=O_{yl}$ bond length of 1.774(6) from reported EXAFS data.[49]

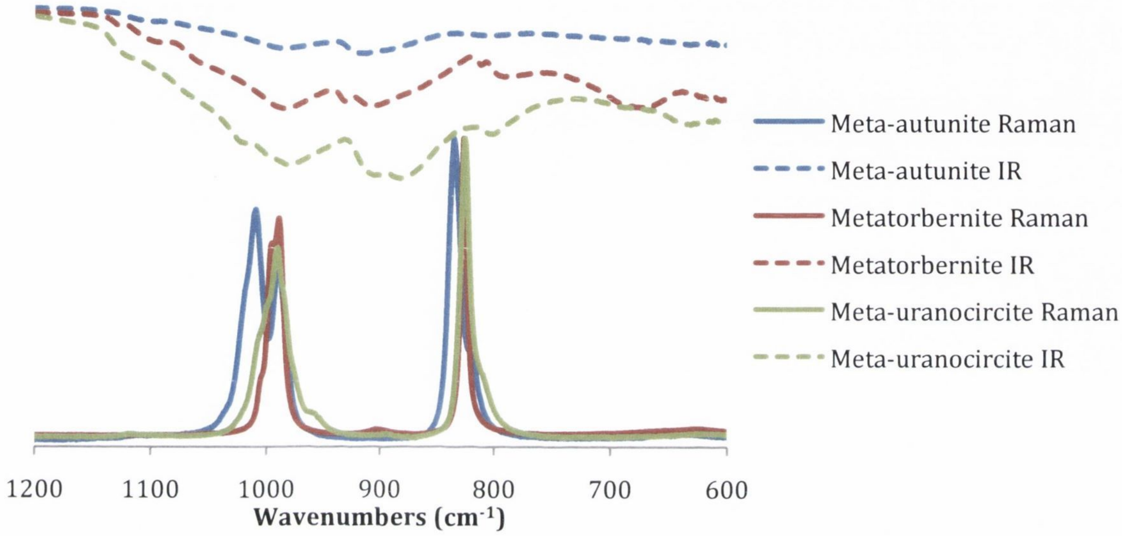

Figure 3.30: Infrared and Raman spectra of uranyl region of uranyl phosphate minerals.

Table 3.5: Raman frequencies of common uranyl phosphate minerals. Bergenite is not a member of the autunite sub-group and is included for comparison.

	Uranyl **$[(UO_2)^{2+}]$**	**Phosphate** **$[(PO_4)^{3-}]$**			**Ref**
	ν_3 symmetric stretch (cm^{-1})	ν_2 asymmetric bend (cm^{-1})	ν_4 symmetric bend (cm^{-1})	ν_3 asymmetric stretch (cm^{-1})	
Bergenite $Ca_2Ba_4[(UO_2)_3O_2(PO_4)_2]_3{\cdot}16H_2O$	798/810	396-444	547/592	1107/1152	51
Autunite $Ca[(UO_2)_2(PO_4)_2]{\cdot}11H_2O$	822/833	399-464	629	1018/1090	52
Meta-autunite $Ca[(UO_2)_2(PO_4)_2]{\cdot}6\text{-}8H_2O$	829	381/455	654	983/1007	47c
Meta-uranocircite $Ba[(UO_2)_2(PO_4)_2]{\cdot}7H_2O$	811/825	403	638	986/ 991/1008	This work
Torbernite $Cu[(UO_2)_2(PO_4)_2]{\cdot}10H_2O$	808/826	399-464	629	995/1004	48
Metatorbernite $Cu[(UO_2)_2(PO_4)_2]{\cdot}8H_2O$	819/827	399-464	640	989/ 996/1005	48

3.3.2. Optical Properties

Comparing the diffuse reflectance spectra of these compounds (**Figure 3.31**) shows the uranyl absorption with vibronic coupling between 450 and 500 nm. There are also Ligand to Metal Charge Transfer (LMCT) bands observed in each spectrum between 400 and 450 nm and at around 360 nm. These have been assigned as the equatorial oxygen LMCT and to the phosphate groups, respectively.

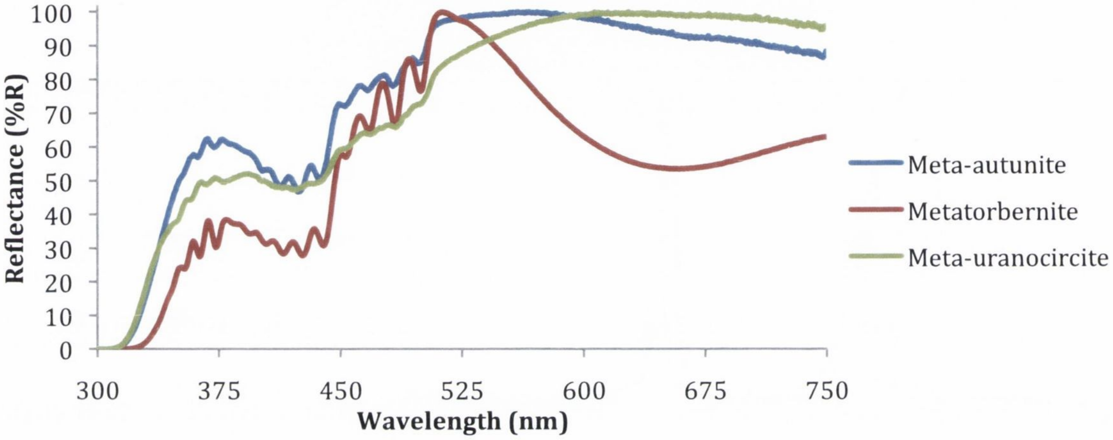

Figure 3.31: Diffuse reflectance spectra of the uranyl phosphate minerals.

The band-gaps of the minerals were calculated from the spectra (**Table 3.6**) and the relationship between the band-gap (i.e. the HOMO/ LUMO gap in a solid) and the reduction potential as well as structural characteristics will be considered.

Table 3.6: The calculated band-gap values of the uranyl phosphate minerals.

Mineral	Band-Gap (eV)	Calculated Band-Gap (eV)	Ref
Meta-autunite	2.74	2.47[a]	53
Metatorbernite	2.58	-	-
Meta-uranocircite	2.76	2.46[a]	54

[a] From emission data.

The metatorbernite spectrum shows a further broad absorption peak from 530 to 750 nm. This feature is consistent with Cu(II) *d*→*d* transitions in an octahedral environment.[55] In this case however the d^9 Cu(II) is in a distorted octahedral complex: the Cu–O_{eq} distances are 1.944(3) Å while the two axial bond distances are 2.685(8) and 2.391(7) Å. The mineral metazeunerite, $Cu[(UO_2)_2(AsO_4)_2]\cdot 8H_2O$, features a similar octahedral distortion around Cu(II), arising from the asymmetric population of the degenerate orbital set in an octahedral complex – also known as the Jahn–Teller effect. The population of the anti-bonding d_{z^2} orbital lengthens the bonds in the z direction, giving rise to axial elongation. A polarised absorption study of metazeunerite confirmed the orbital order to be $d_{x^2-y^2} > d_{xy} > d_{z^2} > d_{xz} \approx d_{yz}$, supporting the orbital splitting caused by Jahn–Teller distortion.[56] Analysis of the transition between the d_{z^2} orbital and $d_{x^2-y^2}$ orbital by *z*-polarised electronic absorption reported a value of 1.12 eV. The Cu(II) $d \rightarrow d$ band centred at ~650 nm is equivalent to an energy of 1.91 eV. This is much higher than that of the Jahn–Teller distorted octahedron and is closer to the range expected for octahedral crystal field splitting, Δ_O.[57] This implies, perhaps, that the distorted octahedral geometry is due to structural constraints rather than electronic rearrangement.

3.3.3. Electrochemical Activity

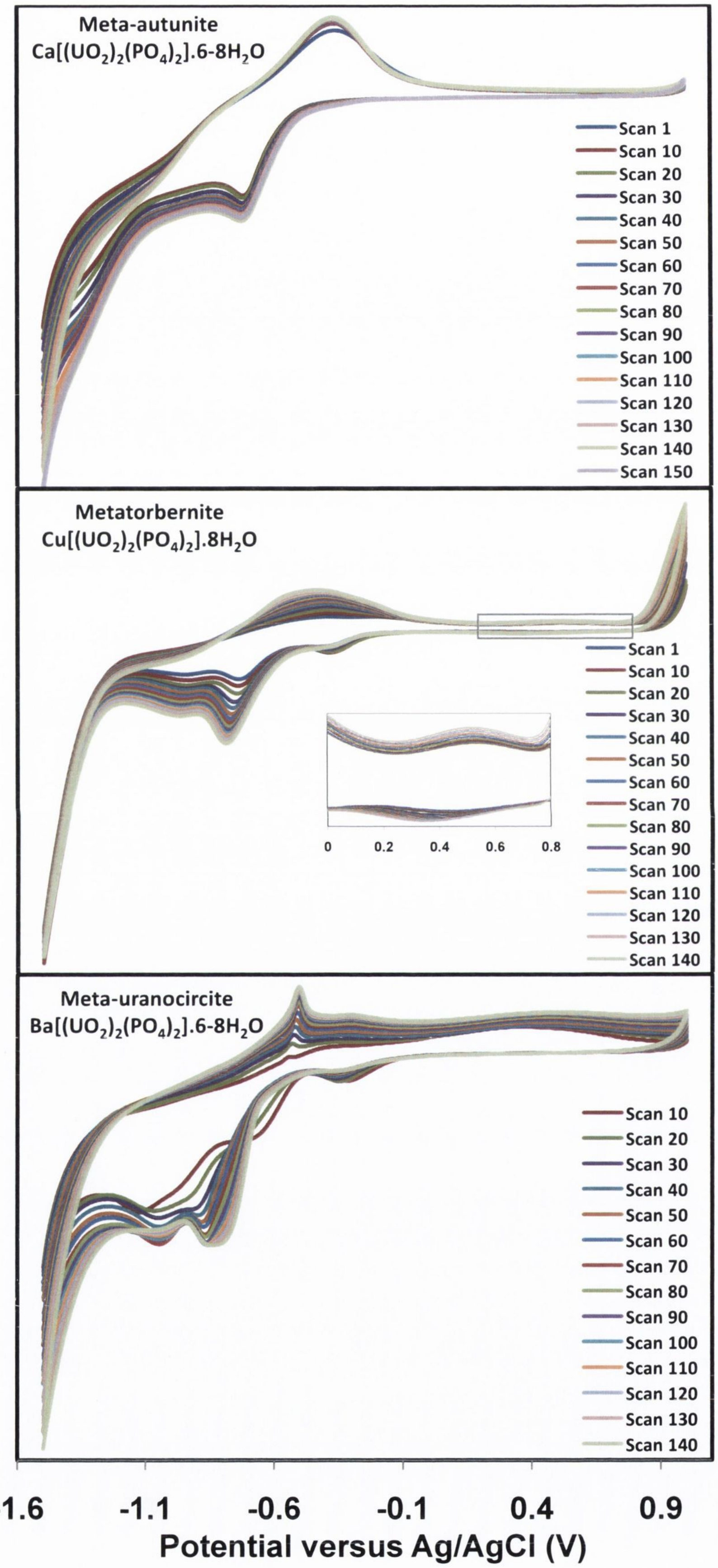

Figure 3.32: Voltammograms of uranyl phosphate minerals cycling between +1 and -1.5 V for one hour in 0.2 M $LiClO_4$.

In the meta-autunite voltammogram there is a growing redox couple visible with a reduction potential of -0.724 V and a broad oxidative peak with a potential of -0.386 V [**Figure 3.32(top)**]. This has been assigned to the U(VI)/(V) couple. There is no visible growth of a U(V)/(IV) couple as observed in the oxyhydroxides but there is a second couple with a reduction potential of -1.349 V. This is possibly the P(V)/(III) couple as the phosphates within the structure are reversibly reduced to phosphite; the recorded redox potential for this couple is -1.202 V *versus* Ag/AgCl (**Equation 3.5**).[58]

$$PO_4^{3-} + H_2O + 2e^- \rightleftharpoons HPO_3^{2-} + 3OH^- \qquad \textbf{3.5}$$

This couple is not noticeable in either the metatorbernite or the meta-uranocircite voltammograms, but the shape of the scans could conceal a weak peak at a potential lower than -1.3 V. There is, however, a reduction peak at -0.383 V in metatorbernite [**Figure 3.32(middle)**] and one at -0.338 V in meta-uranocircite [**Figure 3.32(bottom)**] that could be attributed to the acidic reduction of PO_4^{3-} (**Equation 3.6**).[58] In each case this peak is diminished over time; this is known as the "passivation" phenomenon and arises from the reduced permeation of electrolyte ions through the analyte, often expressed by a very low diffusion coefficient, D_{CT}.[59]

$$PO_4^{3-} + 5H^+ + 2e^- \rightleftharpoons H_3PO_3^{3-} + H_2O \qquad \textbf{3.6}$$

In metatorbernite there is a reduction peak at -0.788 V with a coupled oxidation peak at -0.443 V, and a second reduction peak at -0.965 V with a coupled oxidation process that grows to overlap with the primary oxidative process to give a broad peak centred at -0.476 V [**Figure 3.32(middle)**]. The two reduction peaks are assigned as the U(VI)/(V) and U(V)/(IV), respectively. There is also a small redox couple with a reduction potential of 0.349 V and oxidation potential of 0.520 V [**Figure 3.32(middle: inset)**]. The small difference (~170 mV) implies a single electron redox process, therefore this couple has been assigned to the Cu(II)/(I) couple, which has previously been reported as 0.350 V with respect to Ag/AgCl.[58]

The one-hour voltammogram for meta-uranocircite is more complex [**Figure 3.32(bottom)**]. In the case of the major reductive process – assigned to the U(VI)/(V) couple – at -0.839 V and its couple at -0.512 V, the intensity of the voltammetric waves increases with increasing number of scans, over a period of several hours. This is not the case for the other processes visible, however. The initial scans contain two reduction peaks (-0.259 and -0.701 V) that decrease and disappear with successive scans. The peak at -0.259 V that diminishes to a broad peak at -0.338 V after one hour has already been described and assigned to the P(V)/(III) couple. The peak that appears at -0.701 V in scan 1 and grows until scan 70 is assigned to the U(V)/(IV) couple. The later scans of meta-uranocircite become more regular, and in the 12-hour voltammogram there is only one redox couple observed: the U(VI)/(V) reduction peak at -0.839 V with a coupled oxidation peak at -0.501 V (**Figure 3.33**).

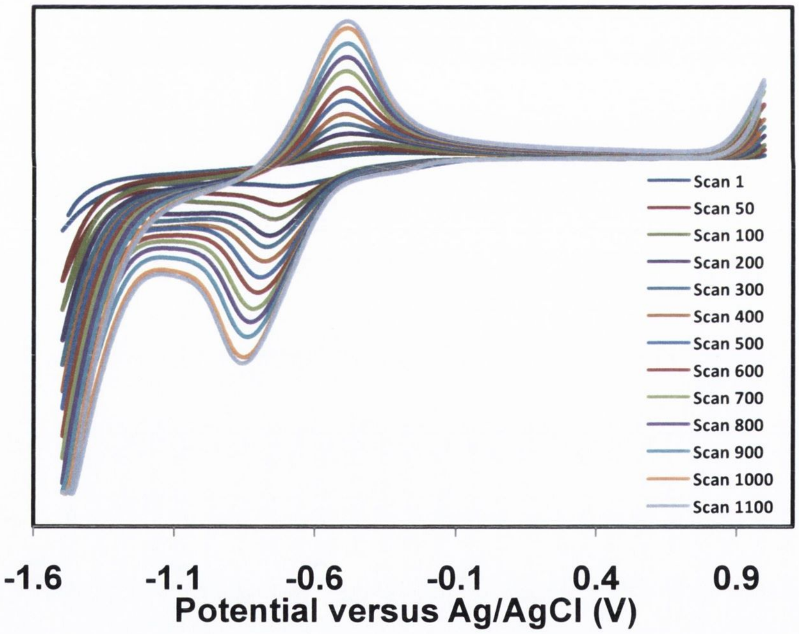

Figure 3.33: Voltammogram of 12 hour CV of meta-uranocircite in 0.2 M $LiClO_4$.

Table 3.7: Summary of the electrochemical features of the uranyl phosphate minerals (Figure 3.32).

Mineral	U(VI)/ (V) (V)	U(V)/ (IV) (V)	P(V)/ (III) (V)	Assignment	Additional Couple (V)	Assignment
Meta-autunite	-0.724	-	-1.349	PO_4^{3-}/HPO_3^{2-}	-	-
Metatorbernite	-0.788	-0.965	-0.383	PO_4^{3-}/ PO_3^{3-}	0.349	Cu(II)/(I)
Meta-uranocircite	-0.839	-1.013	-0.338	PO_4^{3-}/ PO_3^{3-}	-	-

As the film is reduced, it is expected to incorporate electrolyte ions to maintain charge stability. The increase of the peaks in the CV appears slow relative to the oxyhydroxide minerals, but is still indicative of improved penetration of ions through the film. Examination of these electrolysed products by SEM and Raman spectroscopy shows that meta-autunite somewhat retains the sheet structure after cycling for one hour [**Figure 3.34(a)** and **(b)**], while there is little change to the morphology of metatorbernite after cycling for one hour [**Figure 3.34(d)** and **(e)**]. However with a wider view it is clear that dissolution occurs [**Figure 3.34(c)** and **(f)**]. Raman spectroscopy of the cycled meta-autunite sample showed that the uranyl was almost completely destroyed, however EDX analysis implied the retention of meta-autunite – there remained phosphorus and calcium within the product, as well as traces of chlorine. Both techniques were repeated at several points on the surface so it is likely that the smaller crystals reduced fully or dissolved into solution, leaving larger crystals of unreduced metatorbernite to form the pattern in **Figure 3.34(c)** and accounting for the conflicting Raman and EDX data.

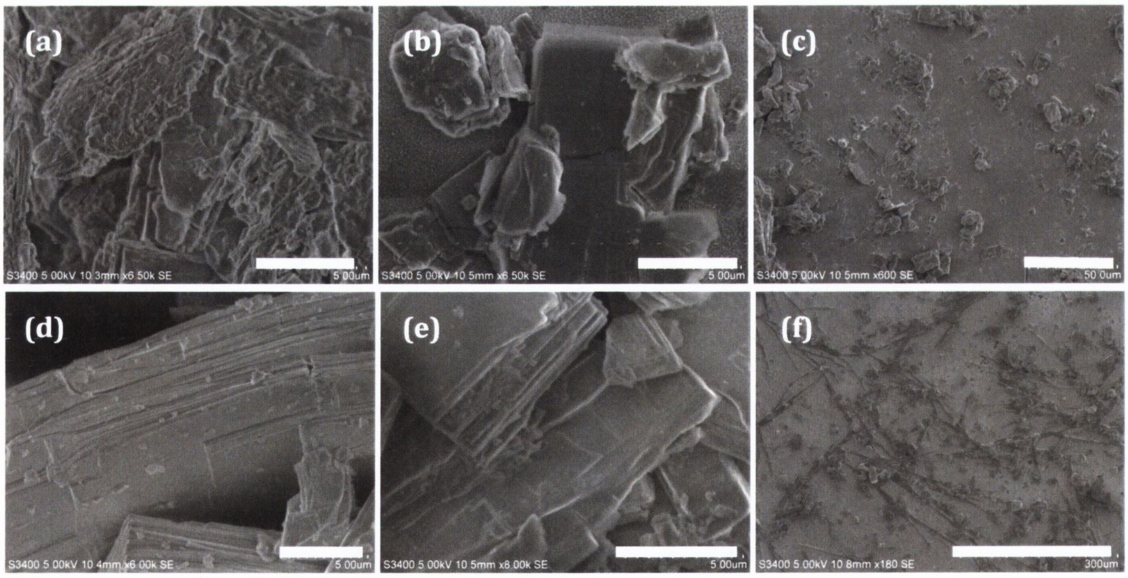

Figure 3.34: SEM micrographs of meta-autunite (a) before and (b) after cycling (Scale bar is 5 μm), and (c) wider view of one hour cycle sample (Scale bar is 50 μm); and metatorbernite (d) before and (e) after cycling (Scale bar is 5 μm); and (f) wider view of one hour cycle sample (Scale bar is 300 μm). In each case the samples were cycled for one hour between +1 and -1.5 V in 0.2 M $LiClO_4$.

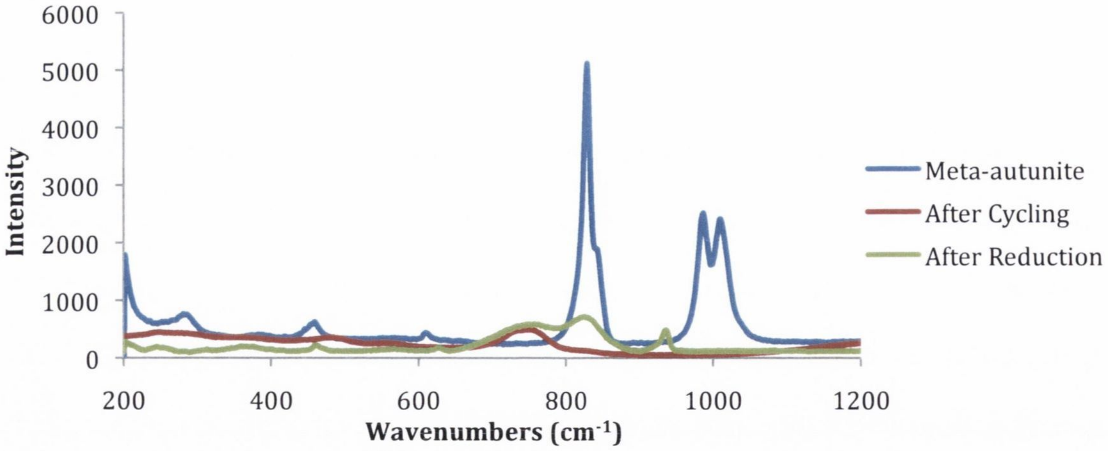

Figure 3.35: Raman spectra of meta-autunite before and after electrochemical treatment.

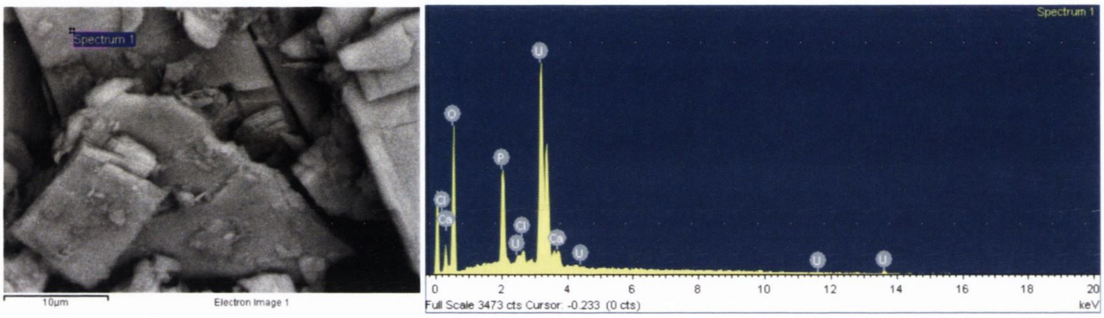

Figure 3.36: SEM micrograph and EDX spectrum of sample of meta-autunite after one hour CV in 0.2 M $LiClO_4$. Three spectra were taken at different points on the sample. For meta-autunite, U, O, P, Ca, and traces of Cl were detected.

The elongated deposits on the surface of the cycled metatorbernite sample [**Figure 3.34(f)**] are consistent with the mechanism of becquerelite dissolution: the quasi-reversible U(VI)/(V) reduction results in the disproportionation of U(V) to yield a black, insoluble U(IV) solid and U(VI) that either remains at points on the electrode as metatorbernite or forms stable aqueous uranyl complexes in solution. Previous reports on the dissolution of metatorbernite showed a preference for dissolution layer by layer *via* etch pit formation in a high pH in a manner similar to becquerelite.[60] This is supported by Raman evidence of both degradation of the mineral structure and retention of it after electrolysis (**Figure 3.37**). EDX analysis shows phosphorus and copper, indicating the retention of the metatorbernite structure (**Table 3.13**).

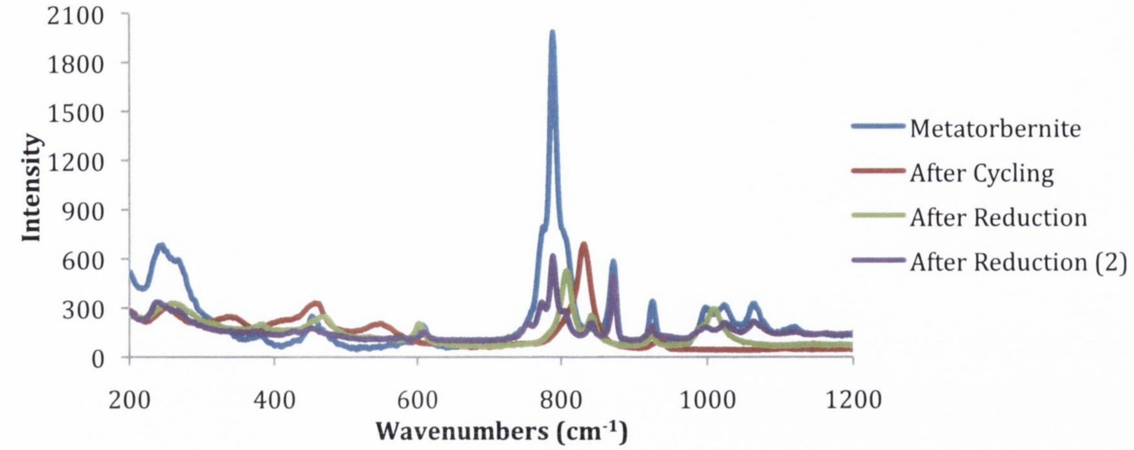

Figure 3.37: Raman spectra of metatorbernite before and after electrochemical treatment.

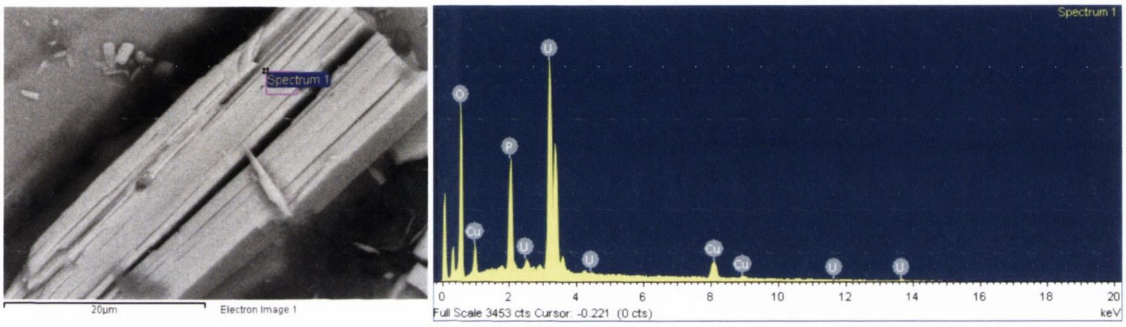

Figure 3.38: SEM micrograph and EDX spectrum of sample of metatorbernite after one hour CV in 0.2 M $LiClO_4$. Three spectra were taken at different points on the sample. For metatorbernite, U, O, P and Cu were detected.

In the case of meta-uranocircite, there is almost no visible effect of reduction on the mineral: the sheet structure is maintained in the mineral crystals [**Figure 3.39(a)** and **(b)**]. After 12 hours there is a change on the surface [**Figure 3.39(c)**], showing the dissolution of the sample. Raman and EDX spectroscopy show that the product after cycling for one hour is almost identical to unreacted meta-uranocircite (**Figures 3.40** and **3.41**) and this is still true after 12 hours cycling.

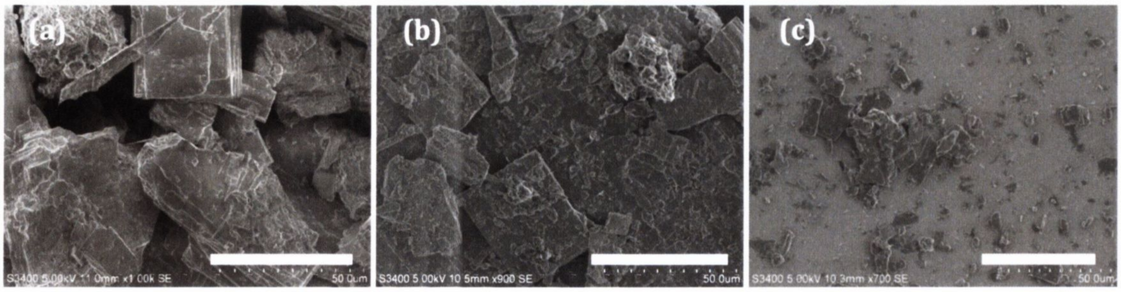

Figure 3.39: SEM micrographs of meta-uranocircite (a) before and (b) after cycling for one hour between +1 and -1.5 V in 0.2 M $LiClO_4$ and (c) after 12 hours (Scale bar is 50 µm).

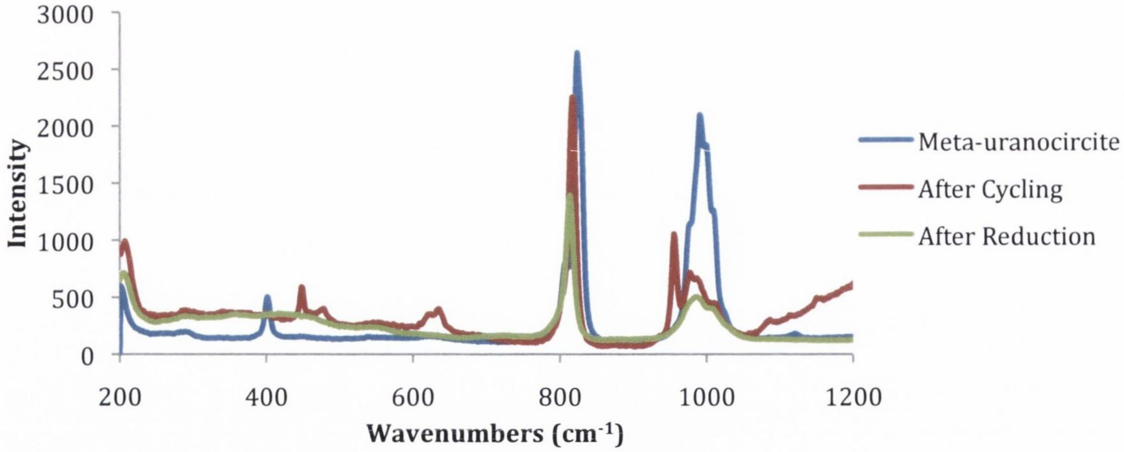

Figure 3.40: Raman spectra of meta-uranocircite before and after electrochemical analysis.

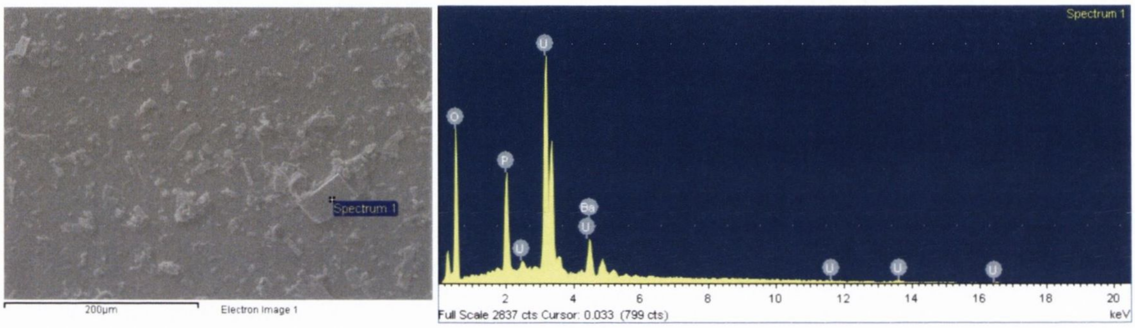

Figure 3.41: SEM image and EDX spectrum of sample of metatorbernite after one hour CV in 0.2 M $LiClO_4$. Three spectra were taken at different points on the sample. For metatorbernite, U, O, P and Ba were detected.

Upon electrochemical treatment, the only mineral that showed signs of destruction (i.e. the loss of Raman features, the decomposition of the crystals and loss of cations from between layers) was meta-autunite. It is possible that if meta-autunite is structurally similar to autunite but with weakly bound interstitial water molecules and calcium ions, the reduced stability may result from the absence of cation–cation interactions. The lack of alteration to the other two phosphate minerals and retention of their elemental composition is reminiscent of their inherent stability[5] and implies that they are resistant to redox processes. This may be why, in contrast to the uranyl oxyhydroxide minerals, there were only allusions to anion transport in the uranyl phosphate minerals. A perchlorate stretch was observed in the Raman spectrum of the electrolysed meta-autunite and the cycled meta-uranocircite (930 and 955 cm^{-1}, respectively) and chlorine was detected by EDX in some of the spectra of meta-autunite and metatorbernite. To determine the mode of electrolyte ion transport in uranyl phosphate minerals, the diffusion coefficients were measured for each cycled and reduced sample. The results are given in **Table 3.8**.

Table 3.8: Reductive and oxidative diffusion coefficients for the uranyl phosphate minerals during one hour cycle.

Mineral	Reductive Diffusion Coefficient ($cm^2\ s^{-1}$) U(VI)/(V) in 0.2 M $LiClO_4$	Oxidative Diffusion Coefficient ($cm^2\ s^{-1}$) U(VI)/(V) in 0.2 M $LiClO_4$
Meta-autunite $Ca(UO_2)_2(PO_4)_2 \cdot 6–8H_2O$	5.186×10^{-16}	4.668×10^{-15}
Metatorbernite $Cu[(UO_2)(PO_4)] \cdot 8H_2O$	3.581×10^{-14}	1.399×10^{-14}
Metatorbernite 12 hours cycling	2.014×10^{-14}	1.097×10^{-13}
Meta-uranocircite $Ba[(UO_2)_2(PO_4)_2] \cdot 8H_2O$	5.679×10^{-14}	1.840×10^{-13}

Once again, in each case the oxidative D_{CT} was larger than the D_{CT} for the reductive step, meaning that the oxidation process is the rate-determining step. In the case of metatorbernite this was not readily apparent until examination of the 12 hour CV sample, where the reductive D_{CT} was found to be 2.014×10^{-14} $cm^2\ s^{-1}$ and the oxidation peak to be 1.097×10^{-13} $cm^2\ s^{-1}$. The oxidation process being the rate-determining step is consistent with anion transport, which would be required for charge balance during a slower oxidative process, however it is possible that the perchlorate anion was perhaps adsorbed onto the surface rather than absorbed into the network.

Table 3.9: Reduction potentials and structural features of uranyl phosphate minerals.

Mineral	U(VI)/ (V) Potential (V)	U(V)/ (IV) Potential (V)	Average $U=O_{yl}$ Bond Length (Å)	Distance between layers (Å)
Meta-autunite $Ca(UO_2)_2(PO_4)_2 \cdot 6–8H_2O$	-0.788	-0.965	1.7885[b]	6.61[a]
Metatorbernite $Cu[(UO_2)(PO_4)] \cdot 8H_2O$	-0.724	-0.949	1.7853	7.00
Meta-uranocircite $Ba[(UO_2)_2(PO_4)_2] \cdot 8H_2O$	-0.839	-1.034	1.7843	7.20

[a] Taken from crystal structure for meta-autunite, $Ca(UO_2)_2(PO_4)_2 \cdot 6H_2O$.47c

[b] Taken from crystal structure for autunite, $Ca(UO_2)_2(PO_4)_2 \cdot 11H_2O$.47a

While investigating trends within the data (**Table 3.9**), it was found that the longer the uranyl bond length in the uranyl phosphate mineral, the higher the reduction potential. This is seemingly the inverse of the relationship between uranyl bond length and reduction potential in the oxyhydroxide series (**Figure 3.42**). It appears that the shorter uranyl bond implies a more stable uranyl mineral, thus making it more difficult to reduce.

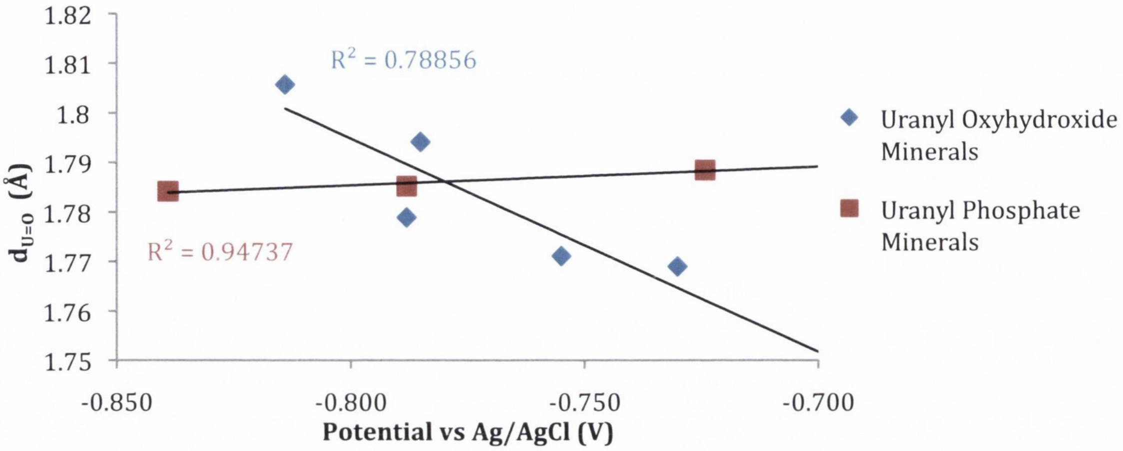

Figure 3.42: Graph of the uranyl bond length, $d_{U=O}$, *versus* U(VI) reduction potential for uranyl oxyhydroxide minerals (blue) and uranyl phosphate minerals (red).

Another feature investigated was the distance between uranyl moieties in adjacent layers. The uranyl moieties in the uranyl phosphate minerals are connected *via* hydrated cations (**Section 3.3.1**). It was found that the shorter distance between uranyl moieties in adjacent layers implies a higher reduction potential, i.e. an "easier" reduction, which in turn implies more efficient communication between the layers (**Figure 3.43**).

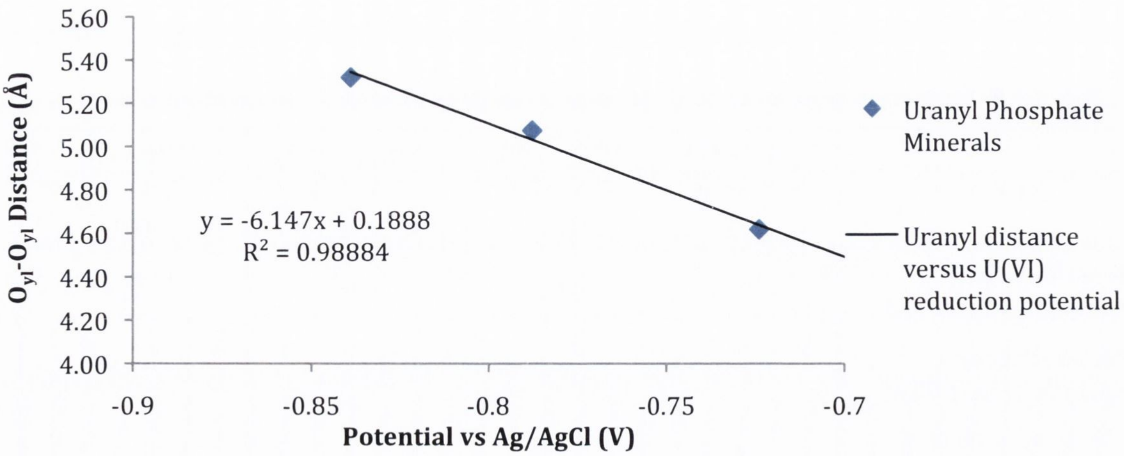

Figure 3.43: Graph of interlayer distance in the uranyl phosphate minerals *versus* U(VI) reduction potential.

3.4. Uranyl Carbonate Minerals

As mentioned in **Chapter 1** and in the introduction to this chapter, uranyl carbonate minerals are readily formed in nature and are of pivotal importance to understanding the properties of uranium in the environment.[13,61] Two uranyl carbonate minerals, grimselite, $K_3Na[(UO_2)(CO_3)_3]\cdot H_2O$, and andersonite, $Na_2Ca[(UO_2)(CO_3)_3]\cdot 6H_2O$, were synthesised and the structures verified by XRD.

3.4.1. Structural Comparison

The uranyl tricarbonate unit is the building block for many uranyl carbonate minerals.[1,9] Thermodynamic factors such as Lewis Acid-Base interactions come into play to give these minerals such favourable enthalpies of formation.[5a] Grimselite and andersonite have very different arrangements of cations around the $[UO_2(CO_3)_3]^{4-}$ unit (**Figure 3.44** and **3.45**).

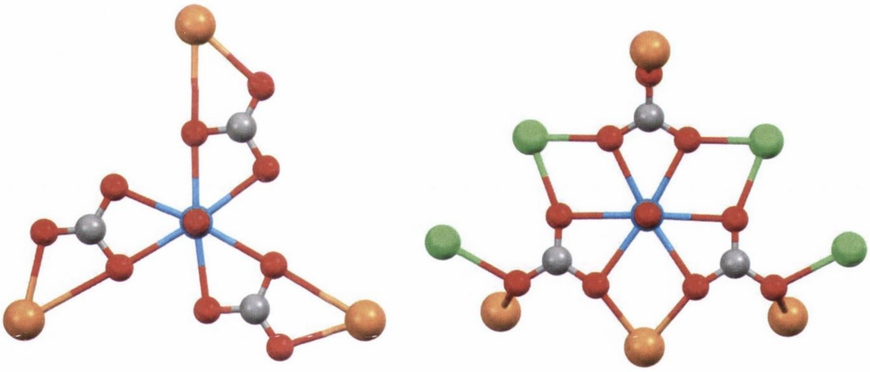

Figure 3.44: Uranyl tricarbonate unit in the structure of (a) grimselite, $K_3Na[(UO_2)(CO_3)_3]\cdot H_2O$,[62] and (b) andersonite, $Na_2Ca[(UO_2)(CO_3)_3]\cdot 6H_2O$.[63]

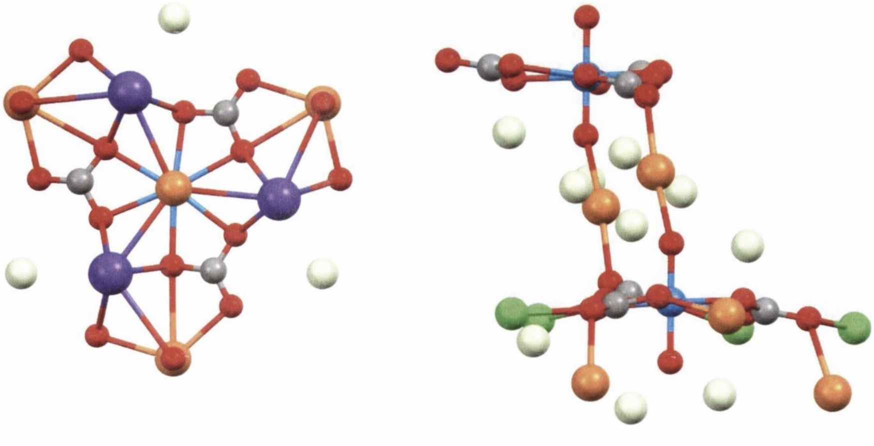

Figure 3.45: Packing around the uranyl tricarbonate unit in the structure of (a) grimselite, $K_3Na[(UO_2)(CO_3)_3]\cdot H_2O$,[62] and (b) andersonite, $Na_2Ca[(UO_2)(CO_3)_3]\cdot 6H_2O$.[63]

The uranyl in grimselite occupies D_{3h} symmetry with three equivalent carbonate ligands coordinating to three equivalent sodium cations in the equatorial plane [**Figure 3.44(a)**]. The uranyl interacts with two equivalent axial sodium cations, giving a symmetrical uranyl with $d_{U=O}$ of 1.795(5) Å [**Figure 3.45(a)**].[62] There are only two uranyl carbonate minerals that display this symmetrical cation–cation interaction at uranyl: grimselite and agricolaite, $K_4[(UO_2)(CO_3)_3]\cdot H_2O$, with a symmetrical uranyl bond length of 1.799(3) Å.[64] The arrangement of carbonate anions and sodium and potassium cations surrounding the grimselite uranyl creates a tripodal structure with regular pores of 5.96 Å in diameter [**Figure 3.46(right)**].

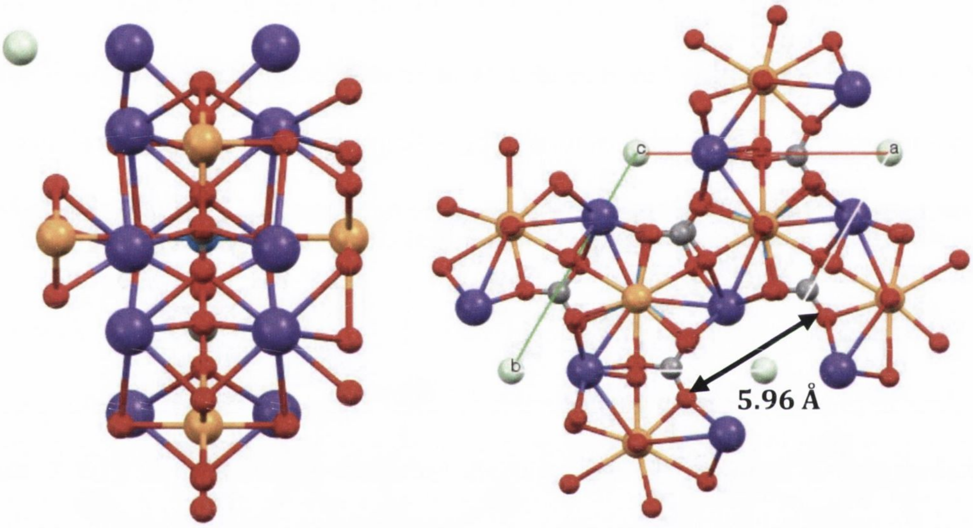

Figure 3.46: View along b axis (left) of the unit cell of grimselite, $K_3Na[(UO_2)(CO_3)_3]\cdot H_2O$,[62] and the view along the c axis (right) of the packing structure showing the trigonal uranyl tricarbonate units connected *via* cation–cation interactions with sodium and potassium cations leaving hydrated pores within the structure. (Key: Blue = U; Red = O; Grey = C; Orange = Na; Purple = K; Beige = Water)

In the structure of andersonite, the unit cell is composed of six uranyl tricarbonate units that connect via 6-coordinate calcium and 4-coordinate sodium cations [**Figure 3.44(b)**].[63] These unit cells are then connected *via* bridging sodium cations extending axially from the uranyl [**Figure 3.45(b)**] to give rise to the asymmetric uranyl with bond lengths of 1.776(4) (external) and 1.808(5) Å (internal). This cation–cation interaction facilitates packing to create the pore structure seen in **Figure 3.47(bottom).**

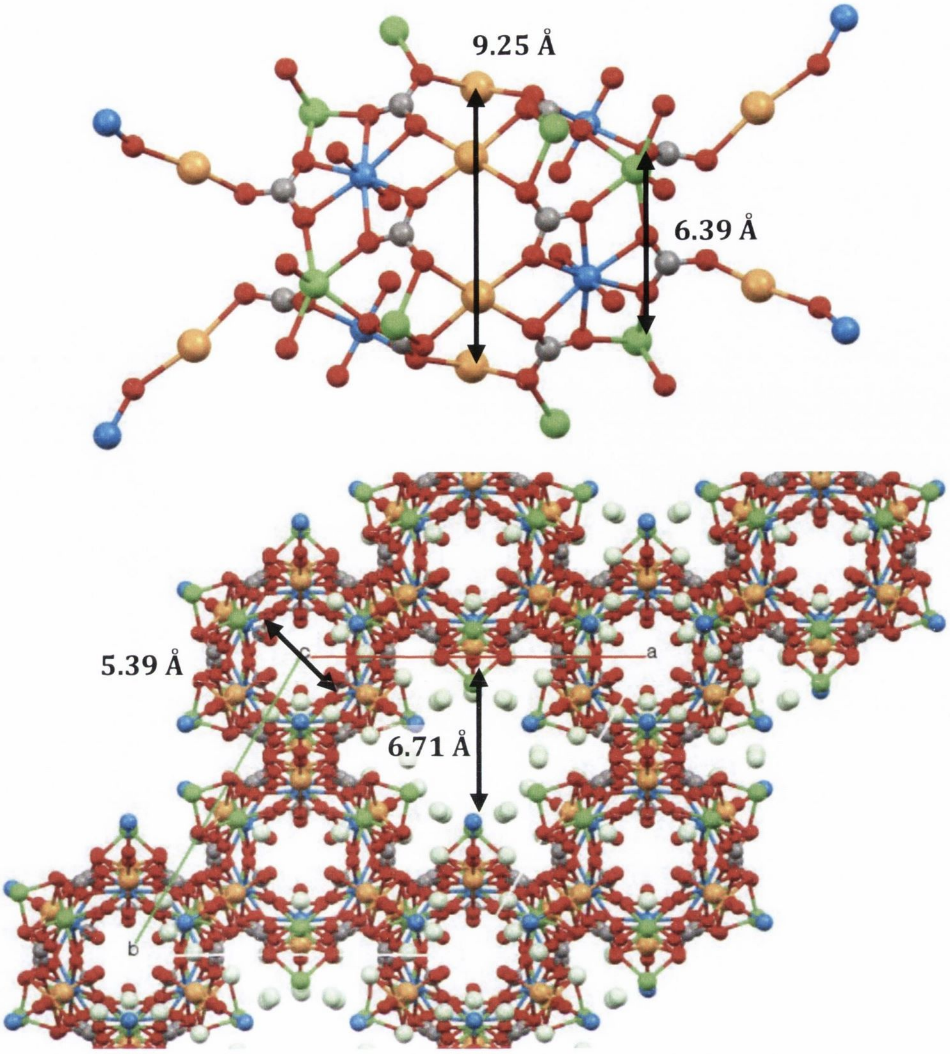

Figure 3.47: View along b axis (top) of the unit cell of andersonite, $Na_2Ca[(UO_2)(CO_3)_3]\cdot 6H_2O$,[63] and the view of the packing structure along the c axis (bottom), showing the uranyl tricarbonate units connected *via* calcium and sodium cations in a tripodal structure that creates a cylindrical unit cell with a tunnel along the c axis. (Key: Blue = U; Red = O; Grey = C; Orange = Na; Green = Ca; Beige = Water)

When comparing the vibrational spectra of these two minerals it is clear that the carbonate anions differ significantly in each mineral (**Figure 3.48**). The symmetric carbonate stretch in the Raman for grimselite is found at 1063 cm^{-1} but in the andersonite spectrum there are two signals at 1080 and 1092 cm^{-1}, implying two unique carbonate species in andersonite; this is clearly visible in the crystal structure of the uranyl unit [**Figure 3.44(b)**]. The corresponding peaks in the IR also show a different environment: the symmetric carbonate stretch appears as a weak signal at 1081.5 cm^{-1} for andersonite and a strong, sharp signal at 1055 cm^{-1} for grimselite. The ν_2 carbonate bend overlaps with the ν_2 uranyl stretch in the IR spectrum, but it is apparent that the similar peaks at ~850 cm^{-1} are carbonate signals, while the stronger signals at 915 and 901 cm^{-1} in the andersonite spectrum and 902 and 878 cm^{-1} in the grimselite spectrum can be attributed to uranyl. Using Bartlett and Cooney's equation for calculating bond length from uranyl vibrational data (**Equation 3.1**)[33] these stretches can be equilibrated to average bond lengths of 1.792 Å for grimselite and 1.779 Å for andersonite – within 3σ of the crystal data. Repeating this for the Raman stretches, the andersonite peaks at 806 and 832 cm^{-1} become bond lengths of 1.805 and 1.779 Å, and for grimselite the 813 cm^{-1} corresponds to a bond length of 1.798 Å, again almost identical to the XRD data. A table of the Raman features of common uranyl minerals is included for comparison (**Table 3.10**).

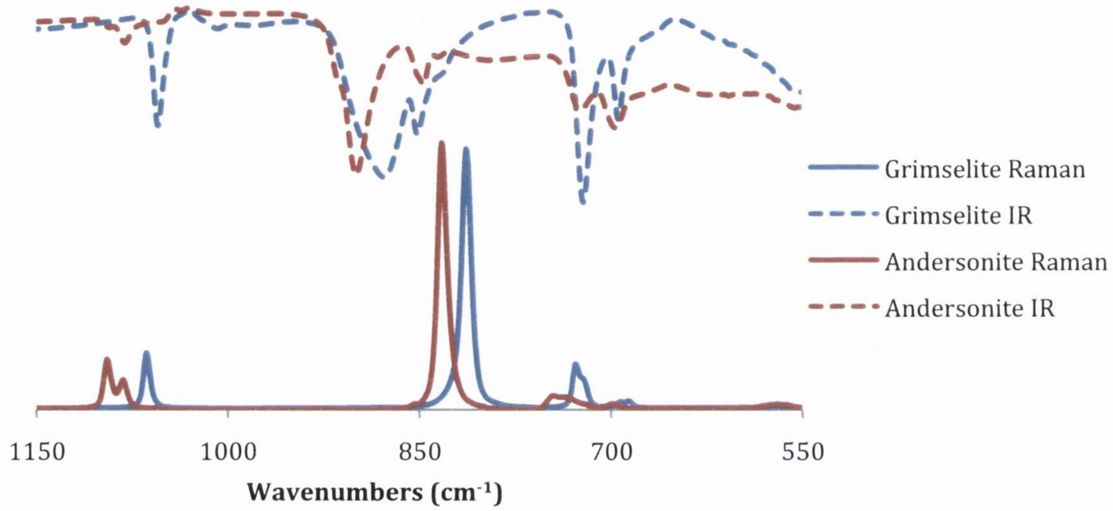

Figure 3.48: Uranyl region of IR and Raman spectra of uranyl carbonate minerals.

Table 3.10: Raman stretches of common uranyl carbonate minerals

	Uranyl [$(UO_2)^{2+}$]	**Carbonate [$(CO_3)^{2-}$]**			
	ν_1 symmetric stretch (cm^{-1})	ν_4 symmetric bend (cm^{-1})	ν_2 asymmetric bend (cm^{-1})	ν_1 symmetric stretch (cm^{-1})	Ref
Rutherfordine UO_2CO_3	886	784/799	838	1115	**65**
Voglite $Ca_2Cu[(UO_2)(CO_3)_4]\cdot 6H_2O$	836	709/747	-	1094	**66**
Schroeckingerite $Ca_3Na[(UO_2)(CO_3)_3F(SO_4)]\cdot 10H_2O$	815	707/742	-	1092	**67**
Grimselite $K_3Na[(UO_2)(CO_3)_3]\cdot H_2O$	813	688/696	726/730	1063	This work
Andersonite $Na_2Ca[(UO_2)(CO_3)_3]\cdot 6H_2O$	832	697/746	926	1080/1092	**52**

3.4.2. Optical Properties

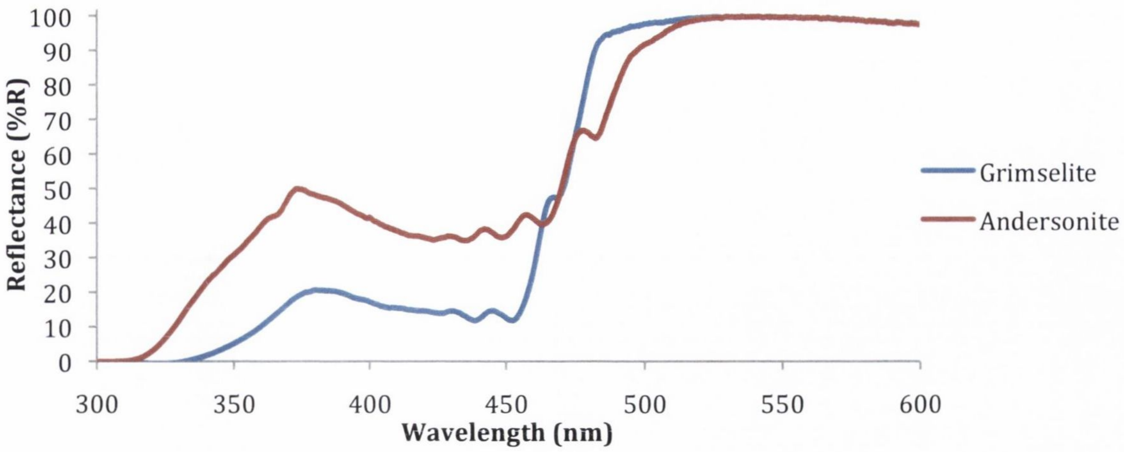

Figure 3.49: Diffuse reflectance spectra of grimselite and andersonite.

The reflectance spectra show the uranyl vibronic coupling between 420 and 500 nm. There does not appear to be a band from equatorial LMCT.

Table 3.11: Calculated band-gaps of grimselite and andersonite.

Mineral	Band-Gap (eV)	Reported Band-Gap (eV)	Ref
Grimselite	2.71	-	-
Andersonite	2.72	2.33[a]	68

[a] From emission data

3.4.3. Electrochemical Activity

During the examination of studtite, **Section 2.2.3.3**, several electrolytes were examined to examine the effect of cation and anion identity on the studtite: $LiClO_4$, $NaClO_4$, $KClO_4$ and Na_2SO_4. It was found that the variation from lithium to sodium to potassium affected the reduction potential, but the change from perchlorate anions to sulphate did not. The increasingly cathodic reduction potentials observed with increasing cation size suggested that cation diffusion was a limiting factor, a feature observed before by Bond *et al.* when examining the U(VI)/U(V) electron transfer in uranium oxides attached to graphite electrodes,[24b] and supported by diffusion studies which indicated that oxidation was the rate determining step for the redox processes.

The two carbonate minerals chosen for analysis, grimselite, $K_3Na[(UO_2)(CO_3)_3]\cdot H_2O$, and andersonite, $Na_2Ca[(UO_2)(CO_3)_3]\cdot 6H_2O$, are the only uranyl minerals analysed within this thesis that contain different cations within their unit cell. For this reason it was decided that using $LiClO_4$ alone was not sufficient and $KClO_4$ would also be used to identify cation dependence, if any. It was also decided that carbonate electrolytes would be used to investigate the effect of the acidic perchlorate anion on the uranyl carbonate minerals. Li_2CO_3 and K_2CO_3 were used on both minerals, $CaCO_3$ was used with andersonite - andersonite contains monovalent sodium and divalent calcium cations and it was deemed prudent to test Ca^{2+} in this system.

3.4.3.1. Perchlorate Electrolytes

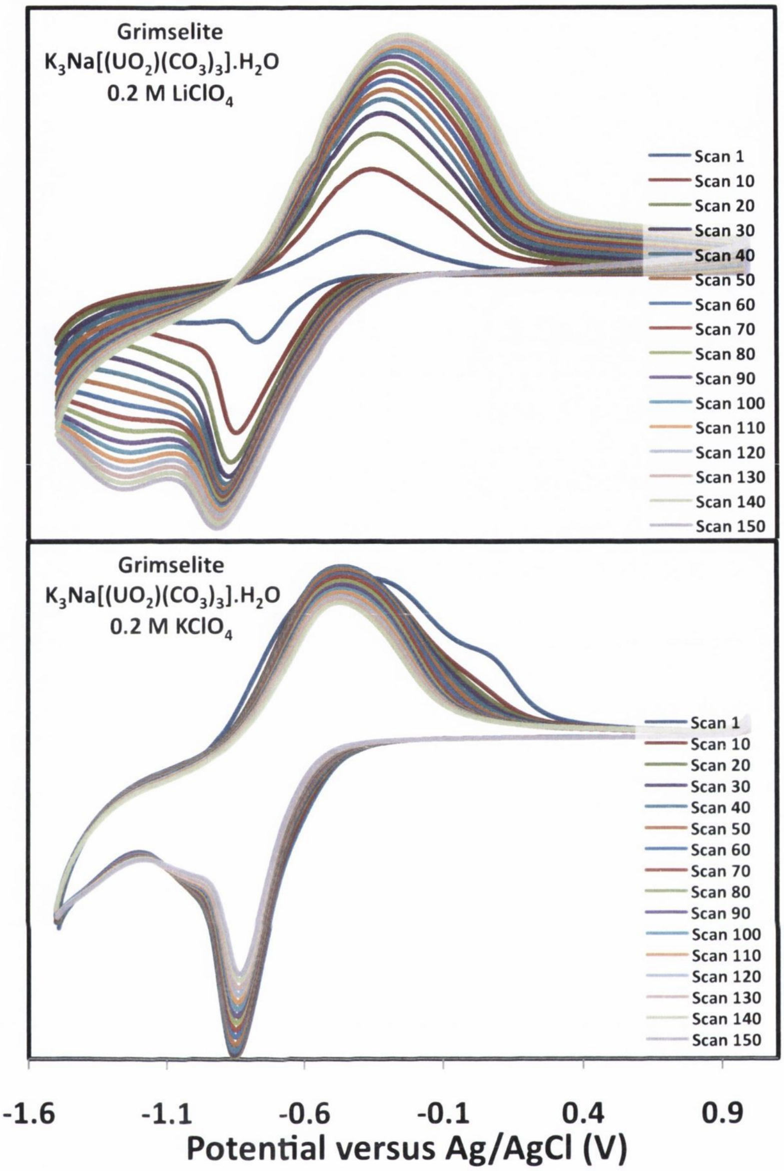

Figure 3.50: One-hour voltammograms of grimselite cycling in perchlorate electrolytes.

For grimselite, it was surprising to see very different voltammograms for $LiClO_4$ and $KClO_4$ (**Figure 3.50**). In 0.2 M $LiClO_4$ there is a sharp growth of a reduction peak at -0.910 V and a second, more diffuse, peak that settles at -1.246 V. The two coupled oxidation peaks overlap to give a broad signal centred at -0.263 V. The sharp peak has been assigned to the U(VI)/(V) with the second peak assigned as the U(V)/(IV) reduction. The U(V)/(IV) peak is slow to appear but grows rapidly to stabilise at a similar current value to the U(VI)/(V) reduction. In the 12 hour voltammogram the U(V)/(IV) peak exceeds the U(VI)/(V) peak after scan 600. In 0.2 M $KClO_4$, however, the potassium cations appear to produce a passivation effect, causing the current values of the peaks to decrease over time. There is a clear major U(VI)/(V) reduction peak visible at -0.820 V and a minor U(V)/(IV) peak at -1.006 V, with a single oxidation peak at -0.482 V. This passivation effect appears to be overcome in the 12 hour voltammogram as the current values begin to increase after scan 400. The U(V)/(IV) reduction is hidden under the growth of the U(VI)/(V) couple. The features of each of these experiments are summarised in **Table 3.12**. It is interesting that the U(V)/(IV) reduction peak is so much smaller in the $KClO_4$ voltammogram, implying that the rate of dissociation of U(V) to U(IV) and U(VI) is much faster in this system than with the lithium electrolyte – the U(VI) and U(V) reductions seem to proceed equally.

Table 3.12: Summary of electrochemical features in analysis of grimselite with perchlorate electrolytes.

Electrolyte	U(VI)/(V) after one hour (V)	U(V)/(IV) after one hour (V)	U(VI)/(V) after 12 hours (V)	U(V)/ (IV) after 12 hours (V)
0.2 M $LiClO_4$	-0.910	-1.246	-0.879	-1.219
0.2 M $KClO_4$	-0.820	-1.006	-0.859	-

As before, the cycled and reduced products were analysed using SEM, EDX and Raman spectroscopy to investigate changes in the film. It appears that the reversible reduction of grimselite in $LiClO_4$ leads to decomposition of the crystal morphology [**Figure 3.51(b)**] but retains the molecular structure of grimselite according to Raman spectroscopy (**Figure 3.52**). EDX analysis shows that after 12 hours the major alteration of the composition of grimselite is in the cation concentration: there is no potassium and a drastic reduction in the sodium concentration (**Figure 3.53**). This implies that the product is most likely a mixture of uranyl carbonate and sodium uranyl carbonates. In the electroanalysis of the uranyl oxyhydroxide minerals the charge is balanced by incorporation of electrolyte anions, it appears that in the case of grimselite the charge is balanced by the removal of cations.

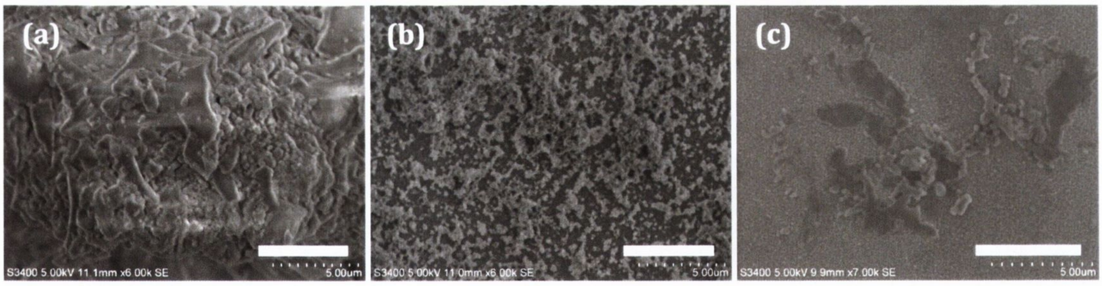

Figure 3.51: SEM images of grimselite on FDTO (a), after one hour cycling in 0.2 M $LiClO_4$ (b) and after one hour cycling in 0.2 M $KClO_4$. Scale bar is 5 μm.

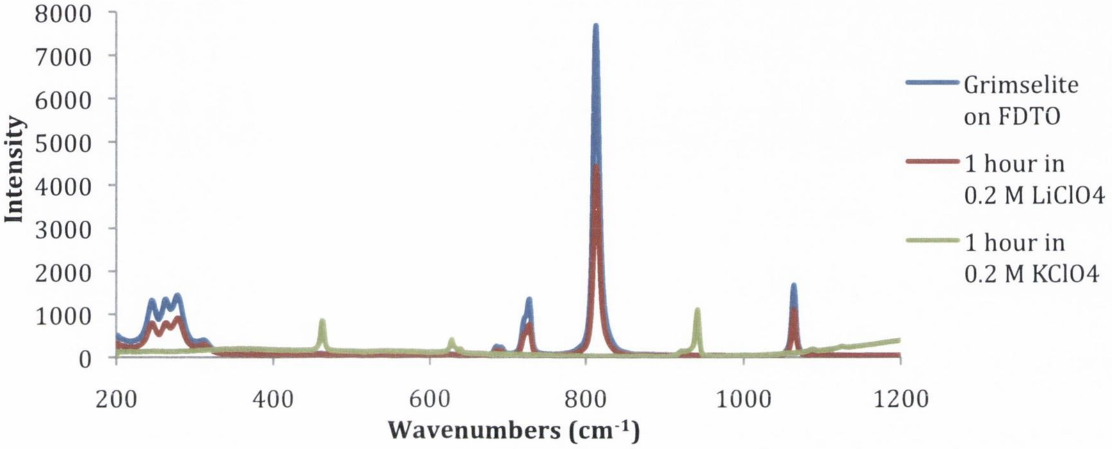

Figure 3.52: Raman spectra of grimselite before and after electrochemical analysis.

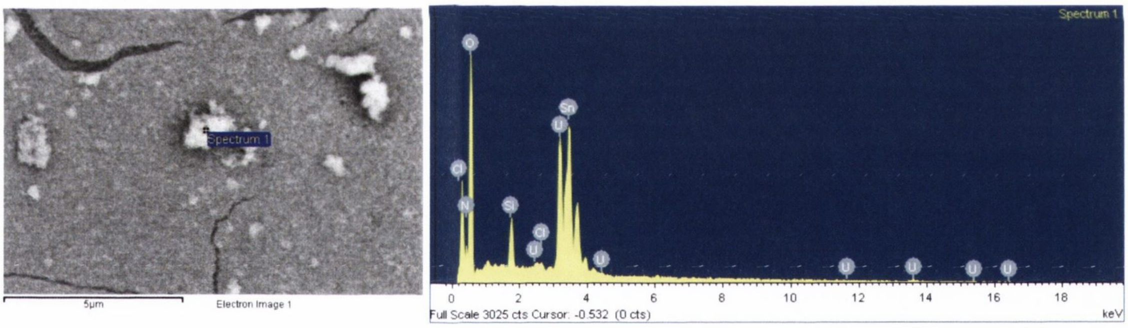

Figure 3.53: SEM micrograph and EDX spectrum of sample of grimselite after 12 hours CV in 0.2 M $LiClO_4$. Three spectra were taken at different points on the sample. For grimselite, U, O, Sn and traces of Cl and Na were detected. Sn most likely was from the FDTO electrode. C and K were not detected.

In the case of $KClO_4$, the morphology after one hour cycling was found to change drastically: the crystals have decomposed, leaving a black amorphous solid [**Figure 3.51(c)**]. This solid has no identifiable carbonate Raman signals implying the breakdown or dissolution of the carbonate anions (**Figure 3.52**); this is consistent with the evidence for dissociation of U(V) in the voltammogram and is supported by the lack of carbon in the EDX data (**Figure 3.54**). The EDX data shows that the uranium concentration is particularly high and the cation (Na^+ and K^+) concentrations are lower than the expected values for grimselite. This combined with the Raman data implies that grimselite is reduced to a combination of uranium oxides and uranium alkaline earth salts. There is a small signal in the Raman spectrum at 940 cm^{-1} that can be assigned to surface-bound perchlorate anions although there is no indication of chlorine at the points on the surface examined. It is likely that charge balance is achieved by removal of cations, rather than anion incorporation.

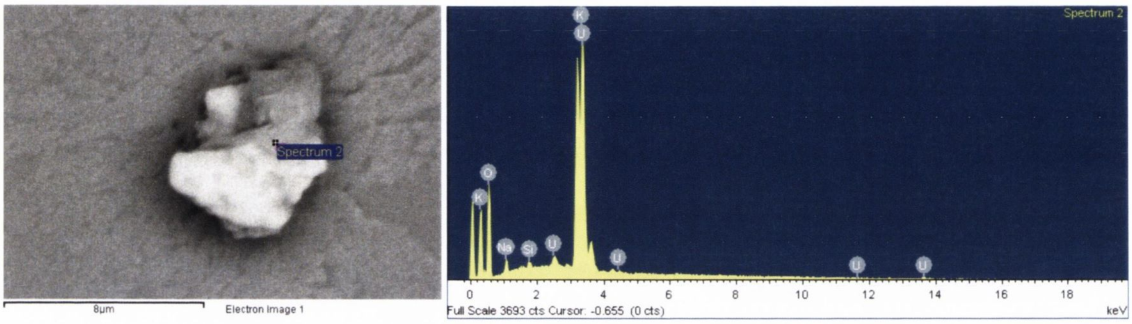

Figure 3.54: SEM micrograph and EDX spectrum of sample of grimselite after one hour CV in 0.2 M $KClO_4$. Three spectra were taken at different points on the sample. For grimselite, U, O, Na, K and traces of Si were detected.

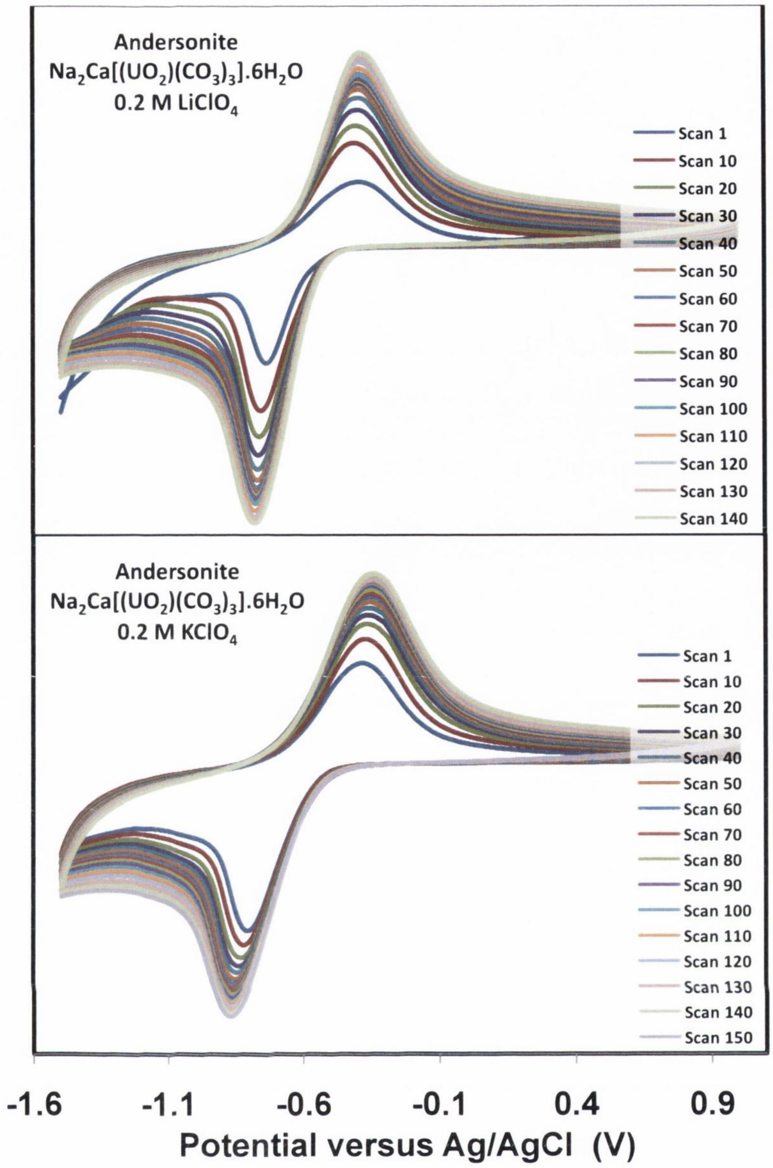

Figure 3.55: One-hour voltammograms of andersonite cycling in perchlorate electrolytes.

In the case of andersonite, there is little difference between the voltammograms with the two perchlorate electrolytes: in each voltammogram there is a single strong quasi-reversible redox process. For $LiClO_4$ the initial scan shows overpotential in the form of a tail towards -1.5 V but successive scans smooth to yield a single sharp reduction peak at -0.767 V and an oxidation peak at -0.398 V. This has been assigned to the U(VI)/(V) couple. There is a flattening of the cathodic end of the peak that could correspond to a weak U(V)/(IV) signal. This is also visible in the $KClO_4$ voltammogram, at the cathodic side of the U(VI)/(V) reduction peak at -0.871 V. The features of these are summarised in **Table 3.13**.

Table 3.13: Summary of electrochemical features in analysis of andersonite with perchlorate electrolytes (Figure 3.55).

Electrolyte	U(VI)/(V) after one hour (V)	U(VI)/(V) after 12 hours (V)
0.2 M $LiClO_4$	-0.767	-0.839
0.2 M $KClO_4$	-0.871	-0.919

The cycling experiments appear to have little effect on the morphology of andersonite; the sample cycled in $KClO_4$ has still retained some of the crystalline nature of andersonite [**Figure 3.56(c)**], although for $LiClO_4$ the product appears to be amorphous [**Figure 3.56(b)**]. In contrast, the Raman spectra of the cycled samples shows almost complete destruction of the uranyl peak at 832 cm^{-1} (**Figure 3.57**). It is likely that the small peaks at 811 cm^{-1} in the $LiClO_4$ sample and 809 cm^{-1} in the $KClO_4$ sample are from U(V) salts. The U(VI)/U(V) couple is considered to be quasi-reversible, however, U(V) will disproportionate into U(IV) and U(VI) over time. U(VI) in the form of uranyl carbonate species will most likely dissolve[5a,69] and leave the insoluble U(IV) on the surface. This is consistent with EDX data (**Table 3.23** and **Table 3.24**) as in both the lithium and potassium samples the uranium concentration is very low.

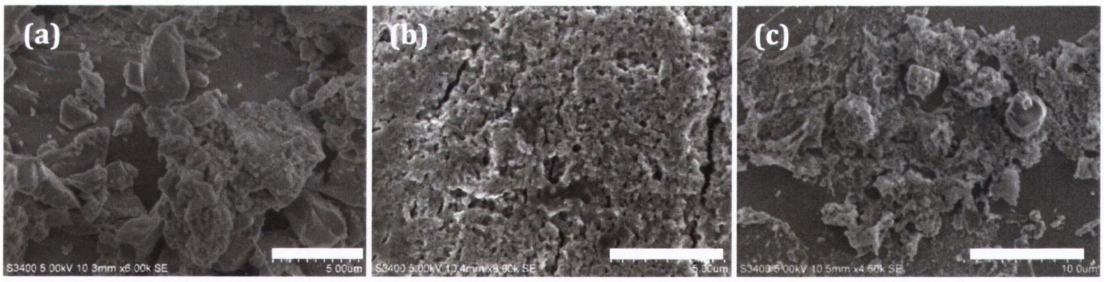

Figure 3.56: SEM micrographs of andersonite (a) on FDTO (scale bar is 5 μm); (b) after one hour cycling in 0.2 M $LiClO_4$ (scale bar is 5 μm); and (c) after one hour cycling in 0.2 M $KClO_4$ (scale bar is 10 μm).

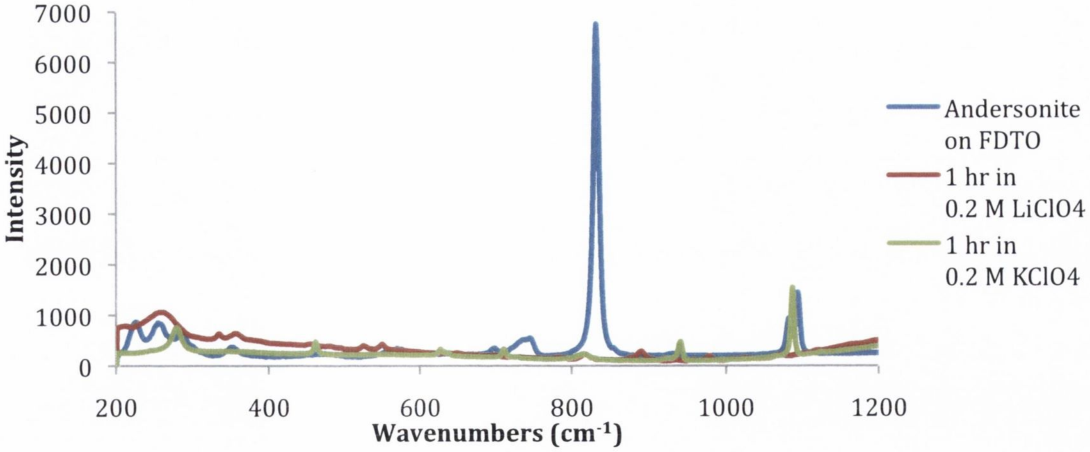

Figure 3.57: Raman spectra of andersonite before and after electrochemical treatment.

An interesting difference between the samples is the mode of ion diffusion. The lithium sample has lost the carbonate anion and there is evidence of perchlorate incorporation from the EDX data (**Figure 3.58**). In the potassium sample the carbonate anions are still present, although Raman spectroscopy suggests that now the carbonate species present are of the same symmetry – the v_1 symmetric carbonate stretches at 1089 and 1079 cm^{-1} in andersonite have become one peak at 1087 cm^{-1}. There is no chlorine detected in EDX (**Figure 3.59**) so it is possible that the Raman stretch at 939 cm^{-1} is from the carbonate v_2 asymmetric bend (926 cm^{-1} in andersonite). The presence of potassium and omission of sodium implies an ion-exchange pathway, or that the U(VI) dissolved as sodium uranyl carbonate species and the potassium ions were required for charge balance. Given the evidence that the andersonite has not been retained, it is likely that the crystals seen in **Figure 3.56(c)** are in fact $CaCO_3$ crystals. This would support the high Ca, C and O% in the product.

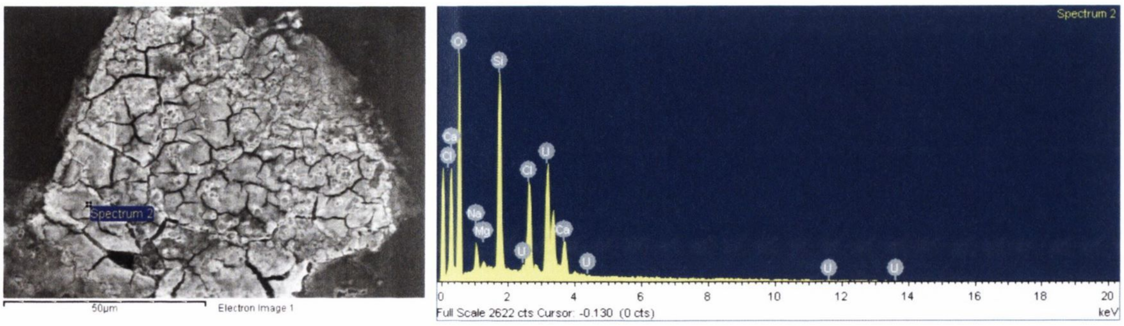

Figure 3.58: SEM micrograph and EDX spectrum of sample of andersonite after 1 hour CV in 0.2 M $LiClO_4$. Three spectra were taken at different points on the sample. For andersonite, U, O, Cl, Si and traces of Ca and Na were detected. Si most likely was from the FDTO electrode. C was not detected.

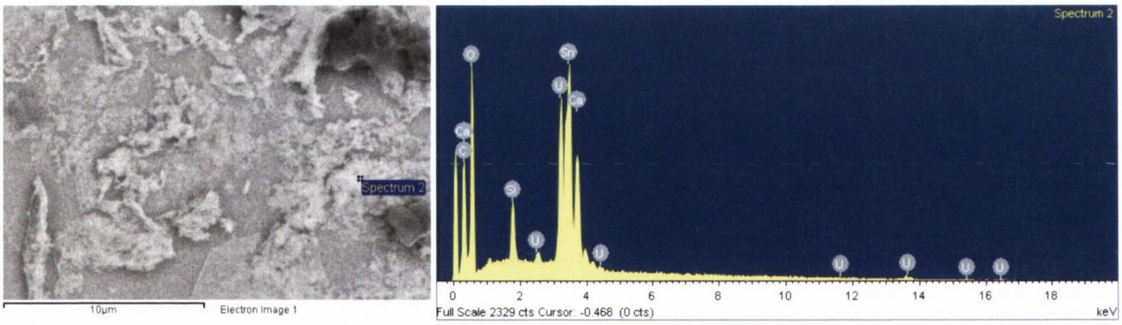

Figure 3.59: SEM micrograph and EDX spectrum of sample of andersonite after 1 hour CV in 0.2 M $KClO_4$. Three spectra were taken at different points on the sample. For andersonite, U, O, C, Ca and traces of K and Sn were detected. Sn was most likely from the FDTO electrode. Na and Cl were not detected.

In the case of both grimselite and andersonite, 12 hour electrolysis at -1.2 V yields an amorphous black compound that is not an efficient Raman scatterer and is composed primarily of uranium and oxygen. Electrolysed grimselite contained traces of sodium, while electrolysed andersonite contained evidence of perchlorate incorporation. The differences in ion transport may be linked to the pore size: the andersonite structure can better accommodate the incorporation of the perchlorate complex anion.

3.4.3.2. Carbonate Electrolytes

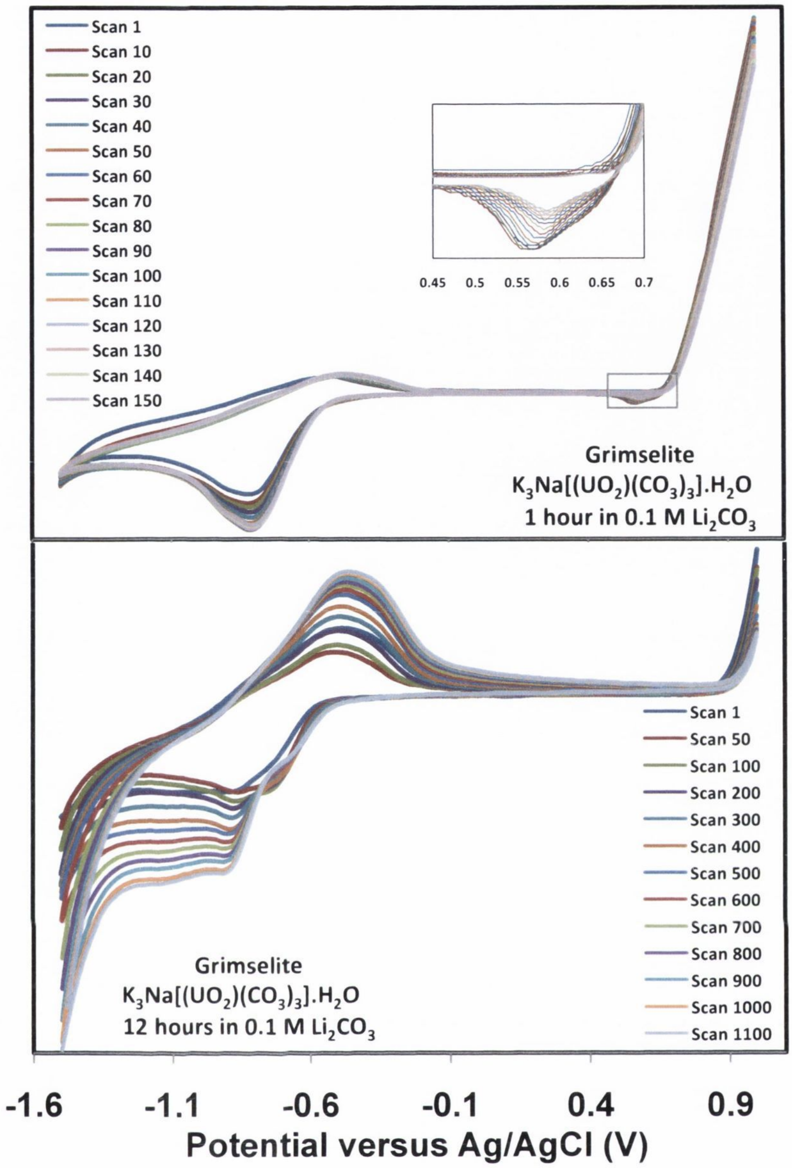

Figure 3.60: Voltammograms of grimselite cycling in 0.1 M Li_2CO_3.

The grimselite voltammogram of cycling in Li_2CO_3 shows a small redox couple with a faint shoulder [**Figure 3.60(top)**]. The couple has a reduction peak at -0.797 V and a coupled oxidation peak at -0.482 V and has been assigned to be the U(VI)/(V) reduction. There is a small couple that decreases in intensity over time to settle on -0.587 V after one hour, with a coupled oxidation at -0.486 V. This peak is in the region of the two electron reduction of uranyl (**Equation 3.7**) that has been reported to fall at 0.524 V.[58]

$$UO_2^{2+} + 4H^+ + 2e^- \rightleftharpoons U^{4+} + 2H_2O \qquad \mathbf{3.7}$$

If uranyl is being reduced directly to U(IV) then this would account for the low intensity of the peak that has been assigned to the U(V)/(IV) reduction at -0.904 V. This presents as a small shoulder on the major reduction peak with a coupled oxidation of -0.813 V and becomes more noticeable as the peak at -0.587 V decreases. In the 12 hour voltammogram this shoulder has grown to form a diffuse peak centred at -1.099 V with equal intensity to the U(VI)/(V) reduction at -0.899 V [**Figure 3.60(bottom)**]. The two coupled oxidation processes have merged into an asymmetric oxidation peak centred at -0.481 V. There is a shoulder on the cathodic side of the peak at -0.821 V that could be attributed to the U(IV)/(V) oxidation. Again there is an additional peak in the voltammogram but at -0.659 V this is a potential more consistent with the electrolysis of water – reported to occur at -0.631 V with respect to the Ag/AgCl electrode (**Equation 3.8**).

$$2H_2O + 2e^- \rightleftharpoons 2OH^- + H_2\uparrow \qquad \textbf{3.8}$$

In the one-hour cycle with K_2CO_3 [**Figure 3.61(top)**] there are two very similar redox couples with reduction peaks at -0.662 and -0.875 V and coupled oxidation peaks at -0.587 and -0.788 V. In the 12-hour voltammogram [**Figure 3.61(bottom)**] the reduction peak at -0.662 V is observed to decrease after scan 100 to a final value of -0.639 V. This decrease is not consistent with the U(VI)/(V) couple, therefore it is likely that this peak is in fact the same feature observed in the Li_2CO_3 voltammograms, i.e. the two electron reduction of water. The reduction peak at -0.875 V in the one-hour voltammogram is therefore assigned to the U(VI)/(V) couple. There is a flattening on the cathodic side of the peak that could be attributed to a weak U(V)/(IV) signal. This is more obvious in the 12-hour voltammogram where the diffuse U(V)/(IV) peak appears at -1.099 V with a coupled oxidation at -0.541 V; the sharper signal at -0.919 V with a coupled oxidation at -0.681 V has been assigned to the U(VI)/(V) couple. These features are summarised in **Table 3.14**.

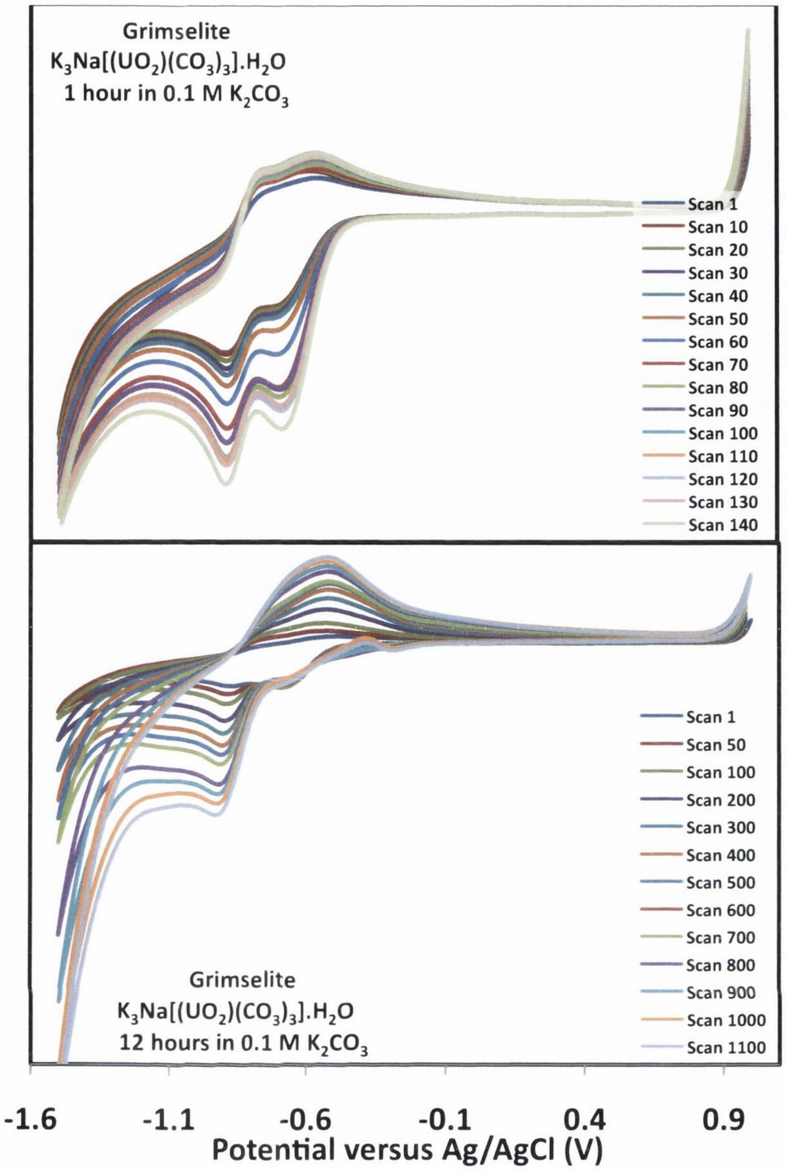

Figure 3.61: Voltammograms of grimselite cycling in 0.1 M K_2CO_3.

Table 3.14: Summary of electrochemical features in analysis of grimselite with carbonate electrolytes.

	After one hour			After 12 hours		
Electrolyte	**U(VI)/(V) (V)**	**U(V)/(IV) (V)**	**Additional Peak**	**U(VI)/(V) (V)**	**U(V)/(IV) (V)**	**Additional Peak**
0.1 M Li_2CO_3	-0.797	-0.904	-0.587 V UO_2^{2+}/U^{4+}	-0.899	-1.099	-0.659 V H_2O/H_2
0.1 M K_2CO_3	-0.875	(-1.078)	-0.662 V H_2O/H_2	-0.919	-1.059	-0.639 V H_2O/H_2

In both cases the cycled product was analysed by Raman spectroscopy and in both cases the only peaks remaining were from carbonate salts (**Figure 3.62**). The weak/ diffuse

U(V)/(IV) reductions imply a lower concentration of U(V) in the sample, this is most likely due to the disproportionation of U(V) into U(VI) and U(IV) compounds. As the U(VI) species would be water soluble, it is probable that these would go into solution and leave the insoluble U(IV) on the surface – if this U(IV) species is UO_2 then it is expected to be a poor Raman scatterer.

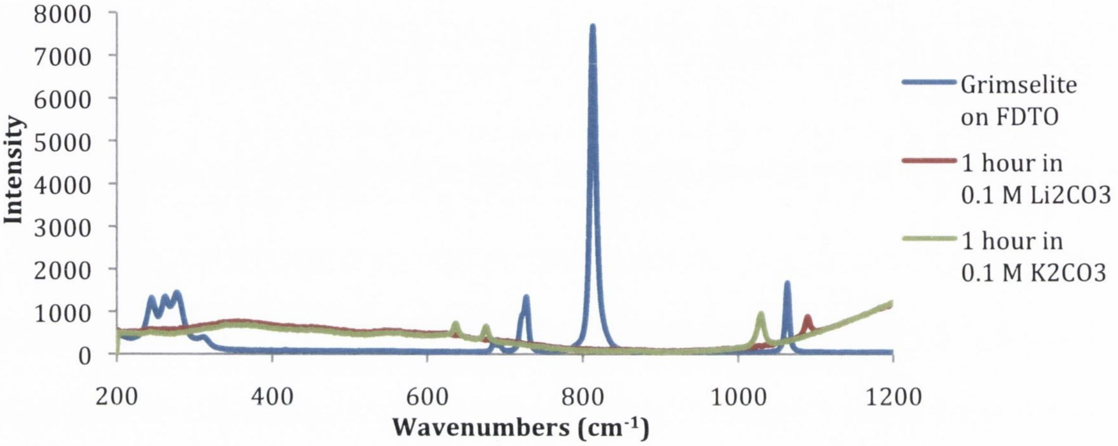

Figure 3.62: Raman spectra of grimselite before and after electrochemical analysis with carbonate electrolytes.

The grimselite cycling products were examined by SEM (**Figure 3.63**) and EDX spectroscopy (**Figure 3.64**). There is a growth of star shaped crystals visible in the SEM micrographs of the sample that was cycled in Li_2CO_3; these are particularly evident after 12 hours [**Figure 3.63(c)**]. These crystals appear to consist of carbonate salts – the high carbon and oxygen content of these crystals relative to natural grimselite implies carbonate anion incorporation and the formation of uranium(IV) and alkaline earth metal carbonate salts.

Figure 3.63: SEM micrographs of grimselite (a) on FDTO; (b) after one hour cycling; and (c) after 12 hours cycling in 0.1 M Li_2CO_3. Scale bar is 10 μm.

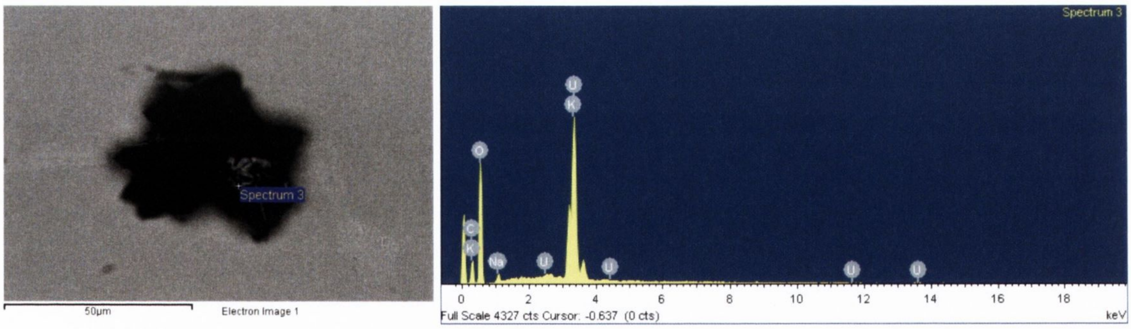

Figure 3.64: SEM micrograph and EDX spectrum of sample of grimselite after 1 hour cycling in 0.1 M Li_2CO_3. Spectra were taken at 3 distinct points on the surface of the cycled product. For grimselite, U, O, C, K and traces of Na were detected.

The K_2CO_3 samples were also analysed and SEM showed a substantial phase alteration to the grimselite structure (**Figure 3.65**). The Raman spectrum showed no peaks except for weak carbonate stretches and this is supported by EDX spectroscopy as one area surveyed had indication of carbonate anions. However, the other two areas of the surface analysed showed only potassium, chlorine and small amounts of oxygen and silicon (Si is most likely a false positive from the electrode).

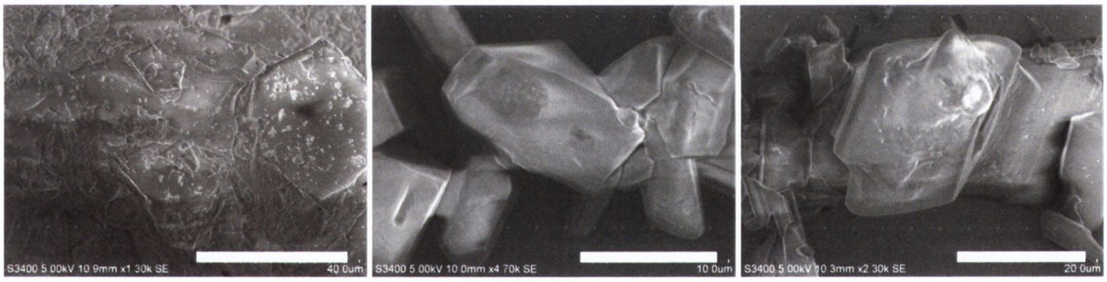

Figure 3.65: SEM micrographs of grimselite (a) on FDTO (scale bar is 40 µm); (b) after one hour cycling (scale bar is 20 µm); and (c) after 12 hours cycling in 0.1 M K_2CO_3 (scale bar is 20 µm).

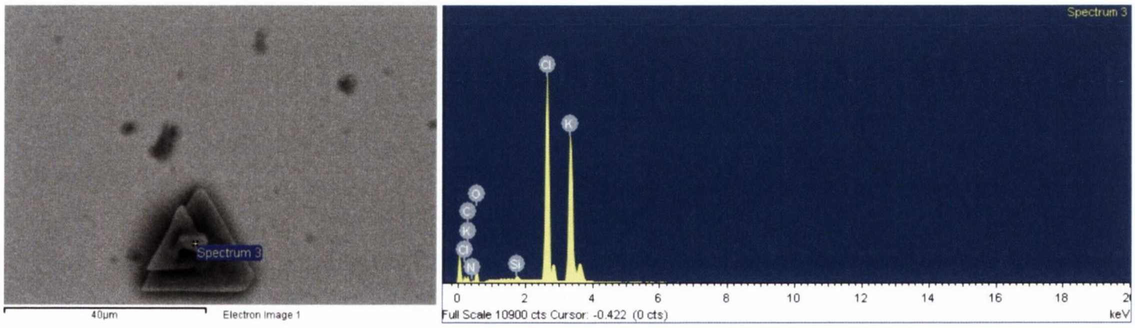

Figure 3.66: SEM micrograph and EDX spectrum of sample of grimselite after 1 hour cycling in 0.1 M K_2CO_3. Spectra were taken at 3 distinct points on the surface of the cycled product. For grimselite, O, K, Cl and traces of C and Si were detected. Na and U were not detected.

This implies that the crystals visible after one and 12 hours are, in fact, potassium chloride. The lack of uranium is surprising although it is suggested that the uranium dissolved into the aqueous solution as sodium or potassium uranyl carbonates.

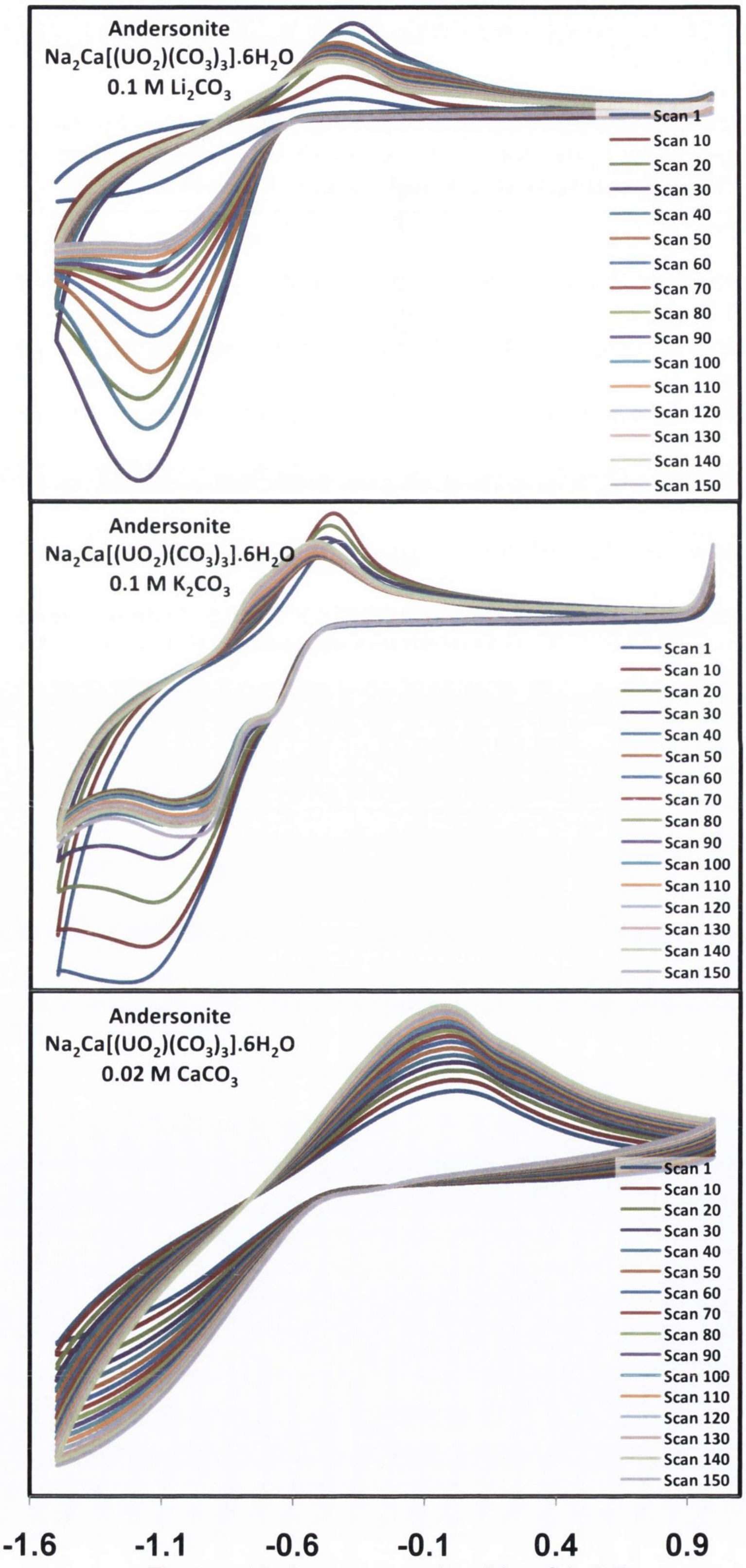

Figure 3.67: One-hour voltammograms of andersonite cycling in carbonate electrolytes.

When andersonite is cycled with the carbonate electrolytes, the shapes of the voltammograms are very different. In the Li_2CO_3 voltammogram there is a rapid growth in the intensity of the peaks until scan 30 (with a local minimum at -1.167 V) before the peaks begin to decrease – most likely due to the hindrance of ion mobility in the sample – to yield a reduction peak at -1.075 V with a broad coupled oxidation peak centred at -0.428 V. This has been assigned as the U(VI)/(V) couple. There appears to be a second oxidation peak at 0.022 V but there is no obvious coupled reduction peak – scan 1 seems to have a diffuse peak on the anodic side of the U(VI)/(V) peak (centred at approximately -0.75 V) but this has merged into the major process by scan 10. The 12-hour voltammogram shows three reduction peaks – at -0.699, -0.859 and -1.099 V – that have merged to create one steep graph. The peak at -0.859 V has been assigned to the U(VI)/(V) couple and the peak at -1.099 V to the U(V)/(IV) couple. The coupled oxidation peaks occur at -0.721 and -0.421 V, respectively. The third peak at -0.699 V is possibly due to hydrolysis of water (predicted to occur at -0.631 V with respect to the Ag/AgCl electrode,[58] **Equation 3.8**).

In andersonite with K_2CO_3 the potassium cations appear to produce a passivation effect (as with grimselite in 0.2 M $KClO_4$), causing the current values of the peaks to decrease over time until approximately scan 80, whereupon the peaks begin to grow again, presumably from increased permeation of ions through the sample. There is a clear major U(VI)/(V) reduction peak visible at -0.922 V and a minor U(V)/(IV) peak at -1.042 V, with coupled oxidation peaks at -0.521 and -0.764 V. In the 12-hour voltammogram these peaks continue to grow to yield a U(VI)/(V) peak at -0.919 V and a diffuse U(V)/(IV) peak centred at -1.059 V. The coupled oxidation peaks are at -0.681 and -0.561 V. There are extra features in both the one and 12-hour voltammograms at -0.661 and -0.639 V, respectively, that can most likely be attributed to the reduction of water (**Equation 3.8**).[58]

When andersonite was cycled in 0.002 M $CaCO_3$ the reduction peak was broad and diffuse and difficult to identify. The peak was centred at approximately -1.16 V and was accompanied by a large oxidation peak at -0.41 V. This couple was assigned as the

U(VI)/(V) reduction; no U(V)/(IV) peak could be discerned. After 12 hours the reduction peak was centred at approximately -1.36 V with a coupled oxidation peak at -0.101 V. This was assigned to be the U(VI)/(V) redox couple and again, no U(V) reduction was observed.

Table 3.15: Summary of electrochemical features in analysis of uranyl carbonates with carbonate electrolytes (Figure 3.67).

	After one hour			After 12 hours		
Electrolyte	**U(VI)/(V) (V)**	**U(V)/(IV) (V)**	**Additional Peak**	**U(VI)/(V) (V)**	**U(V)/(IV) (V)**	**Additional Peak**
0.1 M Li_2CO_3	-1.075	-	-	-0.859	-1.099	-0.699 V H_2O/H_2
0.1 M K_2CO_3	-0.922	-1.042	-0.667 V H_2O/H_2	-0.919	-1.059	-0.639 V H_2O/H_2
0.002 M $CaCO_3$	-1.16	-	-	-1.36	-	-

In each of the three carbonate electrolytes Raman spectroscopy shows the destruction of the uranyl and the alteration of the carbonate anions (**Figure 3.68**). There are small stretches in the uranyl region of the Li_2CO_3, K_2CO_3, $CaCO_3$ spectra of 830, 807 and 817 cm^{-1}, respectively. The lower wavenumbers than that of andersonite (832 cm^{-1}) indicate reduced species. For the case of the K_2CO_3 product, the Raman stretch of 807 cm^{-1} can be converted to a uranyl bond length of 1.804 Å using Bartlett and Cooney's relationship (**Equation 3.2**).[33] This is only 0.1 Å longer than the average bond length of 1.792 Å in andersonite, but is consistent with reported experimental[40] and theoretical[39,41] values for uranyl(V) bond lengths.

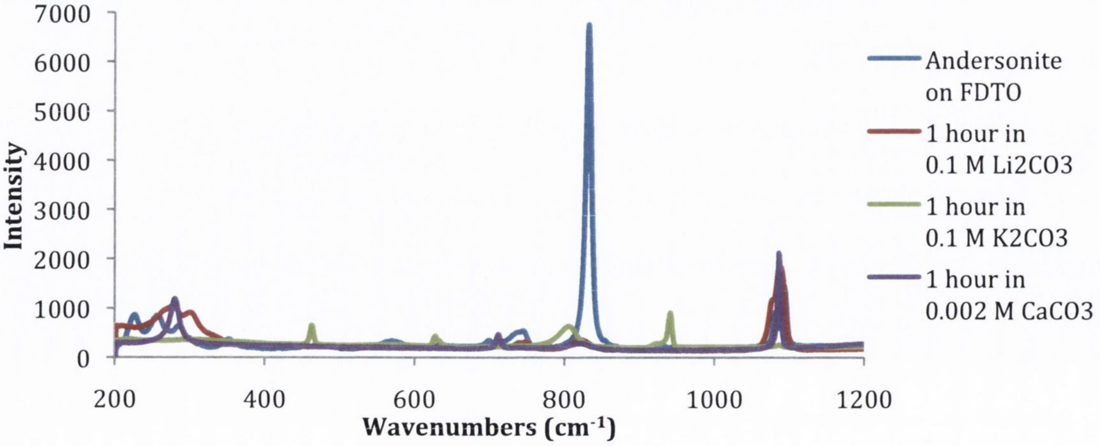

Figure 3.68: Raman spectra of andersonite before and after electrochemical treatment.

When comparing the Li_2CO_3 samples, SEM shows a substantial morphology change. After one hour cycling long, thin crystals have formed on the surface [**Figure 3.69(c)**]. These appear to dissolve after 12 hours [**Figure 3.69(c)**]. According to EDX analysis, it is possible that some andersonite is retained in the cycling products – consistent with a weak Raman signal at 830 cm^{-1} – but a majority of the products are a mixture of carbonate salts, namely $CaCO_3$ (**Figure 3.70**). After 12 hours much of the sample has dissolved, yielding small crystals of uranium(IV), calcium and sodium carbonates (**Figure 3.71**).

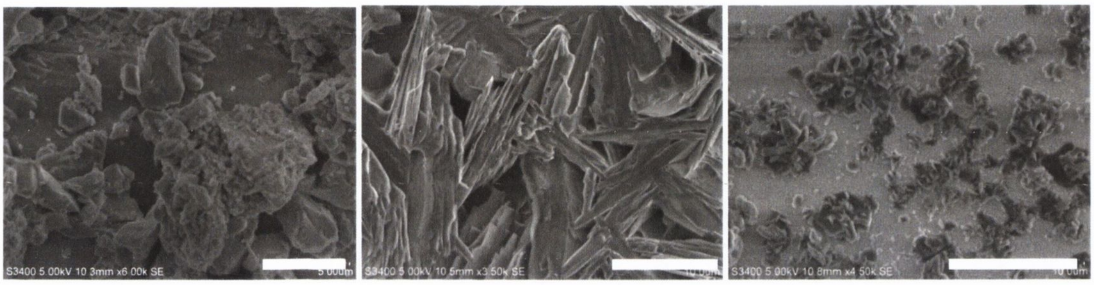

Figure 3.69: SEM images of andersonite (a) before cycling (scale bar is 5 μm); after (b) one hour and (c) 12 hours cycling in 0.1 M Li_2CO_3 (scale bar is 10 μm).

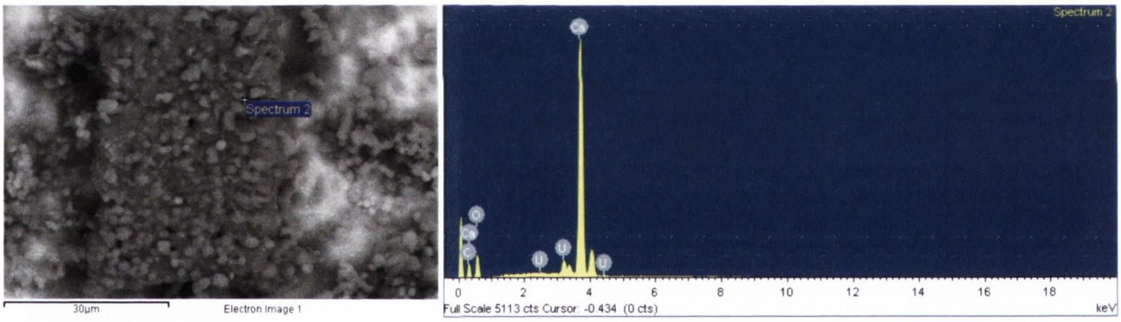

Figure 3.70: SEM micrograph and EDX spectrum of sample of andersonite after 1 hour cycling in 0.1 M Li_2CO_3. Spectra were taken at 3 distinct points on the surface of the cycled product. For andersonite: U, O, Ca, C and traces of Sn and Na were detected. Sn was most likely from the FDTO electrode.

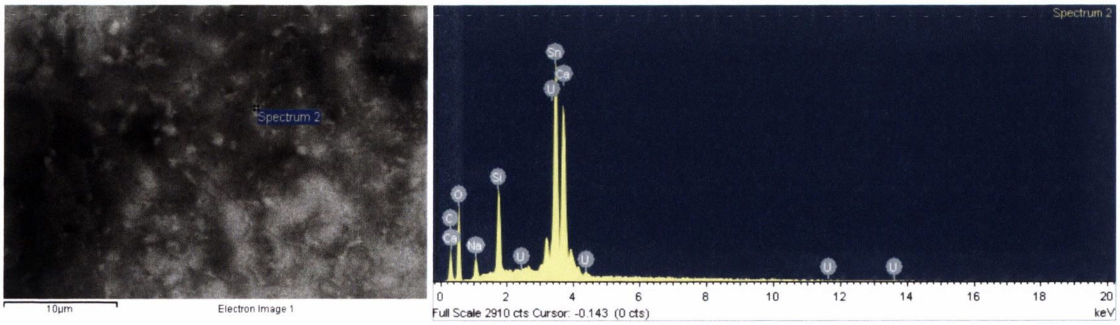

Figure 3.71: SEM micrograph and EDX spectrum of sample of andersonite after 12 hours cycling in 0.1 M Li_2CO_3. Spectra were taken at 4 distinct points on the surface of the cycled product. For andersonite: O, Sn, Ca, C, U, and traces of Si, and Na were detected. Sn was most likely from the FDTO electrode.

SEM micrographs of the samples cycled in K_2CO_3 show the growth of crystals on the surface over time (**Figure 3.72**). Examining the Raman (**Figure 3.68**) and elemental composition of these crystals (**Figure 3.73**) implies that these crystals are most likely U(V) carbonate salts. Rutherfordine (UO_2CO_3) has a uranyl Raman stretch at 886 cm^{-1}[165] while the crystals formed after 12 hours cycling have a Raman stretch of 807 cm^{-1}, implying a U(V) species. After 12 hours EDX shows that there is no sodium or calcium remaining in the sample although there is 5% potassium in the sample (**Figure 3.74**).

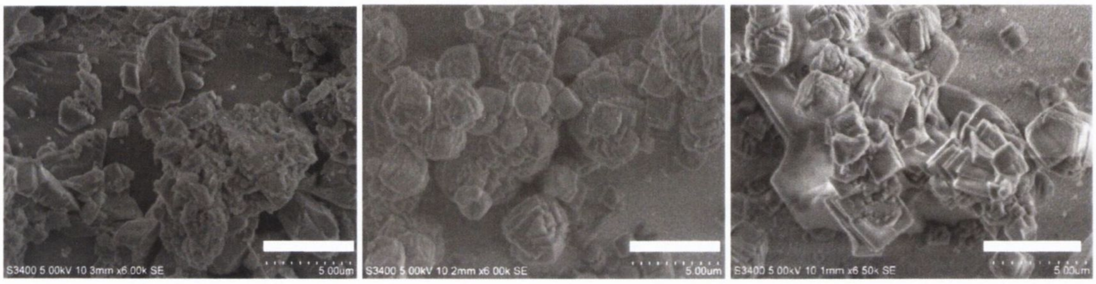

Figure 3.72: SEM images of andersonite (a) before cycling; after (b) one hour and (c) 12 hours cycling in 0.1 M K_2CO_3 (scale bar is 5 μm).

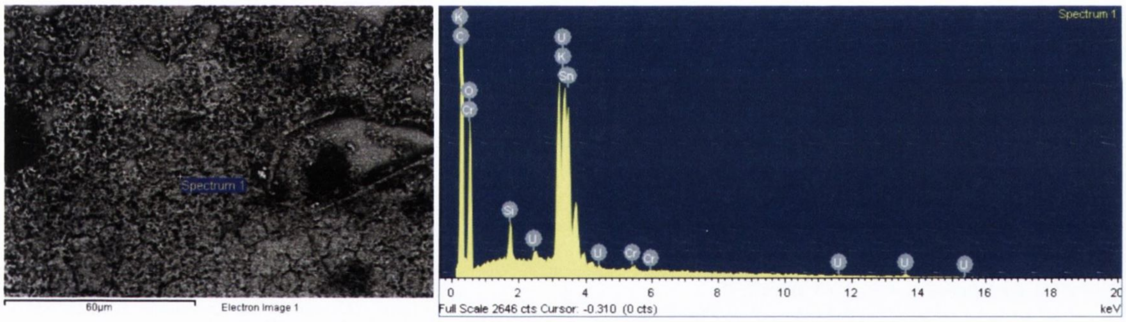

Figure 3.73: SEM micrograph and EDX spectrum of sample of andersonite after 1 hour cycling in 0.1 M K_2CO_3. Spectra were taken at 3 distinct points on the surface of the cycled product. For andersonite, C, U, O, Ca, and traces of Sn and K were detected. Sn was most likely from the FDTO electrode.

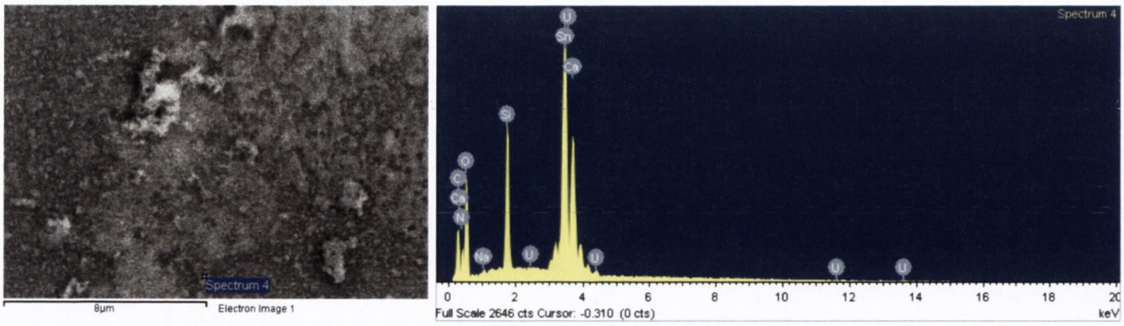

Figure 3.74: SEM micrograph and EDX spectrum of sample of andersonite after 12 hours cycling in 0.1 M K_2CO_3. Spectra were taken at 3 distinct points on the surface of the cycled product. For andersonite, O, Ca, C, U, and traces of Sn and Na were detected. Sn was most likely from the FDTO electrode.

The alteration of cation concentration with longer cycling times suggests that it is in fact cation transport necessary for charge balance in these systems and it is therefore interesting to note the retardation effect observed with the potassium electrolyte.

The structure of andersonite is decomposed during cycling with $CaCO_3$ [**Figure 3.75(b)**], but slowly over time crystals re-appear on the surface [**Figure 3.75(c)**]. These crystals appear to be calcite ($CaCO_3$) precipitating on the surface of the electrode (**Figure 3.76** and **3.77**). After 12 hours there is only a fraction of the expected concentration of uranium remaining on the surface; the disproportionation of U(V) has led to the dissolution of the uranyl carbonate species and the deposition of U(IV) on the surface.

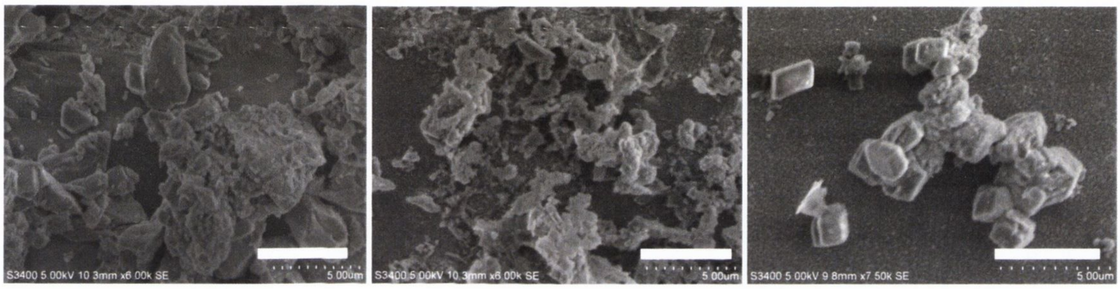

Figure 3.75: SEM images of andersonite (a) before cycling; after (b) one hour and (c) 12 hours cycling in 0.002 M $CaCO_3$ (scale bar is 5 μm).

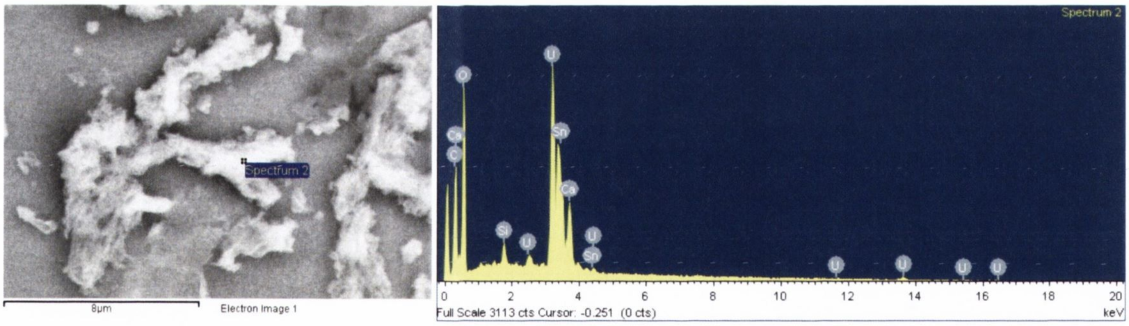

Figure 3.76: SEM micrograph and EDX spectrum of sample of andersonite after 1 hour cycling in 0.002 M $CaCO_3$. Spectra were taken at 3 distinct points on the surface of the cycled product. For andersonite: U, O, C, Ca, and traces of Sn and Si were detected. Sn was most likely from the FDTO electrode. Na was not detected.

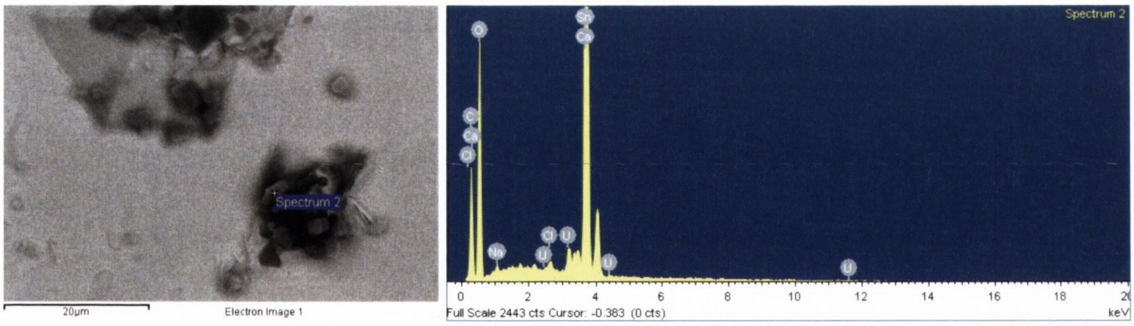

Figure 3.77: SEM micrograph and EDX spectrum of sample of andersonite after 12 hours cycling in 0.002 M $CaCO_3$. Spectra were taken at 3 distinct points on the surface of the cycled product. For andersonite: O, C, Ca, U and traces of Na and Sn were detected. Sn was most likely from the FDTO electrode.

3.4.3.3. Summary

It is interesting that in all of the studies of the two carbonate minerals there was evidence of potassium and calcium incorporation from EDX analysis – it is not possible to detect lithium using EDX so this is the only example in this work of cation incorporation into the mineral. The presence of potassium in the andersonite products with $KClO_4$ and K_2CO_3 could only have come from cation incorporation as andersonite does not contain potassium. This is very different to the analyses of the uranyl oxyhydroxide and phosphate minerals.

Table 3.16: Summary of electrochemical features in different electrolytes of the two uranyl carbonate minerals examined.

	1 hour Cycling				12 hours Cycling			
Grimselite	**U(VI)/(V) (V)**	**U(V)/(IV) (V)**	**Extra Peak**	**Assigned**	**U(VI)/(V) (V)**	**U(V)/(IV) (V)**	**Extra Peak**	**Assigned**
$LiClO_4$	-0.91	-1.246			-0.879	-1.219		
$KClO_4$	-0.82	-1.006			-0.859	-		
Li_2CO_3	-0.797	-0.904	-0.587	UO_2^{2+}/U^{4+}	-0.899	-1.099	-0.659	H_2O/H_2
K_2CO_3	-0.875	(-1.078)	-0.662	H_2O/H_2	-0.919	-1.059	-0.639	H_2O/H_2
Andersonite	**U(VI)/(V) (V)**	**U(V)/(IV) (V)**	**Extra Peak**	**Assigned**	**U(VI)/(V) (V)**	**U(V)/(IV) (V)**	**Extra Peak**	**Assigned**
$LiClO_4$	-0.767				-0.839			
$KClO_4$	-0.871				-0.919			
Li_2CO_3	-1.075	-			-0.859	-1.099	-0.699	H_2O/H_2
K_2CO_3	-0.922	-1.042	-0.667	H_2O/H_2	-0.919	-1.059	-0.639	H_2O/H_2
$CaCO_3$	-1.16	-			-1.36	-		

For grimselite the passivation effects from potassium electrolytes were unexpected given the presence of potassium cations within grimselite; in $KClO_4$ the intensity of the peaks decreased for the first few hours of the voltammogram and in K_2CO_3 the peaks increased slowly for the duration of the experiments. The products of the $KClO_4$ experiments were alkali metal uranium oxide salts indicating the dissolution of the carbonate anion. There was no evidence of perchlorate incorporation but there was a decrease in cation concentration. In K_2CO_3 the structure of grimselite was dissolved but crystals appeared to grow on the surface. These were found to be mostly KCl and K_2CO_3 crystals from EDX data, although it is unclear from where the chlorine originates. The dissolution of carbonate minerals and formation of carbonate salts on the electrode surface is a known phenomenon in the studies on uranyl carbonates[5a] and is demonstrated by the growth of thin crystals in grimselite and andersonite samples with Li_2CO_3 and K_2CO_3 and with andersonite with $CaCO_3$.

Table 3.17: Diffusion constants of uranyl carbonate U(VI)/(V) couples after 12 hours cycling.

Mineral	**Electrolyte**	**Reduction Diffusion Coefficient ($cm^2 s^{-1}$)**	**Oxidation Diffusion Coefficient ($cm^2 s^{-1}$)**
Grimselite	$LiClO_4$	1.208×10^{-13}	**3.491×10^{-13}**
	$KClO_4$	4.349×10^{-14}	**2.042×10^{-13}**
	Li_2CO_3	3.020×10^{-16}	**2.446×10^{-14}**
	K_2CO_3	**2.718×10^{-15}**	1.208×10^{-15}
Andersonite	$LiClO_4$	7.360×10^{-14}	**1.259×10^{-13}**
	$KClO_4$	1.572×10^{-13}	**3.414×10^{-13}**
	Li_2CO_3	3.919×10^{-15}	**1.568×10^{-14}**
	K_2CO_3	**2.134×10^{-16}**	6.968×10^{-17}
	$CaCO_3$	4.355×10^{-14}	**6.271×10^{-14}**

Examining the diffusion constants of the U(VI)/(V) redox couples (**Table 3.17**) shows that, contrary to the other minerals examined, there is a mixture of ion transport pathways in the minerals. For both minerals in K_2CO_3 the reduction D_{CT} was higher (in bold), indicating cation transport when K_2CO_3 is the electrolyte. This is consistent with the analysis of the products and the evidence of potassium incorporation during the experiment.

3.5. Conclusions

3.5.1. Potential Redox Mechanisms with Radionuclides in Spent Nuclear Fuel

The reduction potentials of the minerals examined above and the reported values for studtite[23] and U_3O_8[22] are given in **Table 3.18**.

Table 3.18: The U(VI)/(V) reduction potentials of uranium minerals.

Mineral	U(VI)/(V) Reduction Potential (V)
Meta-autunite	-0.724
Studtite	-0.730
Na-metaschoepite	-0.755
Andersonite	-0.778
Becquerelite	-0.785
Schoepite	-0.788
Metatorbernite	-0.788
Compreignacite	-0.814
Meta-uranocircite	-0.839
U_3O_8	-0.87[a]
Grimselite	-0.907

[a] From Dueber and Bond's solid-state electrochemical analysis of U_3O_8, cycling in 0.1 M LiCl.[22]

The formal redox potential of the Np(V)/(IV) couple in acidic media is +0.801 V with respect to the Ag/AgCl reference electrode.[70] This is within range of each of the uranyl minerals tested (with the possible exception of meta-autunite). This implies that the suggested mechanism for the reduction of studtite and concomitant oxidation of the discrete insoluble Np(IV) phase[4e] to Np(V) as $[NpO_2]^+$ is possible for all of the minerals in the series.

Studies into the incorporation of neptunium into uranyl sheet minerals have found that Np will preferentially associate with minerals that have sheets of charged polyhedra. Burns *et al.* suggested that the interlayer cations in these minerals were necessary for charge balance when $[NpO_2]^+$ replaces uranyl.[38] This was supported by the incorporation of neptunium into crystals of sodium substituted metaschoepite, but not metaschoepite.[71] The electroneutral sheets of schoepite and metaschoepite cannot incorporate the Np(V) as there is no capacity for charge balance.

Previous investigations of neptunium incorporation into torbernite show that it is neptunium(VI) that is incorporated into the phosphate and that uptake is increased by hydrothermal conditions.[72] The reduction potential of metatorbernite is -0.788 V which allows the possibility of a redox mechanism occurring but this is unlikely.

The two carbonate minerals examined showed reduction potentials of -0.778 and -0.907 V which would be capable of oxidising Np(IV) but given the instability of the reduced compounds it is likely that a stable Np-substituted phase would not form.

3.5.2. Structure-Reactivity relationships in Uranyl Minerals

There have been previous studies associating the U(VI)/(V) reduction potential with uranyl Raman stretching frequency: the lower the frequency, the more negative the reduction potential.[41] This was investigated during the examination of the ten uranyl minerals: studtite, schoepite, Na-metaschoepite, compreignacite, becquerelite, meta-autunite, metatorbernite, meta-uranocircite, grimselite and andersonite (**Figure 3.78**).

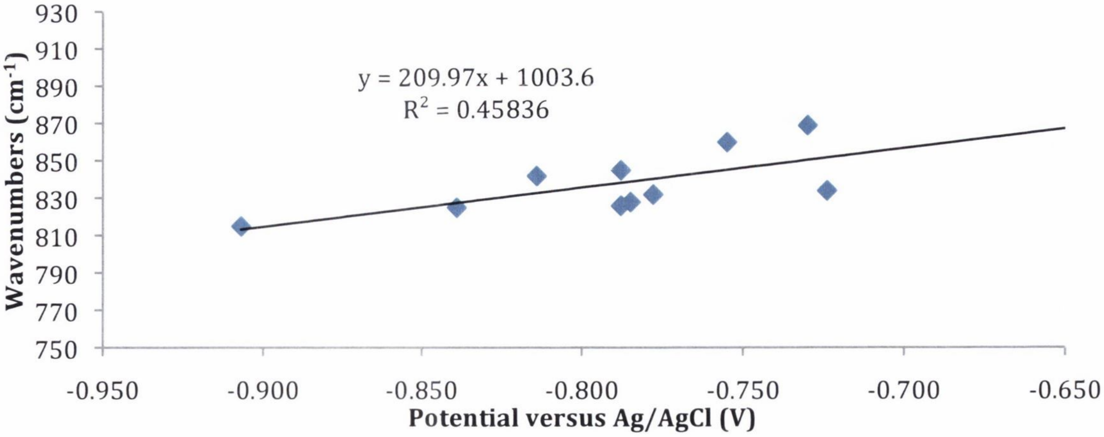

Figure 3.78: Uranyl Raman stretching frequency versus U(VI)/(V) reduction potential.

Upon closer examination it is possible to decipher two groups within this graph: the minerals with cation–cation interactions (CCIs) at the uranyl and those without. It is clear that CCIs exist in grimselite – the uranyl occupies D_{3h} symmetry and interacts with two equivalent sodium cations. For andersonite there is a uranyl-sodium interaction that gives rise to the asymmetry in the uranyl moiety. The uranyl phosphates each have cations occupying the interstitial spaces, but the connectivity between the uranyl and the cations differ: in the autunite structure the hydrated calcium ions have Ca–O$_{\text{yl}}$ distances of >3.2 Å, implying no CCIs; in metatorbernite the copper sits in a distorted octahedral arrangement with Cu–O$_{\text{yl}}$ bonds of 2.391(7) and 2.685(8); in meta-uranocircite the barium connects with two uranyl oxygens but with Ba–O$_{\text{yl}}$ distances of 2.934(14) and 2.952(15) Å. This is much longer than the Ca–O$_{\text{yl}}$ interactions in becquerelite (2.444(8), 2.448(8) and 3.000(9) Å to uranyl oxygens from one sheet and a distance of 2.368(7) Å to a uranyl in the opposite sheet), therefore it is also possible to categorise meta-uranocircite as not having CCIs. Schoepite has no interstitial cation and so therefore has no CCIs. In compreignacite, one uranyl oxygen intracts with four K$^+$ cations with an average distance of 2.871(5) Å and in Na-metaschoepite the average Na–O$_{\text{yl}}$ distance is 2.614 Å. These however also show interactions between interstitial cations and so the effect of CCI on the uranyl is decreased.

Table 3.19: Uranyl minerals grouped to show minerals with and without cation–cation interactions. Compreignacite and Na-metaschoepite have weak CCIs marking them as the deciding point between the series.

Mineral	**Cation**	**Average O$_{\text{yl}}$–M$^+$ distance (Å)**	**$d_{U=O}$ (Å)**	**Uranyl Raman Stretch (cm^{-1})**	**U(VI)/(V) Reduction (V)**	
Studtite	-	-	1.769	869	-0.730	No CCI
Schoepite	-	-	1.779	845	-0.788	
Meta-uranocircite	Ba	2.94	1.774	825	-0.839	
Na-metaschoepite	Na	2.61	1.771	860	-0.755	
Compreignacite	K	2.87	1.806	842	-0.814	Weak CCI
Meta-autunite	Ca	[a]	1.774[b]	834	-0.724	CCI
Becquerelite	Ca	2.56	1.794	828	-0.785	
Metatorbernite	Cu	2.54	1.785	826	-0.788	
Andersonite	Na	2.47	1.792	832	-0.778	
Grimselite	Na	2.34	1.795	815	-0.907	Strong CCI

[a] No structural information for meta-autunite exists.
[b] From EXAFS data.[49]

Compreignacite has been categorised as having weak CCIs, therefore it has been assigned to either series when plotting data to give the better fit (**Figure 3.79** and **3.80**).

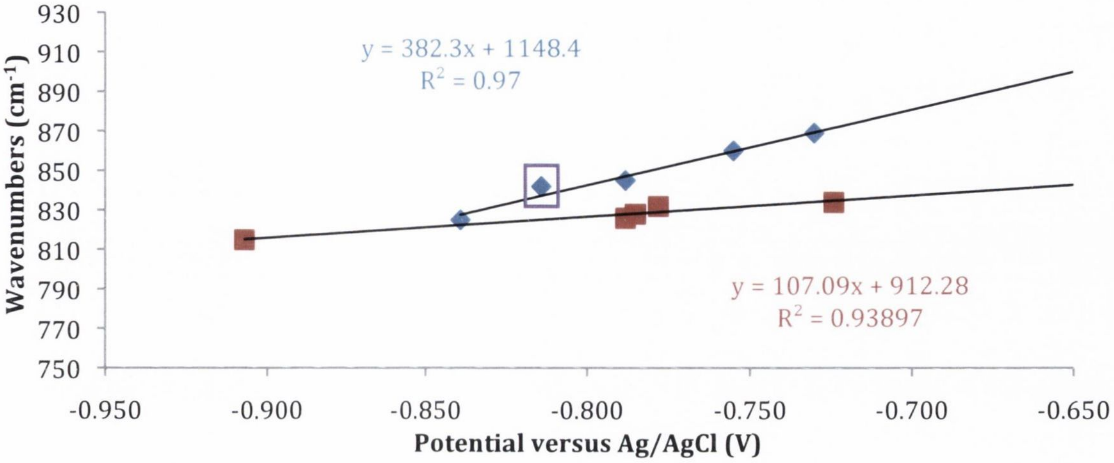

Figure 3.79: Graph of uranyl ν_3 stretch Raman frequency versus U(VI) reduction potential. Uranyl minerals without cation-cation interactions at the uranyl are in blue. Minerals with cation-cation interactions at the uranyl are in red. Compreignacite is highlighted in purple.

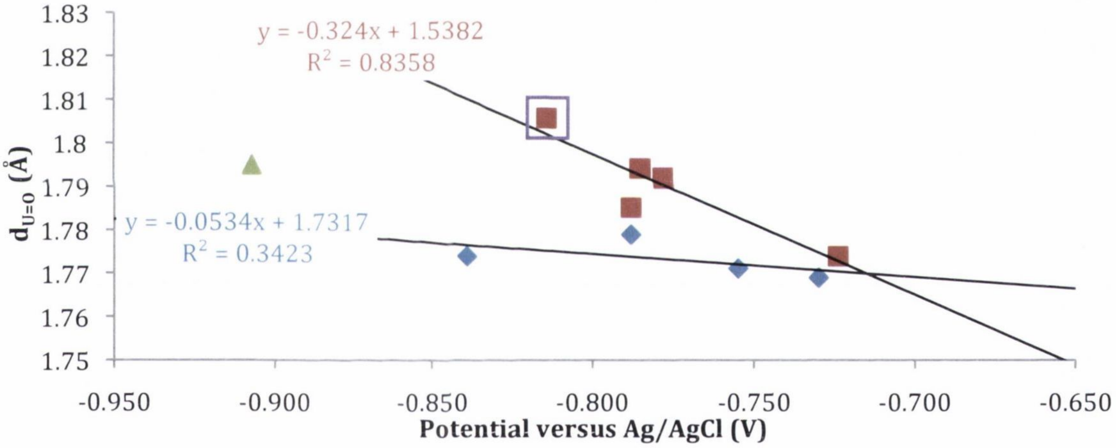

Figure 3.80: Graph of uranyl bond length versus U(VI) reduction potential. Uranyl minerals without cation-cation interactions at the uranyl are in blue. Minerals with cation-cation interactions at the uranyl are in red. Compreignacite is highlighted in purple. Grimselite, with strong cation-cation interactions, is in green.

From this data a relationship between $d_{U=O}$ and the reduction potential is plain to see: the longer the uranyl bond, the more difficult it is to reduce U(VI) to U(V) (**Figure 3.80**). This is likely due to the same reason behind the relationship between the donor strength of the equatorial ligands and the Raman stretching frequency: increased π donation competes with the U(*6d*) orbitals in the U=O_{yl} π_u bond, thus weakening the bond (**Section 1.1.2.**). In this case increased electron density on the metal would elongate the uranyl bond while at the same time making it more difficult to add an electron to reduce U(VI).

The reduction potential is also clearly dependent on the environment of the uranyl. CCIs will affect the likelihood of reduction: both meta-autunite and meta-uranocircite have average uranyl bond lengths of 1.774 Å, but the increased CCIs in meta-autunite account for the increased reduction potential (-0.839 to -0.724). This can be verified by calculating the force constant of the uranyl bond:

$$k = 4.713 \times 10^{-6}\left[v_1 + \left(\frac{v_3^{\ 2}}{1.314}\right)\right] \qquad \textbf{3.9}$$

where k is the force constant of the uranyl bond in mdyne Å^{-1}, v_1 is the uranyl Raman stretch and v_3 is the uranyl stretch from the infrared.[73]

Table 3.20: Minerals and force constants of uranyl bonds.

Mineral	Uranyl Force Constant, k (mdyne Å^{-1})	Uranyl v_3 Raman Stretch (cm^{-1})	$d_{U=O}$ (Å)
Schoepite	2.52	845	1.779
Na-metaschoepite	2.50	860	1.771
Compreignacite	2.78	842	1.806
Becquerelite	2.76	828	1.794
Meta-autunite	2.97	834	1.774
Metatorbernite	2.87	826	1.785
Meta-uranocircite	2.89	825	1.774
Grimselite	2.85	815	1.795
Andersonite	2.96	832	1.792

There does appear to be a relationship between the force constant of the uranyl, k, and the reduction potential (**Figure 3.81**). This is to be expected as the force constant is a measure of the strength of the uranyl bond and is related to the Raman stretching frequency – which does depend on the cation–cation interactions.

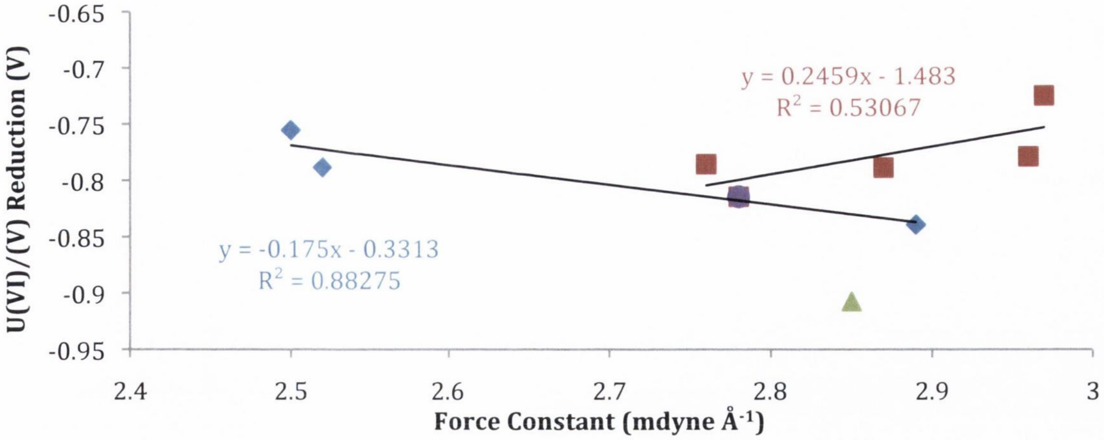

Figure 3.81: Uranyl reduction potential versus the uranyl bond force constants for uranyl minerals. Uranyl minerals without cation-cation interactions at the uranyl are in blue. Minerals with cation-cation interactions at the uranyl are in red. Compreignacite (purple) is included in both series. Grimselite (green) is not included.

Another characterisation technique used throughout this chapter was diffuse reflectance spectroscopy. The calculation of the band-gap of the minerals was to act as a guide for the relative reduction potentials – the band-gap calculation gives insight into the HOMO/LUMO gap, which is the energy required for reduction. These are given in **Table 3.21**.

Table 3.21: The calculated band-gap values for the uranyl minerals.

Mineral	Band-Gap (eV)
Studtite	3.45
Schoepite	2.68
Na-metaschoepite	2.66
Compreignacite	2.53
Becquerelite	2.56
Meta-autunite	2.74
Metatorbernite	2.76
Meta-uranocircite	2.58
Grimselite	2.71
Andersonite	2.71

There is no obvious trend in the band-gap values (**Figure 3.82**), however, given that the outlying points are from studtite and grimselite, it was decided to graph the CCI series separately. This was found to give better fits for the data (**Figure 3.83**).

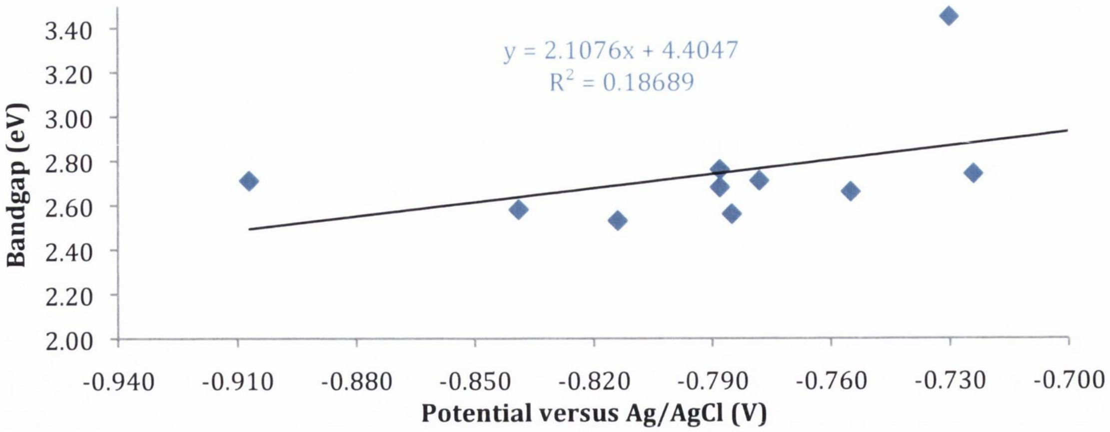

Figure 3.82: Uranyl mineral band-gap against the uranyl reduction potential.

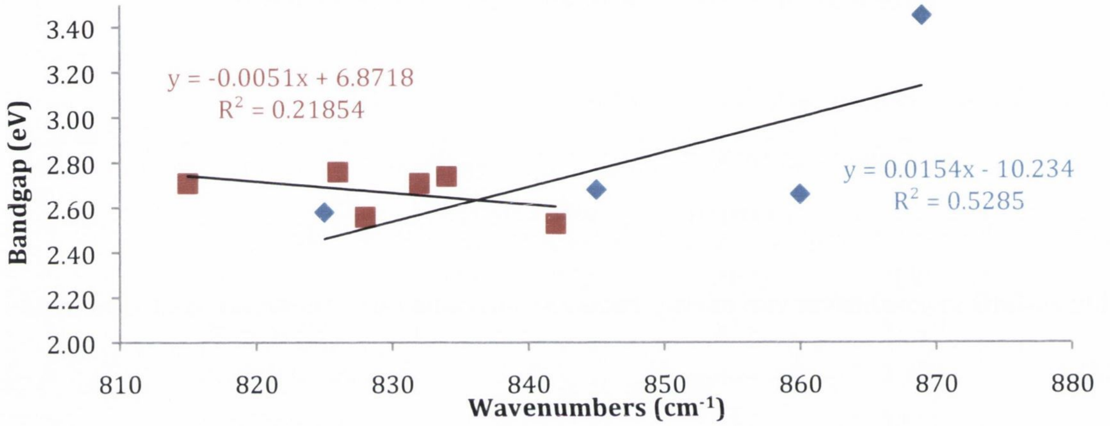

Figure 3.83: Uranyl mineral band-gap against the uranyl reduction potential. Uranyl minerals without cation–cation interactions at the uranyl are in blue. Minerals with cation–cation interactions at the uranyl are in red.

It appears that each of the electronic characteristics (length, Raman frequency, reduction potential, force-constant, band-gap) of the uranyl bonds within the uranyl minerals were affected by CCIs in the structure, indicating a strong structure-reactivity relationship between the local environment at the uranyl and its chemistry.

3.6. Experimental

3.6.1. General

$[UO_2(OAc)_2]\cdot 5H_2O$ was synthesised by literature methods.[74] Schoepite,[75] Na-metaschoepite,[71] compreignacite[27] and becquerelite[32] were synthesised and characterised using Raman and IR spectroscopy and PXRD (below). Single crystals of grimselite[62] and andersonite[63] were synthesised and compared to reported crystal structures. Autunite, torbernite and uranocircite were purchased from eBay and characterised *via* IR and Raman spectroscopy, powder XRD and EDX.

Mineral Powder Patterns:

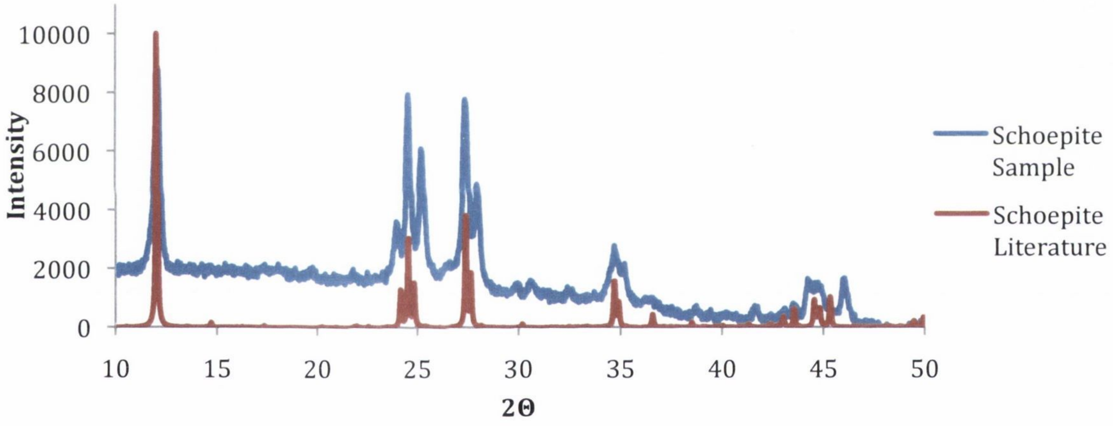

Figure 3.84: Literature[76] and found powder patterns of schoepite.

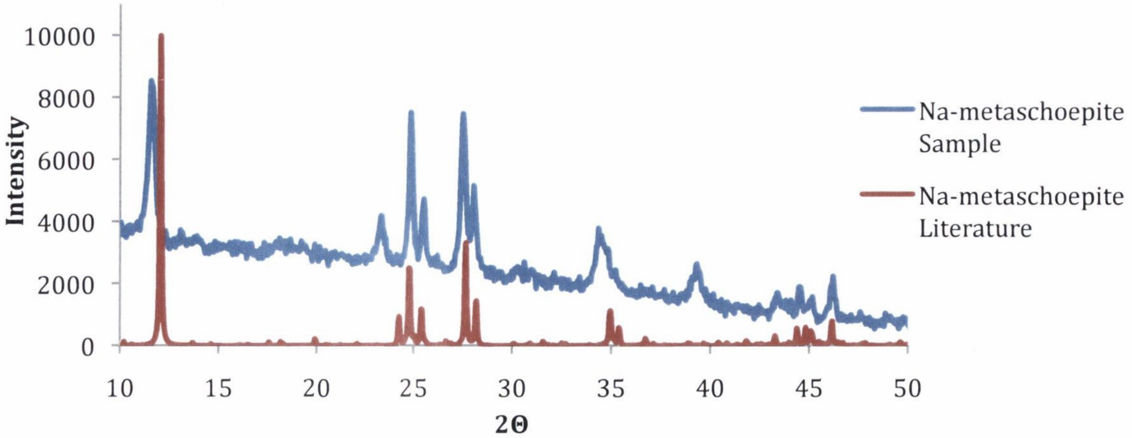

Figure 3.85: Literature[71] and found powder patterns of Na-metaschoepite.

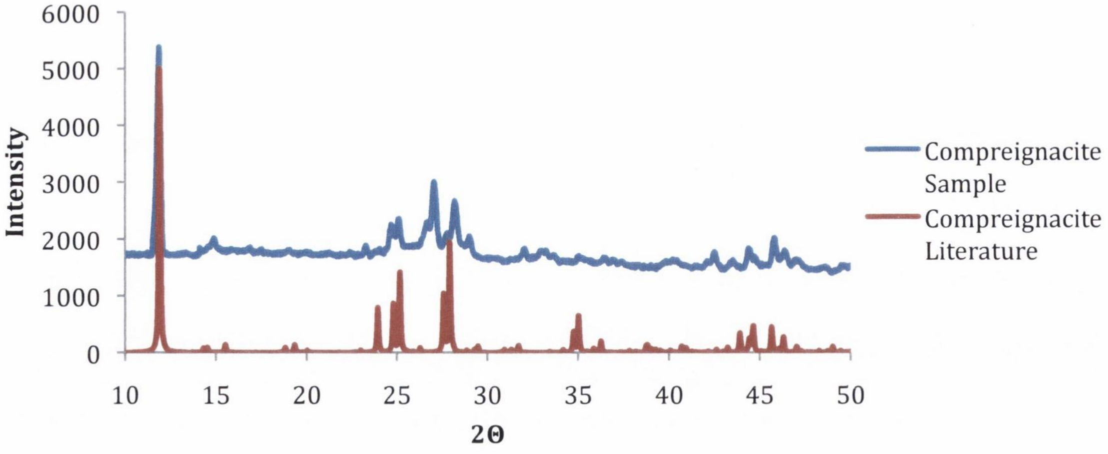

Figure 3.86: Literature[27] and found powder patterns of compreignacite.

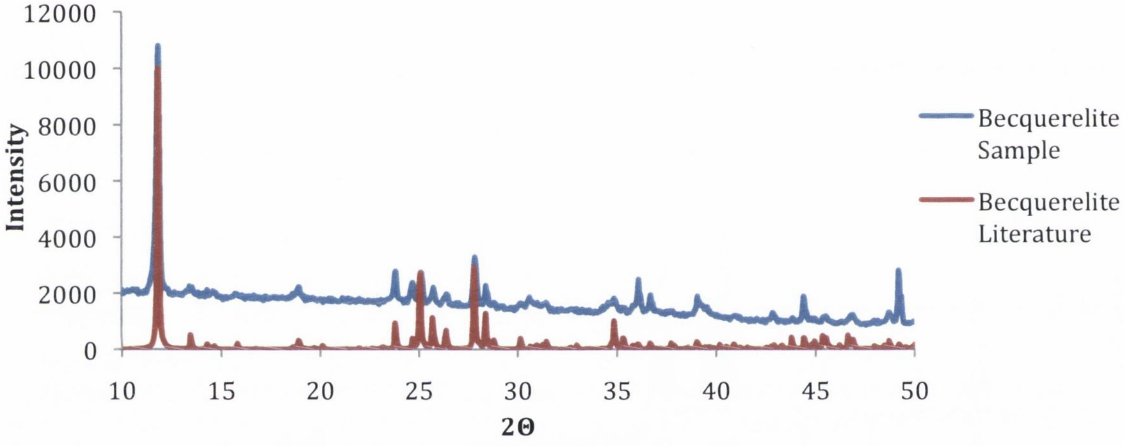

Figure 3.87: Literature[77] and found powder patterns of becquerelite.

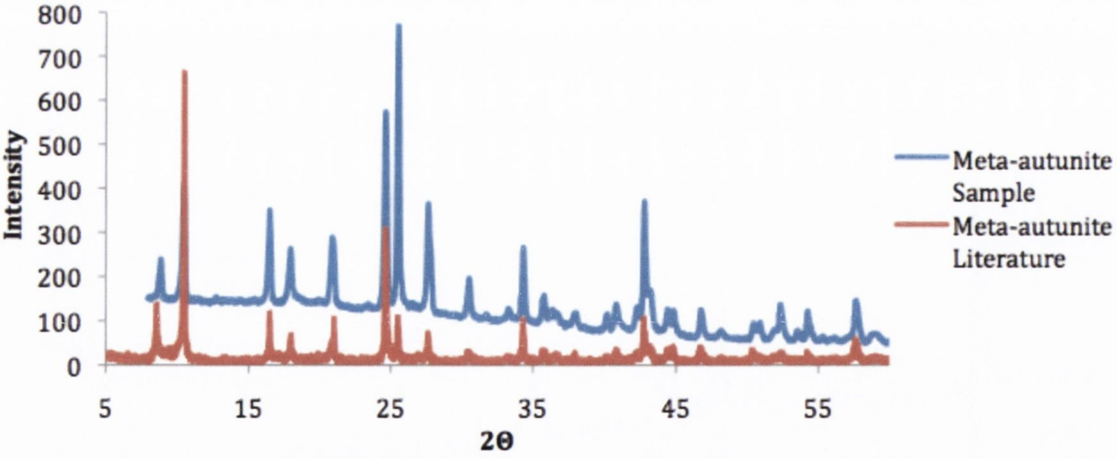

Figure 3.88: Meta-autunite has the formula $Ca[(UO_2)_2(PO_4)_2]\cdot xH_2O$ where for samples I, II, and III x equals 8, 6 and 7, respectively, as defined by Locock *et al.*[50]

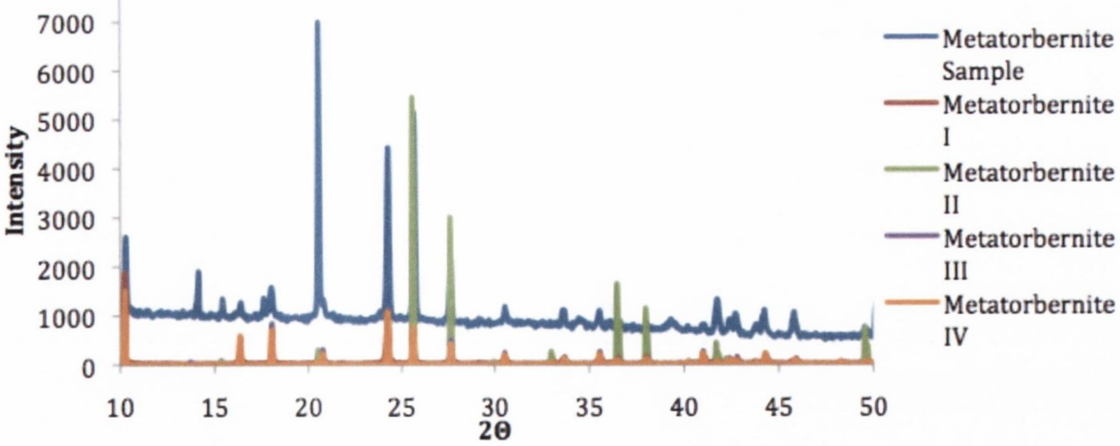

Figure 3.89: Metatorbernite has the formula $Cu[(UO_2)_2(PO_4)_2]\cdot 8H_2O$ for samples I, II, and III, as defined by Locock *et al.*[47b]

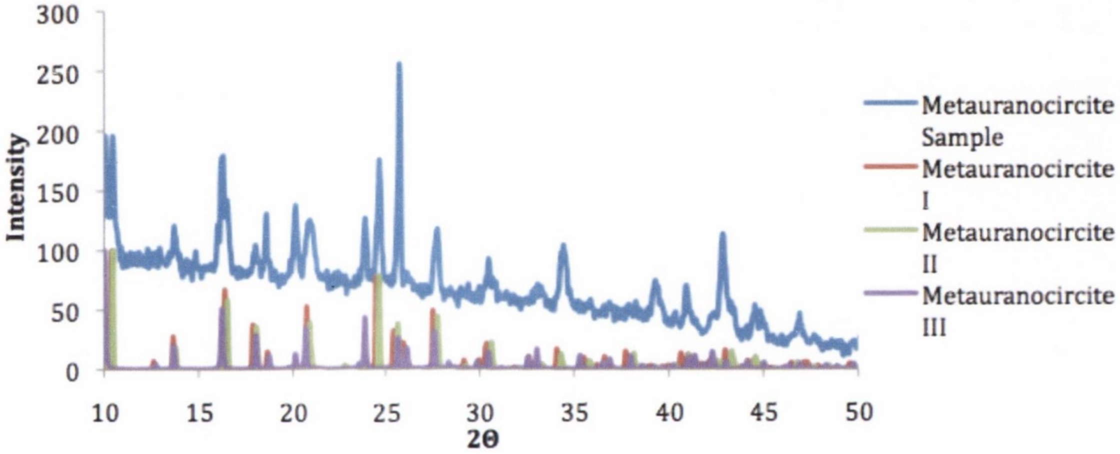

Figure 3.90: Meta-uranocircite has the formula $Ba[(UO_2)_2(PO_4)_2]\cdot xH_2O$ where for samples I, II, and III x equals 8, 6 and 7, respectively, as defined by Locock *et al.*[50]

Powder diffraction was performed on a Siemens D500 diffractometer using Bragg-Brentano geometry with step size of 0.02° at 16 s per step. Infrared spectra were recorded on a Perkin Elmer Spectrum 100 FTIR Spectrometer with ATR attachment. Raman spectra were recorded on a Renishaw 1000 spectrometer. Diffuse Reflectance spectra were recorded on a Perkin Elmer Lambda 900 UV/VIS spectrometer with an integrating sphere attachment. Cyclic voltammetry was performed on a CH Instruments Model 600 electrochemical workstation. Scanning electron microscopy was performed on a Hitachi S3400n scanning electron microscope with a Tungsten system. EDX spectroscopy was undertaken at the TCD Centre for Microscopy and Analysis on a Zeiss Ultra Plus Field Emission Scanning Electron Microscope with attached Wavelength Dispersive X-ray microanalysis chamber.

3.6.2. Solid-state Electrochemistry

Solid-state electrochemistry was performed in a standard three-electrode configuration using a platinum mesh as a counter electrode and a Ag/AgCl (sat. KCl) reference electrode. Fluorine doped tin oxide (FDTO) coated glass was employed as the working electrode. The minerals were suspended in acetone and the slurry mixture was dropped onto the FDTO electrode. The insolubility of the minerals in question in aqueous solutions ensured that no dissolution occurred. Although some material detaches from the electrode over the course of the measurements, this does not affect the results. $LiClO_4$, $KClO_4$, Li_2CO_3, K_2CO_3 and $CaCO_3$ were purchased from Sigma Aldrich and used as found. Electrolyte solutions were made using Millipore water.

The diffusion coefficient of each electrochemical product was found by performing short CV scans at scan rates from 10 to 500 mV s^{-1} and measuring the growth of the reduction and oxidation peaks. Diffusion coefficients were calculated using the Randles-Sevyk equation using the slope of a graph of current (area of peak in question) against the square root of the scan rate after each experiment.

3.7. References

(1) Burns, P. C. *Can. Mineral.* **2005**, *43*, 1839.

(2) (a) Wronkiewicz, D. J.; Bates, J. K.; Wolf, S. F.; Buck, E. C. *J. Nucl. Mater.* **1996**, *238*, 78(b) Wronkiewicz, D. J.; Bates, J. K.; Gerding, T. J.; Veleckis, E.; Tani, B. S. *J. Nucl. Mater.* **1992**, *190*, 107(c) Bruno, J. E., Rodney C. *Elements* **2006**, *2*, 343.

(3) (a) Reyes-Cortés, M.; Fuentes-Cobas, L.; Torres-Moye, E. *Mineral. Petrol.* **2010**, *99*, 121(b) Zhao, D.; Ewing, R. C. *Radiochim. Acta* **2000**, *88*, 739(c) Finch, R. J.; Ewing, R. C. *J. Nucl. Mater.* **1992**, *190*, 133(d) Buck, E. C.; Hanson, B. D.; McNamara, B. K. *Geological Society, London, Special Publications* **2004**, *236*, 65(e) Bargar, J. R.; Bernier-Latmani, R.; Giammar, D. E.; Tebo, B. M. *Elements* **2008**, *4*, 407.

(4) (a) McNamara, B.; Buck, E.; Hanson, B. *Mater. Res. Soc. Symp. Proc.* **2002**, *757*, 401(b) Hanson, B. D.; McNamara, B.; Buck, E. C.; Friese, J. I.; Jenson, E.; Krupka, K.; Arey, B. W. *Radiochim. Acta* **2005**, *93*, 159(c) Kubatko, K.-A. H.; Helean, K. B.; Navrotsky, A.; Burns, P. C. *Science* **2003**, *302*, 1191(d) Clarens, F.; de Pablo, J.; Díez-Pérez, I.; Casas, I.; Giménez, J.; Rovira, M. *Environ. Sci. Technol.* **2004**, *38*, 6656(e) Forbes, T. Z.; Horan, P.; Devine, T.; McInnis, D.; Burns, P. C. *Am. Mineral.* **2011**, *96*, 202.

(5) (a) Shvareva, T. Y.; Fein, J. B.; Navrotsky, A. *Ind. Eng. Chem. Res.* **2012**, *51*, 607(b) Gorman-Lewis, D.; Shvareva, T.; Kubatko, K.-A.; Burns, P. C.; Wellman, D. M.; McNamara, B.; Szymanowski, J. E. S.; Navrotsky, A.; Fein, J. B. *Environ. Sci. Technol.* **2009**, *43*, 7416.

(6) (a) Jerden Jr, J. L.; Sinha, A. K. *Appl. Geochem.* **2003**, *18*, 823(b) Murakami, T.; Ohnuki, T.; Isobe, H.; Sato, T. *Am. Mineral.* **1997**, *82*, 888(c) Jensen, M. P.; Nash, K. L.; Morss, L. R.; Appelman, E. H.; Schmidt, M. A. In *Humic and Fulvic Acids - Isolation, Structure, and Environmental Role*; Gaffney, J. S., Marley, N. A., Clark, S. B., Eds.; Amer Chemical Soc: Washington, 1996; Vol. 651(d) Gauglitz, R.; Holterdorf, M.; Franke, W.; Marx, G. *MRS Online Proceedings Library* **1991**, *257*, 331.

(7) Jerden Jr, J. L.; Sinha, A. K.; Zelazny, L. *Chem. Geol.* **2003**, *199*, 129.

(8) (a) Dacheux, N.; Clavier, N.; Robisson, A. C.; Terra, O.; Audubert, F.; Lartigue, J. E.; Guy, C. *C. R. Chim.* **2004**, *7*, 1141(b) Terra, O.; Dacheux, N.; Audubert, F.; Podor, R. *J. Nucl. Mater.* **2006**, *352*, 224.

(9) Clark, D. L.; Hobart, D. E.; Neu, M. P. *Chemical Reviews* **1995**, *95*, 25.

(10) Denecke, M. A. *Coord. Chem. Rev.* **2006**, *205*, 730.

(11) Reeder, R. J.; Elzinga, E. J.; Tait, C. D.; Rector, K. D.; Donohoe, R. J.; Morris, D. E. *Geochim. Cosmochim. Acta* **2004**, *68*, 4799.

(12) Reeder, R. J.; Nugent, M.; Tait, C. D.; Morris, D. E.; Heald, S. M.; Beck, K. M.; Hess, W. P.; Lanzirotti, A. *Geochim. Cosmochim. Acta* **2001**, *65*, 3491.

(13) Kim, K.-W.; Kim, Y.-H.; Lee, S.-Y.; Lee, J.-W.; Joe, K.-S.; Lee, E.-H.; Kim, J.-S.; Song, K.; Song, K.-C. *Environ. Sci. Technol.* **2009**, *43*, 2355.

(14) Kubatko, K. A.; Helean, K. B.; Navrotsky, A.; Burns, P. C. *Am. Mineral.* **2005**, *90*, 1284.

(15) Wang, Z.; Zachara, J. M.; Gassman, P. L.; Liu, C.; Qafoku, O.; Yantasee, W.; Catalano, J. G. *Geochim. Cosmochim. Acta* **2005**, *69*, 1391.

(16) Parker, A.; Rae, J. E. *Environmental Interactions of Clays: Clays and the Environment*, 2010.

(17) Cantrell, K. J.; Deutsch, W. J.; Lindberg, M. J. *Environ. Sci. Technol.* **2011**, *45*, 1473.

(18) Scholz, F.; Meyer, B. *Chemical Society Reviews* **1994**, *23*, 341.

(19) Roullier, L.; Laviron, E. *J. Electroanal. Chem. Interfac. Electrochem.* **1982**, *134*, 181.

(20) (a) Nafadya, A.; Bond, A. M.; Bilyk, A.; Harris, A. R.; Bhatt, A. I.; O'Mullane, A. P.; De Marco, R. *J. Am. Chem. Soc.* **2007**, *129*, 2369(b) Bond, A. M.; Colton, R.; Daniels, F.; Fernando, D. R.; Marken, F.; Nagaosa, Y.; Van Steveninck, R. F. M.; Walter, J. N. *J. Am. Chem. Soc.* **1993**, *115*, 9556.

(21) Grygar, T.; Marken, F.; Schröder, U.; Scholz, F. *Collect. Czech. Chem. Commun.* **2002**, *67*, 163.

(22) Dueber, R. E.; Bond, A. M.; Dickens, P. G. *J. Electrochem. Soc.* **1992**, *139*, 2363.

(23) Mallon, C.; Walshe, A.; Forster, R. J.; Keyes, T. E.; Baker, R. J. *Inorg. Chem.* **2012**, *51*, 8509.

(24) (a) Gregory, T. D.; Hoffman, R. J.; Winterton, R. C. *J. Electrochem. Soc.* **1990**, *137*, 775(b) Dueber, R. E.; Fleetwood, J. M.; Dickens, P. G. *Solid State Ionics* **1992**, *50*, 329.

(25) Grambow, B. *J. Contam. Hydrol.* **2008**, *102*, 180.

(26) Weller, M. T.; Light, M. E.; Gelbrich, T. *Acta Crystallogr., B* **2000**, *56*, 577.

(27) Klingensmith, A. L., University of Notre Dame, 2008.

(28) Klingensmith, A. L.; Burns, P. C. *Am. Mineral.* **2007**, *92*, 1946.

(29) Finch, R. J.; Cooper, M. A.; Hawthorne, F. C.; Ewing, R. C. *Can. Mineral.* **1996**, *34*, 1071.

(30) Hawthorne, F. C. *Geol. Ore Depos.* **2003**, *45*, 88.

(31) Frost, R. L.; Dickfos, M. J.; Čejka, J. *J. Raman Spectrosc.* **2008**, *39*, 1158.

(32) Frost, R. L.; Čejka, J.; Weier, M. L. *J. Raman Spectrosc.* **2007**, *38*, 460.

(33) Bartlett, J. R.; Cooney, R. P. *J. Mol. Struct.* **1989**, *193*, 295.

(34) Shuller, L. C.; Ewing, R. C.; Becker, U. *Am. Mineral.* **2010**, *95*, 1151.

(35) Ostanin, S.; Zeller, P. *Phys. Rev. B: Condens. Matter* **2007**, *75*, 073101.

(36) Amayri, S.; Arnold, T.; Foerstendorf, H.; Geipel, G.; Bernhard, G. *Can. Mineral.* **2004**, *42*, 953.

(37) Arnold, T.; Baumann, N. *Spectrochimica Acta Part A: Molecular and Biomolecular Spectroscopy* **2009**, *71*, 1964.

(38) Burns, P. C.; Deely, K. M.; Skanthakumar, S. *Radiochim. Acta* **2004**, *92*, 151.

(39) Graves, C. R.; Kiplinger, J. L. *Chem. Commun.* **2009**, 3831.

(40) (a) Schnaars, D. D.; Wu, G.; Hayton, T. W. *Inorg. Chem.* **2011**, *50*, 9642(b) Arnold, P. L.; Patel, D.; Wilson, C.; Love, J. B. *Nature* **2008**, *451*, 315(c) Fortier, S.; Brown, J. L.; Kaltsoyannis, N.; Wu, G.; Hayton, T. W. *Inorg. Chem.* **2012**, *51*, 1625(d) Hayton, T. W.; Wu, G. *J. Am. Chem. Soc.* **2008**, *130*, 2005(e) Hayton, T. W.; Wu, G. *Inorg. Chem.* **2009**, *48*, 3065.

(41) (a) Fortier, S.; Hayton, T. W. *Coord. Chem. Rev.* **2010**, *254*, 197(b) Arnold, P. L.; Hollis, E.; Nichol, G. S.; Love, J. B.; Griveau, J.-C.; Caciuffo, R.; Magnani, N.; Maron, L.; Castro, L.; Yahia, A.; Odoh, S. O.; Schreckenbach, G. *J. Am. Chem. Soc.* **2013**, *135*, 3841(c) Odoh, S. O.; Schreckenbach, G. *Inorg. Chem.* **2012**, *52*, 245(d) Hay, P. J.; Martin, R. L.; Schreckenbach, G. *J. Phys. Chem. A.* **2000**, *104*, 6259.

(42) Goldstein, J.; Newbury, D. E.; Joy, D. C.; Lyman, C. E.; Echlin, P.; Lifshin, E.; Sawyer, L.; Michael, J. R. *Scanning Electron Microscopy and X-ray Micronalysis*; 3rd ed.; Springer, 2003.

(43) Wang, L.; Zhao, R.; Gu, Z.-j.; Zhao, Y.-l.; Chai, Z.-f.; Shi, W.-q. *Eur. J. Inorg. Chem.* **2014**, *2014*, 1158.

(44) Schindler, M.; Hawthorne, F. C.; Mandaliev, P.; Burns, P. C.; Maurice, P. A. *Radiochim. Acta* **2011**, *99*, 79.

(45) Lasaga, A. C.; Luttge, A. *Science* **2001**, *291*, 2400.

(46) Zazhogin, A. A.; Lutz, H. D.; Komyak, A. I. *J. Mol. Struct.* **1999**, *482-483*, 189.

(47) (a) Locock, A. J.; Burns, P. C. *Am. Mineral.* **2003**, *88*, 240(b) Locock, A. J.; Burns, P. C. *Can. Mineral.* **2003**, *41*, 489(c) Makarov, E. S.; Ivanov, V. I. *Doklady Akademii Nauk SSSR Earth Science Sections* **1960**, *132*, 601.

(48) Frost, R. L.; Weier, M. *Spectrochim. Acta, Part A* **2004**, *60*, 2399.

(49) Catalano, J. G.; Brown, G. E. *Am. Miner.* **2004**, *89*, 1004.

(50) Locock, A. J.; Burns, P. C.; Flynn, T. M. *Can. Mineral.* **2005**, *43*, 721.

(51) Frost, R. L.; Cejka, J.; Godwin, A. A.; Weier, M. *Spectrochim. Acta, Part A* **2007**, *66*, 979.

(52) Frost, R. L.; Carmody, O.; Erickson, K. L.; Weier, M. L.; Cejka, J. *J. Mol. Struct.* **2004**, *703*, 47.

(53) Baumann, N.; Arnold, T.; Foerstendorf, H.; Read, D. *Environ. Sci. Technol.* **2008**, *42*, 8266.

(54) Geipel, G.; Bernhard, G.; Rutsch, M.; Brendler, V.; Nitsche, H. *Radiochim. Acta* **2000**, *88*, 757.

(55) Choudhury, B.; Dey, M.; Choudhury, A. *Int Nano Lett* **2013**, *3*, 1.

(56) Billing, D. E.; Hathaway, B. J.; Nicholls, P. *J. Chem. Soc. A* **1969**, *1969*, 316.

(57) Huheey, J. E.; Keiter, E. A.; Keiter, R. L. *Inorganic Chemistry: Principles of Structure and Reactivity*; 4th ed.; Harper Collins: New York, 1993.

(58) Vanysek, P. In *CRC Handbook of Chemistry and Physics*; Lide, D. R., Ed.; CRC Press: Boca Raton, 1998.

(59) Hallik, A.; Alumaa, A.; Tamm, J. r. *J Solid State Electrochem* **2010**, *14*, 909.

(60) Astilleros, J. M.; Pinto, A. J.; Gonçalves, M. A.; Sanchez-Pastor, N.; Fernandez-Diaz, L. *Environ. Sci. Technol.* **2013**, *47*, 2636.

(61) (a) Zhou, P.; Gu, B. *Environ. Sci. Technol.* **2005**, *39*, 4435(b) Stewart, B. D.; Mayes, M. A.; Fendorf, S. *Environ. Sci. Technol.* **2010**, *44*, 928.

(62) Li, Y.; Burns, P. C. *Can. Mineral.* **2001**, *39*, 1147.

(63) Coda, A.; Della Giusta, A.; Tazzoli, V. *Acta Crystallogr., B* **1981**, *B37*, 1496.

(64) Skála, R.; Ondrus, P.; Veselovsky, F.; Císarová, I.; Hlousek, J. *Mineral. Petrol.* **2011**, *103*, 169.

(65) Frost, R. L.; Čejka, J. *J. Raman Spectrosc.* **2009**, *40*, 1096.

(66) Frost, R. L.; Čejka, J.; Ayoko, G. A.; Dickfos, M. J. *J. Raman Spectrosc.* **2008**, *39*, 374.

(67) Frost, R. L.; Čejka, J.; Ayoko, G. A.; Dickfos, M. J. *J. Raman Spectrosc.* **2007**, *38*, 1609.

(68) Amayri, S.; Arnold, T.; Reich, T.; Foerstendorf, H.; Geipel, G.; Bernhard, G.; Massanek, A. *Environ. Sci. Technol.* **2004**, *38*, 6032.

(69) Gorman-Lewis, D.; Burns, P. C.; Fein, J. B. *The Journal of Chemical Thermodynamics* **2008**, *40*, 335.

(70) Runde, W. H.; Schulz, W. W. In *The Chemistry of the Actinide and Transactinide Elements*; 4th ed.; Morss, L. R., Edelstein, N. M., Fuger, J., Eds.; Springer: Dordrecht, The Netherlands, 2010.

(71) Klingensmith, A. L.; Deely, K. M.; Kinman, W. S.; Kelly, V.; Burns, P. C. *Am. Mineral.* **2007**, *92*, 662.

(72) Meredith, N. A.; Polinski, M. J.; Cross, J. N.; Villa, E. M.; Simonetti, A.; Albrecht-Schmitt, T. E. *Crystal Growth & Design* **2012**, *13*, 386.

(73) Jones, L. H. *Spectrochimica Acta* **1958**, *10*, 395.

(74) Wilkerson, M. P.; Burns, C. J.; Paine, R. T.; Scott, B. L. *Inorg. Chem.* **1999**, *38*, 4156.

(75) Nipruk, O.; Knyazev, A.; Chernorukov, G.; Pykhova, Y. *Radiochemistry* **2011**, *53*, 146.

(76) Finch, R. J.; Cooper, M. A.; Hawthorne, F. C.; Ewing, R. C. *Can. Mineral.* **1996**, *34*, 1071.

(77) Burns, P. C.; Li, Y. *Am. Mineral.* **2002**, *87*, 550.

Chapter 4:

Uranyl Complexes as Catalysts for C-O Bond Formation

4.1. Introduction

As described in **Section 1.1.3.**, in recent years there has been a renewal of interest as attempts are made to understand the variety of activations and transformations possible with uranium.[1] Given the highly oxophilic nature of the early actinides it was generally held that oxygen-containing substrates would hinder transformations;[2] this was confirmed experimentally by Lin and Marks in 1987 when comparing the activity of alkyl and alkoxide actinide complexes for actinide-carbon bond hydrogenolysis.[3] It wasn't until Eisen's successful example of uranium(IV) complexes catalysing the ROP of lactones[4] and the Tischenko reaction[5] that uranium was revealed to have a potential for C–O bond formation.

This Chapter will detail the investigation of uranyl complexes as catalysts for ring-opening polymerisation (ROP) of oxygen containing monomers. Previous attempts of ROP with uranium have had mixed results: U(IV), has been shown to be effective as a catalyst for the ROP of εCL – $[U(NEt_2)_3][BPh_4]$ proceeded *via* a cationic mechanism with rates comparable to successful transition metal complexes[4] – while the U(III) complex $U[MeC(NCy)_2]_3$ took five days to go to completion when reacted with 200 equivalents of ε-caprolactone (εCL).[6] In fact, when reacted with 0.5 equivalents, a mixture of U(IV) derivatives formed.

Mandolini and coworkers designed a system for the Michael-type addition of thiophenol to a cyclic α,β-unsaturated ketone: the ketone coordinates to the Lewis acidic U(VI), thereby polarising the carbonyl-alkene conjugated system to allow for easier nucleophilic attack at the β–carbon.[7] This ability to bind and release oxygen is unexpected given the highly oxophilic and Lewis acidic nature of uranyl, which makes the ability to polarise the carbonyl and to allow C–S bond formation significant.

Given the success of uranium(IV) catalysts[4-5] and the breadth of possible transformations with uranyl chemistry,[7a,b,8] it was decided to look at the possibility of $[UO_2]^{2+}$ as a ring-opening polymerisation (ROP) catalyst for oxygen containing monomers such as cyclic ethers or lactones. The results of this work with epoxides[9] and lactones[10] will be examined and explained in detail *vide infra*.

4.1.1. Uranyl as a Ring-Opening Polymerisation Catalyst

The linear uranyl moiety is a hard, Lewis acidic cation, which demands coordination around the equatorial plane, thus creating an environment where labile solvent molecules are mutually *cis* to the ligands. This environment is useful to assist a *cis*-migratory insertion (intramolecular) mechanism during bond activation and formation. Ring-opening polymerisation (ROP) of epoxides is encouraged by a strong Lewis acid[11] but is unlikely to proceed *via* a *cis*-migratory insertion mechanism.[12] Given the literature evidence for metal-chlorides as epoxide ROP catalysts,[13] uranyl chloride was considered as a possible catalyst. Uranyl chloride exists as a monomer in thf, $[UO_2Cl_2(thf)_3]$, or as a dimer in non-coordinating solvents, $[UO_2Cl_2(thf)_2]_2$, therefore enabling both an intramolecular and an intermolecular investigation of the mechanism.

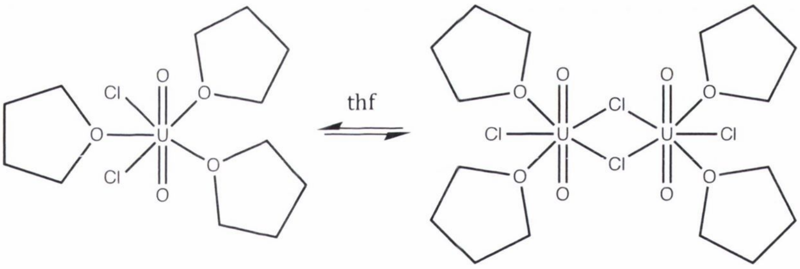

U–Cl **(U–Cl)$_2$**

Figure 4.1: The structures of the monomeric and dimeric species of uranyl chloride: U–Cl and (U–Cl)$_2$.

The previously reported uranyl phenoxide complex, **1**[14] (**Figure 4.2**), was also chosen as a potential candidate for ROP of epoxides. Many examples of uranium catalysis are enthalpically driven: $Cp^*_2UMe_2$ has been shown to catalyse many transformations and the deprotonation/ coordination of the monomer to uranium results in the elimination of methane,[4-5,15] with a calculated loss in enthalpy from -8[4] to -48 kcal mol^{-1}.[15a] Using **1**, one U–O bond will be replaced by another, with minimal change in enthalpy, making entropy the driving force in the polymerisation and any enthalpic gain arising from the monomer, e.g. *via* the release of ring-strain.

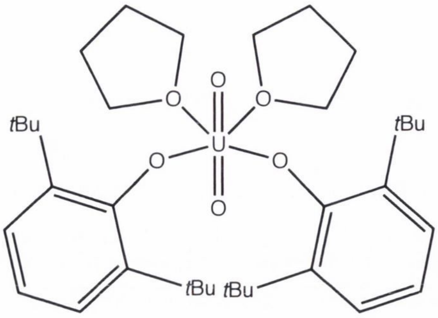

Figure 4.2: The uranyl phenoxide complex 1.

The bulky 2,6–di*tert*butylphenol ligands gave rise to the first reported example of a stable monomeric uranyl phenoxide complex. The complex remains monomeric in solution, important to facilitate a *cis*-migratory coordination-insertion mechanism. This mechanism is known for the ROP of lactones[16] but is hitherto unreported for epoxides. Complex **1** shall be used to investigate the possibility of an intramolecular mechanism for ROP of epoxides.

The monomers used for these investigations were propylene oxide (PO) and cyclohexene oxide (CHO) (**Figure 4.3**). Given the breadth of research into the chiral nature of propylene oxide, the microstructure of the resulting polymer will give insight into the regio- and stereoselectivity of the catalyst.[17] Examining polymers created from dimethylbutene oxide (DMBO) and cyclohexene oxide (CHO) can also reveal the presence of a intra or intermolecular mechanism of the catalyst in question.[18]

PO propylene oxide

CHO cyclohexene oxide

DMBO dimethylbutene oxide

Figure 4.3: Epoxides tested for ROP by uranyl chloride and 1.

4.1.2. Ring-Opening Polymerisation of Lactones

Polyesters such as polycaprolactone (PCL) and polylactide (PL) have been studied increasingly in recent decades as biodegradable polymers with the potential for replacing established plastics such as polyethylene or polystyrene.[19] Originally desired for medical procedures – such as scaffolds in tissue engineering that dissolve naturally and harmlessly *in vivo*[20] or in long-term *in vivo* drug delivery systems[21] – as synthetic methods improved and production costs lowered, these polymers have now become available for commercially viable products with applications in microelectronics,[22] as adhesives,[23] and in packaging.[21d]

There are a wide number of catalysts available for PCL synthesis, making it possible to choose the appropriate system to obtain the polymer with the desired characteristics. There are four known mechanisms for the ROP of PCL: anionic, cationic, monomer-activated and *cis*-migratory insertion ROP.[16b]

1. **Anionic ROP** involves the formation of an anionic species that attacks the carbonyl carbon of the monomer. The monomer is opened at the acyl–oxygen bond and the growing species is an alkoxide. This mechanism is observed with alkali metal-based catalysts and typically gives rise to significant intramolecular transesterification, also called "back-biting". This results either in low molecular weight polymers, if the polymerisation is stopped before back-biting can occur, or in cyclic polymers.
2. **Cationic ROP** involves the formation of a cationic species that is attacked by the carbonyl oxygen of another monomer through a bimolecular nucleophilic substitution (S_N2) reaction. Eisen's polymerisation of εCL with U(IV) showed a rare example of living cationic polymerisation.[4]
3. **Monomer-activated ROP** involves the activation of the monomer molecules by a catalyst, followed by the attack of the activated monomer onto the polymer chain end.
4. ***Cis*-migratory insertion ROP** is the most common form of lactone ROP, seen for Mg, Ca, Al, Sn and many of the transition metals and lanthanides.[16b] It is actually a pseudo-anionic ROP. The propagation is proposed to proceed through the coordination of the monomer to the catalyst and the insertion of the monomer into

a metal–oxygen bond of the catalyst. During propagation, the growing chain is attached to the metal through an alkoxide bond.

An initial test reaction of **1** in neat ε-Caprolactone (εCL) yielded the formation of a gelatinous solid after 72 hours. A series of controlled experiments were undertaken to better understand the reaction mechanism and the optimum conditions for the ROP of εCL to occur, and the resulting polymer was analysed to deduce the mechanism for the reaction. To investigate the effect of ring strain on the reaction, a series of lactones of different ring sizes were tested in a similar fashion (**Figure 4.4**). If the release of ring-strain is a driving force for the ROP then γBL is not expected to ring-open as ring-opening of the five-membered ring is in fact endergonic.[24] In contrast, βBL has high ring-strain but has been shown to be significantly less reactive than other lactones;[25] βBL will be a suitable test for the efficacy of **1** as a ROP catalyst.

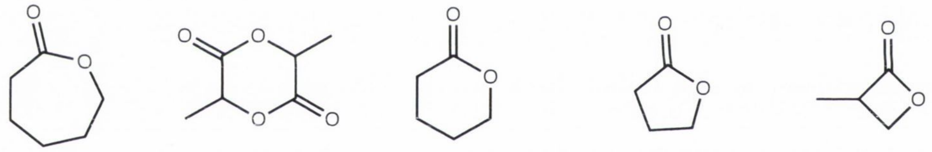

εCL **lac** **δVL** **γBL** **βBL**

ε-Caprolactone lactide δ-Valerolactone γ-Butyrolactone β-Butyrolactone

Figure 4.4: Series of lactones tested by 1.

Not all epoxide ROP catalysts work for lactone polymerisation: many aluminium chloride complexes that have been demonstrated to be highly successful for the ROP of PO are completely inactive towards lactide.[13] The initiation step – the cleavage of the acyl C–O bond by the nucleophilic attack of Cl^- – is unfavourable. Conversely, the same is true for lactone catalysts and epoxides,[26] even when epoxides such as propylene oxide (PO) are seen to coordinate to the metal.[11a] Block copolymers are possible, however, when the alkoxide chain arising from ROP of PO is the nucleophile attacking the lactide.[13]

4.1.3. Characterisation Techniques

Monitoring the progress of the reaction required a spectroscopic method capable of *in situ* examination of the interactions of the monomers and the uranium catalyst. 2D NMR spectroscopy provided an ideal analytical tool to determine chemical exchange, chemical kinetics and to measure the shape and size of molecules in solution or to examine the fine structure of the product.

The main NMR techniques used over the course of the investigations were:

1. Exchange Spectroscopy (EXSY)
2. *J*-Resolved Spectroscopy
3. Diffusion Spectroscopy (DOSY)

and will be discussed in the following sections.

4.1.3.1. Exchange Spectroscopy: EXSY

Exchange spectroscopy is a 2D NMR technique in which the vertical axis shows the intersection of signals that exchange in solution. In the case of our system, the exchanging monomer and solvent molecules can be observed (**Figure 4.5**). The rate of exchange at the metal, *k*, can be obtained from the relationship between the integral of the spectrum and the mixing time according to the formula:

$$k = \frac{1}{t_m\left(\frac{I_D}{I_C}+1\right)} \qquad \textbf{4.1}$$

where I_D and I_C are the integrations of the diagonal peaks and the cross-peaks, respectively.[27]

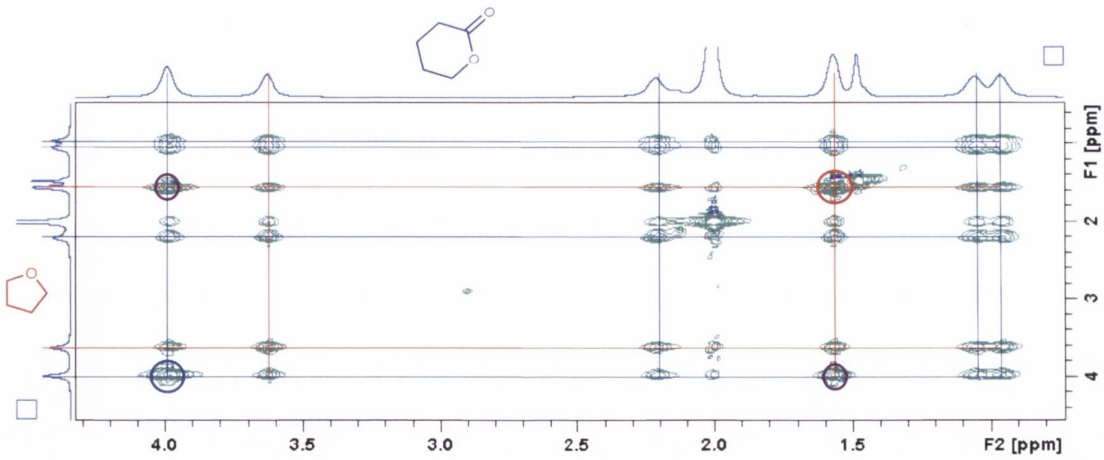

Figure 4.5: An EXSY spectrum showing the exchange of thf and δ-Valerolactone at the uranium in C_6D_6. The diagonal peaks are circled in red and blue, the cross-peaks in purple.

4.1.3.2. *J-Resolved Spectroscopy*

J-Resolved spectroscopy uses 45° pulses to turn a high-resolution 1D spectrum into a 2D spectrum, with the coupling patterns displayed along the F1 axis.[27] This is a useful tool for isolating and deconvoluting overlapping multiplets in a ^1H spectrum, such as that of a polymer, enabling a detailed examination and deduction of the microstructure (**Figure 4.6**).[17]

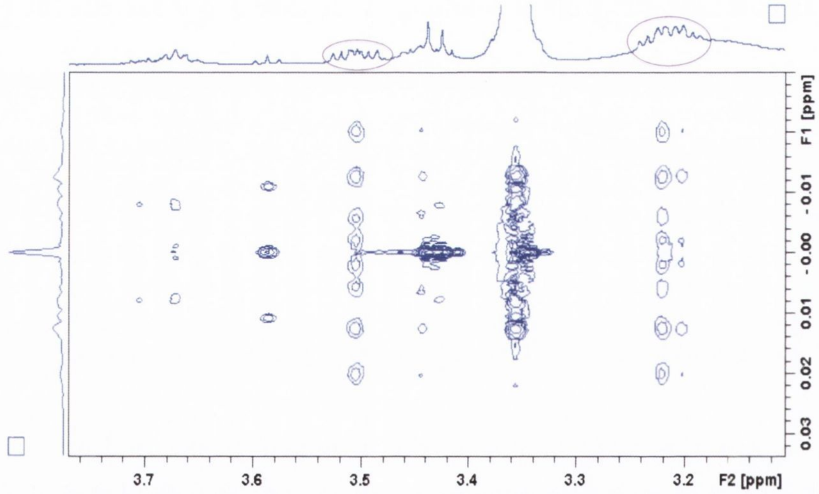

Figure 4.6: An example of a *j*-resolved spectrum showing the expanded multiplets, allowing facile calculation of the coupling constants within.

4.1.3.3. Diffusion Oriented Spectroscopy: DOSY

Using the Topspin diffusion programme, the 2D spectrum shows D_t along the F1 axis, allowing easy calculation of the experimental hydrodynamic radius, r_H, through the Stokes-Einstein equation:[28]

$$D_t = \frac{kT}{c\,\pi\,\eta\,r_H} \qquad \textbf{4.2}$$

Where k is Boltzmann's constant, T is the temperature in Kelvin, η is the viscosity of the solvent (a temperature dependent property) and c is a constant that is related to the approximate shape of the molecule in solution – DOSY is designed for spherical molecules and this constant corrects for oblate (disc) and prolate (cigar) shapes.[29]

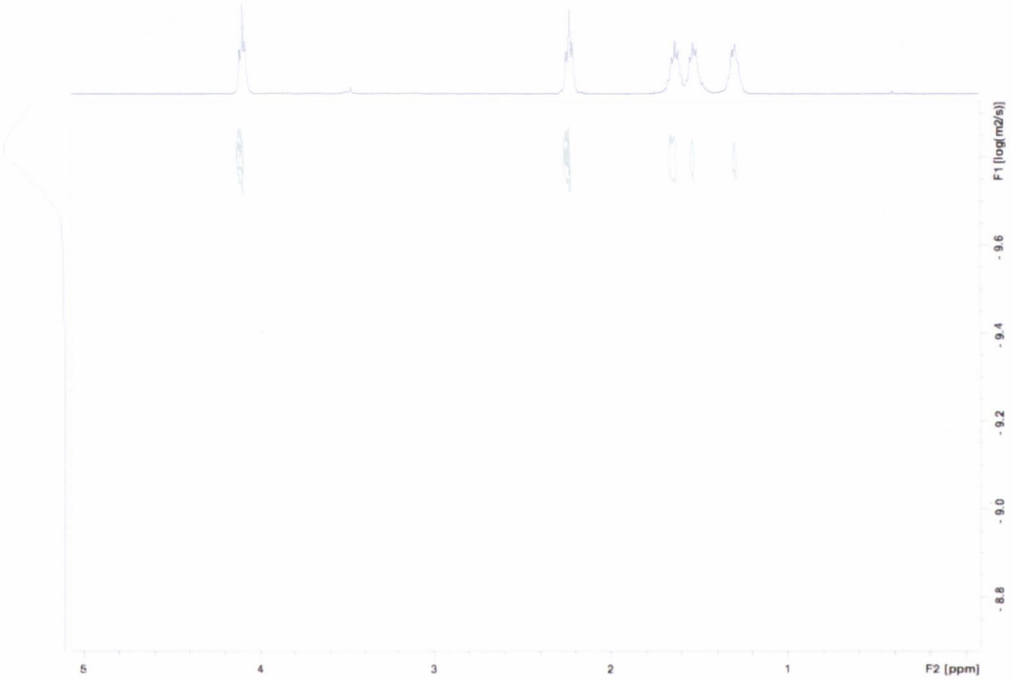

Figure 4.7: The DOSY spectrum of polycaprolactone in C_6D_6. The F1 value is 9.77, corresponding to a value for the hydrodynamic radius of 33.90 Å (c = 4) at 25 °C.

The units of the F1 axis are log ($m^2\ s^{-1}$), so D_t can therefore be found as 10^{F1}. This value can then be solved for r_H.

4.2. Uranyl and the Ring-Opening of Epoxides

4.2.1. Experimental Investigations

Propylene oxide (PO) and cyclohexene oxide (CHO) were reacted with 1% loadings of **1** or uranyl chloride in thf or toluene. PO has a boiling point of 36°C so PO reactions were undertaken at temperatures of 25 and 40°C in each solvent, CHO was also reacted at 70 in each solvent and at 100°C in toluene. Graphs of percentage conversion against time show a quick conversion of PO and CHO to polypropylene oxide (PPO) and polycyclohexene oxide (PCO) (**Figures 4.8** to **4.10**). There does not seem to be a drop in the rate for the thf solutions, implying that there is no competition between solvent and monomer for active sites on the catalyst. A selection of polymer characteristics is detailed in **Table 4.1**.

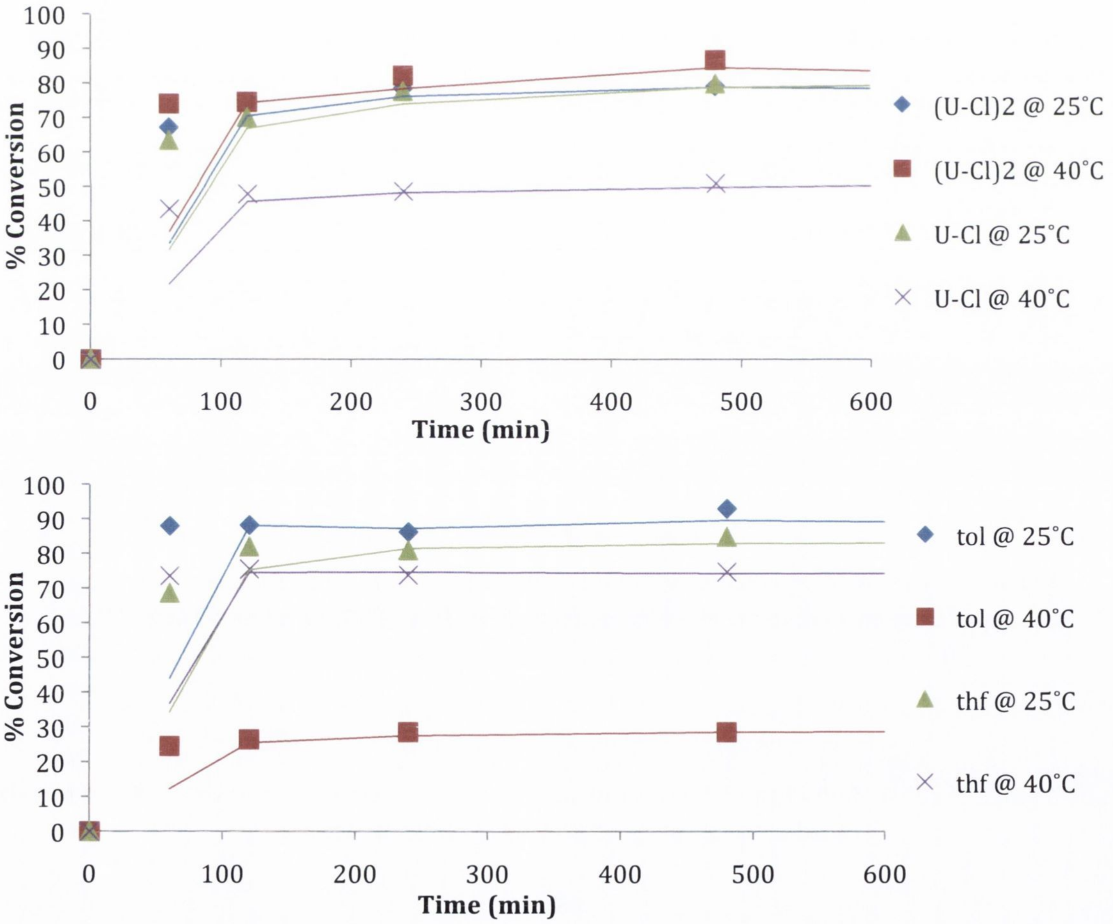

Figure 4.8: Graphs of % conversion of propylene oxide (PO) to poly(propylene oxide) (PPO) against time with 1% loading of uranyl chloride (top) and 1 (bottom).

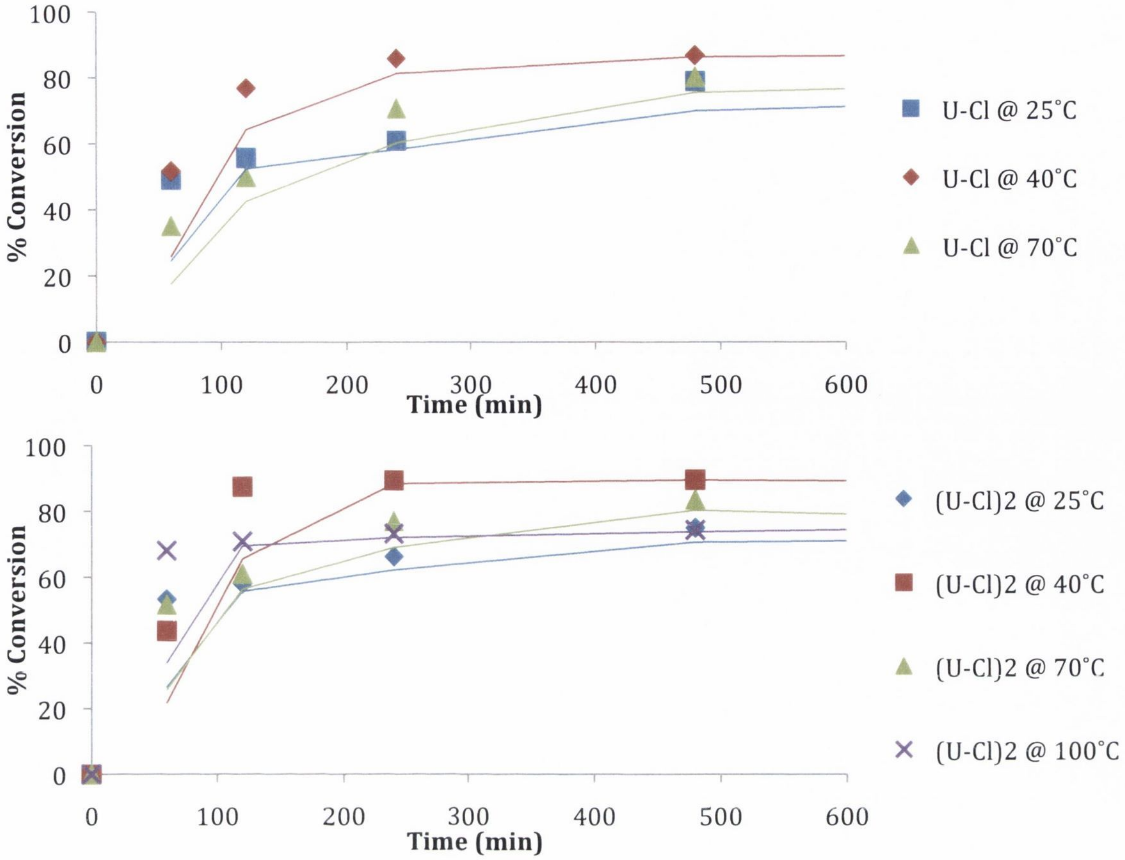

Figure 4.9: Graphs of % conversion of cyclohexene oxide (CHO) to poly(cyclohexene oxide) (PCO) against time with 1% loading of uranyl chloride in thf (top) and toluene (bottom).

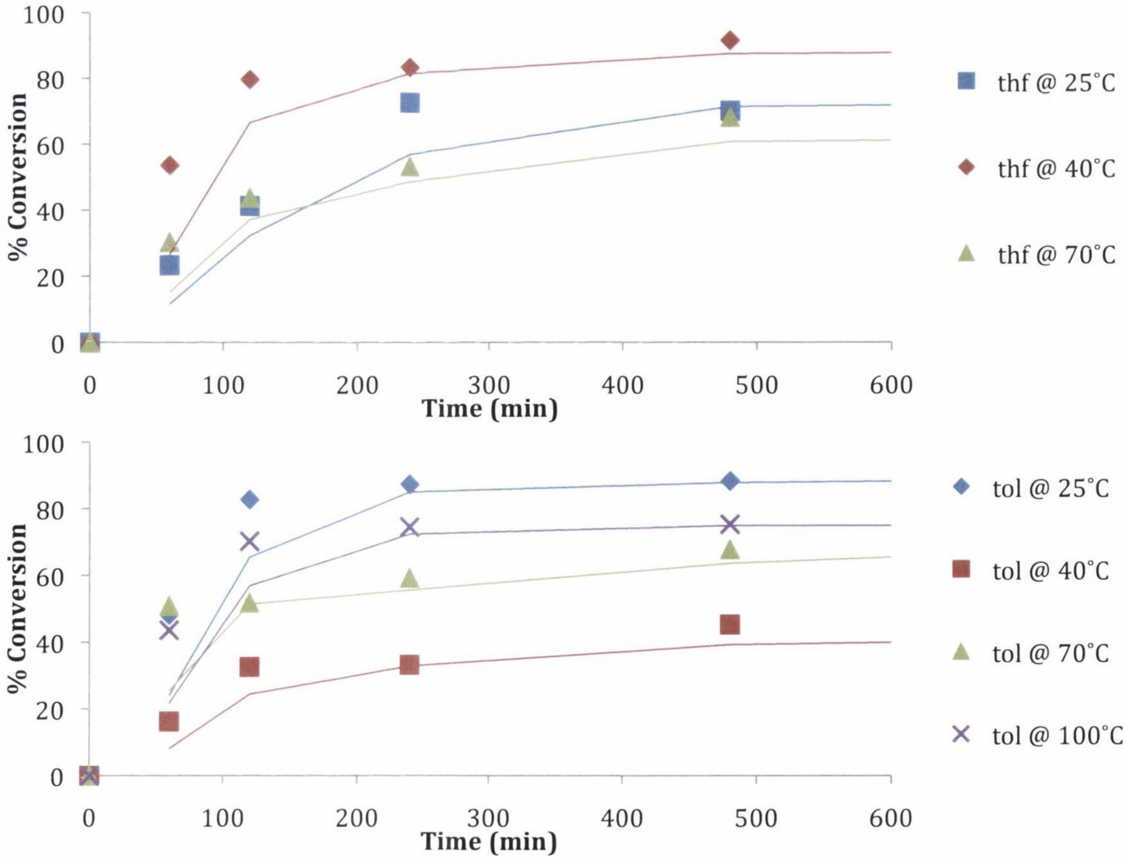

Figure 4.10: Graphs of % conversion of cyclohexene oxide (CHO) to poly(cyclohexene oxide) (PCO) against time with 1% loading of 1 in thf (top) and toluene (bottom).

Table 4.1: A sample of the epoxide polymer characteristics after 24 hrs.

Run	Monomer	Catalyst	Solvent	Temp (°C)	% Conv.	M_n[a]	PD_i
1	PO	**1**	thf	25	83	219	1.170
2	PO	**1**	tol	25	89	389	1.061
3	PO	**U–Cl**	thf	40	77	100	1.325
4	PO	**$(U–Cl)_2$**	tol	40	87	88	1.237
5	CHO	**1**	thf	70	94	179	1.393
6	CHO	**1**	tol	100	88	378	1.044
7	CHO	**U–Cl**	thf	70	87	87	1.512
8	CHO	**$(U–Cl)_2$**	tol	100	88	72	1.474

[a] M_n values are corrected from the polystyrene calibrants using the Mark-Houwink factor.[30]

The GPC analysis of the poly(propylene oxide) (PPO) and poly(cyclohexene oxide) (PCO) show low molecular weight oligomers with polydispersity (PD_i) values between 1 and 1.5. MALDI-ToF analysis showed diol fragments, consistent with hydrolysis on the column. ^{1}H NMR spectroscopy of the PPO formed showed no end groups from the catalysts (i.e. no observable C-Cl bond or phenoxide), however spin-selective TOCSY analysis of PCO showed the choride end group [**Figure 4.11(a)**] and the methoxy end group from quenching the polymer with acidified methanol [**Figure 4.11(b)**]. The lack of phenoxide end group is consistent with a back-biting mechanism for the polymerisation; this would explain the low molecular weights of the products.

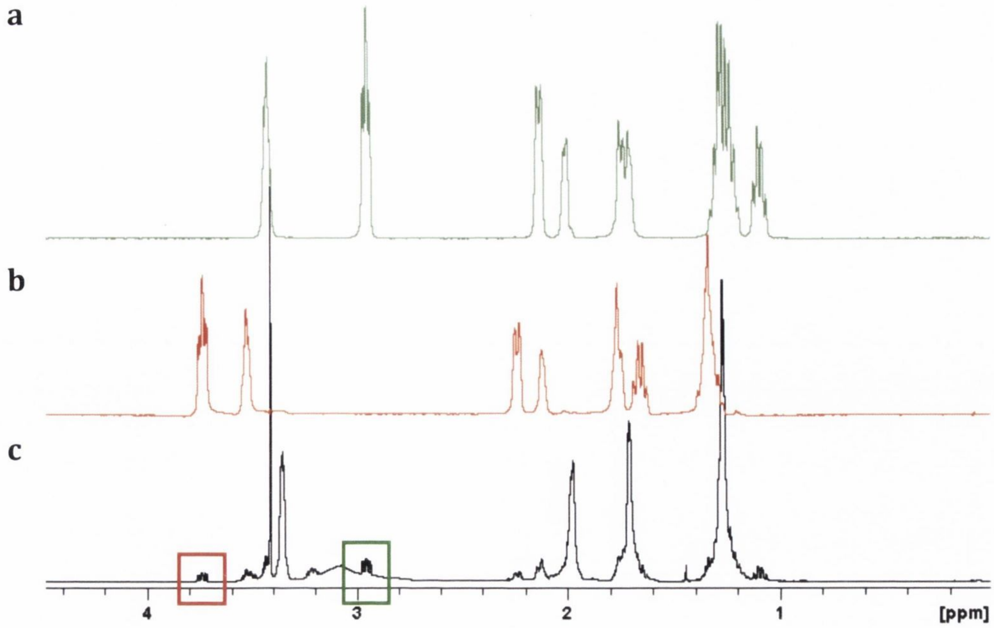

Figure 4.11: Selective TOCSY of polymer obtained from cyclohexene oxide in (U–Cl)$_2$ at 25°C. (a) Irradiation at δ_H = 3.735 ppm shows protons attached to cyclohexane ring with Cl end-group; (b) irradiation at δ_H = 2.955 ppm shows protons attached to cyclohexane ring with OMe end-group; (c) full ^{1}H spectrum.

^{13}C[^{1}H] NMR spectroscopy was used to identify the microstructure of PPO from diad to tetrad level.[12-13,17,31] Using established assignments of the methane and methylene carbons it can be deduced that the polymerisation is regio-irregular with H-T, H-H and T-T diads observed, suggesting that there is poor regio-control over the ring opening of the epoxide [**Figure 4.12(a)**]. There is a bias towards syndiotactic diads and triads in the regio-regular portions of the polymer, suggesting that there is an inversion of stereochemistry. In order to confirm this observation *s*-PO was used and the ^{13}C[^{1}H] NMR spectrum of the polymer shows the expected atacity [**Figure 4.12(b)**]. The multitude of signals in the methyl region of the spectrum relative to the *rac*-PO polymerisation product shows that the chiral nature of *s*-PO is lost, supporting the theory that stereochemistry is lost at the metal. Further evidence for the regio-irregular nature of the polymer comes from measurement of the optical rotation of the polymer obtained from *s*-PO: $[\alpha]_{D20}$ = 0.002 deg cm^3 g^{-1} dm^{-1} (c = 0.006 g cm^{-3} in CH_2Cl_2); the optical rotation measurement for *s*-PO was 0.538 (c = 0.10 g cm^{-3} in CH_2Cl_2), consistent with the poor regioselectivity of the catalyst causing the loss of chirality.[32]

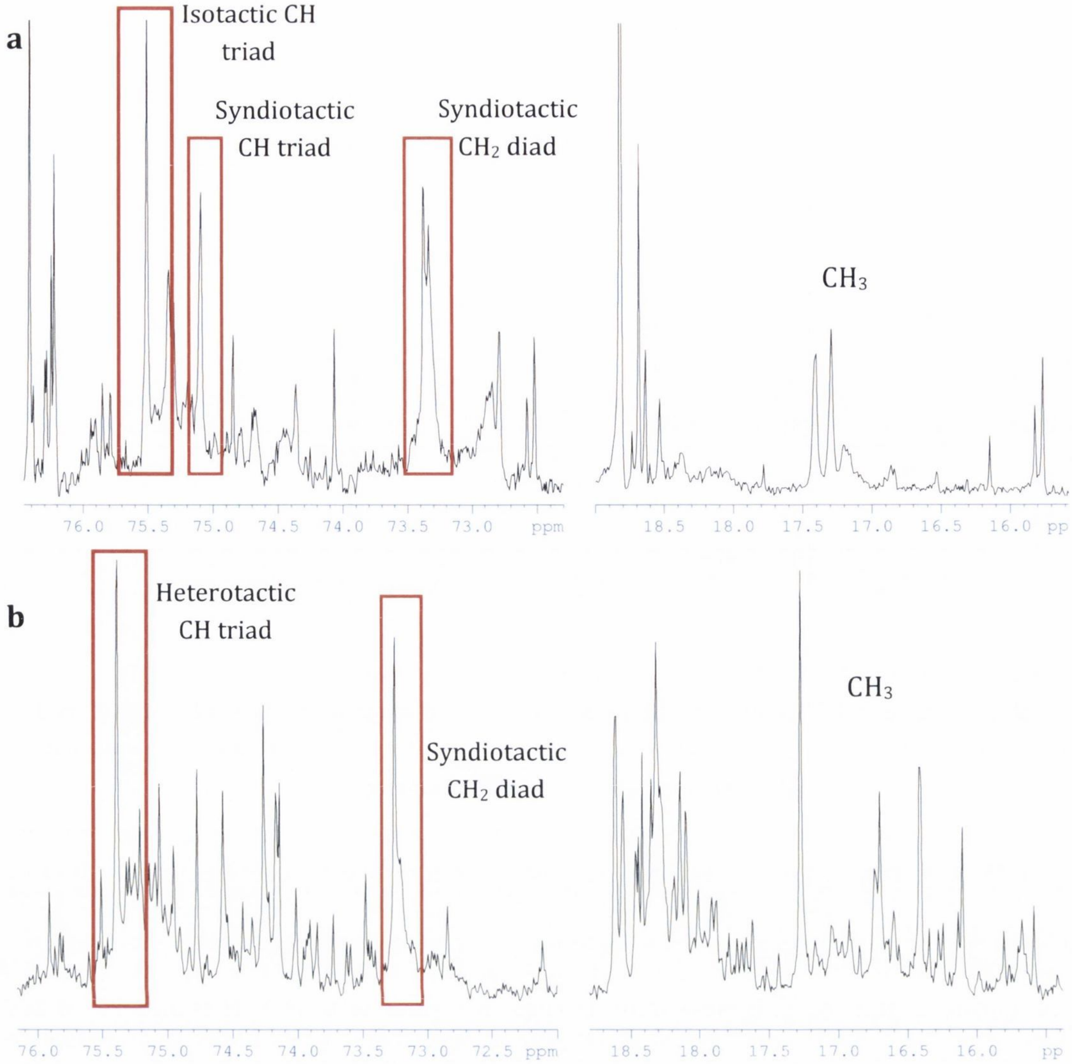

Figure 4.12: (a) ^{13}C[H] NMR for the backbone of PPO synthesised from racemic PO; (b) ^{13}C NMR for the backbone of PPO from *s*-PO.

Another typical test for stereochemistry to gain insight into the mode of ROP is the ROP of dimethylbutene oxide (DMBO),[18a] however, DMBO did not undergo ROP with **1** or with uranyl chloride. This is surprising given that the ring strain in DMBO and PO is almost identical (114.2 and 114.3 kJ mol^{-1}, respectively). Steric hindrance is unlikely as CHO undergoes ROP despite the steric bulk of the cyclohexene ring, therefore it appears that there is an electronic reason for the inhibition of the ring-opening. To investigate this, the 2D NMR technique Exchange Spectroscopy (EXSY) was used to monitor the coordination at the uranyl by monitoring the exchange of PO and DMBO with bound thf molecules (**Figure 4.13**). By monitoring the rate of exchange at different temperatures the activation energy, E_a, enthalpy, ΔH°, and entropy, ΔS°, of coordination can be calculated from

Equation 4.1. These experiments were performed with **1** as **(U–Cl)$_2$** was sparingly soluble in C_6D_6.

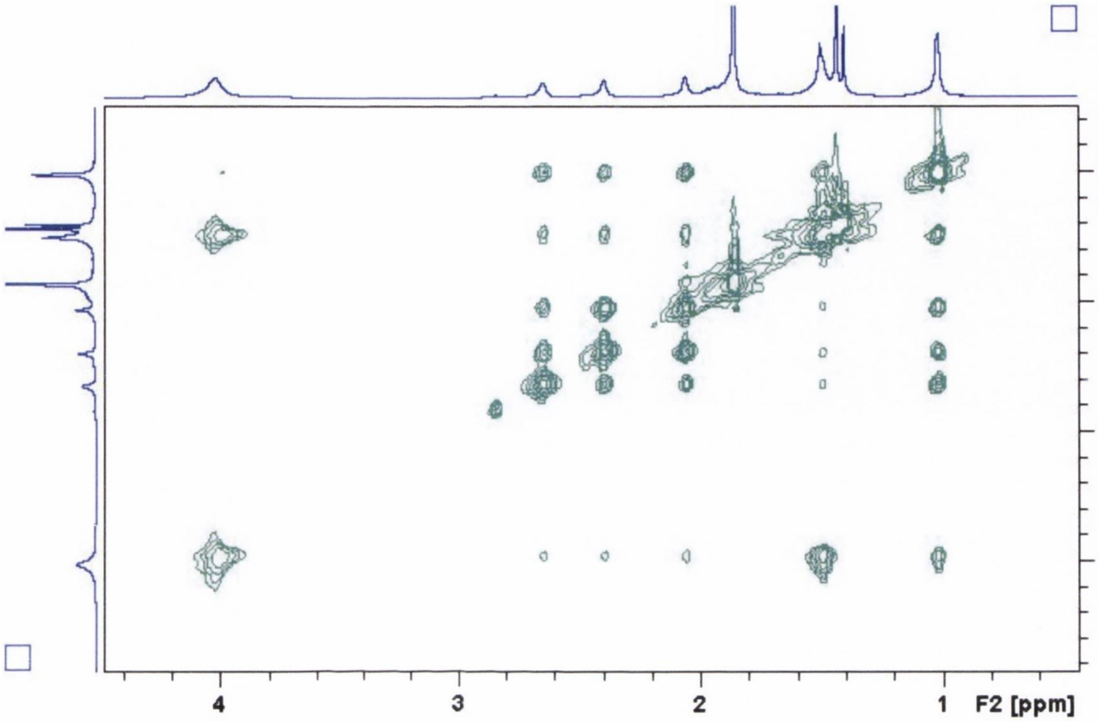

Figure 4.13: 2D ^{1}H EXSY spectrum of PO in C_6D_6 at 25°C, t_m = 0.8 s. Crosspeaks indicate signals that exchange in solution. Thf peaks at 1.52 and 3.95 ppm exchange with PO signals at 1.04, 2.05, 2.42 and 2.66 ppm.

To determine the reason for the failure to ring-open DMBO, the thermodynamic parameters of the coordination to **1** were calculated using previously reported methods (**Section 4.1.3.1**).[27,33] The results (**Table 4.2**) imply that coordination of DMBO to the uranyl centre is exothermic and entropically favourable. The negative values for ΔS° imply an associative mechanism for coordination so it is possible that the DMBO adduct does not readily lose the thf and thus inhibits the next step in the mechanism. The CHO was shown to coordinate using EXSY, but the overlapping ether and thf proton signals rendered thermodynamic calculations unreliable.

Table 4.2: Thermodynamic parameters of coordination of epoxide monomers to 1.

Monomer	Ring Strain (kJ mol^{-1})	E_a (kJ)	ΔH° (kJ)	ΔS° (kJ)
DMBO	114.2	-70.905	-73.473	-0.533
PO	114.3	43.306	40.739	-0.1394

As DMBO did not polymerise, it was decided to examine the microstructure of PCO to determine the mechanism of ring-opening. The ROP of CHO turns a *cis* ring system into either a *cis* or *trans* diol (**Figure 4.14**), therefore examining PCO using *J*-resolved ^1H NMR spectroscopy can identify the mode of ROP (**Figure 4.15**).[18b] The potential isomers from the ROP of CHO have been examined and the *J*-values calculated theoretically. The experimental results (**Figure 4.16**) were compared with the theoretical and the ddd coupling pattern for the multiplets at 3.51 and 3.22 ppm indicate that the polymer consisted of repeating units of the **Trans A** structure (**Table 4.3**).

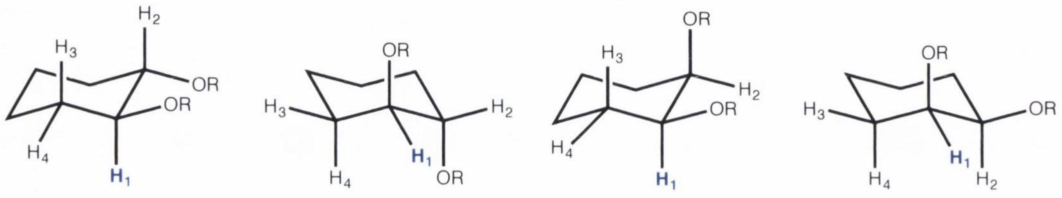

Trans A **Trans B** **Cis A** **Cis B**

Figure 4.14: Possible isomers of the diol resulting from the ROP of CHO.

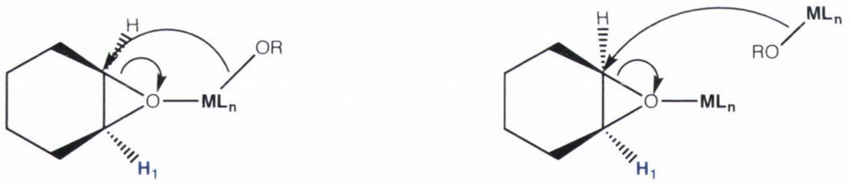

***cis*-Migratory Insertion**
Retention of stereochemistry at carbon
cis product formed

Backside attack
Inversion of stereochemistry at carbon
trans product formed

Figure 4.15: The modes of ROP of CHO and the resulting stereochemistry.

Table 4.3: Comparison of theoretical and experimental *J* values for 1,2-cyclohexenediol.

	Theoretical *J* Values (Hz)					Experimental (Hz)		
	Trans A	Trans B	Cis A	Cis B	Cis A+B	(U–Cl)	$(U–Cl)_2$	OAr
H1-H2	11.3 ± 0.1	2.6 ± 0.1	11.4 ± 0.1	2.5 ± 0.1	5.2 ± 3.8	11.0	11.0	10.9
H1-H3	8.5 ± 0.2	3.1 ± 0.3	2.2 ± 0.3	2.5 ± 0.1	2.3 ± 0.3	8.7	8.7	8.7
H1-H4	4.3 ± 0.3	3.6 ± 0.1	3.9 ± 0.4	3.7 ± 0.1	5.2 ± 3.8	4.6	4.5	4.6

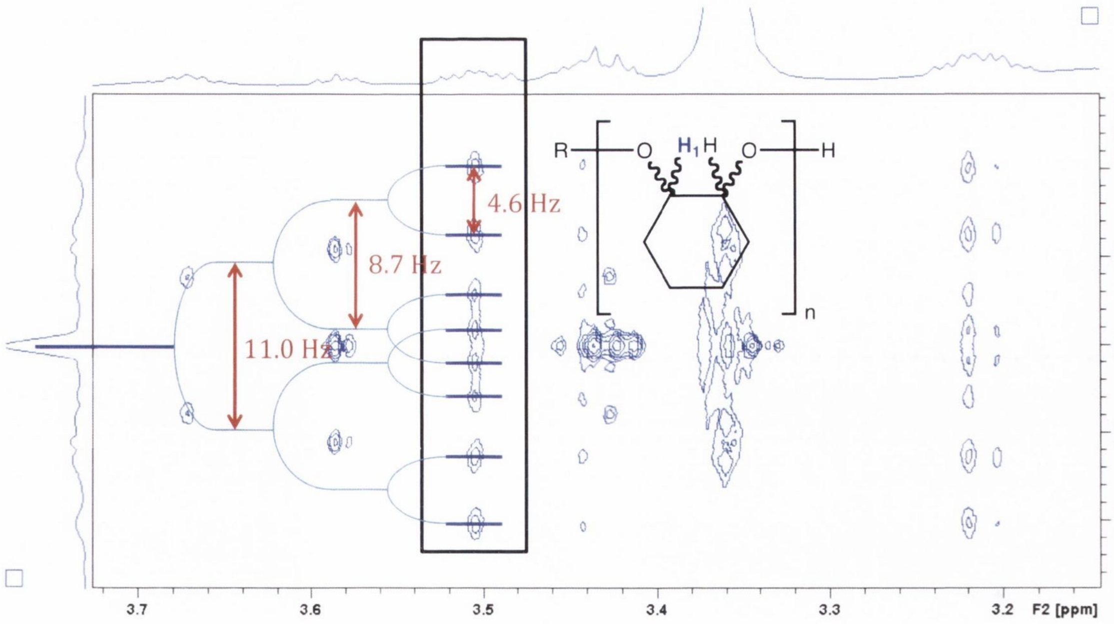

Figure 4.16: ^{1}H *J*-resolved spectrum of PCO, ((U–Cl)$_2$, at 100°C).

The existence of a *trans* polymer suggests a "back-side" attack mechanism which implies a bimetallic mechanism. A back-side attack would result in inversion of stereochemistry which is consistent with the ^{13}C analysis of PPO and PPO synthesised from *s*-PO. Diffusion Spectroscopy (DOSY) was used to identify the probable pathway for the propagation by approximating the size of molecules in solution.[29,34] The calculated radius of **1** from the x-ray structure is 6.2 Å. The experimental hydrodynamic radius of the catalyst was found to be 4.82 Å. This increases to 5.43 Å upon addition of PO (**Table 4.4**), indicating that the dominant species in solution is monomeric.

Table 4.4: The experimental hydrodynamic radii found from DOSY experiments.

Solvent	Components	C[a]	D_t (m^2 s^{-1})	R_h (Å)
CD_3CN	**1**	4	1.98 E-09	4.82
CD_3CN	**1** + 10 eq. PO	4	1.76 E-10	5.43

[a] Where c is the frictional coefficient, c = 4 for the slip-boundary condition.[28]

DOSY was not a sufficient tool for examining the uranyl chloride system as no specific ^{1}H resonances could be attributed to any propagating species, however, emission spectroscopy has proven to be a very sensitive technique and has proven useful in the determination of uranyl speciation in solution.[35] Low temperature (77 K) emission in thf gives a spectrum dominated by "hot-bands" that are slightly shifted in relation to $UO_2Cl_2(thf)_3$ (**Figure 4.17**). This indicates that the dominant species in solution is electronically very similar to the monomer. The 7 ns lifetime is indicative of significant quenching, most likely due to exchange of thf and/ or PO. This spectroscopic evidence suggests that the propagating species in solution is either monomeric or vibrationally isolated dimers.

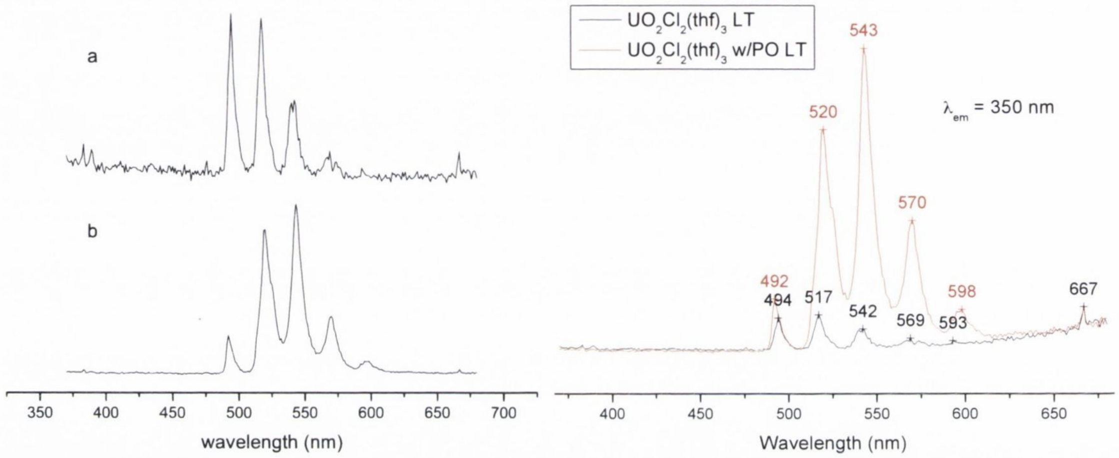

Figure 4.17: Emission spectra of uranyl chloride (a) and uranyl chloride and 20 eq. PO (b) in thf at 77 K (λ_{ex} = 350 nm).

To summarise, the uranyl aryloxide **1** and uranyl chloride (**U–Cl** and **(U–Cl)$_2$**) are catalysts for the ROP of epoxides. These undergo coordination to the metal *via* an associative mechanism. Analysis of the microstructure of the polymers showed significant evidence for an intermolecular, bimetallic mechanism that could not be confirmed with *in situ* solution investigations. To verify the proposed bimetallic mechanism, and to give a deeper understanding of the process, comprehensive computational investigations were undertaken by Professor Luarent Maron, INSA Toulouse, to examine the probable interactions with PO and uranyl chloride, **U–Cl** and **(U–Cl)$_2$**, and with the uranyl aryloxide complex **1**.

4.2.2. Theoretical Investigations

The two first insertions of PO were considered and in all cases the ring-opening on the two different carbon centres has been computed. Due to the well-known problem of correctly computing the entropy, the profiles are reported in enthalpy at 298.15 K. For the sake of clarity, the uranyl chloride and uranyl aryloxide catalysts will be discussed separately.

4.2.2.1. Theoretical Investigations: Uranyl Chloride

As mentioned previously, uranyl chloride exists as the monomeric species **(U–Cl)** in coordinating solvents and as the dimeric **(U–Cl)$_2$** in non-coordinating solvents. Although it is postulated that upon coordination of the epoxide there will only be monomeric species in the form of [$UO_2Cl_2(thf)_x(epoxide)_y$], the reaction mechanism involving both the monomer and dimer were considered for intramolecular additions (**Scheme 4.1**). The possibility of a bimetallic intermolecular mechanism is also considered. In each case, attack at the two carbon centres on the epoxide is examined.

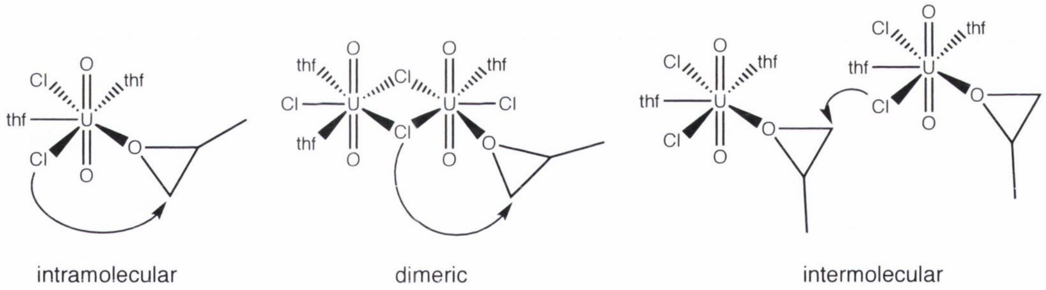

Scheme 4.1: Possible mechanisms for the first insertion of PO of uranium chloride.

In all computed cases, the replacement of a coordinated thf molecule by PO is computed to be favourable, at around 1 kcal mol^{-1} in the best cases. In these adducts, the PO coordinates to the uranium via its oxygen atom (U–O_{PO} distance of 2.460 Å) and the C–O bond distances in the three membered ring are slightly lengthened to 1.456 Å and 1.444 Å (c.f. 1.427 Å and 1.425 Å in the free PO). The U=O_{yl} bond length is known to be somewhat sensitive to the electronic environment,[36] and in these adducts it is shortened slightly to 1.735 Å from 1.766 Å in **U–Cl**.[37] For comparison, the U–O bonds of the coordinated thf in

U–Cl are 2.443(6), 2.464(5) and 2.467(6) Å, whilst the U=O_{yl} bond length is indicating a small shift of electron density from the uranium upon ligand exchange.

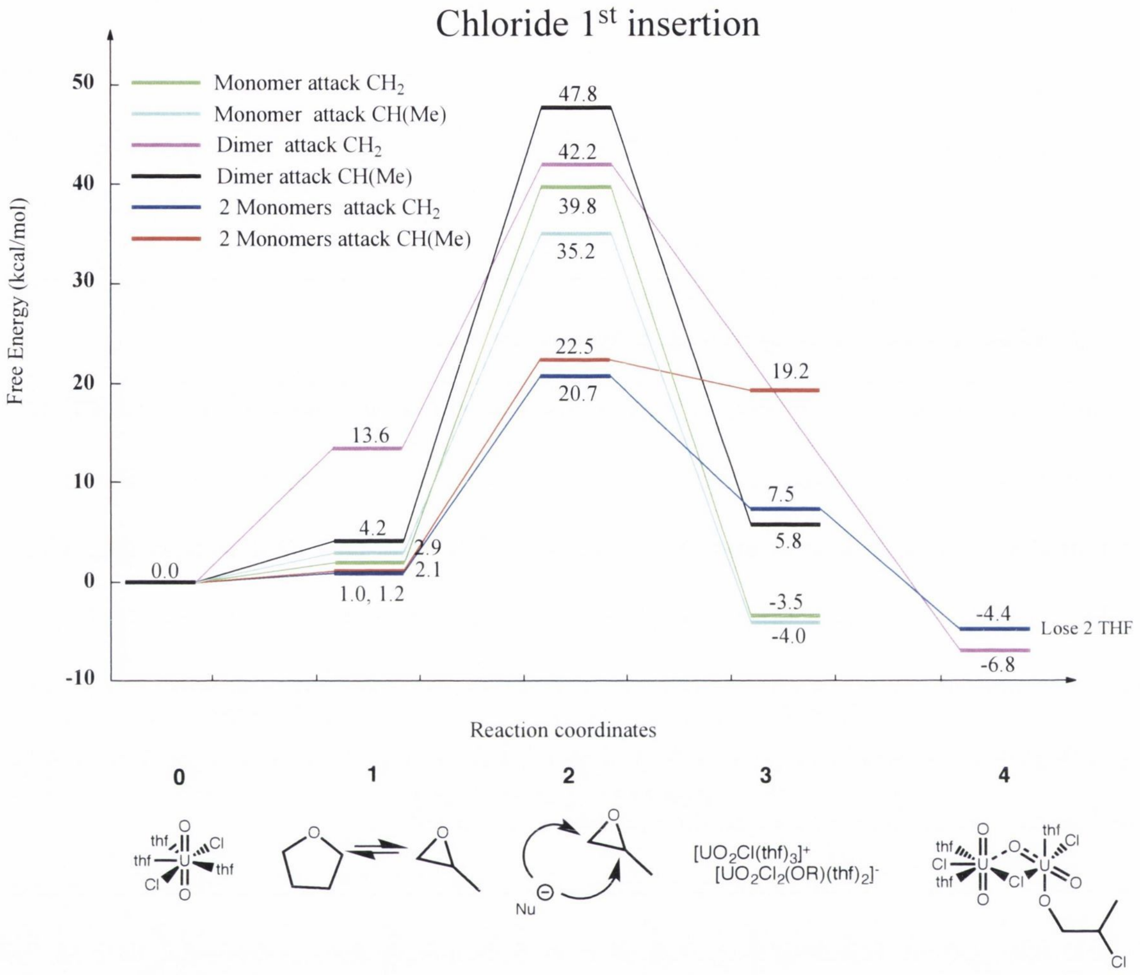

Figure 4.18: Enthalpy energy profile at 298.15K for the first step of the reaction of PO with $[UO_2Cl_2(thf)_3]$. The reaction coordinates are shown for clarity.

From the adduct, the system has to reach the NA TS (Reaction coordinate 2, **Figure 4.18**). At this stage, important differences are observed between the three set catalysts that were considered. The highest barrier (more than 40.0 kcal.mol^{-1}) is found for the dimer, indicating that the polymerisation reaction cannot occur with this species. This is due to the fact that the U-U distance is fixed in the dimer by the bridging chlorine atom. Thus, the stabilising presence of the bridge induces a steric constraint that destabilises the transition state [**Figure 4.19(b)**].

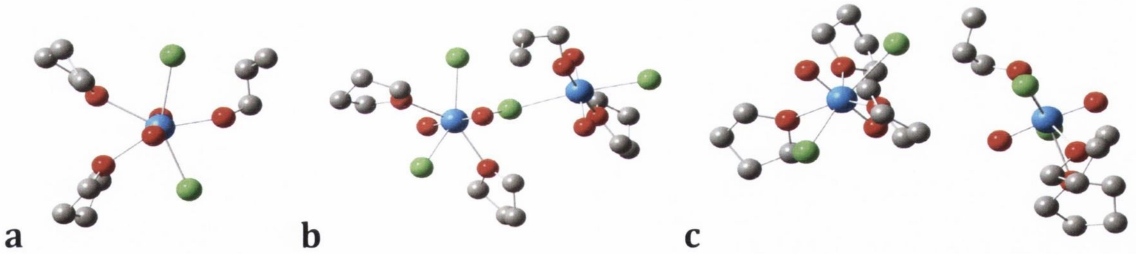

Figure 4.19: Predicted structures of the (a) monomeric, (b) dimeric, and (c) intermolecular transition state (TS) arrangements for uranyl chloride.

The monomer system [**Figure 4.19(a)**] leads to barriers around 35.2 and 39.8 kcal mol^{-1}. This result is in excellent agreement with the experimental study which showed that chloride ligands are not efficient as initiator ligands for ring opening polymerisation compared to the uranyl aryloxide (*vide infra*). This is due to the strong directionality of the chloride orbitals that are needed to point toward the empty orbital developing on the PO. Certainly the coordination to only one metal centre in the dimer does not allow an easy process [**Figure 4.19(b)**]. On the other hand, removing the geometric constraint by involving a second metal centre clearly improved the results (**Figure 4.18**, the red and blue paths). Indeed, when the activated PO is coordinated to one uranium centre and the chloride is coordinated to another uranium centre, this allows an optimal orientation of the chloride lone pair toward the empty σ* orbital of the PO due to the lack of the constraining, rigid structure of the dimer (**Figure 4.20**). This leads to a substantial lowering of the activation barrier (by over 20 kcal mol^{-1}), indicating that this is the kinetically favoured pathway. Thus, only the geometry of this TS will be discussed below.

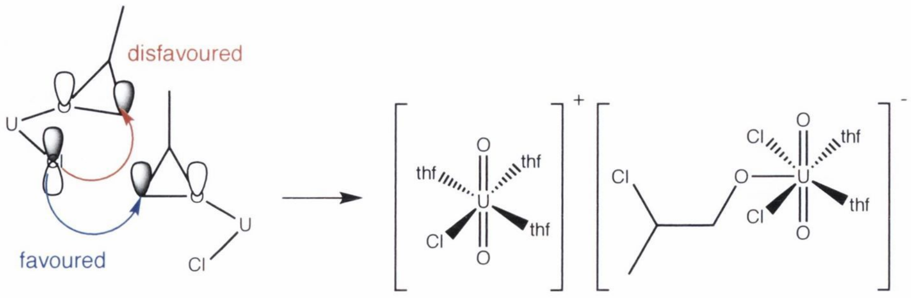

Figure 4.20: The ring-opening step with uranyl chloride and PO.

At the intermolecular TS [**Figure 4.19(c)**], the ring is almost opened (C–O distances of 2.0248 Å and 1.394 Å) but neither the C–Cl nor the $U–O_{PO}$ bonds are already fully formed

(2.346 Å and 2.223 Å respectively). The TS is thus strongly ionic in character – further substantiated by the NBO analysis (APT charges: C: 1.1809; O: -1.4090). This is also in line with the computed slight kinetic preference for the nucleophilic attack to take place at the secondary carbon rather than at the primary carbon of the PO molecule (although the difference is within the error bar of the method). This preference was also reported experimentally, although some regio-irregular insertions were noted in the polymer (*vide supra*).[9b] Attack of the chiral centre induces a better stabilisation of the carbocation at the TS, allowing a facile attack of the chloride. From a thermodynamic point of view, the reaction is predicted to be endergonic by 7.5 kcal mol^{-1} because of the lack of stabilising orbital interaction of the formed ion pair $[UO_2Cl(thf)_3]^+[UO_2Cl_2(OCH_2CClHMe)(thf)_2]^-$ (**Figure 4.20**). However, this ion pair can undergo an isomerisation process to form a weakly bonded dimer with a bridging chloride concomitant with the loss of a second thf molecule (Reaction coordinate 4, **Figure 4.18**). This is reminiscent of a cation–cation interaction, with a $U \cdots O_{yl}$ distance of 2.387 Å. It is noteworthy that this isomerisation was observed during the course of the geometry optimisation of the product and no double bridging chloride dimer was found (it may exist but was not observed during this optimisation). The stabilisation due to this isomerisation is computed to be 11.9 kcal mol^{-1}, leading to an overall exergonic reaction. These results show that coordination of the epoxide is not significantly affected by the nature of the uranyl complex and is not the rate-determining step – something that is consistent with studies of analogous solvated and unsolvated compounds.[38] The calculations suggest that the rate-determining step is the ring opening of the epoxide, and this is consistent with previous reports on other metal-based catalysts.[39]

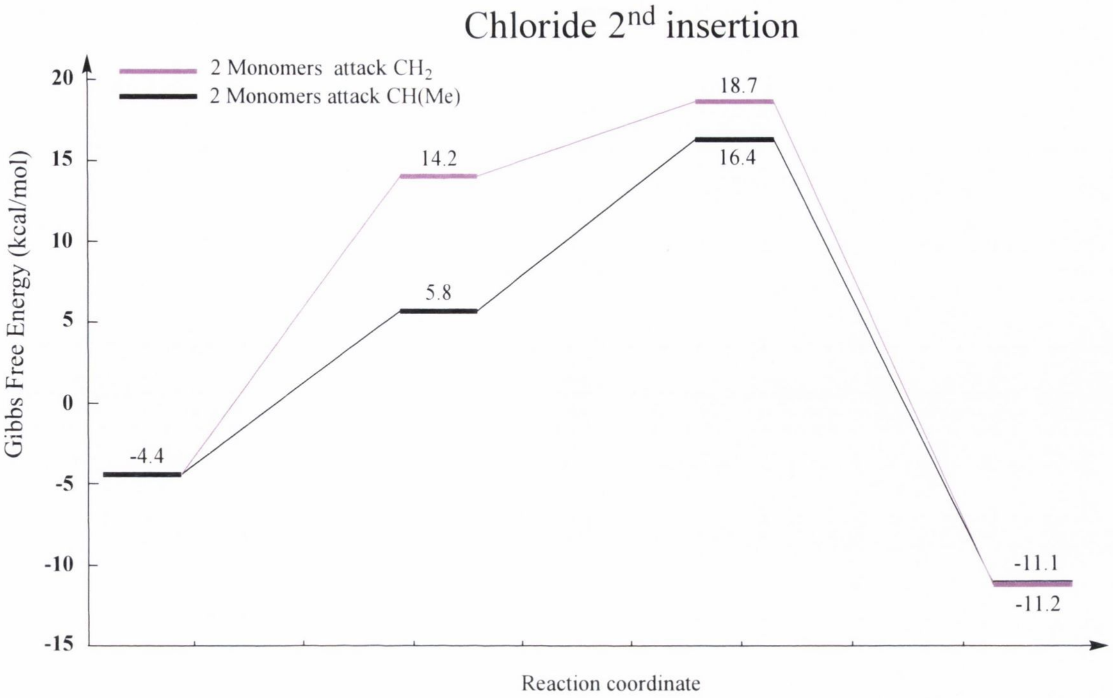

Figure 4.21: Enthalpy energy profile at 298.15K for the second step of the reaction of PO with [$UO_2Cl_2(thf)_3$].

The second insertion has been computed starting from this weakly bonded dimer (Reaction coordinate 4, **Figure 4.18**). It is noteworthy that the ring-opening of PO creates a second active site on the metal centre in the form of an alkoxide. However, given that the reaction is first order in catalyst concentration it is unlikely that the alkoxide and the chloride participate in the mechanism. The relative propensity of chlorides and alkoxides for nucleophlic attack infers that only the alkoxide will participate in the propagation step and so only the alkoxide propagation will be discussed.

The coordination of the incoming second PO molecule at the cationic uranium centre disrupts the stabilised dimer, and so is predicted to be endergonic by 10.2 or 18.6 kcal mol^{-1} – corresponding to overcoming the stabilisation energy of the dimeric reaction coordinate 4. The coordination is very similar to the one found in the first insertion reaction. The U–O_{PO} distance is 2.340 Å and the C–O bond lengths are 1.480 Å and 1.463 Å. The TS is similar to the one found at the first insertion with an opened ring but with the U–O_{PO} and C–O bonds not yet fully formed (2.245 Å and 2.238 Å). The TS is thus still strongly ionic (charges of C: 1.1157; O: -1.5277), explaining again the slight preference for the nucleophilic attack at the chiral carbon centre (secondary carbon). Again, the difference of the energy barrier is within the error bar of the method, consistent with the regio-irregular regions in the polymer ^{13}C NMR spectrum (**Figure 4.12**). The thermodynamics of the reaction are favourable for this insertion because it leads to the formation of two neutral species: $[UO_2Cl(O\text{-}CH_2CHMe)_2\text{-}Cl(thf)]$ and $[UO_2Cl_2(thf)]$. These do not require dimerisation making this an exergonic process (by 6.7 kcal mol^{-1}).

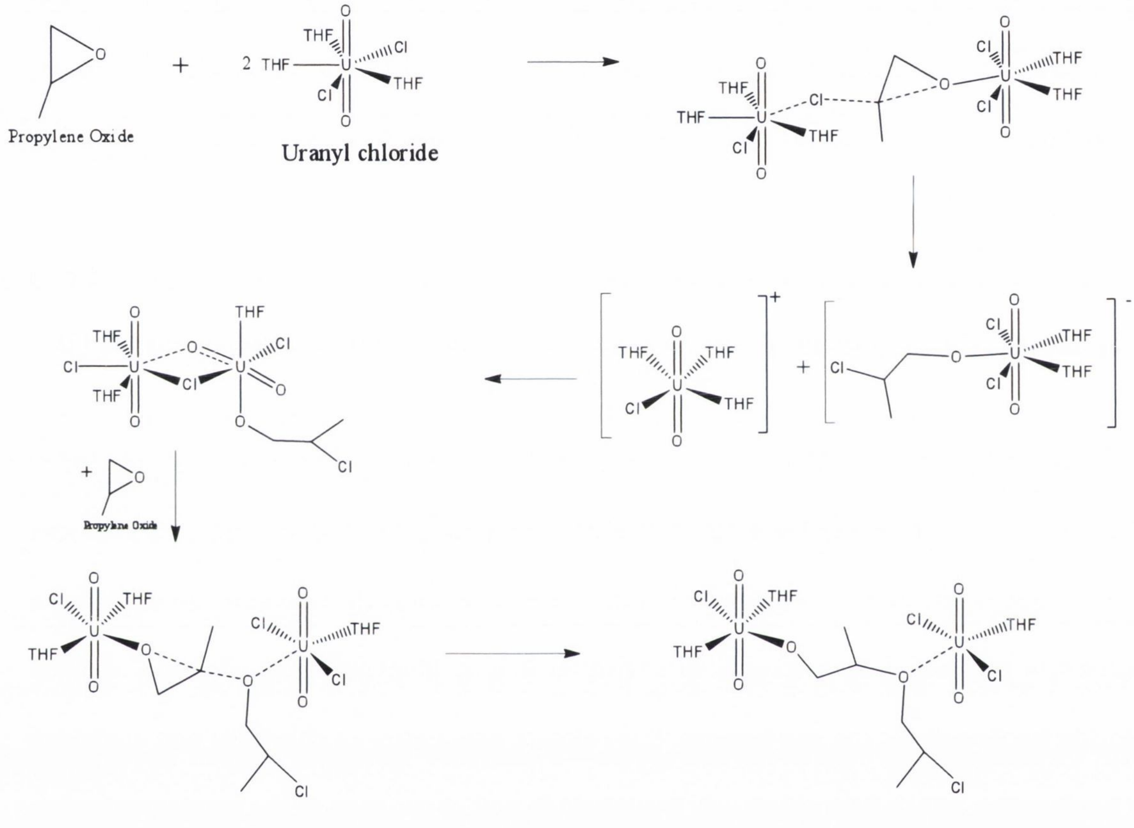

Scheme 4.2: Computed mechanism of the ring opening polymerisation of propylene oxide catalysed by uranyl chloride.

To summarise the computational and experimental studies utilising uranyl chloride as a catalyst, **Scheme 4.2** illustrates the first two insertions of PO. The experimental results indicated that the ROP of CHO occurred *via* an intermolecular mechanism; the studies into PO indicate a similar mechanism is the most favourable route due to orbital control in the TS (**Figure 4.20**).

4.2.2.2. Theoretical Investigations: Uranyl Aryloxide 1

Unlike the uranyl chloride catalyst where a dimeric structure has been demonstrated experimentally, the uranyl aryloxide **1** exists as a monomer in solution.[14] As such, only the pathways involving an inter- or intramolecular ring-opening have been computed for **1** (**Figure 4.22**). The reaction begins by a thf/ PO exchange that is computed to be accessible (between 1.0 and 7.0 kcal mol^{-1}), and in line with the experimentally derived kinetic data. The PO coordination is similar to the manner for uranyl chloride. The NA TS is reached from this adduct and a clear difference between the considered pathways is observed: the intermolecular pathway is found to be far less accessible than the intramolecular pathway. This is mainly ascribed to the steric effect of the bulky aryloxide that inhibits the possible approach of a second uranyl-aryloxide molecule. However, unlike the chloride, the bending of the aryl group allows a lone pair to point toward the empty σ* orbital of the activated PO, thus enabling an intramolecular route. Indeed, the U–O–C_{phen} angle is 167° (compared to 180° in **1**) showing the reorientation of a lone pair of the aryl oxygen toward the empty orbital at the PO. Consequently, due to these two effects, the first insertion will occur through an intramolecular route. This is the known pathway for the ring opening polymerisation of lactones, but it is not common for epoxide ring-openings without extensive ligand design.[12]

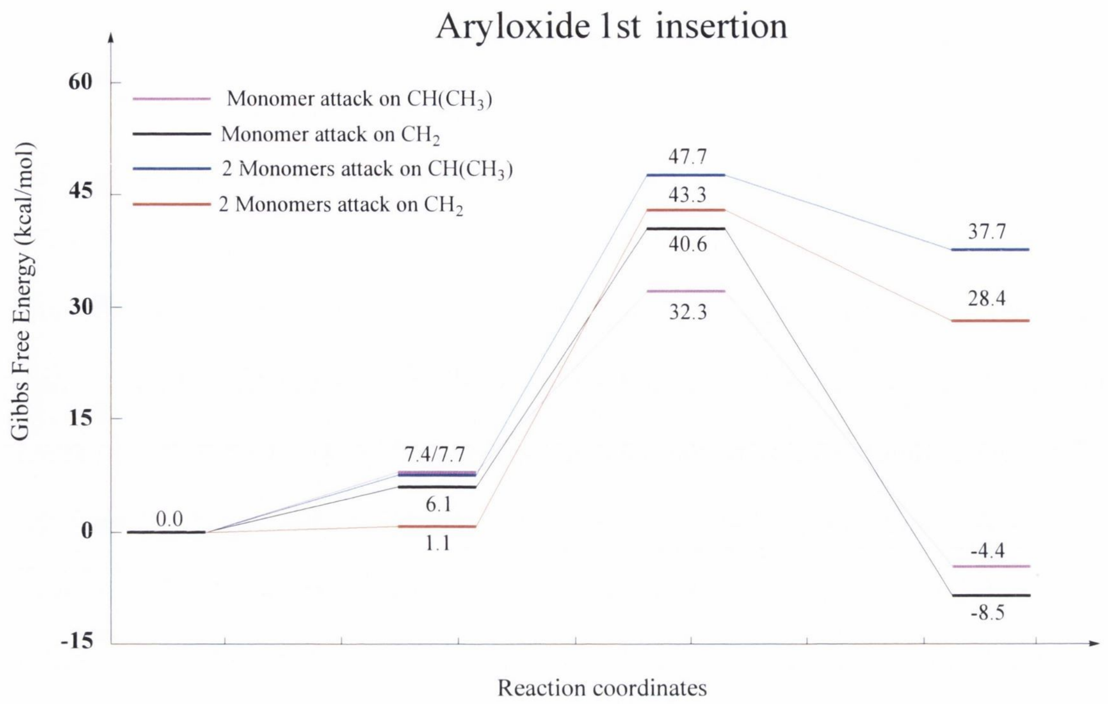

Figure 4.22: Enthalpy energy profile at 298.15K for the first reaction of PO with the aryloxide catalyst.

Spectroscopic analysis of this system and other literature reports show that the propagation step is intermolecular. As found for the chloride catalyst, the TS is highly ionic (C: 0.2989; O: -1.1091) explaining the kinetic preference for the attack at the PPO chiral centre (**Figure 4.23**). It is noteworthy that the difference is clearly marked (difference of 8.3 kcal mol^{-1}). Comparing the activation barrier for the two catalysts, it is interesting to note that although the aryloxide is a better nucleophile than the chloride, its bulkiness induces an important steric repulsion that makes the aryloxide catalyst less efficient than the chloride for this first step. From a thermodynamic point of view, the overall reaction is exergonic. Interestingly, the product arising from the NA at the CH_2 centre is found to be more stable than the other one, which is the kinetic product – this can account for the experimental observation of misinsertion in the polymer chain. Subsequently, in the second insertion, both the kinetic and the thermodynamic product have been considered. In each case, the four pathways considered in the first step were computed, leading to 8 different pathways (**Figure 4.23**).

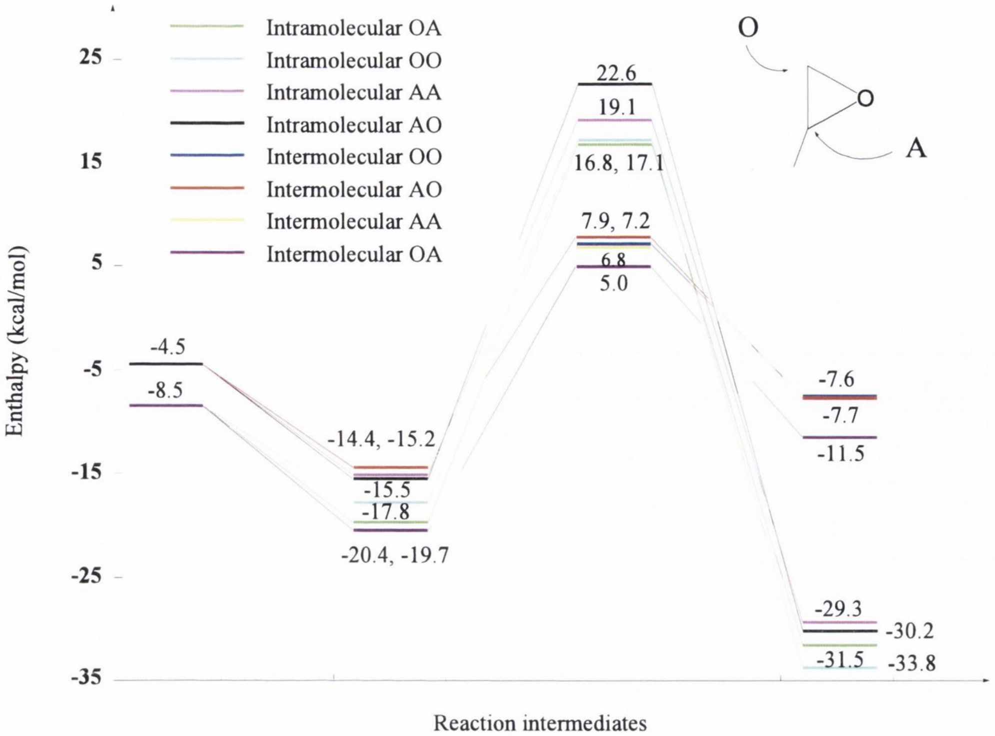

Figure 4.23: Enthalpy energy profile at 298.15K for the second reaction of PO with the aryloxide catalyst.

As for the chloride catalyst, only the propagation step with the alkoxide has been considered. Moreover, the reaction profile is very similar to that reported before. The major difference is that the PO coordination is calculated to be an exergonic process by roughly 10.0 kcal.mol^{-1}. For this second insertion, the intramolecular pathway is found to be kinetically less favourable than the intermolecular by 11.0 to 15.0 kcal.mol^{-1}. This can be attributed once again to steric effects. Indeed, the steric hindrance at the uranium centre in the intramolecular pathway makes the second insertion less favourable than the first one. Hence, the intermolecular route becomes competitive and, in part, more favourable than the intramolecular route. As in all previously described cases, the TS is strongly ionic in line with the fact that the NA at the chiral centre is more favourable than at the other carbon. Interestingly, starting from both products of the first insertion, this attack is the most favourable one. From the kinetic point of view, the reaction is found to be exergonic and is leading to the formation of an ion pair. However, unlike the chloride catalyst, the aryloxide ligand has a lower ability to adopt a bridging position. Thus, the propagating species is also predicted to be intermolecular, as already found for the chloride catalysts (**Scheme 4.3**).

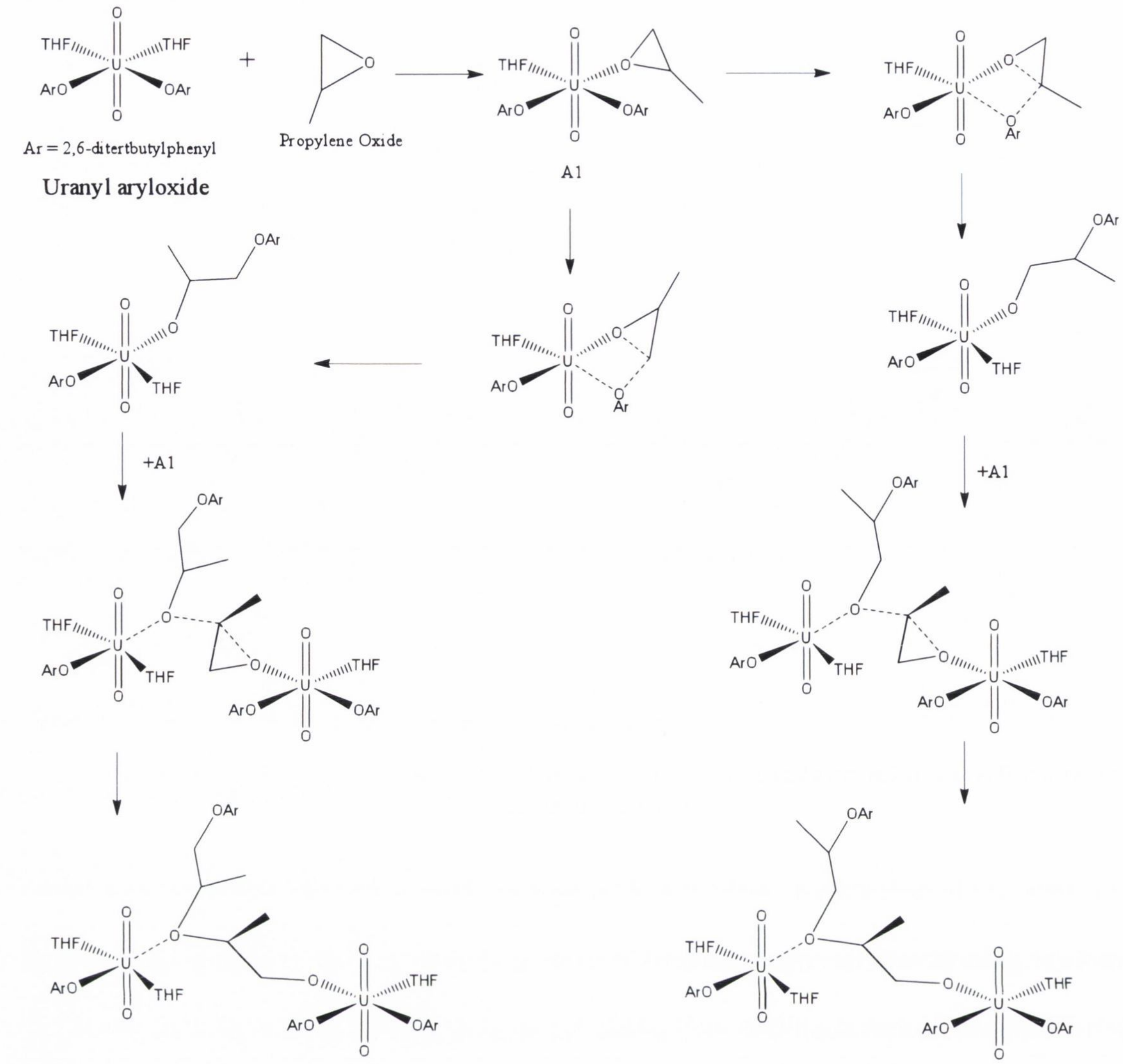

Scheme 4.3: Computed scheme for ROP of PO with uranyl aryloxide catalyst 1, showing the first insertion products of NA at the 1° and 2° carbon centres on PO and the preferential attack at the 2° carbon during the second insertion.

To summarise the reaction of PO with **1**, one can see that the greater steric requirements of the bulkier aryloxide force the initiation step to be intramolecular but the propagation pathway is preferentially intermolecular. In thf solutions this final structure will most likely undergo a similar dimerisation as before to yield an intermediate $[UO_2OAr(thf)_3]^+[UO_2(OAr)_2(thf)P]^-$ complex. When combined with experimental data, it appears that there is a monomeric species in solution. Given the steric hindrance around the uranyl moiety, it is reasonable that the mechanistic pathway is dictated by the presence of the aryloxides. It is likely that the resting state of the system is a monomeric uranyl phenoxide species.

4.3. Uranyl and the Ring-Opening Polymerisation of Lactones

The ROP of lactones is known to occur *via* intramolecular, *cis*-migratory insertion mechanisms.[16b,40] Given the evidence for a bimetallic ROP mechanism with the studied epoxides, it was considered that the potential of uranyl complexes for catalysing *via* an intramolecular mechanism should be examined.

4.3.1. Experimental Investigations

1 was reacted with 100, 300 and 600 molar equivalents of ε-Caprolactone (εCL) at temperatures of 25, 70 and 100°C in thf or toluene. From graphing the conversion of monomer to polymer, it is easy to see that the reactions in toluene achieve a higher conversion, indicating a possible competition between thf and εCL at the active site [**Figure 4.24(a)–(c)**]. **Table 4.5** contains a sample of the polymer characteristics. While the molecular masses are not very high, the results at room temperature are interesting: one of the most active catalysts known for ROP of lactide does not operate below 70°C,[11a] but our system has similar conversion at the three temperatures examined. It is also interesting to note the lack of the end group (2,6-di*tert*butylphenol) in the polymer according to ^{1}H NMR (**Figure 4.25**) and MALDI-ToF analysis (**Figure 4.26**). This could be indicative of a transesterification or back-biting termination step, consistent with the anionic mechanism, which is a common pathway at higher temperatures for lactone ROP.[16b] The polydispersities (PD$_i$) vary between ~1.2 and ~1.75, indicating that there is good control at the single active site on the catalyst. The closeness of the PD$_i$ to 1 stimulated a question of a living polymer, however a test of sequential addition of monomer to the reaction showed that the average weight, M$_n$, did not change (**Table 4.6**). This is consistent with the back-biting termination step as this will limit the size and growth of the polymer.

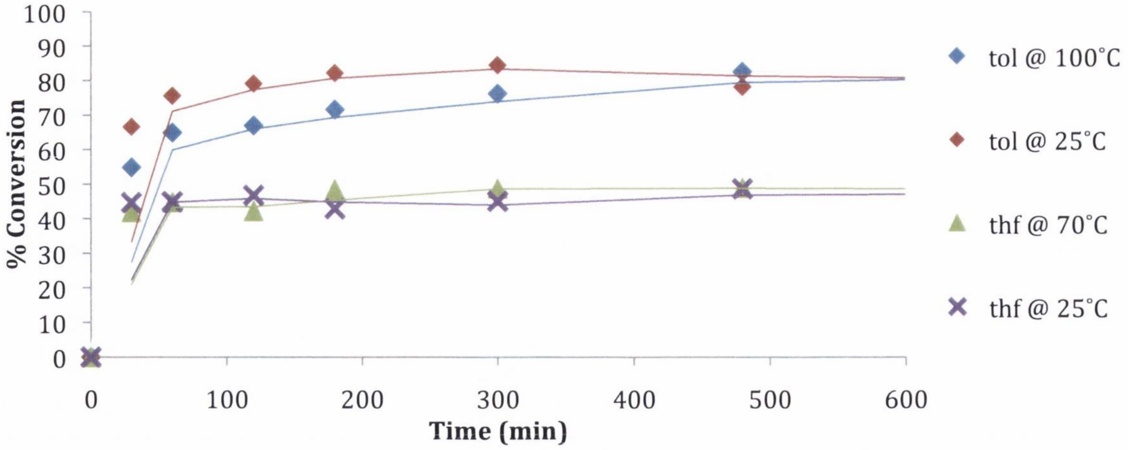

Figure 4.24(a): % Conversion of εCL to PCL against time with 1:100 catalyst:monomer ratio.

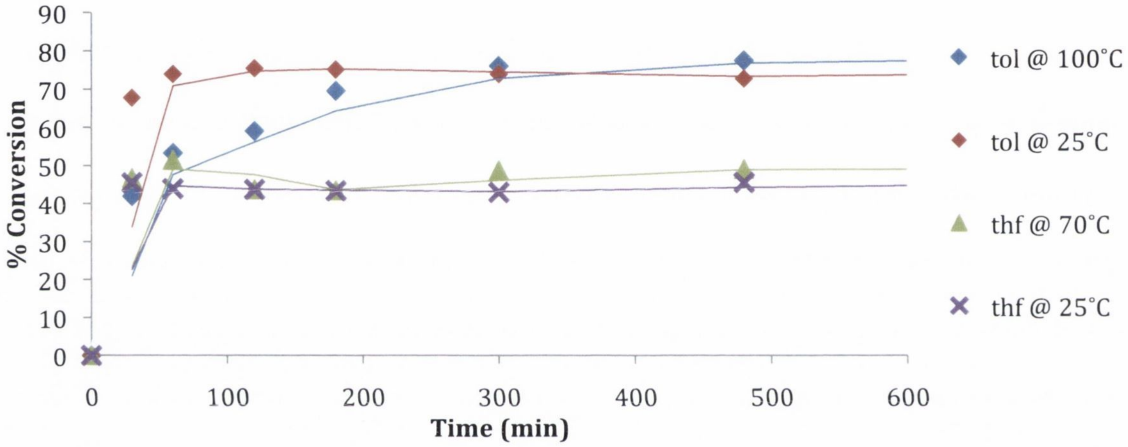

Figure 4.24(b): % Conversion of εCL to PCL against time with 1:300 catalyst:monomer ratio.

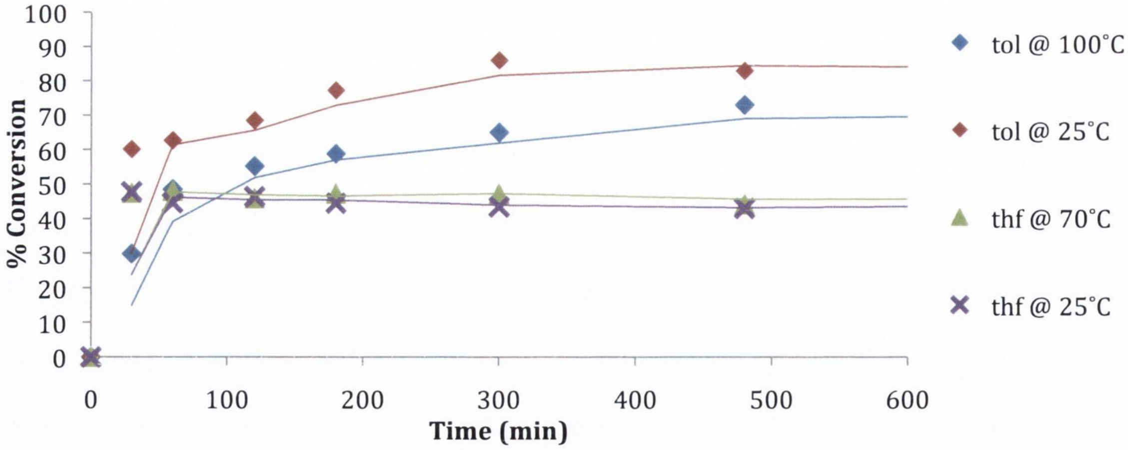

Figure 4.24(c): % Conversion of εCL to PCL against time with 1:600 catalyst:monomer ratio.

Table 4.5: PCL characteristics from GPC

Run	Solvent	Temp (°C)	Catalyst Loading	Time (h)	M_n[a]	PD_i
1	thf	25	1:100	5	3821	1.637
2	thf	25	1:100	24	3418	1.562
3	thf	25	1:300	24	3881	1.464
4	thf	25	1:600	24	3734	1.533
5	thf	70	1:100	5	3033	1.446
6	thf	70	1:100	24	2843	1.466
7	thf	70	1:300	24	3263	1.504
8	thf	70	1:600	24	2704	1.353
9	toluene	25	1:100	5	2340	1.296
10	toluene	25	1:100	24	2311	1.288
11	toluene	25	1:300	24	2379	1.268
12	toluene	25	1:600	24	2586	1.392
13	toluene	70	1:100	5	1829	1.328
14	toluene	70	1:100	24	692	1.373
15	toluene	70	1:300	24	1083	1.300
16	toluene	70	1:600	24	1416	1.178
17	toluene	100	1:100	5	2840	1.479
18	toluene	100	1:100	24	3637	1.753
19	toluene	100	1:300	24	5278	1.246
20	toluene	100	1:600	72	2331	1.221

Table 4.6: Results of Living Test (εCL).

Solvent	Temp (°C)	Catalyst Loading	Time (h)	M_n[a]	PD_i
toluene	100	1:100	72	6223	1.823
toluene	100	1:100	144	4283	1.602

[a] M_n values are corrected from the polystyrene calibrants using the Mark-Houwink factor.[30]

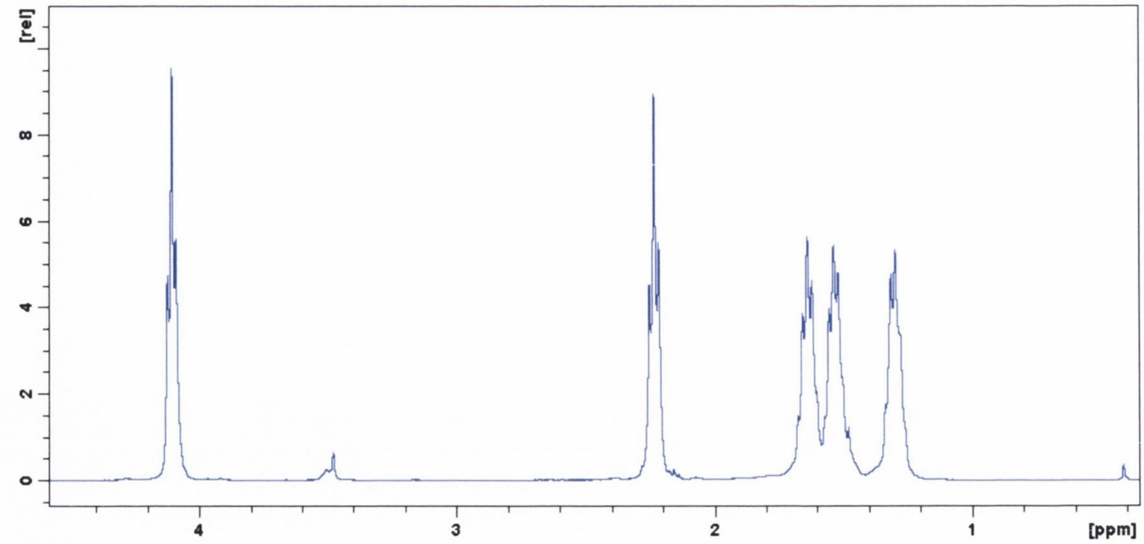

Figure 4.25: ^{1}H NMR spectrum of polycaprolactone. There is no evidence of aryl protons in the spectrum, implying that there is no end-group on the polymer.

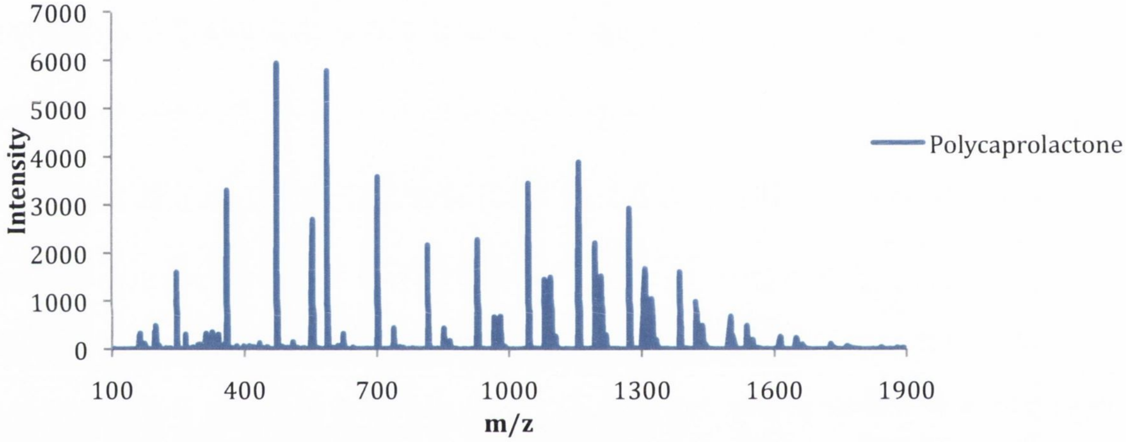

Figure 4.26: Mass spectrogram of polycaprolactone. The major series corresponds to $[H_2O(C_6H_{10}O_2)_nH]^+$ for increasing values of n. The minor series corresponds to $[H_2O(C_6H_{10}O_2)_nNa]^+$ for increasing values of n.

If enthalpy is a driving-force for ROP, then the propagation is expected to be driven by the release of ring strain within the monomer, a theory examined by the reaction of a series of lactones with **1** (**Figure 4.4**). The first test was with *rac*-lactide (lac), a typical test for catalysts suitable for εCL ROP. Tests with **1** and lac, however, were not promising: only 12% conversion to PL was observed after 72 h reflux in thf. The steric hindrance of the α-methyl was considered to be the limiting factor; to confirm this, EXSY was used to identify the rate of coordination of lactide to the uranyl. It was found that there was no exchange – or that the rate of exchange was too slow to be detected (**Figure 4.27**).

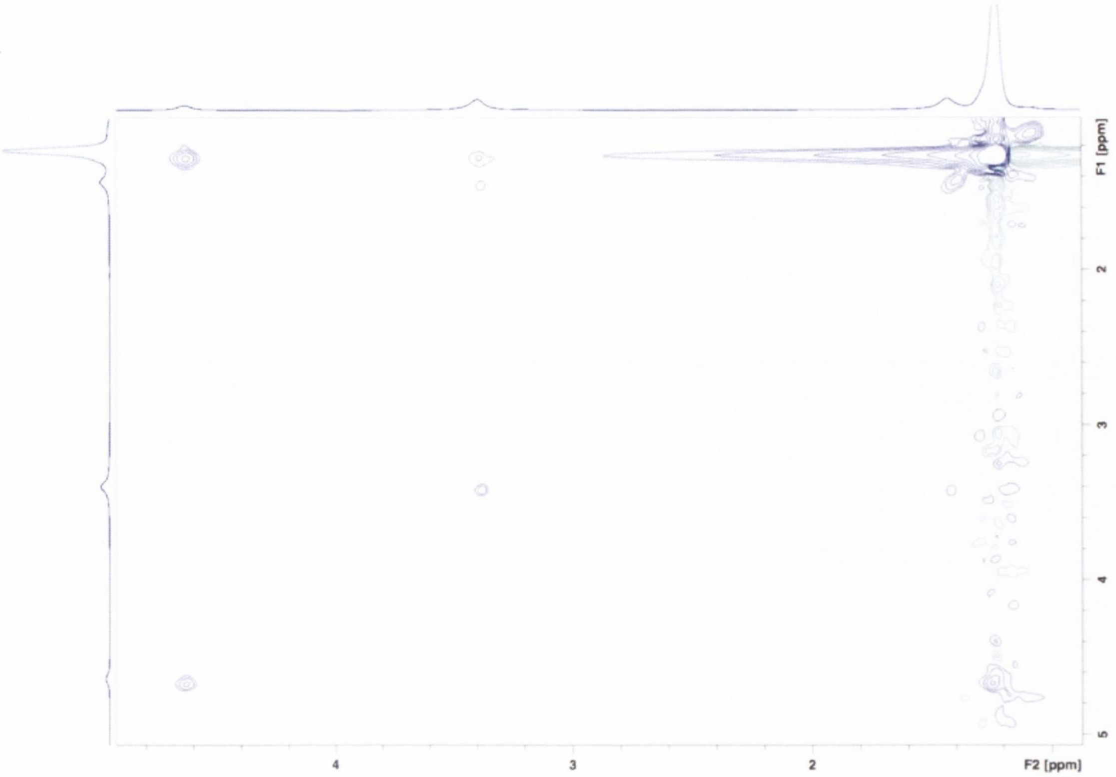

Figure 4.27: EXSY spectrum of lactide and 1 in CD_3CN at 20°C.

To negate the effect of the α-methyl, the sterically unhindered six-membered ring δ-Valerolactone (δVL) was examined and found to undergo ROP, albeit at poorer conversions than for the seven-membered εCL (**Figure 4.28**). Complex **1** is the first example of an actinide catalyst for the ROP of δVL.

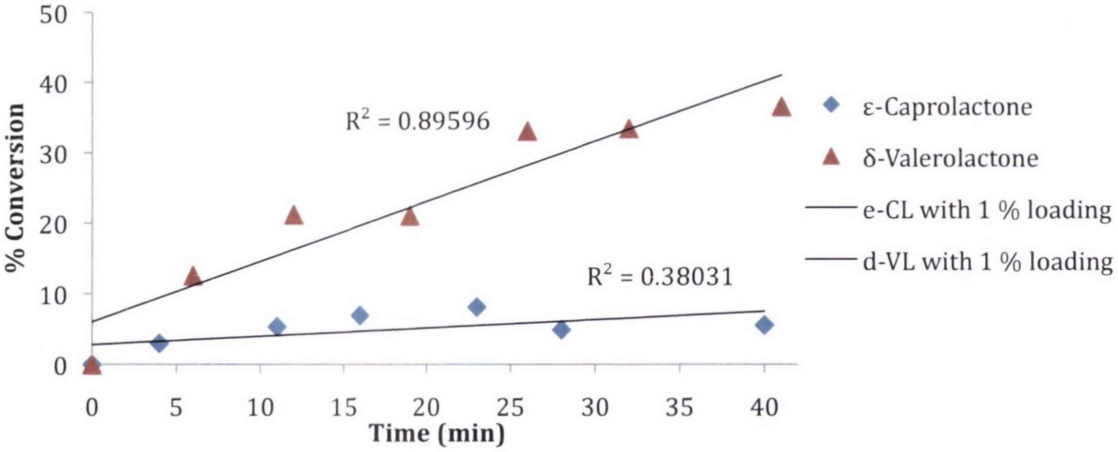

Figure 4.28: Conversion against time of εCL and δVL in tol @ 100°C.

Two other monomers, γ-Butyrolactone, (γBL), and β-Butyrolactone, (βBL), were examined, but neither monomer reacted. As mentioned previously, γBL is a monomer with very little ring-strain; the negative result implies that ring-strain is indeed a driving-force in the system. βBL is a monomer that has been shown to be resistant to ROP;[40b,41] the negative result in this case is in line with the apparent success of **1**. To identify if the negative result was due to the steric effect of the α-methyl, as it was in the case of lac, or a electronic effect, as in the case of DMBO, EXSY was used to monitor the coordination at the uranyl. An examination of **1** and εCL, δVL, γBL and βBL in C_6D_6 showed that each monomer coordinated to the uranyl. To gain insight into the electronic reasons why βBL and γBL coordinate but do not ring-open, the thermodynamic parameters of the exchange were calculated using previously established methods (**Table 4.7**).[27,33]

Table 4.7: Thermodynamic properties gleaned from EXSY spectra.

Monomer	Rate of Coordination at 293 K (s^{-1})	E_a (kJ)	ΔH° (kJ)	ΔS° (kJ)
βBL	0.0314	-57.240	-59.769	-0.478
γBL	0.0224	-31.868	-34.434	-0.3953
εCL	0.1614	10.328	7.761	-0.234
δVL	0.0430	28.130	25.562	-0.1845

The thermodynamic results show a trend in the activation energy, E_a, and enthalpy, ΔH°, for coordination that is related to susceptibility to ROP. γBL and βBL do not undergo ROP with **1** and yet the E_a for γBL and βBL is exothermic. This will be examined more closely using DFT methods to reveal the energetics of the system.

Mechanistic information can also be gleaned from the EXSY data: the negative entropy implies an associative transition state for the coordination. To gain insight into the mechanism of initiation and propagation, a more detailed kinetic analysis was undertaken, showing first order dependence on catalyst concentration (**Figure 4.29**).

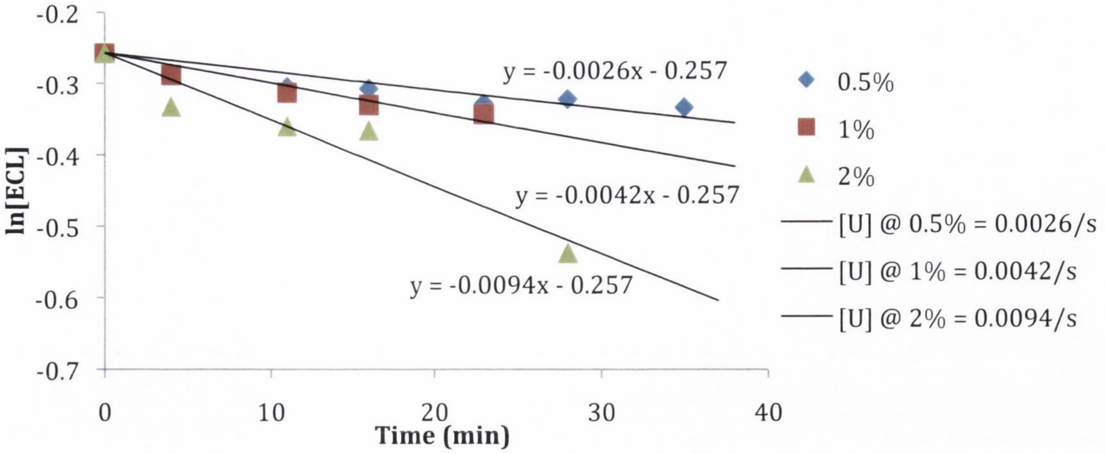

Figure 4.29: Initial rates with varying concentration of 1 showing first order dependence.

The reaction was also shown to be 0th order in monomer concentration - consistent with previous data that conversion rate and polymer mass are apparently independent of catalyst loading (**Figure 4.30**). This result implies that neither coordination nor propagation is the rate-determining step, as these would both be affected by the concentration of monomer in solution. In accordance with these results, and given the initial steric hindrance of the two 2,6-di*tert*butylphenoxide ligands around the uranyl, it is probable that the rate-determining step is an intramolecular initiation step: the nucleophilic attack of a *cis* phenoxide resulting in the breaking of the acyl bond i.e. initiation *via* a coordination-insertion (*cis*-migratory insertion) mechanism.

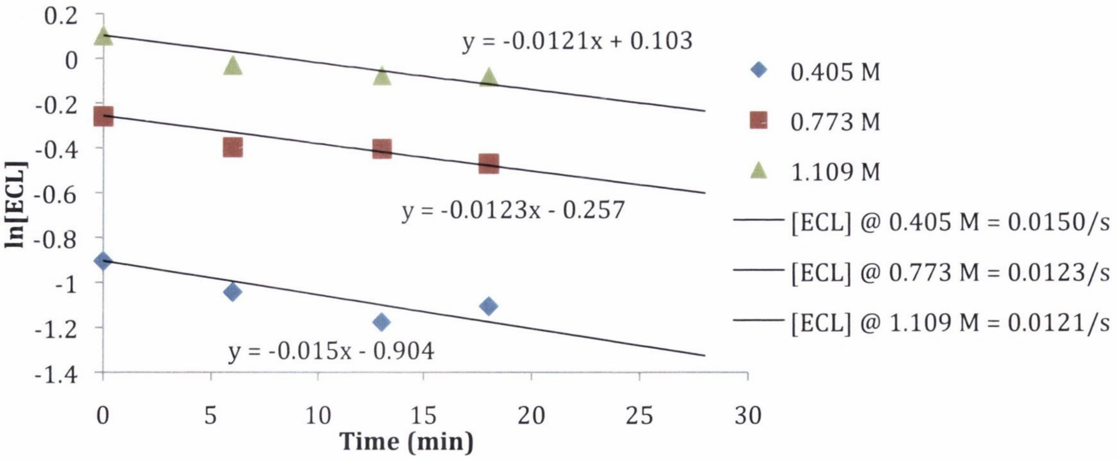

Figure 4.30: Initial rates with varying concentration of εCL showing 0th order dependence.

Diffusion Spectroscopy (DOSY) was used to identify the probable pathway for the propagation by approximating the size of molecules in solution (**Figure 4.31**).[29,34] The calculated radius of **1** from the x-ray structure is 6.2 Å. The experimental hydrodynamic radius of the catalyst was found to be 4.82 Å. This difference can be attributed to the non-spherical shape of the catalyst – DOSY is optimised for spherical molecules – or to the interactions of the catalyst with the non-coordinating C_6D_6. The hydrodynamic radius increases to 9.80 Å upon addition of εCL (10 eq.). It is possible therefore that there are two chains growing from one uranium centre or that the mechanism involves two or more metals during the propagation step. There are examples of metal lactone ROP catalysts with more than one active site with postulated mechanisms that seem to involve simultaneous growth at two metal centres[42] or metal clusters.[43] It is likely however, that the dominant species in solution is a dimer of **1**.

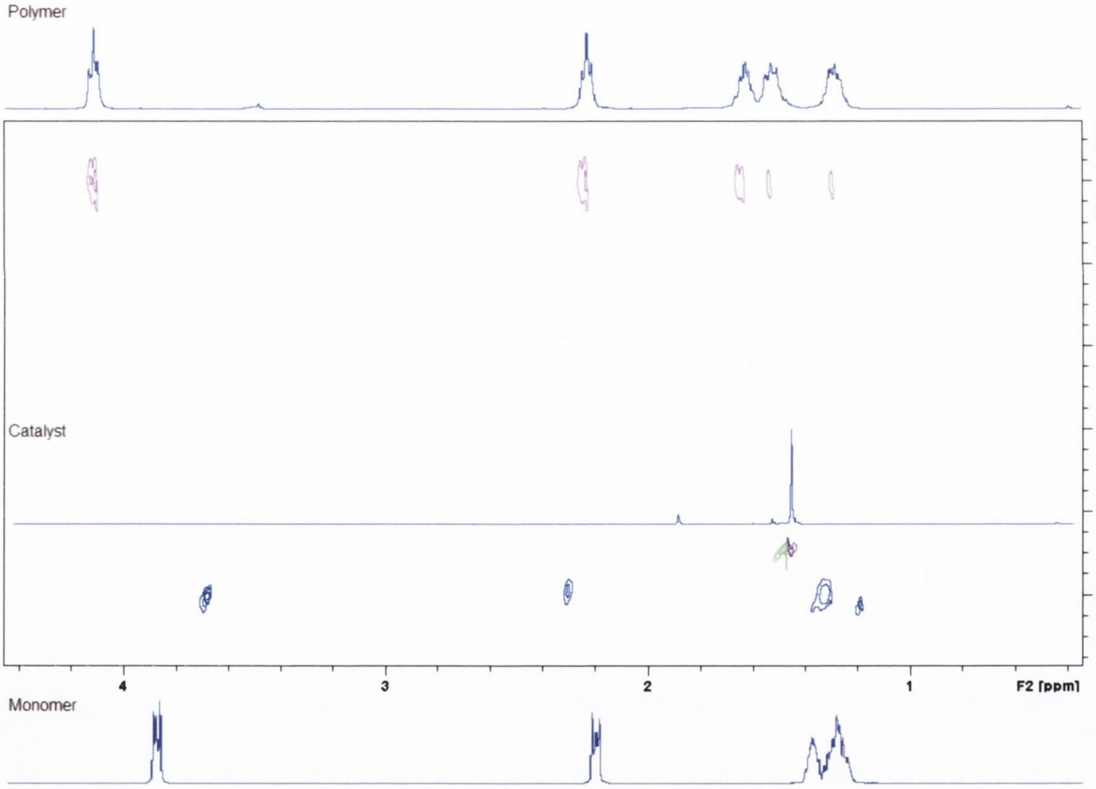

Figure 4.31: Overlay of the ^1H and DOSY NMR spectra of PCL, 1 and εCL.

Table 4.8: The experimental hydrodynamic radii found from DOSY experiments.

Solvent	Components	C[a]	D_t (m^2 s^{-1})	R_h (Å)
C_6D_6	Catalyst	4	1.107×10^{-9}	4.82
C_6D_6	Catalyst + 10 eq. εCL	4	5.444×10^{-10}	9.80
C_6D_6	PCL	4	1.574×10^{-10}	33.90
C_6D_6	PCL	6	1.574×10^{-10}	22.60

[a] Where c is the frictional coefficient. As the shape of the polymer in solution is unknown, the calculated R_h is given for both c = 4 (for the slip-boundary condition) and c = 6 (when applying the stick-boundary condition).[28]

To summarise the experimental findings: the uranyl aryloxide **1** catalyses the cyclo-oligomerisation of lactones. These undergo coordination to the metal *via* an associative mechanism before nucleophilic attack from the phenoxide ligand. This intramolecular initiation step is postulated to be the rate-determining step. The propagation occurs at one active site per uranium centre; however, a bimetallic mechanism is considered for the propagation.

The catalyst will only work with monomers that are able to coordinate to the metal and that have sufficient ring-strain for the propagation to be entropically favourable.

4.3.2. Theoretical Investigations

Once again, to clarify the mechanism Professor Laurent Maron performed extensive DFT calculations to determine if the kinetic analysis or the spectroscopic analysis was correct.

The mechanism computed is "classical" of the ROP of cyclic lactones: nucleophilic attack by the aryloxide leads to the formation of a tetrahedral intermediate that results in the ring-opening. This has been an established template for many lactone ROP systems, including lanthanide εCL ROP catalysts, and has been calculated by Professor Maron before.[44]

Given the experimental data, only an intramolecular initiation step was examined for εCL and δVL. Two possible propagation mechanisms (inter or intramolecular) were considered for propagation, but given the greater degree of freedom in εCL it has not been possible to fully characterise the ring opening transition state for the intermolecular pathway (the frequency calculations failed even on a supercomputer centre). Therefore it was necessary to calculate δVL and apply the results to εCL. The discussion will focus on the energy differences.

Before modelling the reaction mechanism, the coordination of each of the monomers was explored theoretically through extensive DFT calculations and it was found that the displacement of thf by the monomer was endothermic – 5.2 and 4.9 kcal mol^{-1} for βBL and γBL, respectively – in good agreement with the EXSY data. Although coordination occurs through the carbonyl in each case, it is found that the rigid 4 and 5 membered rings reduce the favourable acyl C–H···π interaction that is observed for the 6 and 7 membered rings. This renders the coordination more difficult and may explain the lack of reactivity of these monomers. These results also show that the coordination is not the rate-determining step, which is consistent with kinetic analysis.

4.3.2.1. *Theoretical Investigations: δVL*

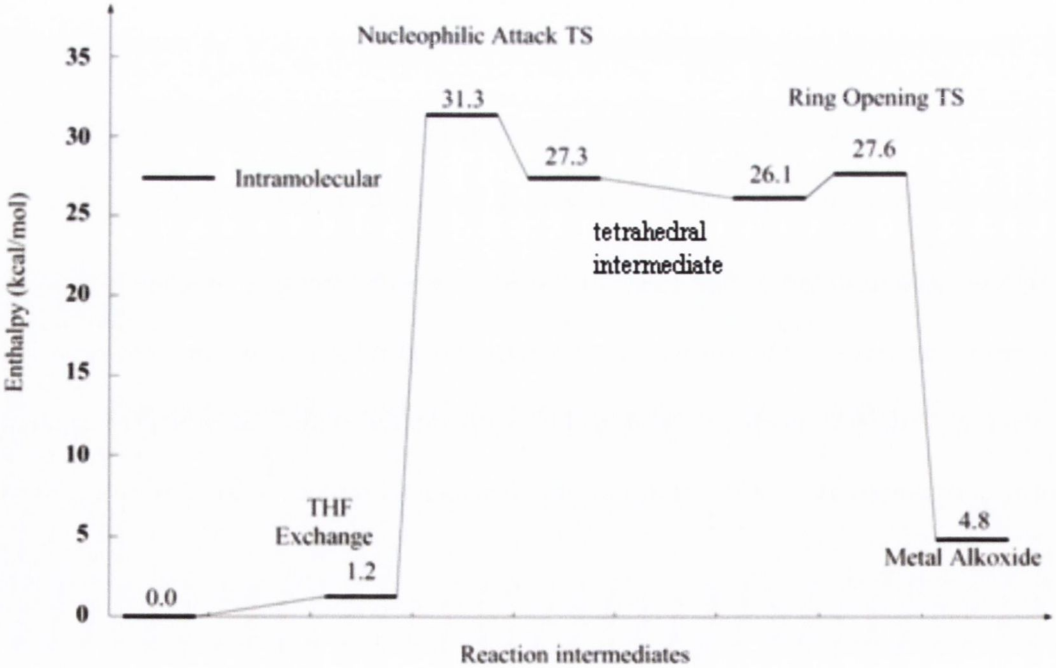

Figure 4.32: Computed Reaction Profile for the first insertion of δVL.

The reaction begins by the displacement of one thf molecule by a δVL. This is predicted to be almost thermoneutral (+1.2 kcal mol^{-1}) and in fair agreement with the experimental observation. The system then reaches the Nucleophilic Attack Transition state (NA TS), with an activation barrier of 31.3 kcal mol^{-1} indicating a quite demanding energy process that is still kinetically accessible. This barrier is mainly due to the intrinsic stability of the six-membered ring, making it hard to react with any nucleophile. This allows the formation of a transient tetrahedral intermediate (at the carbon of the former ester), which is highly unstable, and leads to a ring opening (**Scheme 4.4**). The barrier for the formation of the Ring-Opening Transition State (RO TS) with an elongated acyl bond (a computed length of 1.80 Å) is very low (1.5 kcal mol^{-1}); it could be considered to be a spontaneous process after the nucleophilic attack (NA). NA is thus the rate-determining step of this first insertion, consistent with the experimental hypothesis.

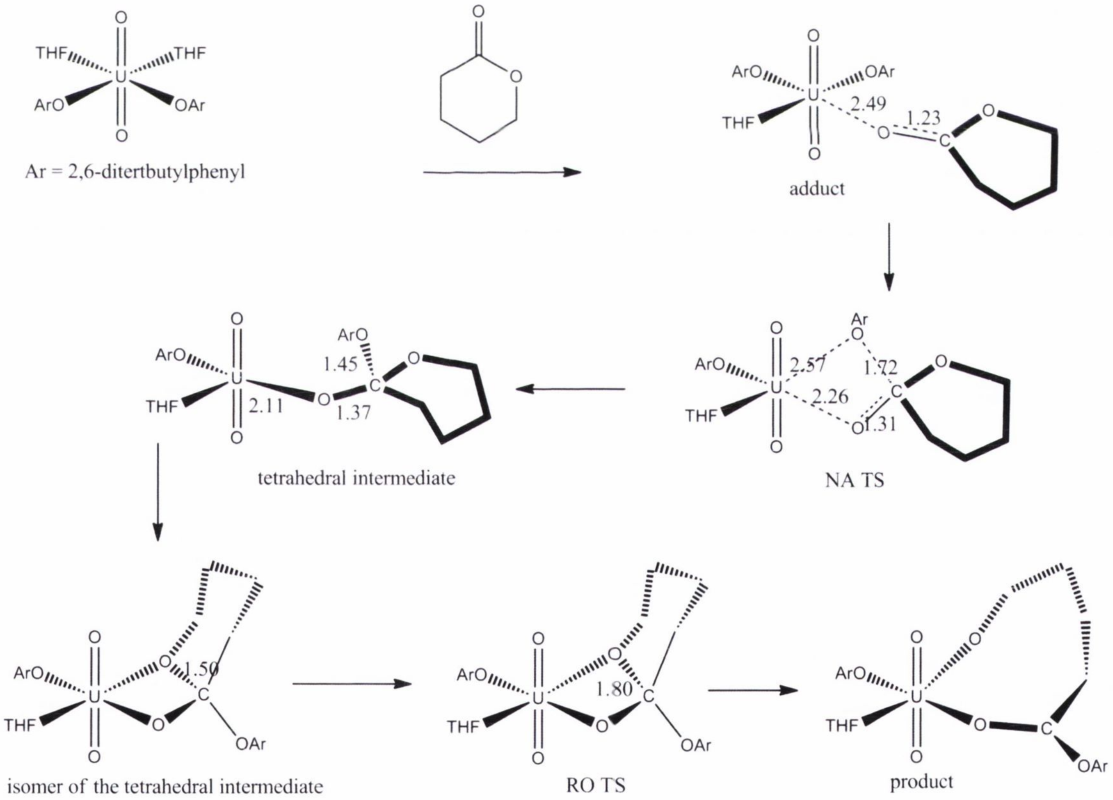

Scheme 4.4: The first insertion of the δVL ROP catalysed by 1. All intermediates and transition states are depicted, along with important bond distances (Å).

The reaction mechanism for the second insertion is very similar to the one of the first insertion and the discussion will focus more on the difference between the intra- and intermolecular pathways.

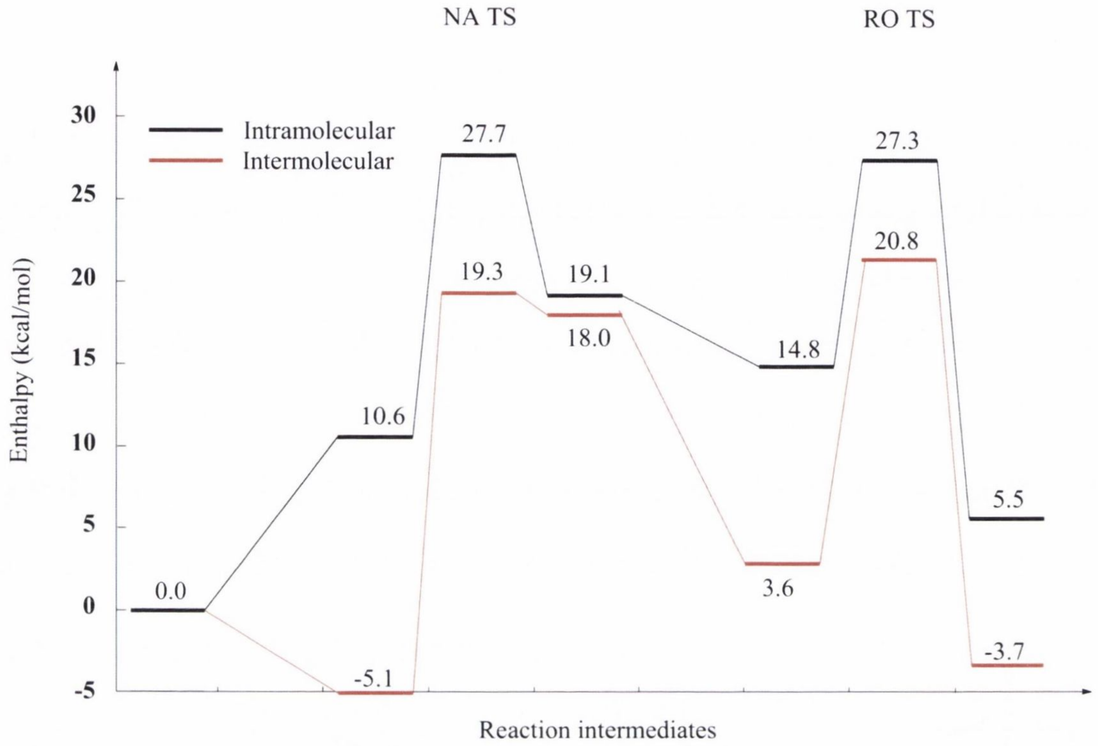

Figure 4.33: Computed Reaction Profile for the second insertion of δVL.

The intermolecular pathway is found to be favoured thermodynamically and kinetically over the intramolecular one. The main difference already occurs upon the coordination of the monomer to the metal centre: the classical coordination of the δVL *cis* to the alkoxide is disfavoured due to steric effects. This makes the intramolecular reaction pathway less favourable than the intermolecular one – in which case the coordination to a second uranium centre is even found to be exothermic by 5.1 kcal mol^{-1}, a coordination energy that is in excellent agreement with the experimental observation (6.7 kcal mol^{-1}). The NA TS is then reached (**Figure 4.34**) with an activation barrier that is higher than the barrier for the intramolecular mechanism (24.6 *vs.* 10.1 kcal mol^{-1}), but, given the preference for the intermolecular coordination step, it is likely that the intermolecular path will still be chosen.

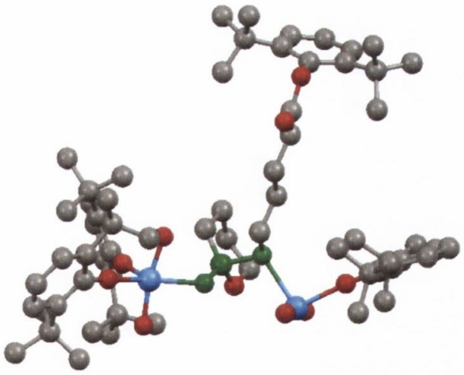

Figure 4.34: Geometry of the intermolecular NA TS. The green atoms are directly involved in the TS, the thf molecules have been omitted for clarity.

It is noteworthy that for both scenarios the energy barrier is lower than the first insertion NA barrier (30.1 kcal mol^{-1}). The second insertion pushes the aryl group far from the uranium centres, thus reducing steric hindrance. The NA TS becomes the tetrahedral intermediate (again at the carbon of the ester), which is also found to be relatively unstable in both pathways and rapidly isomerises. The intermolecular pathway allows for a 10.1 kcal mol^{-1} difference in stability at this point, making the intermolecular path more favourable, although the origin of this enhanced stability is not known at this stage. The reaction energy is also more favourable when two metal centres are involved rather than with a single uranium catalyst. This is due to the formation of a very stable alkoxide dimer in the former case (**Scheme 4.5**). This complex can be viewed as the resting state of the polymerisation with a calculated hydrodynamic radius of ~10 Å which corroborates the DOSY analysis (9.80 Å).

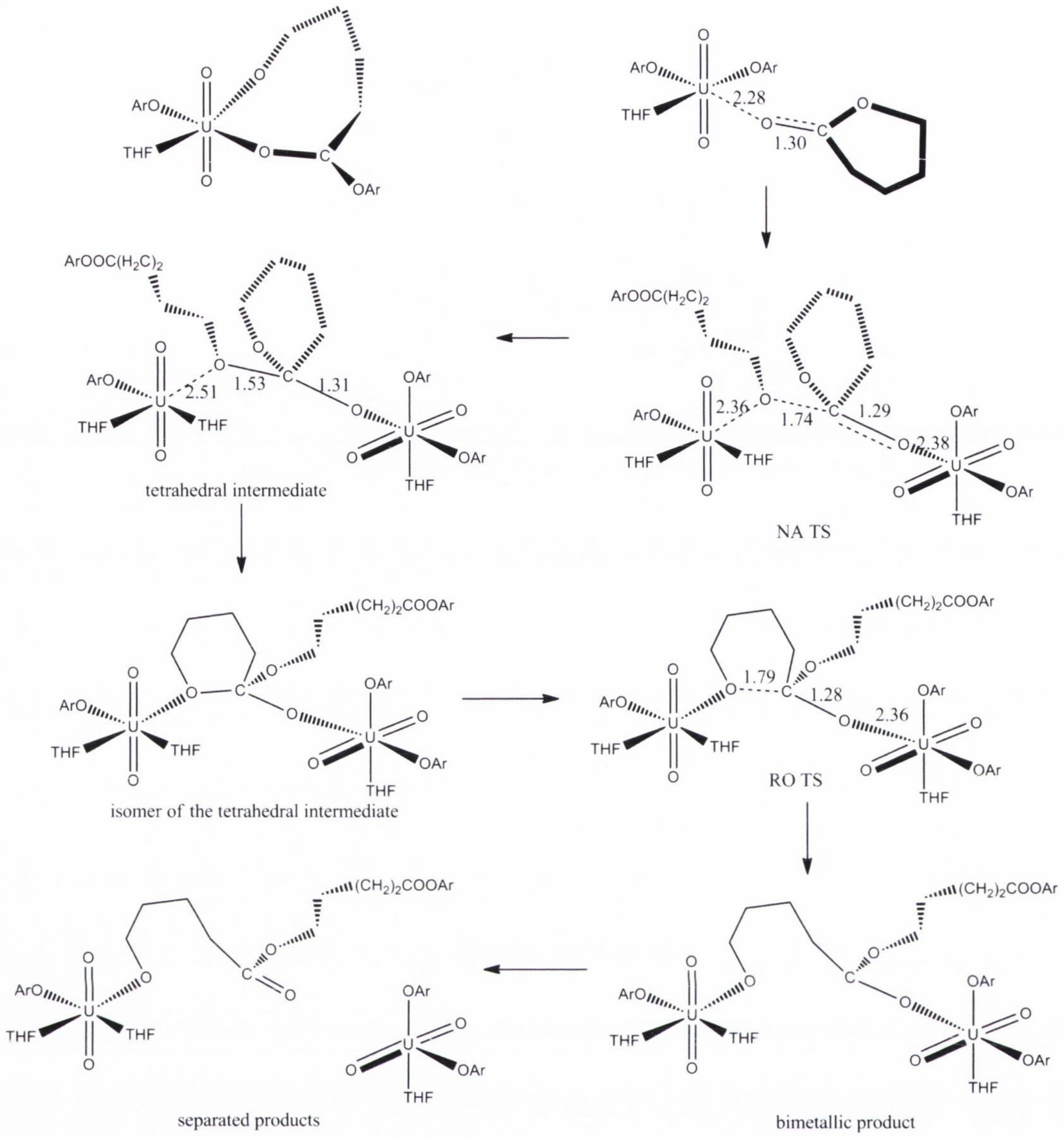

Scheme 4.5: Computed scheme for the second step of the δVL ROP catalysed by 1. All intermediates and transition states are depicted, along with important bond lengths (Å).

To summarise, the computed most favourable reaction pathway involves two uranium centres in an intermolecular propagation mechanism. Previously reported mechanisms include two metals, but – to the best of our knowledge – a mechanism where ring-opening is split across two metal centres has not been reported in the case of lactone ROP. However, due to the precision of the method, it is possible that both intra- and intermolecular pathways are operative.

4.3.2.2. Theoretical Investigations: εCL

The first insertion was also investigated only for the intramolecular pathway (**Figure 4.35**). As expected and in agreement with the better polymerisation ability of the εCL, the barriers are roughly 4.0 kcal mol^{-1} lower for εCL than the δVL. As for the δVL case, both the intermolecular and the intramolecular second insertion pathway were investigated.

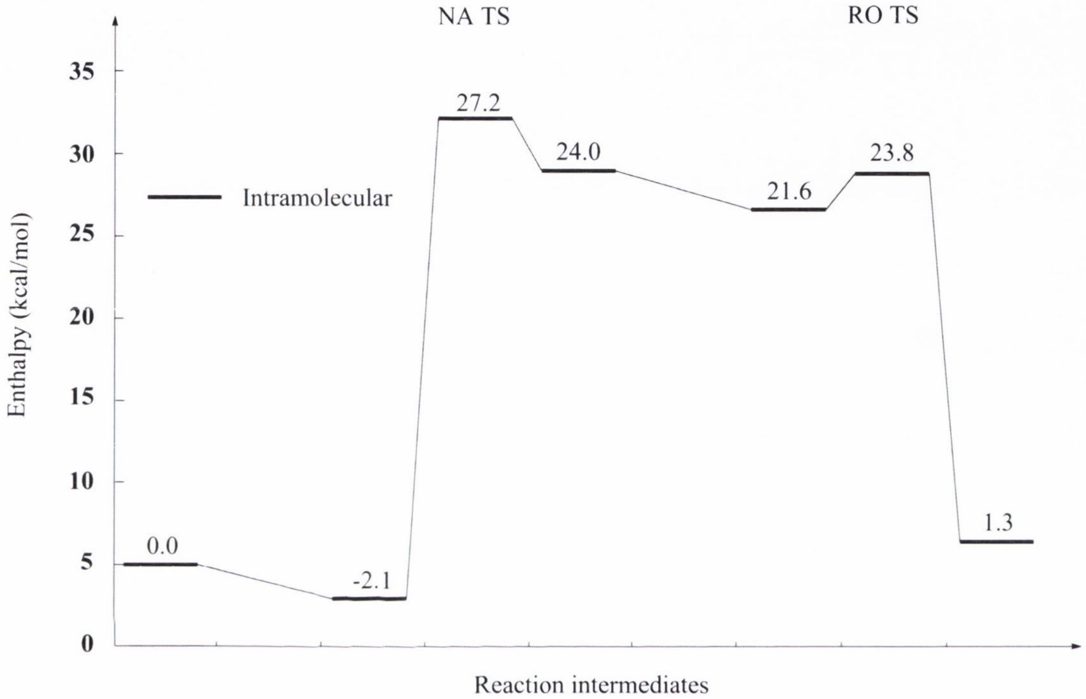

Figure 4.35: Computed Reaction Profile for the first insertion of ε CL.

Interestingly, the coordination of εCL with displacement of thf is found to be exothermic by 2.1 kcal mol^{-1}, indicating a favourable process, and in line with the experimental observation (+1.85 kcal mol^{-1} from EXSY experiments, i.e. almost thermoneutral).

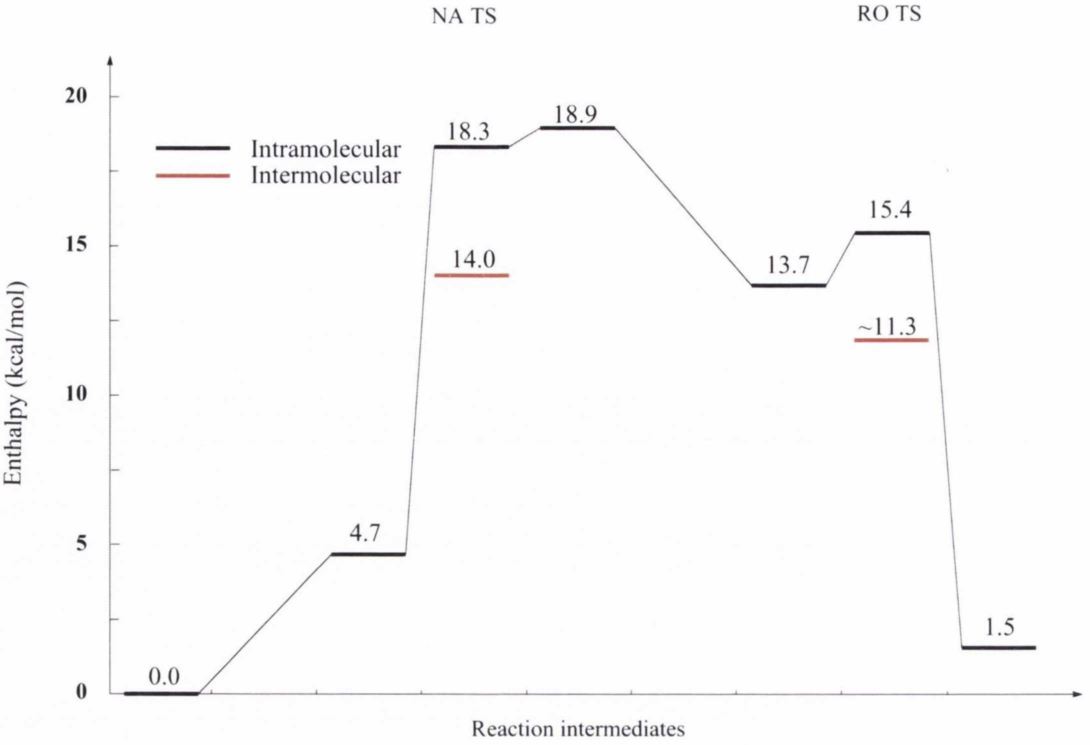

Figure 4.36: Computed Reaction Profile for the second insertion of ε CL.

As already found in the first insertion, the barriers are lower for εCL than for δVL but for the NA TS the difference is roughly 10.0 kcal.mol^{-1}. Similarly to that calculated for δVL, the calculated intermolecular barriers are lower than the intramolecular ones by approximately 4.0 kcal.mol^{-1}. Hence, the intramolecular mechanism seems to be the favoured pathway in the case of the εCL monomer also. The available data was used to propose a mechanism for the ROP of εCL by **1** (**Scheme 4.6**).

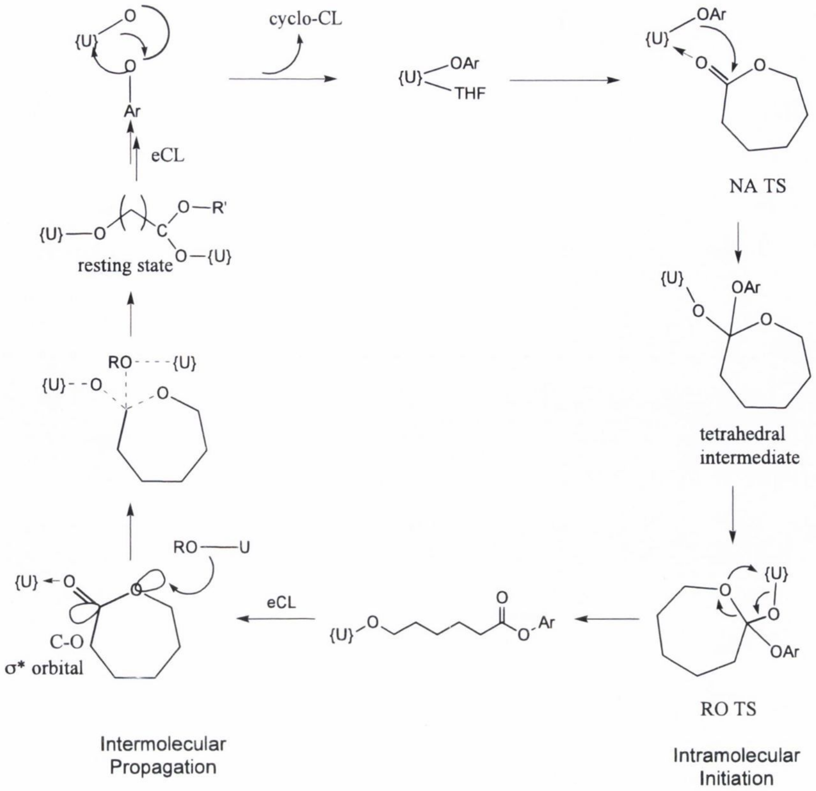

Scheme 4.6: Postulated mechanism for ring opening polymerisation of εCL from experimental and computational results.

To summarise the proposed εCL mechanism: the initiation is an intramolecular process, and is the rate-determining step due to the steric constraints of the aryloxide ligand, but propagation may involve both intra- and inter-molecular pathways, with a binuclear resting state that has been observed by DOSY NMR studies.[45] The hydrodynamic radius for the proposed resting state to compare with the DOSY experimental numbers has not been calculated, however, due to the expense of the necessary computational studies.

4.4. Conclusions

The uranyl phenoxide complex, **1**, is the first example of a uranyl ring-opening polymerisation catalyst.[9] The successful ring-opening by a uranyl complex has hitherto been perceived to be unlikely,[4] although uranyl compounds have been shown to activate carbonyls in advance of coupling reactions.[7] A previous attempt for lactone ROP by uranyl nitrate showed 2:1 adducts of δVL and εCL.[46] The nitrate anion is presumably insufficiently nucleophilic to facilitate ring-opening. Uranyl chloride, however, is sufficiently nucleophilic for the ring-opening of epoxides, as seen by the successful experiments with PO and CHO. Also of note is that the change in enthalpy for the ring opened monomer compared to the catalyst is small, validating the initial postulate that uranyl ions can react with and turn over oxygen containing monomers providing that a U–O bond is present in the catalyst.

1 has been shown to be an active catalyst in the ring opening *cyclo*-oligomerisation of εCL and δVL to form cyclo-oligomers. Interestingly, there is no evidence of the ring opening of thf in any of the reactions, something that has been noted in lower oxidation state uranium chemistry.[47] A combination of spectroscopic and computational examinations has led to a proposed bimetallic mechanism with an intramolecular initiation step. The bimetallic propagation mechanism involves a coordinated monomer being ring-opened by an alkoxide chain on another metal. This shuttling between two metal centres is a mechanism hitherto unknown for lactone ROP.[16b] The energetic stability of the bimetallic alkoxide product, formed in the intermolecular mechanism, infers that this complex is the resting state of the polymerisation, rather than its monomeric analogue.

1 and uranyl chloride have been found to ring-open epxoides to form low-molecular weight oligomers. The uranyl chloride system is deduced to progress through an intermolecular mechanism; the strong directionality of the chloride orbital that has to be forced to point toward the empty σ* orbital on the PO carbon centres inhibits an intramolecular pathway. This hypothesis was tested in solution *via* fluorescence spectroscopy and the data suggests that the propagating species in solution is either monomeric or vibrationally isolated dimers. The latter is predicted computationally, but the former could be possible as the dimeric compound is weakly bound (roughly 11.0 kcal mol^{-1}) and if it exchanges with thf then it will split into two monomers. In the case of **1**, the greater steric requirements of the bulkier aryloxide force the initiation to be intramolecular – which is very rare for epoxides[12] – but the propagation proceeds *via* an intermolecular pathway.

Another point of interest is the viability of the monomers: during the course of the study it was found that the thermodynamic properties of the coordination can indicate the feasibility of a monomer as a potential reactant. For three monomers coordination was exothermic and for all three monomers there was no ring-opening observed.

Table 4.9: Available thermodynamic parameters for coordination to 1.

Monomer	E_a (kJ)	ΔH° (kJ)	ΔS° (kJ)	Reaction?
DMBO	-70.905	-73.473	-0.533	No
βBL	-57.240	-59.769	-0.478	No
γBL	-31.868	-34.434	-0.3953	No
εCL	10.328	7.761	-0.234	Yes
δVL	28.130	25.562	-0.1845	Yes
PO	43.306	40.739	-0.1394	Yes

This computational study explains a number of the experimental features. The computations on the mechanism are some of the largest carried out for any uranium-based study in the literature and suggest that, despite the inherent difficulties in actinide computational chemistry, DFT is a powerful technique for studying catalysis featuring uranium atoms.

4.5. Experimental

4.5.1. General

All manipulations were carried out using standard Schlenk and glove box techniques under an atmosphere of high purity argon. Toluene, hexanes and thf were distilled over potassium; diethyl ether was distilled over Na/K whilst dichloromethane and acetonitrile were distilled from calcium hydride. Starting material $[UO_2Cl_2(thf)_2]_2$ was synthesised by literature methods.[37]

Infrared spectra were recorded on a Perkin Elmer Spectrum 100. Raman spectra were recorded on a Renishaw 1000 spectrometer. ^1H and ^{13}C NMR spectra were recorded on either a Bruker AV400 spectrometer operating at 400.13 (^1H) or 100.65 (^{13}C), or a Bruker Avance II 600 NMR with a TCI cryoprobe operating at 150.92 MHz (^{13}C), and were referenced to the residual ^1H or ^{13}C resonances of the solvent used.[48] EXSY spectra were recorded using Bruker's NOESY pulse sequence. DOSY spectra were recorded using a 2D ledbpgp2s pulse sequence. Mass spectra were measured on a MALDI QTOF Premier MS system. GPC data was recorded on a Varian ProStar with a 350 RI Detector using a PLgel 5μm MIXED-D column and calibrated with EasiCal polystyrene standards. Optical rotation measurements were made on a Rudolph Research Analytical Autopol IV instrument, and quoted in units of 10^{-1} deg cm^2 g^{-1}.

DFT calculations were performed by Professor Laurent Maron at LPCNO, INSA Toulouse. Calculations were performed at the B3PW91 level of theory on all stationary points of the potential energy surfaces using the Gaussian09 program suite.[39b] The equilibrium and transition structures were fully optimised at the Becke's three- parameter hybrid functional[39a] combined with the nonlocal correlation functional provided by Perdew/Wang.[49] RECP (augmented by an f polarisation function, $\alpha = 1.0$) adapted to the oxidation state VI+ was used for the reactions.[50] The correctness of the latter is well documented in previous publications from our collaborators.[51] For the rest of nonmetal atoms, the 6-31G(d,p) basis set was used.[52] In all computations, no constraints were imposed on the geometry. Full geometry optimisation was performed for each structure using Schlegel's analytical gradient method,[53] and attainment of the energy minimum was verified by calculating the vibrational frequencies that result in the absence of imaginary eigenvalues. All stationary points have been identified for minimum (number of imaginary frequencies $N_{imag} = 0$) or TS_s ($N_{imag} = 1$). The vibrational modes and corresponding frequencies are based on a harmonic force field. This was achieved with a self-consistent-field convergence on the density matrix of at least 10^{-9} and a root-mean-square force of less than 10^{-4} au. All bond lengths and angles were optimised to better than 0.001 Å and 0.1°, respectively. Gibbs free energies were obtained at T = 298.15 K within the harmonic approximation. Intrinsic reaction paths (IRPs)[54] were traced from the various transition structures to ensure that no further intermediates exist.

Liquid reagents for catalysis were dried over CaH_2 and distilled under Ar. Unless otherwise stated, all other chemicals were obtained from Sigma Aldrich and used as received.

4.5.2. The Catalyst

$UO_2(O\text{-}2,6\text{-}(tBu)_2C_6H_3)_2(thf)_2$, **1**, was synthesised according to the literature method.[14] This was further characterised using Raman spectroscopy and cyclic voltammetry:

Raman (probe): ν (cm^{-1}) = 886 ($UO_{2(s))}$); E_{red}: (eV) = -1.42 eV

4.5.3. The Catalysis

The general procedures for the catalytic reactions and NMR experiments are outlined below.

4.5.3.1. Propylene oxide

General Procedure: Propylene oxide (1 mL, 14.3 mmol) was added to a solution of the required catalyst (uranyl chloride or complex **1**, 0.143 mmol) in thf or toluene (10 mL) at the required temperature (25 or 40°C). The reaction was stirred vigorously. 1 mL aliquots were removed at specific intervals and quenched with a 90:10 MeOH:HCl solution. These quenched aliquots were analysed by ^1H NMR in $CDCl_3$ to determine % conversion with respect to time by monitoring the relative integration of the methyl protons on the monomer (1.29 ppm) and on the polymer (1.10–1.26 ppm).

4.5.3.2. Cyclohexene oxide

General Procedure: Cyclohexene oxide (1 mL, 9.9 mmol) was added to a solution of the required catalyst (uranyl chloride or complex **1**, 0.099 mmol) in thf or toluene (10 mL) at the required temperature (25, 40, 70 or 100°C). The reaction was stirred vigorously. 1 mL aliquots were removed at specific intervals and quenched with a 90:10 MeOH:HCl solution. These quenched aliquots were analysed by ^1H NMR in $CDCl_3$ to determine % conversion against time by monitoring the relative integration of the monomer CH (2.91 ppm) and the polymeric CH peak (3.55 ppm).

4.5.3.3. ε-Caprolactone

General Procedure: ε-Caprolactone (1 mL, 9.0 mmol) was added to each of three schlenks containing a solution of complex **1** (0.090, 0.030 and 0.015 mmol) in thf or toluene (10 mL) at the required temperature (25, 70 or 100°C). The reaction was stirred vigorously. 1 mL aliquots were removed at specific intervals and quenched with a 90:10 MeOH:HCl solution. These quenched aliquots were analysed by ^1H NMR in $CDCl_3$ to determine % conversion against time by monitoring the relative integration of the ether protons in the monomer (4.13 ppm) and the polymer (3.68 ppm).

4.5.3.4. Lactide

General Procedure: *rac*-Lactide (1 g, 6.9mmol) was added to a solution of complex **1** (0.069, 0.023 or 0.013 mmol) in thf (10 mL) and heated to reflux. The reaction was stirred vigorously. 1 mL aliquots were removed at specific intervals and quenched with a 90:10 MeOH:HCl solution. These quenched aliquots were analysed by ^1H NMR in $CDCl_3$ to determine % conversion against time by monitoring the relative integration of the CH proton in the monomer (4.15 ppm) and the polymer (5.05 ppm).

4.5.3.5. δ-Valerolactone

General Procedure: δ-Valerolactone (1 mL, 10.8 mmol) was added to a solution of the required catalyst (complex **1**, 0.108 mmol) in thf or toluene (10 mL) at the required temperature (25, 70 or 100°C). The reaction was stirred vigorously. 1 mL aliquots were removed at specific intervals and quenched with a 90:10 MeOH:HCl solution. These quenched aliquots were analysed by ^{1}H NMR in $CDCl_3$ to determine % conversion against time by monitoring the relative integration of the monomer CH_2 (2.91 ppm) and the polymeric CH_2 peak (3.55 ppm).

4.5.3.6. β-Butyrolactone

General Procedure: β-Butyrolactone (1 mL, 12.3 mmol) was added to a solution of the required catalyst (uranyl chloride or complex **1**, 0.123 mmol) in thf or toluene (10 mL) at 70°C. The reaction was stirred vigorously. 1 mL aliquots were removed at specific intervals and quenched with a 90:10 MeOH:HCl solution. These quenched aliquots were analysed by ^{1}H NMR in $CDCl_3$ to determine % conversion against time.

4.5.3.7. γ-Butyrolactone

General Procedure: γ-Butyrolactone (1 mL, 13.0 mmol) was added to a solution of the required catalyst (uranyl chloride or complex **1**, 0.130 mmol) in thf or toluene (10 mL) at the required temperature (70 or 100°C). The reaction was stirred vigorously. 1 mL aliquots were removed at specific intervals and quenched with a 90:10 MeOH:HCl solution. These quenched aliquots were analysed by 1H NMR in CDCl3 to determine % conversion against time.

4.5.4. The Analysis

4.5.4.1. Exchange Spectroscopy

General Procedure: In the glove box, **1** (30 mg, 0.036 mmol) was weighed into a Young's NMR tube. The tube was sealed and removed to the schlenk-line. 0.5 mL of the appropriate deuterated solvent (C_6D_6 or CD_3CN for lactide) was added followed by 2 equivalents of the monomer to be tested (0.073 mmol) *via* Gilson pipette. The tube was sealed, shaken and brought to the NMR machine for analysis. The mixing time was determined at 20°C. For thermodynamic analysis, the experiment was repeated at a range of temperatures between 20 and 50°C, depending on the boiling point of the monomer in question. Thermodynamic parameters were extracted using established methods.[27,55]

4.5.4.2. Diffusion Oriented Spectroscopy

General Procedure: In the glove box, **1** (30 mg, 0.036 mmol) was weighed into a Young's NMR tube. The tube was sealed and removed to the schlenk-line. C_6D_6 (0.5 mL) was added followed by 10 equivalents of the monomer to be tested (0.36 mmol) *via* Gilson pipette. The tube was sealed, shaken and brought to the NMR machine for analysis at 25°C. The ledbpgp2s bipolar 2D pulse sequence from the Topspin dosy au programme was used. Diffusion parameters were optimised for the catalyst and calibrated with a 1% H_2O/ D_2O solution for the HDO diffusion coefficient, 1.902×10^{-9} m^2 s^{-1}. These parameters (diffusion time = 100 ms, diffusion pulse length = 1 ms, gradient amplitude = 5–95 %, ramp type = quadratic) were then used for the reaction mixture.

4.6. References

(1) Fox, A. R.; Bart, S. C.; Meyer, K.; Cummins, C. C. *Nature* **2008**, *455*, 341.

(2) Burns, C. J.; Eisen, M. S. In *The Chemistry of the Actinide and Transactinide Elements*; Morss, L. R., Edelstein, N. M., Fuger, J., Eds.; Springer: Dordrecht, The Netherlands, 2006; Vol. 5.

(3) Lin, Z.; Marks, T. J. *J. Am. Chem Soc.* **1987**, *109*, 7979.

(4) Barnea, E.; Moradove, D.; Berthet, J.-C.; Ephritikhine, M.; Eisen, M. S. *Organomet.* **2006**, *25*, 320.

(5) Andrea, T.; Barnea, E.; Eisen, M. S. *J. Am. Chem. Soc.* **2008**, *130*, 2454.

(6) Villiers, C.; Thuery, P.; Ephritikhine, M. *Eur. J. Inorg. Chem.* **2004**, 4624.

(7) (a) van Axel Castelli, V.; Cort, A. D.; Mandolini, L.; Reinhoudt, D. N. *J. Am. Chem. Soc.* **1998**, *120*, 12688(b) van Axel Castelli, V.; Dalla Cort, A.; Mandolini, L.; Reinhoudt, D. N.; Schiaffino, L. *Chem. Eur. J.* **2000**, *6*, 1193(c) van Axel Castelli, V.; Dalla Cort, A.; Mandolini, L.; Reinhoudt, David N.; Schiaffino, L. *Eur. J. Org. Chem.* **2003**, *2003*, 627.

(8) Enthaler, S. *Chem. Eur. J.* **2011**, *17*, 9316.

(9) (a) Fang, J.; Walshe, A.; Maron, L.; Baker, R. J. *Inorg. Chem.* **2012**, *51*, 9132(b) Baker, R. J.; Walshe, A. *Chem. Commun.* **2012**, *48*, 985.

(10) Walshe, A.; Fang, J.; Maron, L.; Baker, R. J. *Inorg. Chem.* **2013**, *52*, 9077.

(11) (a) Chisholm, M. H.; Eilerts, N. W.; Huffman, J. C.; Iyer, S. S.; Pacold, M.; Phomphrai, K. *J. Am. Chem. Soc.* **2000**, *122*, 11845(b) Chatterjee, C.; Chisholm, M. H. *Inorg. Chem.* **2012**, *51*, 12041.

(12) Antelmann, B.; Chisholm, M. H.; Iyer, S. S.; Huffman, J. C.; Navarro-Llobet, D.; Pagel, M.; Simonsick, W. J.; Zhong, W. *Macromol.* **2001**, *34*, 3159.

(13) Chisholm, M. H.; Navarro-Llobet, D.; Simonsick, W. J. *Macromol.* **2001**, *34*, 8851.

(14) Wilkerson, M. P.; Burns, C. J.; Morris, D. E.; Paine, R. T.; Scott, B. L. *Inorg. Chem.* **2002**, *41*, 3110.

(15) (a) Straub, T.; Haskel, A.; Neyroud, T. G.; Kapon, M.; Botoshansky, M.; Eisen, M. S. *Organomet.* **2001**, *20*, 5017(b) Barnea, E.; Andrea, T.; Kapon, M.; Berthet, J.-C.;

Ephritikhine, M.; Eisen, M. S. *J. Am. Chem. Soc.* **2004**, *126*, 10860(c) Weiss, C. J.; Marks, T. J. *Dalton Trans.* **2010**, *39*, 6576(d) Sharma, M.; Andrea, T.; Brookes, N. J.; Yates, B. F.; Eisen, M. S. *J. Am. Chem. Soc.* **2011**, *133*, 1341.

(16) (a) Wu, J.; Yu, T.-L.; Chen, C.-T.; Lin, C.-C. *Coord. Chem. Rev.* **2006**, *250*, 602(b) Labet, M.; Thielemans, W. *Chem. Soc. Rev.* **2009**, *38*, 3484(c) Wheaton, C. A.; Hayes, P. G.; Ireland, B. J. *Dalton Trans.* **2009**, *0*, 4832(d) Stanford, M. J.; Dove, A. P. *Chem. Soc. Rev.* **2010**, *39*, 486.

(17) Schilling, F. C.; Tonelli, A. E. *Macromol.* **1986**, *19*, 1337.

(18) (a) Shimasaki, K.; Aida, T.; Inoue, S. *Macromol.* **1987**, *20*, 3076(b) Chisholm, M. H.; Crandall, J. K.; McCollum, D. G.; Pagel, M. *Macromol.* **1999**, *32*, 5744.

(19) Gross, R. A.; Kalra, B. *Science* **2002**, *297*, 803.

(20) (a) Hutmacher, D. W.; Schantz, T.; Zein, I.; Ng, K. W.; Teoh, S. H.; Tan, K. C. *J. Biomed. Mater. Res.* **2001**, *55*, 203(b) Peña, J.; Corrales, T.; Izquierdo-Barba, I.; Doadrio, A. L.; Vallet-Regí, M. *Polym. Degrad. Stab.* **2006**, *91*, 1424(c) Jenkins, M. J.; Harrison, K. L.; Silva, M. M. C. G.; Whitaker, M. J.; Shakesheff, K. M.; Howdle, S. M. *Eur. Polym. J.* **2006**, *42*, 3145(d) Lam, C. X. F.; Teoh, S. H.; Hutmacher, D. W. *Polym. Int.* **2007**, *56*, 718.

(21) (a) Chandra, R.; Rustgi, R. *Prog. Polym. Sci.* **1998**, *23*, 1273(b) Chen, D. R.; Bei, J. Z.; Wang, S. G. *Polym. Degrad. Stab.* **2000**, *67*, 455(c) Sinha, V. R.; Bansal, K.; Kaushik, R.; Kumria, R.; Trehan, A. *Int. J. Pharm.* **2004**, *278*, 1(d) Ikada, Y.; Tsuji, H. *Macromol. Rapid Commun.* **2000**, *21*, 117.

(22) Hedrick, J. L.; Magbitang, T.; Connor, E. F.; Glauser, T.; Volksen, W.; Hawker, C. J.; Lee, V. Y.; Miller, R. D. *Chem. Eur. J.* **2002**, *8*, 3308.

(23) Joshi, P.; Madras, G. *Polym. Degrad. Stab.* **2008**, *93*, 1901.

(24) Alemaán, C.; Betran, O.; Casanovas, J.; Houk, K. N.; Hall, H. K. *J. Org. Chem.* **2009**, *74*, 6237.

(25) (a) Lutz, J.-F. *Nat. Chem.* **2010**, *2*, 84(b) Thomas, C. M. *Chem. Soc. Rev.* **2010**, *39*, 165.

(26) (a) Duda, A.; Penczec, S. *Macromol.* **1990**, *23*, 1636(b) Nijenhuis, A. J.; Grijpma, D. W.; Pennings, A. *Macromol.* **1992**, *25*, 6419.

(27) Gunther, H. *NMR Spectroscopy: Basic Principles, Concepts, and Applications in Chemistry, 2nd Edition*; 2nd ed.; Wiley, 1995.

(28) Edward, J. T. *J. Chem. Educ.* **1970**, *47*, 261.

(29) Macchioni, A.; Ciancaleoni, G.; Zuccaccia, C.; Zuccaccia, D. *Chem. Soc. Rev.* **2008**, *37*, 479.

(30) (a) Duda, A.; Florjanczyk, Z.; Hofman, A.; Slomkowski, S.; Penczek, S. *Macromol.* **1990**, *23*, 1640(b) Kowalski, A.; Duda, A.; Penczek, S. *Macromol.* **1998**, *31*, 2114.

(31) Le Borgne, A.; Spassky, N.; Lin Jun, C.; Momtaz, A. *Makromol. Chem.* **1988**, *189*, 637.

(32) Borzacchiello, A.; Ambrosio, L.; Nicholas, C. V.; Purbrick, M. D. *Polym. Int.* **2000**, *49*, 122.

(33) Shokhirev, N. V.; Shokhireva, T. K.; Polam, J. R.; Watson, C. T.; Raffii, K.; Simonis, U.; Walker, F. A. *J. Phys. Chem. A* **1997**, *101*, 2778.

(34) Pregosin, P. S.; Kumar, P. G. A.; Fernández, I. *Chem. Rev.* **2005**, *105*, 2977.

(35) (a) Natrajan, L. S. *Coord. Chem. Rev.* **2012**, *256*, 1583(b) Redmond, M. P.; Cornet, S. M.; Woodall, S. D.; Whittaker, D.; Collison, D.; Helliwell, M.; Natrajan, L. S. *Dalton Trans.* **2011**, *40*, 3914.

(36) (a) Hayton, T. W.; Wu, G. *Inorg. Chem.* **2009**, *48*, 3065(b) Fortier, S.; Hayton, T. W. *Coord. Chem. Rev.* **2010**, *254*, 197.

(37) Wilkerson, M. P.; Burns, C. J.; Paine, R. T.; Scott, B. L. *Inorg. Chem.* **1999**, *38*, 4156.

(38) (a) Darensbourg, D. J.; Niezgoda, S. A.; Draper, J. D.; Reibenspies, J. H. *J. Am. Chem. Soc.* **1998**, *120*, 4690(b) Darensbourg, D. J.; Wildeson, J. R.; Lewis, S. J.; Yarbrough, J. C. *J. Am. Chem. Soc.* **2002**, *124*, 7075(c) Darensbourg, D. J.; Billodeaux, D. R.; Perez, L. M. *Organomet.* **2004**, *23*, 5286.

(39) (a) Becke, A. D. *J. Chem. Phys.* **1993**, *98*, 5648(b) Frisch, M. J.; Trucks, G. W.; Schlegel, H. B.; Scuseria, G. E.; Robb, M. A.; Cheeseman, J. R.; Scalmani, G.; Barone, V.; Mennucci, B.; Petersson, G. A.; Nakatsuji, H.; Caricato, M.; Li, X.; Hratchian, H. P.;

Izmaylov, A. F.; Bloino, J.; Zheng, G.; Sonnenberg, J. L.; Hada, M.; Ehara, M.; Toyota, K.; Fukuda, R.; Hasegawa, J.; Ishida, M.; Nakajima, T.; Honda, Y.; Kitao, O.; Nakai, H.; Vreven, T.; Montgomery Jr., J. A.; Peralta, J. E.; Ogliaro, F.; Bearpark, M.; Heyd, J. J.; Brothers, E.; Kudin, K. N.; Staroverov, V. N.; Kobayashi, R.; Normand, J.; Raghavachari, K.; Rendell, A.; Burant, J. C.; Iyengar, S. S.; Tomasi, J.; Cossi, M.; Rega, N.; Millam, J. M.; Klene, M.; Knox, J. E.; Cross, J. B.; Bakken, V.; Adamo, C.; Jaramillo, J.; Gomperts, R.; Stratmann, R. E.; Yazyev, O.; Austin, A. J.; Cammi, R.; Pomelli, C.; Ochterski, J. W.; Martin, R. L.; Morokuma, K.; Zakrzewski, V. G.; Voth, G. A.; Salvador, P.; Dannenberg, J. J.; Dapprich, S.; Daniels, A. D.; Farkas, O.; Foresman, J. B.; Ortiz, J. V.; Cioslowski, J.; Fox, D. J.; Revision A.02 ed.; Gaussian, Inc.: Wallingford, CT, 2009(c) Klaus, S.; Vagin, S. I.; Lehenmeier, M. W.; Deglmann, P.; Brym, A. K.; Rieger, B. *Macromol.* **2011**, *44*, 9508.

(40) (a) Ma, J.; Li, Q.; Song, B.; Liu, D.; Zheng, B.; Zhang, Z.; Feng, Y. *J. Mol. Cat. B***2009**, *56*, 151(b) Iwasa, N.; Fujiki, M.; Nomura, K. *J. Mol. Cat. A***2008**, *292*, 67(c) Majoumo-Mbe, F.; Smolensky, E.; L^nnecke, P.; Shpasser, D.; Eisen, M. S.; Hey-Hawkins, E. *J. Mol. Cat. A***2005**, *240*, 91.

(41) (a) Guillaume, C.; Carpentier, J.-F.; Guillaume, S. M. *Polymer* **2009**, *50*, 5909(b) Kawalec, M.; Smiga-Matuszowicz, M.; Kurcok, P. *Eur. Polym. J.* **2008**, *44*, 3556.

(42) (a) Yamashita, M.; Takemoto, Y.; Ihara, E.; Yasuda, H. *Macromol.* **1996**, *29*, 1798(b) Agarwal, S.; Xie, X. *Macromol.* **2003**, *36*, 3545.

(43) (a) Poncelet, O.; Sartain, W. J.; Hubert-Pfalzgraph, L. G.; Folting, K.; Caulton, K. G. *Inorg. Chem.* **1989**, *28*, 263(b) Stevels, W. M.; Ankoné, M. J. K.; Dijkstra, P. J.; Feijen, J. *Macromol.* **1996**, *29*, 8296.

(44) (a) Barros, N.; Mountford, P.; Guillaume, S. M.; Maron, L. *Chem. Eur. J.* **2008**, *14*, 5507(b) Jenter, J.; Roesky, P. W.; Ajellal, N.; Guillaume, S. M.; Susperregui, N.; Maron, L. *Chem. Eur. J.* **2010**, *16*, 4629.

(45) Walshe, A.; Fang, J.; Maron, L.; Baker, R. J. Inorg. Chem. 2013, 52, xxx

(46) de Aquino, A. R.; Isolani, P. C.; Zukerman-Schpector, J.; Zinner, L. B.; Vicentini, G. *J. Alloy. Compd.* **2001**, *323-324*, 18.

(47) (a) Avens, L. R.; Barnhart, D. M.; Burns, C. J.; McKee, S. D. *Inorg. Chem.* **1996**, *35*, 537(b) Evans, W. J.; Kozimor, S. A.; Ziller, J. W. *J. Am. Chem. Soc.* **2003**, *125*, 14264(c) Takase, M. K.; Siladke, N. A.; Ziller, J. W.; Evans, W. J. *Organomet.* **2011**, *30*, 458.

(48) Gottlieb, H. E.; Kotlyar, V.; Nudelman, A. *J. Org. Chem.* **1997**, *62*, 7512.

(49) Perdew, J. P.; Wang, Y. *Phys. Rev. B* **1992**, *45*, 13244.

(50) Moritz, A.; Cao, X. Y.; Dolg, M. *Theor. Chem. Acc.* **2007**, *118*, 845.

(51) (a) Castro, L.; Yahia, A.; Maron, L. *Dalton Trans.* **2010**, *39*, 6682(b) Castro, L.; Yahia, A.; Maron, L. *ChemPhysChem* **2010**, *11*, 990.

(52) (a) Ditchfield, R.; Hehre, W. J.; Pople, J. A. *J. Chem. Phys.* **1971**, *54*, 724(b) Hehre, W. J.; Ditchfield, R.; Pople, J. A. *J. Chem. Phys.* **1972**, *56*, 2257(c) Hariharan, P. C.; Pople, J. A. *Theor. Chim. Acta* **1973**, *28*, 213.

(53) Schlegel, H. B. *J. Comput. Chem.* **1982**, *3*, 214.

(54) (a) Gonzalez, C.; Schlegel, H. B. *J. Chem. Phys.* **1989**, *90*, 2154(b) Gonzalez, C.; Schlegel, H. B. *J. Phys. Chem.* **1990**, *94*, 5523.

(55) Perrin, C. L.; Dwyer, T. J. *Chem. Rev.* **1990**, *90*, 935.

Future Work

This Thesis has investigated the physical and electronic properties of ten uranyl containing minerals. The potential of uranyl for C–O bond formation was also investigated. Some possible avenues of research leading from this work could include:

- Studying the redox chemistry of agricolaite, $\mathrm{K4[(UO2)(CO3)3]\cdot H2O}$, as this compound has stronger cation–cation interactions (CCIs) than grimselite and could serve to explore further the effect of CCIs on the stability and redox properties of uranyl minerals.
- Expanding the study to include uranyl silicate minerals would also have significance given the prevalence of these minerals in nature and the effect of these phases on the mobility of radionuclides in the environment.
- Reacting these minerals with Np(V) would also be a long-term goal as this could validate the potential redox activities of these minerals. It could also confirm the mechanism by which neptunium incorporates into minerals – whether through reduction to Np(IV) or oxidation to Np(VI). If metatorbernite behaves as torbernite then one would expect neptunyl to replace uranyl; I would be very interested to examine the electrochemistry of Np-substituted metatorbernite.
- In terms of the activity of uranyl complexes as catalysts, I believe that further investigation into reactions that are catalysed by electropositive or Lewis acidic compounds would give greater insight into the capabilities of uranyl. Expanding the research to investigate C–S or C–N bond formation would be fascinating – I believe that these may be possible given the correct uranyl sulfoxide or imide complex.